NASA Contractor Report 4582 - Vol-2

F/A-18 Forebody Vortex Control Volume 2—Rotary-Balance Tests

Brian R. Kramer, Carlos J. Suárez, Gerald N. Malcolm, and Bert F. Ayers

CONTRACT NAS2-13383
March 1994

National Aeronautics and
Space Administration

NASA Contractor Report 4582 – Vol-2

F/A-18 Forebody Vortex Control Volume 2—Rotary-Balance Tests

Brian R. Kramer, Carlos J. Suárez, Gerald N. Malcolm, and Bert F. Ayers

Eidetics International, Inc.
3415 Lomita Blvd.
Torrance, CA 90505

Prepared for
Ames Research Center
CONTRACT NAS2-13383
March 1994

National Aeronautics and
Space Administration

Ames Research Center
Moffett Field, California 94035-1000

TABLE OF CONTENTS

Table of Contents
(continued)

LIST OF FIGURES

NOMENCLATURE

A_j	blowing jet exit area, ft^2
A_s	blowing slot exit area, ft^2
α, AOA	angle of attack, degrees
β	sideslip angle, degrees
b	wing span, 2.245 ft
C_A	axial force coefficient (body axis)
C_l	rolling moment coefficient (body axis)
C_μ	pitching moment coefficient (body axis)
CN	normal force coefficient (body axis)
Cn	yawing moment coefficient (body axis)
CY	side force coefficient (body axis)
C_μ	blowing coefficient, $\frac{\dot{m}_j V_j}{q S}$
c	mean aerodynamic chord, 0.691 ft
cref	moment reference center, 0.25c
δ	vertical nose strake deflection (+, trailing edge left)
δr	rudder deflection (+, trailing edge left)
F.S.	fuselage station, inches on full-scale aircraft
M	Mach number
$\dot{m}$	mass flow rate, lbm / sec
$\dot{m}_j$	mass flow rate of the jet, $\rho_j A_j V_j$
$\dot{m}_{ref}$	free stream mass flow rate, ρSV
Φ	azimuth angle (from the windward meridian), degrees
q, Q	free-stream dynamic pressure, lbf / ft^2
ρ_j	air density at blowing jet exit, slugs / ft^3
ρ	free stream air density, slugs / ft^3
ω,w	rotation rate, rad/sec
Rn	Reynolds number
S	reference wing area , 1.44 ft^2
V	free-stream velocity, ft / sec
V_j	blowing jet exit velocity, ft / sec
V_s	blowing slot exit velocity, ft / sec
x	distance from tip of nose (model fuselage station), inches

SUMMARY

Forebody vortex control (FVC) techniques have been evaluated on a 6%-scale F/A-18 model in the NASA Ames 7 x 10-ft wind tunnel. Both static and rotary-balance experiments were conducted. Results of the rotary-balance experiments are reported in this volume (2) and static results are in Volume 1. Techniques included jet and slot blowing, rotatable miniaturized tip strakes and a unique tip-mounted vertical strake (rhino horn). Forces and moments and surface static pressures at three fuselage stations were measured. Reynolds numbers ranged from 0.387 to 0.636 x 10^6 based on wing mean aerodynamic chord. Only the techniques that appeared to be the most effective during the static tests were selected for the follow-on tests on the rotary-balance rig. These techniques can be reviewed in Volume 1. Those chosen for the rotary-balance tests were: (1) blowing jet located at F.S. 82.2, 150° azimuth from windward and canted inboard 60°, (2) blowing slot at the maximum half-breadth starting at F.S. 59.8 and extending to F.S. 85.8, (3) single and dual rotatable nose-tip strakes, and (4) pivotable vertical strake. The purpose of the rotary-balance tests was to evaluate the various techniques under rotary-flow conditions comparable to those that would be experienced by a full-scale aircraft rolling about the velocity vector at angles of attack up to 60° at rates at least up to 70°/sec. For a 6%-scale model and velocity of 150 ft/sec, the maximum rotation rate of the rig was 200 rpm. An existing Ames rotary-balance rig was refurbished and updated with new sting support hardware that allowed angles of attack up to 60° and sideslip angles up to 60°, depending on angle of attack. A new Macintosh-based data acquisition system using LabVIEW software was developed specially for these tests. In general, the effectiveness of each of these techniques for producing yawing moments was not diminished under rotary conditions. The effectiveness of the jets is relatively unchanged at non-dimensional rotation rates of $\omega b/2V$ up to 0.28. The slots behave only slightly different than the jets. While with jets the increment observed at static conditions is relatively unchanged with rotation rate, with slots, when the side of the forebody with blowing is rotated into the wind (right side blowing and positive rotation), the effectiveness decreases somewhat compared to static and when rotated away from the wind, it increases with rotation rate. The single strake showed that a positive yawing moment increment at static conditions would increase with positive rotation rate and decrease with negative rotation rate. This behavior is just the opposite to the blowing slots. The effectiveness of the dual strakes (with 150° spacing on the windward side of the forebody) with rotation direction is opposite to that just described for the single strake and is more like the behavior observed with the slot blowing. This opposite behavior with rotation rate is related to the static characteristic of the dual strake producing a yawing moment in the opposite direction to the single strake when rotating the strake(s) about the nose tip in the same direction. The vertical strake behaves much like the single strake under rotary conditions. The effects of Reynolds number on the effectiveness of all of the techniques under rotary conditions is minimal. Selected pressure distributions measured on the forebody and LEX showed clearly the effects of the various FVC techniques on the model surface under rotary conditions and correlated well with the measured forces and moments. Comparisons of baseline F/A-18 (without FVC) force and moment data with an earlier rotary-balance test at NASA Langley showed reasonably comparable results with the exception of axial force, which is due primarily to the differences in base-mounting and top-mounting (Langley) of the model.

1.0 INTRODUCTION

In order to provide for increased agility of existing and future fighter aircraft at high angles of attack, including the ability to roll robustly about the velocity vector, advanced aerodynamic control techniques are the focus of research in government laboratories as well as in industry. One of the techniques that is receiving significant attention and research resources is the technology of forebody vortex control.

The principal reason for the high interest in forebody vortex control technology is that it offers a realistic potential solution to high-angle-of-attack aerodynamic control deficiencies in the region where the vertical tail and conventional rudder become relatively ineffective. Unfortunately, this ineffectiveness often occurs in the angle of attack range for maximum lift and in the post stall regime where it is desirable to perform velocity vector rolls. An illustration of this degradation and the potential advantage of forebody vortex control is shown in Fig. 1. Without rudder power, other means are needed to impart the required yawing moment and coordinated rolling moment to produce a robust roll about the velocity vector. One means is with thrust vectoring, but it is expensive, heavy and, obviously, depends on having adequate engine thrust available.

An alternative, or perhaps complementary method, is through the controlled manipulation of the forebody vortices, either by some mechanical system which activates a strake or surface on the forebody, or by pneumatic means where the vortices are influenced by blowing with jets or slots on the forebody surface at the appropriate location. Control of the vortices provides the means for controlling the local side force on the forebody and the resulting yawing (and sometimes rolling) moments of the entire airframe.

The technology of forebody vortex control (FVC) was originated in the late 1970's and early 1980's and has been actively pursued by many researchers since, as evidenced by the examples of published work in Refs. 1 - 32. References 1 and 2 provide a summary of the technology from its inception until 1991. References 3-31 show the many and varied research investigations that have aggressively advanced our knowledge of this technical area. Reference 32 is an updated review of most of the published FVC research results from 1991 to early 1993. There are many research programs still in progress, with some focused on demonstrating the utility of forebody vortex control for specific aircraft, such as this report which documents forebody vortex control research performed on an F/A-18 model.

Experiments have been conducted under an SBIR Phase II contract with NASA Ames Research Center to evaluate several forebody vortex control techniques, including mechanical and pneumatic, for the F/A-18 fighter configuration. The experiments consisted of both static and rotary-balance tests in the Ames 7 x 10-ft low speed wind tunnel. The results of the static and rotary-balance experiments are reviewed individually in Volumes 1 and 2, respectively. Each of the two volumes stands alone, with some of the same introductory and background material provided in both volumes. Where required, reference is made from one volume to the other.

In addition to the present experiments focused specifically on F/A-18 forebody vortex control, there have also been numerous other experiments on the baseline F/A-18 that are very useful for comparison to the baseline configuration data of the present experiments. A very thorough data base has been documented in Ref. 33 by Erickson et. al. with a 6% scale model. These experiments acquired forces and moments, surface pressures, and extensive flow visualization. Reference 34 by Banks also investigates the baseline F/A-18 with a 16% scale model with heavy emphasis on surface oil flow studies.

The full-scale wind tunnel results reported in Refs. 8 and 18 show baseline F/A-18 data as well as forebody vortex control data. There are also flight data (Refs. 35-37) obtained at NASA Ames-Dryden Flight Research Facility on an F/A-18 (HARV) documenting surface and off-surface flow visualization and surface pressures. Some of these data are used in Volume 1 to compare to the static data from the present tests. Comparisons are also made to previous baseline F/A-18 rotary-balance data reported in Ref. 38, which were obtained in the NASA Langley Spin Tunnel.

1.1 FOREBODY VORTEX CONTROL TECHNIQUES

1.1.1 Pneumatic - Blowing Jets and Slots

The pneumatic techniques that have been investigated in the references and in the Phase I studies for the F/A-18 consist mostly of blowing jets that are tangential to the forebody surface or slots that are located near the forebody maximum half-breadth and blow tangential to the surface towards the leeward side. Both techniques are designed to alter the forebody vortices by controlling the behavior of flow separation and the strength of the vortices.

Early experiments investigated blowing circular jets that were either pointed straight aft or straight forward (Refs. 4-7, 9-11). Later experiments, specifically those conducted on the X-29A configuration (Refs. 12 and 13), discovered that canting the jets inboard up to 60° from the centerline of the forebody and slotting the jets provided a significantly higher forebody side force and yawing moment for the same blowing rate. With this background of experimental data, the present experiments included the investigation of forebody jets at several longitudinal and radial locations and with many different cant angles.

Blowing slots with the flow directed tangential to the forebody surface towards the leeward side were also included in the present tests. The slots were located at the same radial locations as for previous full-scale F/A-18 experiments in the Ames 80 x120-ft wind tunnel. The length of the slot was varied to determine the minimum length required to achieve the goals for producing yawing moments at high AOA. A detailed description of the placement of jets and slots on the model for the present tests is presented later in the discussion of the model.

1.1.2 Mechanical - Rotatable Tip Strakes, Vertical Nose Strake

The alternative to pneumatic systems is to influence the vortices by physically altering the surface of the forebody with a movable strake of some type. An extensive data

base exists for deflectable or retractable strakes on generic configurations (Refs. 3-7). A major research effort has been underway at NASA-Langley for several years and, most recently, full-scale wind tunnel tests were conducted in the Ames 80 x 120-ft wind tunnel to investigate large hinged conformal strakes on the F/A-18 forebody. A brief review of this work is discussed in Ref. 8. The mechanical concept that has been the focus of the work in both the Phase I water tunnel tests and the present wind tunnel tests for the F/A-18 utilizes miniaturized strakes that are fixed at the tip and are rotated around the forebody longitudinal axis. The incentive for the rotating tip strakes is to reduce the size of the physical surfaces required to influence the vortices sufficiently that strakes could realistically be considered for practical application in a production aircraft. The rotatable miniaturized strakes are described briefly in the review of the Phase I water tunnel experiments and in more detail in the discussion of the present wind tunnel tests.

The pivotable vertical nose strake is a small single strake mounted on the leeward meridian line of the forebody near the forebody tip that pivots about an axis perpendicular to the surface of the forebody, similar to a highly-miniaturized all-movable vertical tail or rudder mounted on the nose tip. This is an alternative means of manipulating the vortices with a very small surface without having to rotate the model tip, but instead rotate (pivot) only the strake.

2.0 OBJECTIVES OF EXPERIMENTS

The objective of the work reviewed in the two volumes of this report was to investigate a variety of FVC techniques in the NASA-Ames 7 x 10-ft wind tunnel specifically for the F/A-18, including mechanical devices and pneumatic schemes. The preceding Phase I studies were conducted in the Eidetics International Flow Visualization Water Tunnel and are reviewed in detail in Refs. 17, 21, and 29. Results from the water tunnel tests included both flow visualization and simultaneously measured yawing moments in response to the various techniques for manipulating the forebody vortices.

Blowing was investigated with 1) nozzles that were tangential to the forebody leeside surface, blowing aft and forward at various longitudinal and circumferential locations on the forebody and 2) longitudinal slots that were located near the maximum half-breadth of the forebody at various locations and with various lengths with the blowing sheet directed towards the leeside, creating a "Coanda" effect to enhance flow attachment. In addition, miniature forebody tip strakes, single and dual, that could be rotated to various radial angles around the longitudinal axis of the model were also investigated. The principle of the strakes was based on the well-known phenomena that the forebody vortices and resulting forebody surface pressure distribution is highly sensitive to minute geometry changes near the tip of slender forebodies at medium to high angles of attack. The tip strakes are designed to take advantage of this sensitivity in a controlled manner.

Figure 2 shows a sketch of the F/A-18 forebody model representing some of the techniques explored in the water tunnel. The model, consisting of only the front portion as shown, was 6% scale and the jets and slots were placed in the model as shown. The nose tip strakes were mounted on a rotatable tip section and could be remotely

rotated by hand during the water tunnel tests. The pivotal strake (the rhino-horn) was pivoted manually and set to different angles.

An example of the effect of manipulating the forebody vortices is shown in Fig. 3, where the orientation of the left and right vortices changes with blowing from a slot on either side of the forebody. This forced asymmetry creates a local forebody side force producing a substantial yawing moment.

All methods, pneumatic and mechanical, were found to be effective in generating controlled asymmetric vortices on the forebody and significant resulting yawing moments. All of the methods influence the forebody flowfield, the vortices and resulting moments by controlling flow separation on the surface of the forebody and vortex strength. Controlling separation results in controlling the strength and location of the resulting vortices. Maximizing the effectiveness of any of these methods will require an optimization study to select the proper location and to understand the dependency of the forebody forces on such parameters as blowing rate and direction and, for rotating tip strakes, the proper size, location, and configuration, i.e., single or dual, including spacing.

The results of the Phase I work showed clearly the potential merit of several techniques, and the Phase II work was proposed to investigate these techniques further with wind tunnel tests. The proposed wind tunnel tests were divided into two specific investigations. The first was to perform static tests, and the second was to perform rotary-balance tests to evaluate the effectiveness in the presence of a velocity-vector roll motion, which is primarily what FVC will be used for in real flight. The static experiments were performed in the NASA Ames 7 x 10-ft wind tunnel in the fall of 1992, and were followed by rotary-balance tests in late 1992 and early 1993. The results of the static tests are reported in Volume 1, and the rotary-balance results are presented in Volume 2.

3.0 ROTARY-BALANCE WIND TUNNEL EXPERIMENTS

Rotary-balance experiments determine the forces and moments of a model in a steady rotational motion about the velocity vector at fixed angles of attack and sideslip. The significance of this motion in the early days of rotary-balance testing was to simulate the flow conditions associated with aircraft in a spin motion and determine whether the moments were pro-spin or anti-spin in nature. This was an important test to establish the spin characteristics of an aircraft and to investigate configuration changes to solve any yaw/roll damping problems, if possible. This same motion, rotation around the velocity vector, is now considered to be a key maneuver for enhanced agility in combat for modern fighter aircraft. In order to properly assess the control power to produce a robust velocity vector roll (known as a loaded roll because the aircraft is rolling with significant lift forces due to angle of attack), it is necessary to not only determine the yaw and roll moments statically, but dynamically at the appropriate roll rates.

The focus of the present rotary-balance wind tunnel experiments was to evaluate in a rotary motion the best forebody vortex control techniques determined from the previous static tests. The maximum rotation rate required in the wind tunnel is determined by

matching the non-dimensional roll rate, sometimes referred to as the "reduced rotation rate" that is determined by the desired motion of a full-scale aircraft at typical flight conditions. The non-dimensional roll rate is expressed as $\omega b/2V$, where ω is the rotation rate (rad/sec), b is the wing span and V is the free stream velocity. If we choose a typical condition for a full-scale F/A-18 as velocity-vector roll rate of 60°/sec (up to 60° AOA) and free stream velocity of 150 ft/sec, then the non-dimensional rotation rate around the velocity vector would be 0.1396. For higher velocities, the non-dimensional parameter would be even less.

With the goal of reaching a non-dimensional rotation rate of 0.14 in the wind tunnel with a 6%-scale model at tunnel speeds up to 150 ft/sec, the maximum required rotation rate was 17.5 rad/sec or 168 rpm. As discussed later, the maximum rate of the rig during the experiments was 200 rpm, which resulted in maximum non-dimensional rotation rates of 0.175 for V=150 ft/sec.

3.1 FEASIBILITY STUDY TO REFURBISH EXISTING AMES ROTARY- BALANCE RIG

The initial task in this part of the contract was to perform a feasibility study to determine the level of effort in terms of time and cost required to refurbish the rotary-balance apparatus last used in the Ames 6 x 6-Ft Wind Tunnel in 1984.

The rotary apparatus, as originally built, is shown in the schematic in Fig. 4. A hydraulic motor is used to turn a shaft aligned parallel to the wind stream. The motor is supplied with high pressure hydraulic fluid from a hydraulic power unit with a 10 gpm pump at pressures up to 2200 psi. A pneumatic brake unit is provided as an emergency stopping system and as a "parking" brake to hold the rig when working on the model. A series of interchangeable stings was used to vary the angle of attack up to 30°. A six-component force and moment balance was mounted on the end of the sting. The balance wires pass through the hollow shaft and the center of the motor. A set of slip rings and brushes are used to transfer the signals to the non-rotating portion of the rig. The rig rotational speed is measured by a tachometer generator unit and the rig radial position is measured with a resolver. The rig has an electronic control system that provides commands to a servo valve unit mounted on the bottom of the rig as shown. The rig rotation speed is held constant at selected values with the tach generator signal used as a feedback to the servo controller. For the present tests, no camera mount was needed and the bent sting hardware was replaced by new hardware, described later in Section 3.3.

One feature that was required for the present tests was to provide pressurized air to the model. The rig was originally designed and built with this need in mind. A rotating seal arrangement was constructed to allow pressurized air to be introduced at the fixed shaft and, with a rotating seal, pass through to the interior of the rotating shaft. The air could then exit at the end of the rotating shaft near the model, as desired. The seal was never successfully tested and one of the critical tasks in refurbishing the rig was to provide a seal that would work properly.

The focus of the feasibility study was on finding and identifying all of the mechanical, hydraulic and electronic components of the rotary apparatus at Ames and to estimate

the cost of making the system operational again. This study was completed and a separate report was submitted in August 1991 documenting the results. The recommendations from this study were that the rotary-balance experiments should be pursued and that the development of the rotary-balance apparatus and data acquisition hardware and software appeared to be feasible under the present contract with appropriate support required in certain areas from NASA Ames.

3.2 ROTARY BALANCE REHABILITATION

The initial step to provide an operational rotary-balance system for testing in the Ames 7 x 10-ft wind tunnel was to ship the existing rotary-balance equipment, including rotary-mechanism hardware, hydraulic power supply and controls instrumentation to Eidetics for assembly and checkout in Eidetics' laboratory. The rotary mechanism was disassembled, cleaned and reassembled. The hydraulic power supply was installed and run initially with the existing hydraulic oil in the reservoir to flush the plumbing and the pump and to collect any contaminants in the system filters. After several hours of running, the hydraulic oil was replaced with new oil, all filters were changed and the system, including the hydraulic drive motor and a flushing block, was run again in preparation for operation with a new servo valve (the old servo valve was not available from Ames and a new one had to be purchased). The control system and servo valve were then installed and, after a period of familiarization with the control system electronics, the system was operated with the control system in command up to 200 rpm with no significant load on the motor.

Once the system was functioning as expected, the next, and crucial task, was to design and implement the required rotating seals in the rotary mechanism to provide the means for supplying high pressure air to the model for forebody blowing during rotation. The original rig design had provisions for seals, but preliminary experiments at Ames several years ago did not successfully demonstrate them to work. A new seal retainer ring was designed by Eidetics to use Parker PolyPak seals to provide the required pressure sealing capability (up to 100 psi) with the shaft rotating up to 200 rpm. The seals were installed and tested. After experiencing some problems with the seals heating up and loading the rotating system sufficiently to prevent the maximum 200 rpm rotation rate, the seals were modified by removing the built-in O-ring. This change reduced the friction of the seal on the rotating shaft without losing the ability to hold pressurized air and solved the seal heating problem. For added assurance that the seal problem would not return once the rig was installed in the wind tunnel, the seals were replaced with nearly identical ones, but with an impregnated lubricant to further reduce the friction. As a result of these efforts prior to the wind tunnel tests, the seals were never a problem during the wind tunnel test.

3.3 NEW ROTARY HARDWARE

Use of the existing rotary-balance apparatus for these tests included a plan to design and build new sting apparatus hardware for supporting the model on the rotary hardware. The original hardware was designed for bodies of revolution, and angle of attack could be varied only up to 30° by physically removing and replacing a bent sting for each angle of attack. These stings were not suitable for the F/A-18 tests. The new

hardware shown in Fig. 5 was designed to provide manual changes in angle of attack and sideslip by moving and pinning the sting assembly to pre-drilled hole locations (every 3° from 0° to 60°) on the C-strut. Angles of sideslip at specific angles of attack are provided by rolling the straight sting around its own axis in the strut arm in combination with the appropriate angle setting on the C-strut.

Following design reviews and approval by Ames personnel to verify the designed configuration for functionality and to demonstrate that the new hardware met all safety criteria for testing in the Ames 7 x 10-ft wind tunnel, Eidetics contracted with Dynamic Engineering Incorporated to construct the hardware which was delivered in May 1992. Photographs in Fig. 6 show the assembled rig mounted on the test stand in Eidetics' Laboratory. Also shown are the hydraulic pump apparatus and the protective shield around the rig. The rig is statically balanced around the rotation axis by adding calibrated weights to the end of the appropriate arm. Once the rig was declared operational with rotation rates up 200 rpm, the refurbishment was declared completed and the rig was available for the wind tunnel tests.

It should be noted that the new model support hardware for the rotary rig was designed very conservatively for operation at 200 rpm. Later, in a rotary-balance test on an AGARD generic fighter model immediately after the F/A-18 tests, the rig was cleared to run at a maximum of 350 rpm, a speed that could be considered as a practical maximum speed for any future tests.

A complete description of the new rotary-rig system and hardware and the operational procedures can be found in the "System Description and Operational Procedures Manual" delivered to Ames with the rig in November 1992.

4.0 MODEL AND MODEL INSTRUMENTATION

4.1 MODEL DESIGN AND CONSTRUCTION

The model for these experiments is a new 6% scale model designed and built by Eidetics International. The model exterior lines were determined by borrowing the Navy/McAir 6%-scale force and moment steel model to make a pattern and permanent mold. From this mold, a fiberglass shell with an accurate external shape was fabricated. The forebody part of the mold was then also used to make several forebody (nose portion only) model pieces.

The model structural design was required to accommodate the loads of both the static test and the rotary-balance tests. The fiberglass shell of the model attaches to a structure that consists of base plates, six aluminum bulkheads and stringers. The structural center of the model is a stainless steel balance block with mounting tabs for the wing and the base plates. The wings have a steel core to carry the aerodynamic loads, and the airfoil shape is built up with wood and fiberglass around the structural center. The leading and trailing-edge flaps and ailerons were all deflectable; however, the test was conducted with the leading edge flaps only in the maneuver position (34°) and the trailing-edge flaps undeflected. The ailerons were tested in the plus and minus 10° positions to estimate roll control power. The vertical tails have an aluminum core

and rudders that can be deflected plus and minus 30°. The horizontal tails were fixed at 0° for the entire test. Photographs in Fig. 7 show the model structure, components, and the assembled model.

4.2 REMOVABLE FOREBODIES

The nose section of the model was removable so that different forebody vortex control devices could be studied by replacing the nose section (See Fig. 8). The baseline configuration was an unmodified nose cone (Fig. 8a) that is identified as the "clean nose." There were five blowing jet positions, three of which were at 135° azimuth from the windward meridian, at three fuselage stations (noses 1, 2, 3). The middle position (x = 0.93 inches model scale) corresponded to the furthest aft fuselage station that was tested in the 1992 test of the F/A-18 in the 80x120 Foot Wind Tunnel at NASA Ames (Refs. 8 and 18). The furthest aft position (x = 1.30 inches) corresponds to 0.5 equivalent nose diameters aft of the nose tip. At this fuselage station, in addition to the jet at 135°, there were jets at 150° and 120° (noses 4 and 5). All of the nozzles, except the furthest forward, had the ability to rotate to any desired angle in order to try to duplicate the success of Guyton (see Ref. 12).

In addition to the jet blowing noses, there was a slot blowing nose. The slotted nose was a challenge to build at this scale. The slot width was held to a reasonably constant width with small metal shims between each of the four segments A,B,C and D (Fig. 8b). Unlike the full scale aircraft, size constraints made it impossible to have separate supply pressure lines to each slot segment. Instead, the interior of the nose was made into two plenums, one for the left side and one for the right, that supplied all of the segments. The slot size tested was 0.006 inches wide with a length of 2.58 inches beginning 0.56 inches from the nose tip. This was the slot configuration that showed the highest effectiveness in the 1992 test of the F/A-18 in the 80x120 Foot Wind Tunnel at NASA Ames (Refs. 8 and 18). Different slot lengths were tested by taping over portions of the slot.

In addition to the pneumatic control systems, several mechanical miniaturized strake configurations were tested. The first type of control scheme was the rotating nose tip strake. The strakes were implemented as a single strake or as dual strakes (fixed-pair rotating together) on the very front of the nose cone, as shown in Fig. 8c. Two strake sizes were tested; the one depicted in Fig. 8c is the small strake and the one referred to as large strake in the Results Section has the same length but twice the width. The strakes rotate about the axis of the radome, driven by a 12 Volt electric motor turning at 1 rpm. The position of the strakes is measured by a potentiometer geared to the motor shaft. An additional nose piece with a miniature vertical nose strake is shown in Fig. 8d. Although similar in shape to the rotating nose tip strakes, the vertical nose tip strake is mounted on the leeward meridian line of the forebody and pivots about an axis perpendicular to the surface of forebody.

4.3 MODEL INSTRUMENTATION

The detailed design of the model was significantly influenced by the placement of instrumentation and sensors. The model has a very high density of instrumentation, including a multi-port electronic scanning pressure module, pressure ports and tubing,

unsteady pressure transducers, pneumatic control valves, plenum pressure transducers and thermocouples, dc motor and potentiometer for the rotating tip strakes, etc. in addition to the basic 6-component force and moment balance (Fig. 9a). The model volume is quite small, and the challenge of placing all of the planned instrumentation in the model was significant.

The aerodynamic forces acting on the model were measured using a 1.5 inch Task Mark IIE six component internal strain gage balance. These force measurements were used to calculate the standard body and stability axis coefficients.

A System 8400 (by Pressure Systems, Inc.) electronically scanned pressure acquisition system was used to control a 64 port (ESP-64) module in the model. The model was designed for a 48 port module, but the 64 port was the only one available and the additional size did not cause any problems. Figure 9b shows the location of the 48 pressure taps on the model. The three fuselage stations (F.S. 142, 253, and 357 full scale) that were used corresponded to locations used for the 80X120 test and the F/A-18 HARV experiments. An extra complexity was added for the rotary test because there was no way to pass the PSI reference pressure across the rotating interface (without additional design of another pneumatic slip ring). The back side (reference) of the PSI module was teed to an absolute pressure transducer inside the model which was left open to the model cavity pressure. Knowing the model cavity pressure and the atmospheric pressure, the pressure readings in the PSI system were then corrected to the proper value. The calibration lines were attached with quick disconnect lines to allow calibration of the PSI system transducers when the rig was not spinning. The lines were then disconnected and taped to the rotating part of the support for testing.

The pneumatic forebody vortex control system consisted of a pair (right and left) of two-position valves to turn the flow on and off remotely, and a pair of large diameter plenums with a total pressure probe and transducer, and a thermocouple. These measurements were used to determine the isentropic flow conditions at the jet or slot exit. Based on previous experience at NASA, a flow calibration was performed on both the jet and slot configurations. Using a highly accurate (0.1 gram) Toledo scale and a regulated air supply tank, the true mass change was used to calibrate both an Omega volumetric flow meter and the model's plenum (which used isentropic assumptions). The flow meter was found to be in good agreement (3 percent) with the measured change in mass, but the isentropic equations for the plenum required significant correction in the form of a "discharge coefficient" (on the order of 0.70). Operation of the mechanical systems for the strakes required replacing the pneumatic control components in the forward fuselage section with the strake drive motor and potentiometer.

5.0 EXPERIMENTAL SETUP

5.1 WIND TUNNEL DESCRIPTION

The Ames 7 x 10-ft wind tunnel is a closed-throat, single return atmospheric tunnel with about 10% air exchange accomplished by a ventilating tower. The tunnel is powered by

a single 8-blade, 8.5m (28 ft) diameter fan driven by a 1600 HP synchronous motor located in the nacelle in the return passage.

5.2 ROTARY-BALANCE INSTALLATION

Since the rotary rig had never been operated in the 7 x 10-ft tunnel, a new support structure to mount the rig in the test section had to be designed and built by Ames. This structure along with the rotary-balance rig are shown in the drawings in Fig. 10 and are also shown in the photographs in Fig. 11. The rotary apparatus was mounted in the end of the circular pipe supported by the large A-frame stand. The hydraulic pump system was located under the test section. The hydraulic and electrical lines were routed to the rig along the top of the cylinder. The balance and instrumentation wires were routed to the model through the center of the cylinder.

5.3 TEST CONDITIONS

The test was run at a dynamic pressure of 27 psf (approximately 150 ft/sec) and Reynolds number of 0.92×10^6 per foot. A few runs were made at a dynamic pressure of 10 psf (90 ft/sec) and R= 0.56×10^6 per foot to explore Reynolds number differences and, consequently, extending the maximum non-dimensional rotation rate to a higher value (up to 0.28).

6.0 DATA ACQUISITION AND REDUCTION SYSTEM

The data collection system used for the rotary test was a stand alone, Macintosh based system. The Macintosh based data acquisition system was chosen for several reasons. First, NASA Ames is beginning to use more of this type of system for both data acquisition and instrument control (via the GPIB interface). Secondly, the check out of the rotary balance system was to be done at Eidetics. With a Macintosh system in-house, the entire system could be exercised prior to moving it to NASA for the test. Finally, because Eidetics personnel were not located close to the NASA programmers, it was felt that there would be less chance of error and more flexibility for modifications and updates if they were done in-house by Eidetics. This has proven to be a wise choice.

6.1 DATA ACQUISITION HARDWARE

The data acquisition system consisted of a Macintosh IIfx with 32 MB of RAM, a 300 MB hard drive, a PLI 88 MB removable hard drive, a 21 inch 8 bit Cal Comp monitor, an Asante Ethernet card, an uninteruptable power supply, a LaserWriter IIg printer, a NB-MIO-16XL-18 Analog to Digital (A/D) card, a NB-DMA-2800 Direct Memory Access (DMA) card, and an SCXI signal conditioning system (one SCXI-1001 chassis and four -1121 modules). The assembled system is shown in Fig. 12a. The software used was primarily National Instruments' LabVIEW 2.2.1 with some stand alone code (LabVIEW calls these Code Interface Nodes, or CINs) written in Think C 5.0.2. The Ethernet handling was done with NCSA Telnet and MacTCP. Plotting of the data was done using KaleidaGraph.

This data acquisition system was designed to process 16 channels of transducer input of various types. As shown below, the system handled strain gages, thermocouples, pressure transducers and potentiometers.

CHANNEL

0	forward normal force gage (N1)	8	left blowing pressure
1	aft normal force gage (N2)	9	right blowing pressure
2	axial force gage (AX)	10	blowing temperature
3	forward side force gage (S1)	11	internal ref press
4	aft side force gage (S2)	13	tunnel total pressure (PT)
5	rolling moment gage (RM)	14	tunnel static pressure (PS)
6	rig rotation speed (w)	15	tunnel total temperature (TT)
7	pod roll angle	16	barometric pressure

The signals from the transducers used were first passed through the slip ring and then sent through the SCXI signal conditioning chassis (see Fig. 13). The chassis had four SCXI-1121 modules installed which each had four channels of isolation amplifiers with their own excitation voltages. The gains were jumper selectable on the modules, which meant that changing gains after the beginning of the test was kept to a minimum. The signals were multiplexed together in the chassis processor and passed as Channel 0 input to the NB-MIO-16XL-18, 16 bit analog to digital board in the Macintosh. This signal was then passed to the computer through an NB-DMA-2800 Direct Memory Access board that was also installed in the Macintosh.

6.2 DATA ACQUISITION SOFTWARE

LabVIEW is a graphical programming environment written by National Instruments (see Ref. 39) that translates a graphical flow representation of a system (Fig. 12c) into 'C' code and compiles it. The system proved to be very flexible and easy to use. The one exception to this was the input and output of text files for documenting the data taken. There was only one instance where the built in functions were not adequate to perform the necessary data manipulation. This problem was solved by using a code interface node to read a small 'C' program that sorted rotary tare data.

The routines written for LabVIEW (called Virtual Instruments, or VIs) are written to be callable from one central panel named "Eidetics Main Panel" (Fig.s 12b and c). When this panel is started, it gives the user the option of loading in all the global variables from a default file, or selecting the file of their choice to read the globals from. In almost all cases the default (assorted GLOBALS: global file) should be used because it will contain the most recent values from the previous run. Once this panel is running, the user has several options to choose from which access the main portions of the program. The program is broken up into several major pieces: data acquisition, zero and span correction, balance handling, transducer handling, weight tares, rotary tares, coefficient calculation, and all file input/output. These different pieces are called essentially as subroutines during the appropriate operations. For example, taking a data point will require most of the routines mentioned and will create a raw data file and an engineering units file. Figures 12d and 12e show the front panels used to monitor the signals that are to be acquired.

6.2.1 The Acquisition of Data

The LabVIEW program was used to tell the data system when to take data and provided all of the input parameters needed to configure the system such as data rate, channels to scan and gain settings. The Virtual Instrument (VI) that is called to do all data acquisition tasks is called "acquire SCXI 16 chan." This VI begins the data acquisition process and is then responsible for making sense out of the multiplexed stream of data that it receives through Channel 0 of the A/D converter. The VI returns a two dimensional array of data that includes the channel numbers of the data in the sample and the raw voltages that were read for each channel. At this point the data have been adjusted for the individual channel gains, but not for the steady state zeros, so it indicates the true voltage from the transducer.

6.2.2 Zero and Span Correction

The handling of the zeros and span correction was done in the same manner as the NASA Ames Standard Wind Tunnel System (SWTS) and most of the files that were used are found in the folder "Zeros and Cals." Figure 12j shows the front panel that controls the acquisition of zeros and cals. The methodology explained in Ref. 40 involves taking data before each run and comparing it to similar values obtained during the transducer calibrations. The basic form of the correction equation (Equation 4 in Ref. 40) is as follows:

$$C_X = \frac{REF_X}{(CTS_{XCAL} - CTS_{XZERO})}(CTS_X - CTS_{XZERO})$$

The terms with CTS refer to Beckman counts, which in our case is really raw voltage. The term "REFx" is the span (cal - zero) that was recorded in the calibration lab for a particular transducer. The term "CTSxzero" means that this term was taken at the beginning of the run in a static unloaded condition. The subscript "CTSxcal" refers to the point taken at the beginning of the run where the signal leads of the transducers were shorted across a known shunt resistor that was used during the calibration. "CTSx" is the uncorrected voltage while "CTSxzero" is the data zero.

In order to keep track of these terms for all of the 16 channels, global arrays (file "zero/rcal global 16") were used that could be accessed from any subroutines. These arrays, along with most of the other global variables, are stored in the file "assorted globals: global file" and when used in conjunction with a data run they are also stored in a file in the "Z&R Data" folder which is used if any post processing is required.

6.2.3 Balance Handling

The files associated with the balance are found in the folder "Balance Stuff." In addition to the corrections to the voltage described above, in the Zero and Span Correction section, another term called the bias is added to the equation. The purpose of this term is to make sure that the balance calibration is entered in the correct portion of the curve when the balance is initially loaded when the zeros are taken. This happens regularly

when the model is mounted on the balance. This is handled in the same way as the NASA Ames Standard Wind Tunnel System (SWTS) and can be seen in Equation 5 of Ref. 40.

The amount of voltage in the bias term that is added into the equation must be subtracted back out, in engineering units, after the balance calibration has been applied. In addition to the primary balance calibration terms, a set of interactions between the gages is applied in an iterative manner. This procedure is described in Ref. 40. The LabVIEW routines that are used to do the balance handling, particularly "balance eu 3.0 without read," "interactions read 2.0" and "balance interactions 3.0," were obtained from NASA Ames and were checked out there to assure that they provide the correct interactions.

6.2.4 Transducer Handling

The calibrations for the transducers were applied to the corrected voltages by using a polynomial of up to fifth order. The information for the calibrations is stored in a file called "XDCR Calib File" and the only way to change this file is to edit it with a word processor. While the main program is running, the only option available to the user is to use a different file name. There can be any number of XDCR files available to allow switching to different experimental setups and showing some history if transducers are replaced during the test.

6.2.5 Weight Tares

Weight tares are only necessary so that the weight can be accounted for when the rig is not rotating. This is determined by the program by looking at the rotation speed during the calculation of the final coefficients. The choice was made to use the same method as SWTS for Bias readings to account for the weight. This meant that the weight tares were not used to process the data, but instead were used for a reference to check the magnitude of the Bias corrections. After a significant model change, the model was positioned at 0°,90°,180° and 270° to provide enough data to redundantly solve for the model weight and center of gravity (CG). The weight tare program uses the following equations:

$$W = \frac{-A_2}{\sin\theta} = \frac{N_{F0}+N_{A0}}{\cos\theta} = S_{F1} + S_{A1}$$

$$X_{CG} = X_N\left[\frac{N_{F2}-N_{A2}}{N_{F2}+N_{A2}}\right] - Z_{CG}\tan\theta = X_S\left[\frac{S_{F1}-S_{A1}}{S_{F1}+S_{A1}}\right]$$

$$Y_{CG} = \frac{-R_2}{N_{F2}+N_{A2}} = \frac{-X_S(S_{F0}-S_{A0})}{(N_{F0}+N_{A0})\tan\theta}$$

$$Z_{CG} = \frac{-R_1}{S_{F1}+S_{A1}}$$

The symbols N, S, A and R refer to the balance forces in the direction of Normal, Side, Axial, and Roll. The subscript F indicates the forward gage while A is the aft gage. The

pitch angle θ is set by the 'C' strut. The numerical subscript indicates the point number of the weight tare where 0 is upright, 1 is rolled 90° and so on. To increase accuracy, the data from point 0 and 2 were averaged, as were points 1 and 3, and used in the equations shown.

The equations above calculate the weight and cg in several different ways, but it is up to the user to determine which method will yield the most accurate answer for a given configuration. For example, if the model is level, the axial gage will not provide a reasonable number for the model weight. However, if the model is at an angle of 30° or more, the axial force gage will provide the best answer for weight because the Task 1.5 Mark IIe has a 100 pound axial force gage but two 500 pound gages in the normal force direction. Therefore, the user must be aware of these sensitivities when selecting the method to use for each weight tare. Figure 12i shows the LabVIEW front panel for the weight tare processor.

6.2.6 Rotary Tares

Acquiring force and moment data from a rotary-balance is similar to standard methods for acquiring data for static tests. The main exception is the need to account for wind-off inertial loads generated by the model during rotation. Basically, the model will impart forces and moments to the balance during rotation because of the centrifugal force effects. The following equations describe the moments that are generated:

$$L = \omega^2(\sin\beta)(\sin\alpha)(\cos\beta)(I_Y - I_Z)$$

$$M = \omega^2(\sin\alpha)(\cos\beta)(\cos\alpha)(I_Z - I_X)$$

$$N = \omega^2(\sin\beta)(\cos\alpha)(\cos\beta)(I_X - I_Y)$$

Because the inertias and angles (sting and model deflect slightly under load) are not known precisely, inertial loads must be measured experimentally with the wind off and then subtracted from the wind-on data. For each unique model configuration and attitude on the rig, there must be a wind-off tare to subtract from the wind-on measurements. If the wind-off measurements are to be only those forces contributed by the model mass moments of inertia, then, in principal, the tares must be conducted with the tunnel at vacuum. This is not possible, so the compromise is to measure the forces and moments with the rig rotating in both clockwise and counter-clockwise directions and then the two sets of measurements are averaged. While this is not the same as acquiring the tares at vacuum where there is no influence on the rotation model from surrounding air, it is a good approximation where the influence of ambient air on side force, yawing moment, and rolling moment from equal but opposite rotations tend to cancel each other. Normal force, pitching moment and axial force are not canceled by opposite rotation directions but the ambient air effects are usually small enough to be ignored.

The method for testing is to acquire a rotating tare (using LabVIEW panel in Fig. 12g) prior to each run where either the model is changed or the angle of attack and sideslip have changed. To do this, the model is spun at a number of different rotation speeds, in both directions, and data are recorded for each one. Each balance gage's force output

is then plotted against the rotation speed squared and a polynomial curve fit is calculated. The VI "Curve Fit Selector" (Fig. 12h) allows the user to plot the data on the screen and change the order of curve fit until it appears to match the data in an acceptable manner. A curve for the average of the positive and negative spin direction curve fits is then created. The user steps through all six balance components and after all the curve fits are selected, the program stores all of the "average" curve fit information into a rotary tare file. When the data for a wind-on run are reduced, the rotary tare file is read and a force or moment is derived from the polynomial equation that is then subtracted from the wind-on data. It should be noted that because the choice was made to use the SWTS type Bias system to statically remove the model weight as a zero, all of the balance readings for a rotating run will have their averages offset by this Bias. Because both the rotary tare and the wind-on data had the same offset (in the form of the zero), it was subtracted out when the rotary tare was applied.

7.0 RESULTS AND DISCUSSION

The data presented in this report are in the form of the longitudinal and lateral-directional force and moment coefficients (6 in all) plotted against the non-dimensional rotation parameter, $\omega b/2V$, in both clockwise (+) and counter-clockwise (-) directions. Data were also acquired at zero rotation rate. The maximum rotation rate was 200 rpm (20.93 rad/sec). For the tests at a dynamic pressure of q=27 psf (velocity of 150 ft/sec and Rn = 0.636×10^6), the maximum non-dimensional rotation rate is 0.175. For the few runs at q=10 psf (velocity of 90 ft/sec and Rn = 0.387×10^6), the maximum non-dimensional rotation rate is 0.28. Unless otherwise noted in the figure or in the figure titles, the Reynolds number based on wing mean aerodynamic chord is 0.636×10^6.

7.1 BASELINE CONFIGURATION

The rotary-balance data in this section document the tests on the basic configuration (without forebody vortex control methods active), including the effects of pressurizing the blowing lines to check for balance interference, rudder deflection, and sideslip angles. The data at zero rotation rate are also checked against the data acquired during the static test to determine if there are any significant differences due to the different sting mounting arrangement and, generally, to check for repeatability. The effects of rotation rate on forebody vortex control techniques are discussed in sections following this one.

7.1.1 Force and Moment Coefficients

As in the static tests, the model was installed on the rotary rig with a tube along the sting into the interior of the model to carry pressurized air to the forebody for the blowing jets and slots. To check for possible influence of the tube on the balance readings when pressurized, a simple test was performed over the range of rotation with and without pressure (with no flow through the control valves in the model, i.e., no flow out of the forebody). Figure 14 shows the comparison and, clearly, the influence of the pressurized tube is negligible.

The zero rotation rate datum point was also compared to the data taken previously during the static test. The mounting arrangements for the model are different for these two cases and it is useful to be aware of any differences. Also, rotary-balance data were taken on a 1/10th scale model of an F-18 in the NASA Langley Spin Tunnel in 1984 (NASA CR 3608, Ref. 38). Figures 15 to 18 show the comparisons between the various sets of data at angles of attack of 30°, 45°, 50°(51°) and 60°. Generally, agreement between the static and rotary data is excellent. The present rotary data compare quite favorably to the previous NASA results, particularly the slopes of the coefficients with rotation rate. There are some offsets in axial force, which is the least accurate of all of the force measurements and is quite dependent on the means of mounting. For the present tests the model is mounted through the base, and in the Langley tests it is mounted through the top in front of the vertical tails. At 50° and 60°, there are some offsets in yawing moment and side force, likely due to slight differences in the symmetry characteristics of the forebody flow, and there is a small difference in the slope of the rolling moment with rotation rate. The differences are considered to be small considering the data were taken in different tunnels with different models and very different mounting arrangements.

The effectiveness of a full rudder deflection (trailing edge left) over the rotation rate range is shown in Figs. 19 to 21 for angles of attack of 45°, 51° and 60°. As expected, the rudder does very little above 45° and the incremental forces and moments are constant for all rotation rates.

The effects of -10° sideslip (nose right) are shown in Figs. 22 to 24 for angles of attack of 45°, 51° and 60°. The change in the lateral-directional coefficients are as expected for a nose right sideslip and the incremental changes are nearly non-variant with rotation rate.

7.1.2 Pressure Distributions

Pressure measurements were made on the forebody and the LEX at the three fuselage stations shown in Fig. 9b. These stations were chosen to match some of the locations of pressure taps in the full-scale F/A-18 model tested in the Ames 80 x 120-Ft Wind Tunnel (Refs. 8 and 18) and in the flight test F/A-18 HARV. Only the results from 51° AOA at the two forward fuselage stations (F.S. 142 and 253) are presented here. Figure 25a shows the "clean nose" configuration at 51° AOA as measured in the static test versus the rotary test. (Note the static data were actually obtained at $\alpha = 50°$.) The agreement between data for the two tests for the forward fuselage station is very good. The forebody pressures (at F.S. 142) are seen to be very symmetric about the geometric plane of symmetry, which is consistent with the side force and yawing moment measurements that show nearly zero values for the same angle of attack range. The forebody cross section at this fuselage station is slightly elliptic with the major axis in the vertical direction. The peak suction at all angles of attack is in the vicinity of a radial angle of 70° to 80° from the windward stagnation line. The Reynolds number based on the width of the forebody cross section at this point (2.1 inches at 6% scale) is 0.161×10^6 which means that the flow is most likely laminar in character. There is no surface grit to artificially trip the boundary layer. The pressure distributions indicate that the location for primary separation is near a radial angle of approximately 120° to 130°. There is no evidence of a strong suction peak on the leeward side due to

the primary vortex flow reattachment, as is often seen in flows at higher Reynolds numbers.

The pressure distribution on the LEX (F.S. 253) shows very good agreement on the lower surface (the unfaired points), but a small difference in the magnitude of the suction appears on the top of the LEX (the faired points). The data from the rotary balance tests were acquired at $\alpha = 51°$ and the data from the static test were acquired at $\alpha = 50°$. The static data in Volume 1 (Fig. 28b) showed that the lower surface pressures on the LEX are nearly insensitive to angle of attack; however, the difference between the upper surface pressures between $\alpha = 50°$ and $\alpha = 55°$ is substantial. The difference observed in the present figure between $\alpha = 50°$ and $\alpha = 51°$ is consistent with the trend in the static data in Fig. 18b.

Figure 25b shows the effect of rotation on the forebody and LEX pressure distributions. The forebody (F.S. 142) is now moving in a circular pattern that is producing the equivalent to a local sideslip condition. The most obvious effect is the increase in the pressure suction peak on the leeward side of the body and the decrease on the windward side. The symmetric suction peaks have moved from radial angles of 80° and 280° azimuth to approximately 50° and 250° azimuth for negative ω and 110° for positive ω. Integration of the pressure distributions would show that the forebody, at least at this fuselage station, provides an anti-spin input as expected. The pressure distributions for the positive and negative rotations are nearly mirror images.

The effect of rotation on the LEX is less dramatic because it is closer to the spin axis and therefore has a lower relative velocity. Figure 25b shows the LEX pressures (F.S. 253) also produce a small anti-spin contribution. The windward side of the LEX experiences an increase in pressure while the leeward side shows an increase in suction (more negative pressure). The pressure distributions on the LEX are also near mirror images for positive and negative rotation directions.

7.2 JET BLOWING

Results from the static tests (Volume 1) showed clearly that the best candidate tested with jets was the configuration designated NOSE 4 - 60° INBOARD. This configuration has the jets located 1.3 inches from the nose tip (F.S. 82.2 on full-scale F/A-18) at a radial angle of 150° as shown in Fig. 8, and the nozzles are canted 60° inboard. The rotary-balance tests concentrated on this configuration. One run was made with the jets mounted flush with the forebody (NOSE 6 - 60° INBOARD) at 51° AOA to assess the difference in effectiveness between flush mounted nozzles and nozzles above the surface with the bottom edge adjacent to the forebody surface (as were all the nozzles except NOSE 6). In order to assess the effects of Reynolds number, runs were also made at a reduced dynamic pressure (q=10 psf instead of 27 psf) resulting in a Reynolds number decrease from 0.92×10^6 per foot to 0.56×10^6 per foot (0.636×10^6 to 0.387×10^6 based on wing mean aerodynamic chord of 0.691 ft). Comparisons are shown between data at both Reynolds numbers.

7.2.1 Force and Moment Coefficients

The effects of rotation rate on NOSE 4-60° INBOARD at angles of attack of 30°, 45°, 51° and 60° are shown in Figs. 26 to 29. At 30° AOA the effect of jet blowing is small, as observed in the static tests. There is little variation in the effectiveness with rotation rate, with the exception of rolling moment. The rolling moment indicates that the blowing has almost no effect at positive rotation rates but definitely shows a differential between left and right blowing at zero and negative rotation rates. The differential does not change much, however, with changing negative rotation rates. Why it only appears for negative rotation rates and not positive is not known. At 30° AOA (Fig. 26), there is a very sensitive relationship between the forebody and LEX vortices. Any small asymmetry in the forebody vortices has a significant influence on the LEX vortices, particularly the longitudinal location of vortex burst, which in turn has a large effect on wing lift. A small asymmetry in LEX vortices could significantly affect the flow on the wings and appear as different rolling moments.

At 45° AOA (Fig. 27), there are more significant effects of the jet blowing on the side force, yawing and rolling moments, since the forebody vortices are stronger. The effects of blowing at various rates, left and right, on side force and yawing moment are not appreciably changed by rotation. The rolling moment shows a more complex dependency on blowing rate and rotation rate. Generally, the slopes of the various curves are similar, but the level of rolling moment, particularly for the right side blowing cases, with rotation rate is not well behaved. The direction of the rolling moment increment relative to the baseline with right-side blowing depends on the level and direction of the rotation. Left side blowing does not appear to have this characteristic. Again, as discussed above for 30° AOA, the LEX flow field is quite interactive with the forebody flow field and is very sensitive and responsive to any asymmetric influences from upstream flow.

At 51° AOA (Fig. 28), there is increased effectiveness of the jet blowing on the side force and yawing moment and significantly decreased effect on the rolling moment, demonstrating the decoupling of the forebody flow field and the LEX flow field at higher angles of attack. The LEX vortices are bursting at the LEX apex at this angle of attack and there is little contribution of the LEX to lift or rolling moment, even if the forebody vortices are asymmetric. The change in side force and yawing moment increments with rotation are minimal.

At 60° AOA (Fig. 29), there is less influence of jet blowing on side force and yawing moment than at 45° and 51°. Because there are four blowing rates right and left, the data have been split up to show right and left blowing effects on separate plots. The direction of the increments are as expected but the magnitude of the increments is more variant with rotation rate than at the lower angles of attack. This increased variance is, perhaps, not too surprising since at 60° AOA the forebody vortices have a stronger tendency to be asymmetric and, therefore, are more difficult to control at all rotation rates and consequent local flow angles at the forebody tip. It is interesting to note that at 60° AOA, the higher blowing rates contribute a nose-down pitching moment increment that decreases in magnitude with rotation rate.

The effects of a sideslip angle of -10° (nose right) are illustrated in Figs. 30 to 32 for angles of attack of 45°, 51° and 60°. The sideslip angle causes the baseline data at zero sideslip to shift as shown. This incremental shift in the baseline was shown earlier (Figs. 22 to 24) to be invariant with rotation rate. The increments in side force and yawing moment contributed by the blowing jets are also relatively unaffected by rotation rate with, perhaps, a minor exception at 60° AOA shown in Fig. 32. At this angle of attack, the yawing moment increment is quite small for left-side blowing and appears to improve slightly at large negative rotation rates. The right-side blowing is somewhat more effective and does not depend strongly on rotation rate. Rolling moment is, as seen in previous figures, more difficult to characterize, probably because of the tendency towards more naturally asymmetric flows at this angle of attack and the complications of forebody flows interacting with the rest of the airframe at sideslip.

In order to evaluate Reynolds number effects, even though over a small range, a few tests were performed at a reduced dynamic pressure (q) of 10 psf ($Rn=0.378 \times 10^6$ instead of 0.636×10^6). Comparisons of data at both Reynolds numbers at blowing coefficients that are as closely matched as possible are shown in Figs. 33 to 35 for angles of attack of 45°, 51° and 60°. For the most part there is very little effect of Reynolds number on the results. Because of the reduced dynamic pressure (and consequently the velocity), the non-dimensional rotation rates are higher for the lower q runs. In all cases, the baseline (no blowing) runs are in near perfect agreement. The variation in the levels of the coefficients with blowing coefficient level and with rotation rate are also very similar for these two sets of data. For the Reynolds number range covered by these two conditions, there is no discernible Reynolds number effect. Both are low enough that the forebody flow is undoubtedly laminar in character. Increasing the Reynolds number into a range where the boundary layer can transition to turbulent flow may produce a different conclusion.

A simple test was performed to evaluate the effect of submerging the NOSE 4-60° INBOARD jet configuration into the forebody to make the jet flush with the surface. Results for the submerged (flush) nozzle for 51° AOA are shown in Fig. 36. Comparing these data to the data in Fig. 28 for the normally mounted nozzle, the flush mounted nozzle at the same blowing coefficient provides less than half the effectiveness as the surface jet. In fact, for the flush mounted jet, the maximum yawing moment on the left is at the lower blowing coefficient. One of the problems of the flush mounted jet is that the direction of the jet flow is at an angle to the surface instead of tangential as it is for the surface jet. This provides a velocity component away from the surface that perhaps has little benefit in influencing the flow to stay attached on the blowing side.

The most important conclusion from evaluating all of these data is that the yawing moment increment that is generated by the forebody jet blowing under static conditions does not appreciably deteriorate with non-dimensional rates as high as 0.28. The effect on the rolling moment is more difficult to characterize in a general statement. However, the level of the rolling moments induced by the forebody jet blowing is small enough that the behavior does not need to be nearly as well defined as the yawing moment dependency. These results provide confidence that blowing jets can realistically be employed to generate velocity vector roll rates of the magnitude consistent with aggressive full-scale maneuvers and not suffer from decreased control power at the higher rates.

7.2.2 Pressure Distributions

A comparison of the pressure distribution measured on the forebody and LEX during the rotary experiments and those taken during the static test is shown in Fig. 37a. This comparison was done for Nose 4-60° with no blowing at 51° AOA. The data show very good agreement for the forebody and lower LEX (as did the clean nose), but a lower suction peak is once again measured on the upper LEX surface due, most likely, to the difference in angle of attack between the rotary data (51°) and the static data (50°) as discussed in Section 7.1.2.

Figure 37b is a non-rotating case that nearly repeats the results noted in the static test (Fig. 40, Volume 1) for the effects of jet blowing. The effect of the blowing is to increase the level of the suction on the blowing side compared to that on the opposite side. Reversing the side for blowing at the same mass flow rate provides an approximate mirror image response and reverses the pressure distribution. The non-symmetric suction for either left or right blowing, when integrated around the forebody, produces a localized side force, and due to its distance from the CG, a rather large yawing moment. The effect of blowing left and right on the LEX station (F.S. 253) is symmetric about the baseline no-blowing case on the left hand side, but blowing on the left hand side of the forebody produces comparatively larger loss in suction over the right LEX. This increase in suction on the blowing side (left) indicates that the left blowing has moved the right hand vortex away from the surface of the LEX while moving the left hand vortex down closer to the surface. This is exactly the behavior that has been seen in water tunnel and wind tunnel smoke tests. The result that left and right blowing do not produce mirror images on the LEX pressures left and right is consistent with the lack of mirror image reversal on the forebody.

Figures 37c and 37d investigate the effect of jet blowing in rotating flow (ω = +0.15 and -0.15 respectively). The baseline behavior is similar to the clean nose with an increase in the pressure suction peak on the leeward side of the body and a decrease on the windward side. For negative rotation, blowing on the right is nearly identical to the baseline no-blowing case, but blowing on the left shows distinct differences. For positive rotation, blowing left and right produce near mirror image reversals in the pressure distribution. The reason for the difference in the behavior of the pressure distributions for positive and negative rates is not known. Blowing is able to produce changes in the pressure distribution on the forebody and the LEX regardless of the rotation, which agrees well with the force and moment data.

Figures 37e through 37g present data for the effect of the rotating flow field for fixed values of right and left jet blowing coefficient. Figure 37e shows the case of no blowing, but with the jet blowing nose (Nose 4-60°). It is interesting to compare this pressure distribution to the baseline one shown in Fig. 25b. The jets act like small strakes on the nose which cause the suction peaks, seen on the top of the fuselage for the clean nose, to all but disappear for the jet nose. Therefore, rotation of the jet nose has the greatest effect on the lower surface of the forebody. The small jets actually increase the anti-spin tendency of the forebody. Figure 37f (left jet blowing) shows fairly equal but opposite contributions from rotating positive or negative but with more of an effect on the right hand LEX than the left. Figure 37g (right jet blowing) also shows fairly equal and opposite contributions from positive and negative rotations.

7.3 BLOWING SLOTS

The results from the static tests (Volume 1) showed that the best slot configuration tested was the length consisting of slots A and B together. This configuration can be reviewed in Fig. 8. This SLOT AB configuration is the only configuration that was tested in the rotary-balance tests. The tests were conducted at angles of attack of 45°, 51° and 60° with sideslip at zero and at 51° and 60° with sideslip at -10°. Runs were made at two different dynamic pressures of 27 psf and 10 psf to evaluate Reynolds number effects (Rn = 0.636 and 0.378 x 10^6), as was done for the blowing jet configurations.

7.3.1 Force and Moment Coefficients

The effects of the blowing slots for angles of attack of 45°, 51° and 60° are shown in Figs. 38 to 40. For 45° and 51°, as was found in the static tests, the lowest blowing rates at zero rotation rate produce a yawing moment in the opposite direction to the side of the forebody with the slot, and at higher blowing rates the yawing moment change is in the same direction. Also, with blowing on the left the effectiveness increases with positive rotation rate and decreases at the highest negative rotation rates (Fig. 38a), and blowing on the right produces the opposite effect, i.e., reduced effectiveness for positive rotation rates and increased effectiveness for negative rotation rates (Fig. 38b). In other words, the effectiveness is reduced when the side of the forebody with the blowing slot is rotated into the wind and increased when rotated away from the wind.

The axial force data from Runs 1236 to 1242 are dominated by noise caused by a bad slip ring channel on the axial force gage. The slip ring was replaced after Run 1240 and later runs do not have this scatter in axial force.

Rolling moments for 45° and 51° AOA also show the reversal in direction with blowing rate but do not seem to change much with rotation rate relative to the baseline configuration.

The yawing moment data for 60° AOA (Fig. 40a) show that low blowing rates on the side of the forebody rotated into the wind (right side and positive rotation or left side and negative rotation) show very little effectiveness but show very large effectiveness when the model is rotated in the opposite direction. Higher blowing rates have the opposite effect, i.e., high effectiveness when rotating the blowing side into the wind and low effectiveness when rotated away from the wind. This is opposite to the trend found at 45° and 51° AOA. The response in roll to the different blowing rates and rotation rate is mixed and there is no clearly established pattern.

The effects of -10° sideslip angle are shown in Figs. 41 and 42 for angles of attack of 51° and 60°. At 51° AOA the increments in yawing moment due to the various blowing rates left and right do not change appreciably with rotation rate. With the nose-right sideslip angle of 10°, blowing on the left side has very little effect at any rotation rate. Blowing on the right shows a yawing moment increment to the left for low blowing rates and to the right for higher rates and these differentials are nearly constant throughout the rotation range, with a slight decrease in effectiveness for the right side blowing at

positive rotation rates as was found for zero sideslip. Basically, the set of yawing moment curves for -10° sideslip are shifted approximately 0.04 towards the positive compared to zero sideslip case shown earlier in Fig. 38b. The rolling moment data are similar to the results at zero sideslip with the set of curves shifted approximately 0.015 in the positive direction. As shown in the yawing moment curves, the rolling moment is not affected much by left side blowing and effects of right side blowing are not altered appreciably by rotation rate.

At 60° AOA and -10° sideslip, shown in Fig. 42, the yawing moment behavior is similar to that observed for the zero sideslip case shown earlier in Fig. 40. The variations with rate at each blowing rate are somewhat different but, overall, the results at -10° sideslip are a shift in the data base at zero sideslip by approximately +0.04. Rolling moment data are shifted approximately +0.025 and the behavior with rotation rate is similar.

A few runs were made to asses the effect of changing the Reynolds number by decreasing the wind tunnel dynamic pressure from q=27 psf to q=10 psf. Some results for the lower q are shown in Figs. 43 to 45 for angles of attack of 45°, 51° and 60°. Comparison plots for both q levels are shown in Figs. 46 to 48. The data shown are all for left side blowing only. Because the velocity is reduced, the non-dimensional rotation rate is increased from approximately 0.16 to 0.28. Overall, there are no major differences in the character of the results. The slopes of the moments with rotation rate are consistent and the incremental differences in the level of the moments with blowing coefficient are similar. There are some differences, particularly in rolling moment between the two sets of data, but there are no consistent patterns for the differences. The main difference seems to be different offsets at zero rotation rate which tend to remain with rotation rate. These offsets, particularly at 51° and 60°, are probably determined by subtle differences in the way the flow separates on the forebody at the different Reynolds numbers. The conclusion from these runs, however, is that there are no large differences due to Reynolds number in the range covered by these tests. In any case, the Reynolds numbers are such that both cases have predominantly laminar flow on the forebody.

7.3.2 Pressure Distributions

The response of the pressure field, on the forebody and LEX (F.S. 142 and 253), to blowing during rotation was examined for Slot Segment AB at 51° AOA. Figures 49a through 49c ($C\mu$ = 0, 0.0029 left, 0.0029 right, respectively) shows a comparison of the non-rotating data to similar data obtained in the static test. The agreement was very good overall, with the same reduction in LEX suction noted on preceding configurations.

Figure 49d is the non-rotating effect of slot AB blowing. These results compare well to those discussed in Volume 1 (static test results). When the upper LEX pressures are compared to the results in the jet blowing section (Fig. 37b), it is seen that the effect of blowing on the right side now produces a small decrease in suction on the right hand LEX. Figure 49e shows the slot effectiveness at ω = 0.15. The left slot blowing is more effective than the right at creating a pressure change on the forebody and LEX. In Fig. 49f (ω = -0.15) the difference between right and left blowing is even more pronounced. The right slot is able to create a very pronounced difference in the forebody and LEX

pressures. Therefore, just as the force and moment data showed, the leeward slot is the most effective.

Figure 49g shows the effect of varying rotation with a constant $C\mu = 0$. The suction peaks on the upper fuselage are seen to be almost as prominent as those on the clean forebody (unlike the jet configuration). During negative rotation, there is not much of a suction peak on the upper right forebody. Figures 49h and 49i show left and right slot blowing respectively. At F.S. 142, rotation has the greatest effect on the side of the body with the blowing slot. On the LEX (F.S. 253), the opposite is true with the greatest change occurring on the non-blowing side.

7.4 ROTATING NOSE-TIP STRAKES

From the static test, the best configurations using single and dual strakes were selected for further tests on the rotary rig. Due to lack of test time, all of the evaluations were done at an angle of attack of 51°, which is representative of the high angle of attack regime of interest. The single and dual strake configurations selected for testing on the rotary rig are those that showed the ability for generating the largest yawing moments and also showed smooth variations in the yawing moment with strake roll angle. For example, the single strake was evaluated at the rotation angles between 140° and 220°, which, from the static tests, was found to be the angle range that produced the maximum yawing moments and were well-behaved with changes in rotation angle. Dual strakes with two different spacings are evaluated. A few tests were run to evaluate the effects of sideslip, and Reynolds number was varied by changing the tunnel dynamic pressure.

7.4.1 Force and Moment Coefficients

The performance of a single strake under rotary conditions is shown in Fig. 50. The angle of attack is 51° and the strake is positioned at various rotation angles from 140° to 220°, i.e. rotating up to 40° in each direction from the baseline with the strake on the leeward side at 180°. The yawing moment coefficient at zero rotation rate shows a negative increment relative to the baseline for Φ = 140° and 160° (clockwise rotation from 180° from pilot's view), and a positive increment for 200° and 220°. The negative increment for Φ = 140° and 160° increases with negative rotation and decreases with positive rotation, becoming almost zero at the maximum positive rotation rate. The positive increment at zero rotation rate for Φ = 200° and 220° does the opposite. This effect may be a function of the local roll angle of the strake with respect to the wind, which, of course, is changing with rotation rate. It may also be a function of how the forebody vortices react with the rest of the airframe. There is very little effect on the rolling moment.

The behavior of the dual strakes with a spacing of 150° (strakes are +/- 75° from the windward plane of symmetry) is shown in Fig. 51. For the dual strake, rotation in the clockwise direction (Φ=320° and 340°) produces a positive yawing moment at zero rotation rate. This positive increment relative to the baseline at Φ = 0° increases with negative rotation rates and decreases with positive rotation rates, a behavior opposite to that for the single strake (Fig. 50). This reversed effect is related to the fact that the

single and dual strakes produce opposite yawing moments with strake rotation angles in the same direction from the respective baselines. The single strake, with a baseline at 180°, produces a negative yawing moment when rotated clockwise (Φ<180°) and the dual strake produces a positive yawing moment when rotated clockwise from the baseline at 0°. This relationship of yawing moment direction and effective strake roll angle with respect to the local velocity vector at the nose tip has a strong effect on the magnitude of the resulting yawing moment. However, it is clear that the magnitude of the available yawing moment in either case is sufficient to provide a restoring yawing moment over the envelope of rotation rates examined.

For example, with dual strakes (Fig. 51), the yawing moment of the baseline configuration (Φ=0°) with rotation rate is unstable. That is, increasing positive rotation rate results in increased positive yawing moment up to rates of about 0.1. Beyond 0.1, the yawing moment starts to decrease and there is a stable yaw rate where the curve crosses back over the zero yawing moment axis. With the ability to control the level and direction of the yawing moment with the strakes, a yawing moment can be produced that will oppose the natural rotation direction and prevent the configuration from reaching an equilibrium yaw (spin) rate if it were free to rotate. Either the single or dual strakes would provide the appropriate level of yawing moment control to accomplish this.

Figure 52 shows data for the small dual strakes with spacing of 150° and angle of attack of 51° (same as the previous plots), but with the Reynolds number reduced by running the tunnel at a lower q of 10 psf instead of 27 psf. As a result, the non-dimensional rotation rate is increased, since the free-stream velocity is decreased. Compared to the data in Fig. 51, there is not a significant difference in the behavior. This can best be seen by the direct comparison of the data at both Reynolds numbers (dynamic pressures) in Fig. 53. For all of the coefficients and with different strake angles, there is very little difference between the results at the two different Reynolds numbers.

The effect of sideslip in the presence of rotated dual strakes with 150° spacing was evaluated and is shown in Fig. 54. The angle of attack is 51° and the sideslip angle is β = -10°. At zero rotation rate the yawing moment coefficient is near zero with 10° sideslip, as it is for zero sideslip. At this angle of attack, the directional stability is neutral to unstable which agrees with the fact there is no visible restoring moment with sideslip angle. The side force is positive, as expected for a nose right orientation. The interesting result is that the nose strakes are effective for positive rotation but are less effective and eventually become ineffective at negative rotation rates. This was not the case for zero sideslip shown previously in Fig. 51. With a static nose-right sideslip angle of 10° and the added effective sideslip angle due to negative rotation (the relative velocity vector is rotated to the left side with rotation rate), the total sideslip angle at the nose tip is apparently too large for the strakes to be very effective. Conversely, when rotating in the positive direction, there is an effective decrease in sideslip angle at the nose tip towards zero and the strake rotation is still effective.

Changing the separation angle of the dual strakes from 150° to 120° results in the data shown in Fig. 55. The angle of attack is 51°, as in the previous cases. The effect of changing from 150° to 120° was shown earlier in Volume I in the discussion of the static

test data, and is presented again in Fig. 56. For the $\Delta\Phi = 120°$ case, the best gradient is seen along $\Phi = 0°$. Unfortunately, data along this gradient from the rotary test are not available. The data presented in Fig. 55 show selected dual strake rotations along the $\Phi = 180°$ gradient. The change in yawing moment at $\Phi = 140°$ and 220° relative to the baseline at 180° is small (<0.02). The behavior of the yawing moment with rotation rate at the strake angles of 140° and 220° is not as one might expect. The increment of yawing moment for 140° is not the mirror image of the increment for 220° with rotation rate. Overall, the $\Delta\Phi = 120°$ dual strake does not give good results along the $\Phi = 180°$ gradient because the levels of yawing moment are low and not well behaved.

Figure 57 shows the difference between the $\Delta\Phi = 120°$ dual strakes located at $\Phi = 0°$ (strakes at +/-60°, windward side), and at $\Phi = 180°$ (strakes at 120° and 240°, leeward side). The difference in the yawing moment variation with rotation rate shows that, with the strakes on the leeward side, there is little effect on the yawing moment due to the strake effects, i.e., the yawing moment with rotation rate is nearly perfectly linear. However, with the strakes on the windward side, there is some effect of the strakes and the relationship of the local flow angle due to rotation introduces some nonlinear effects on the yawing moment. The strakes on the windward side give a propelling yawing moment out to rotation rates near +/-0.15.

7.4.2 Pressure Distributions

The pressure distribution for the single strake at $\phi = 180°$ is compared to results from the static test in Fig. 58a. Of all the configurations tested, the single strake showed the poorest comparison to the static test. The yawing moment gradient is very steep through $\phi = 180°$, so if the angle is not set exactly the same, some mismatch in the pressures could be expected. However, since we are primarily interested in obtaining the incremental effect of moving the strake while in the influence of a rotating flow field, the data are quite useful. Figure 58b shows the same level of agreement with the static test. However, Fig. 58c has a much better match for the case of $\phi = 160°$.

Figure 58d shows the effect of strake angle at 51° AOA and $\omega = 0$. The pressures indicated that the 160° strake is providing a bit more yaw than the 200° case. This matches the force and moment data well. As the aircraft is rotated in the positive direction (see Fig. 58e), the 200° strake is providing an increased suction on the upper right side of the forebody, and a positive pressure increment on the left side, causing a positive side force contribution from the forebody. The LEX shows an increase in suction on the right side and a decrease on the left. The strake at $\phi = 160°$ has very little net effect on the forebody side force, with a slight increase in suction on both the left and right sides of the fuselage. Likewise on the LEX, the 160° strake increases the suction on the left and right side nearly equally. Figure 58f shows the case of $\omega = -0.15$. Unfortunately, the 160° strake data for this comparison were "misplaced" by the SWTS system. The 200° strake shows that it's side force effect is now in the opposite direction with increased suction on the left side and increased pressure on the right side of the forebody. This is consistent with the force data discussed for Fig. 50 above. If the $\phi =$

160° data were available, it is expected that, based on the force data, they would show a similar pressure distribution to the 200° data.

The data are also viewed as the effect of rotation on a fixed strake angle (Fig. 58g). The data are very nearly symmetric about zero rotation. As the strake was moved to 200° (Fig. 58h) the effect is shown as a "tilting" of the pressure distribution on the forebody and LEX. In general, there is a higher suction peak on the right side of both the forebody and LEX which indicates a positive side force and yawing moment. The rotation has the same effect that it did on the clean nose of moving the suction peaks around the body (from 80° to 120° for positive rotation) as it experienced an apparent sideslip angle. Even with the data for $\omega b / 2v = -0.15$ missing, the data for $\Phi = 160°$ (Fig. 58i) appears to be a mirror image of the 200° strake data.

The pressure data for the 150° dual strake at 51° AOA are not compared to static data because these data were not collected during the static test. Figure 58j shows the effect of strake rotation angle for the non-rotating case. The pressure distributions are very symmetric around the 0° case. The forebody shows that a strake angle of $\Phi = 40°$ causes an increase in the suction peak on the left side of the forebody and a corresponding decrease on the right side, causing a negative side force and yawing moment. This agrees well with Fig. 51, which shows the forces and moments. On the LEX, the same strake angle ($\Phi = 40°$) produces increased suction on the right side and an equal decrease on the left. This causes a positive rolling moment input, which also agrees with the force data. The data for $\Phi = 320°$ are essentially a mirror image in effectiveness.

When the aircraft is rotated in the positive direction (Fig. 58k), the 40° deflected dual strake still generates increased suction on the left side and decreased on the right side of the fuselage. The 320° deflection now also generates increased suction on the left side and decreased on the right (though a smaller magnitude) instead of being a mirror image of the 40° case. The opposite is true when the aircraft is rotated in the negative direction (Fig. 58l). Now, the 320° deflected strake generates an increased suction peak on the right side and a decreased suction on the left side of the forebody while the 40° deflection does virtually nothing. The LEX experienced a similar effect with 320° producing less suction on the left side (while 40° did nothing) and increasing suction on the right side. On the right side the 40° deflection also produced a smaller suction increase.

When the data are viewed as the effect of rotation on a fixed strake angle (Fig. 58m), it is apparent that the strakes are in a position that at F.S. 142 the pressures show a suction peak on the top of the fuselage similar to the clean nose. Figures 58n and 58o show 40° and 320° strake rotation respectively. As described in the single strake section above, the major effect is a "tilting" of the pressure distributions.

7.5 VERTICAL STRAKE

7.5.1 Force and Moment Coefficients

The effectiveness of a small strake (rhino horn) on the leeward side of the forebody which pivots about a vertical axis perpendicular to the forebody surface was evaluated in the static wind tunnel tests. The strake geometry is shown in Fig. 8d. The variation of the yawing moment with the strake pivot angle was investigated at angles of attack up to 60°. The effect of rotation rate on the aerodynamics for this strake at 51° AOA is shown in Fig. 59 for several different deflection angles (trailing edge left is positive). The yawing moment variation at zero rotation rate shows, as was observed in the static tests, that trailing-edge left deflections of +20° and +36° result in positive yawing moments relative to the baseline. Negative deflections result in negative yawing moments. The characteristics of the yawing moment (and side force) with rotation rate are very similar to those observed earlier for the single strake in Fig. 50. For example, positive deflection provides a positive yawing moment but the increment decreases with negative rotation rate and increases with positive rates. Negative deflections experience decreasing effectiveness with positive rotation rate and increasing effectiveness with negative rotation rates. The rolling moment shows small effects of strake deflection with rotation rate.

The effect of nose-right sideslip angle of -10° is shown in Fig. 60. A sideslip angle of -10° results in an offset of the baseline yawing moment of approximately 0.04. The increments due to the strake deflection are about the same as for zero sideslip at zero and positive rotation rates. However, at negative rotation rates the effectiveness decreases to near zero, especially the negative deflection of -50°. At zero sideslip, the negative deflection showed the largest increment at negative rotation rates (Fig. 59).

The effect of a smaller (thinner) strake (Fig. 8) is shown in Fig. 61. Comparing these results to those for the baseline strake in Fig. 59, the largest difference is in the behavior of the 0° deflection case. The "thin rhino" is much more anti-spin as evidenced by the slope of the Cn plot. This also means that this strake is much more effective at producing a negative increment in yawing moment when the aircraft is rotating in the negative ω direction (as great as $\Delta Cn = 0.14$ at $\omega b/2V = -0.28$). This means that with an active flight control system any level of anti-spin behavior can be created, from neutral (or even pro-spin) to very damped. The thin strake was then tested at a lower Reynolds number by lowering the tunnel dynamic pressure from 27 psf to 10 psf. A comparison of the two sets of data is shown in Fig. 62. There is little difference in the results for the two Reynolds numbers.

7.5.2 Pressure Distributions

A comparison was made between the vertical nose strake pressure data at 51° AOA at deflection angles of δ = 0°, 36°, -36° and the data from the static test (Figs. 63a-c). The agreement is very good (suction on LEX is still low due to 1° difference in angle of attack) with the possible exception of the -36° case where it appears that the deflection angles were not set exactly the same (the rotary test appears to have a higher deflection angle).

Figure 63d shows the effect of deflecting the strake while in a non-rotating flow field. The negative 36 degree deflection shows both a greater increase in suction on the left side and a greater decrease on the right side than the positive deflection generated. This agrees with the force data that show positive natural asymmetry in the yawing moment that provides a larger possible negative increment. The LEX pressures indicate that $\delta = -36°$ will have a positive rolling moment input because the suction is increased slightly on the left side and decreased substantially on the right side. The opposite is true for the positive deflection. When the aircraft is rotated in the positive direction ($\omega = 0.15$) the strake has an influence on the windward (right) side of the fuselage with either +/- deflection. However, on the leeward (left) side, only a deflection in the negative direction has an effect on the pressure distribution. When the rotation is reversed (Fig. 63f) both positive and negative deflections have effects on the leeward side (right) and neither has an effect on the windward (right) side.

Figures 63g-i show the effect of rotation for a fixed strake deflection angle. The results are similar to the other strakes investigated. The LEX (F.S. 253) is contributing a larger anti-spin component, for the deflected strake cases, than for any of the other configurations (in their "deflected" or blowing configurations).

7.6 Application to a Future Flight Control System

All of the devices studied (jets, slots, single and dual rotating nose tip strakes, and a vertical nose tip strake) have shown the ability to create large yawing moments in a rotary flow field. The overall effectiveness of each of these devices can be thought of as an envelope of yaw control power (Cn) as a function of non-dimensional spin rate as shown in Fig. 64. The baseline F/A-18 is shown as a single line that indicates that the aircraft would have anti-spin behavior (negative slope). As expected, when jets or slots (non-blowing condition) are added to the aircraft nose, there is little change in the slope of this line (Fig.'s 28 and 39). Blowing at different rates produce the envelope shown in Fig. 64. The dual rotating nose tip strakes, in an undeflected configuration ($\Phi=0°$), cause the spin characteristics to be pro-spin at low spin rates and anti-spin at higher spin rates (Fig. 51). However, by rotating the strakes, the envelope shown in Fig. 64 is obtained. The single rotating tip strake and the vertical nose strake (rhino horn) both cause the aircraft to be even more anti-spin in their undeflected positions (Fig.'s 50 and 61). Their deflected control envelopes are also shown in Fig. 64.

If a stability augmentation system (SAS) is used in a flight control system, it is clear that the aircraft's anti-spin characteristics can be modified by any of these devices. The envelopes shown in Fig. 64 illustrate the design space that can be generated for each of the devices. The flight control engineer can use rate feedback and choose to make the aircraft perform exactly like a standard F/A-18 or design the system to provide more, or less, anti-spin behavior (even to the point of making it pro-spin if desired).

In addition to a SAS, a command augmentation system (CAS) can be designed into the flight control system. This system would blend the forebody vortex control with the conventional aerodynamic surface controls at angles of attack above approximately 30°. The CAS would provide the increased maneuverability that is needed in future fighter aircraft for increased agility at high angles of attack.

8.0 CONCLUSIONS

In order to provide for increased agility at high angles of attack, including the ability to roll robustly about the velocity vector, forebody vortex control has been investigated for the F/A-18 on a rotary balance. Pneumatic (jets and slots) and mechanical (single and dual rotating nose tip strakes, and a vertical nose tip strake) forebody vortex control devices were first tested in a static test, and then the most effective configurations were tested on the rotary balance. The following are the major conclusions of the rotary test.

1) The difference in interference effects between the mounting arrangements for the static and rotary tests are not significant. There is very good agreement between tests.

2) The baseline data agree well with data from a similar configuration tested at the NASA Langley Spin Tunnel (CR-3608, Ref. 38).

3) Jet blowing (Nose 4 with nozzles canted 60° inboard) provided the same level of side force and yawing moment observed in the static test, with little degradation at non-dimensional rotation rates as high as 0.28. The level of rolling moment produced is small enough to not be a factor.

4) Jet blowing is effective at sideslip angles of 10° in a rotating flow field.

5) There is no difference in jet blowing performance at Reynolds numbers of 0.378×10^6 and 0.636×10^6.

6) Slot blowing (Slot AB) produces yawing moments to the left when low blowing rates are used on the right side. This reverses for higher blowing rates to produce a yawing moment to the right.

7) Slot blowing is more effective on the leeward side of the fuselage during rotation. Blowing on the windward side becomes less effective with higher rotation rates.

8) Slot blowing is effective at sideslip angles of 10° in a rotating flow field.

9) Slot blowing is not adversely effected by a Reynolds number change from 0.636×10^6 to 0.378×10^6.

10) The single strake, from a baseline of $\Phi = 180°$, produces a negative increment relative to the baseline for $\Phi = 140°$ and 160° (clockwise rotation from 180° from pilot's view) and a positive yawing moment increment for 200° and 220°. The negative increment for $\Phi = 140°$ and 160° increases with negative rotation and decreases with positive rotation, becoming almost zero at the maximum positive rotation rate. The positive increment at zero rotation rate for $\Phi = 200°$ and 220° does the opposite.

11) The 150° dual strakes, from a baseline of $\Phi = 0°$, produce a positive yawing moment when moved in the clockwise direction (Φ=320° and 340°). This positive increment increases with negative rotation rates and decreases with positive rotation rates, a behavior opposite to that for the single strake.

12) At $\beta = -10°$, the 150° dual strakes are effective for positive rotation but are less effective and eventually become ineffective at negative rotation rates. This was not the case for zero sideslip. The total effective sideslip angle at the nose tip is apparently too large for the strakes to be very effective.

13) There are no differences in the 150° dual strake performances at Reynolds numbers of 0.378×10^6 and 0.636×10^6.

14) The vertical nose strake (rhino horn), from a baseline of $\delta = 0°$, produces a positive yawing moment increment for positive (trailing edge left) δ's and a negative yawing moment increment for negative δ's. The positive increment increases with positive rotation and decreases with negative rotation, becoming almost zero at the maximum negative rotation rate. The negative deflection increment does the opposite (similar to the single strake).

15) The vertical nose strake is effective at sideslip angles of 10° in a rotating flow field.

16) The vertical nose strake (rhino horn) produced the largest maximum yawing moment increment ($\Delta Cn = -0.14$ at $\omega b/2V = -0.28$) of any device tested.

17) All of the forebody vortex control methods tested appear to be usable in an advanced flight control system as either a SAS or CAS system, or both.

9.0 ACKNOWLEDGMENTS

The authors wish to acknowledge the support and encouragement of our technical monitors, Dr. Lewis Schiff, and our alternate monitor, Dr. James Ross, who both maintained a high level of interest and active participation in the technical discussions throughout the period of this contract. We would also like to recognize the significant efforts of Mr. Kevin James of Sterling Federal Systems who performed as Test Director for NASA Ames Research Center for both the static and the rotary-balance tests and the NASA support personnel responsible for the operation of the 7 x 10-ft wind tunnel, including the tunnel mechanics, technicians, and programmers. We would particularly like to acknowledge the help of Mr. Art Silva for his conscientious commitment to providing the best instrumentation support possible.

10.0 REFERENCES

1) Malcolm, G. N.,"Forebody Vortex Control," Special Course on Aircraft Dynamics at High Angles of Attack: Experiments and Modeling presented at NASA Langley Research Center April 8-11, 1991 and von Karman Institute, April 22-25, 1991, AGARD Report No. 776, March 1991.

2) Malcolm, G. N., "Forebody Vortex Control," Progress in Aerospace Sciences, Vol. 28, pp. 171-234,1991.

3) Murri, D. G. and Rao, D. M., "Exploratory Studies of Actuated Forebody Strakes for Yaw Control at High Angles of Attack," AIAA Paper 87-2557-CP.

4) Malcolm, G. N., Ng, T. T., Lewis, L. C. and Murri, D. G., "Development of Non-Conventional Control Methods for High Angle of Attack Flight Using Vortex Manipulation," AIAA Paper 89-2192.

5) Malcolm, G. N., Ng, T. T., "Forebody Vortex Manipulation for Aerodynamic Control of Aircraft at High Angles of Attack," SAE Paper 892220.

6) Malcolm, G. N., Ng, T. T., Lewis, L. C. and Murri, D. G., "Development of Non-Conventional Control Methods for High Angle of Attack Flight Using Vortex Manipulation," AGARD CP 465, Paper No. 11, April 1990.

7) Malcolm, G. N. and Ng, T. T., "Aerodynamic Control of Fighter Aircraft by Manipulation of Forebody Vortices," AGARD CP-497, Paper No. 15, November 1991.

8) Lanser, W. R. and Murri, D. G., "Wind Tunnel Measurements on a Full-Scale F/A-18 with Forebody Slot Blowing or Forebody Strakes," AIAA Paper 93-1018.

9) Skow, A. M., Moore, W. A. and Lorincz, D. J.,"Forebody Vortex Blowing - A Novel Concept to Enhance the Departure/Spin Recovery Characteristics of Fighter Aircraft," AGARD CP-262, May 1979.

10) Moore, W. A., Skow, A. M. and Lorincz, D. J., "Control of the Forebody Vortex Orientation by Asymmetric Air Injection - Application to Enhance Departure/Spin Recovery," AIAA Paper 80-0173.

11) LeMay, S. P., Sewall, W. G. and Henderson, J. F., "Forebody Vortex Flow Control on the F-16C Using Tangential Slot and Jet Nozzle Blowing," AIAA Paper 92-0019.

12) Guyton, R. W. and Maerki, G., "X-29 Forebody Jet Blowing," AIAA Paper 92-0017.

13) Cornelius, K. C., Pandit, N., Osborn, R. F., and Guyton, R. W., "An Experimental Study of Pneumatic Vortex Flow Control on High Angle of Attack Forebody Model," AIAA Paper 92-0018.

14) Pellicano, P. and Krumenacker, J. L., "Flight Test Techniques, Simulation and Data Analyses During a High Angle of Attack Vortex Flow Control Flight Test Program," 23rd Symposium of Society of Flight Test Engineers, August 3-7, 1992.

15) Hancock, R. and Fullerton, G., "X-29 Vortex Flow Control Tests," Proceedings of the Thirty Sixth Symposium of the Society of Experimental Test Pilots, pp. 209-219, September, 1992.

16) Rosen, B. S. and Davis, W. H., "Numerical Study of Asymmetric Air Injection to Control High Angle-of-Attack Forebody Vortices on the X-29 Aircraft," AIAA Paper 90-3004-CP.

17) Ng, T. T and Malcolm, G. N., "Aerodynamic Control Using Forebody Blowing and Suction," AIAA Paper 91-0619.

18) Lanser, W. R. and Meyn, L. A., "Forebody Flow Control on a Full-Scale F/A-18 Aircraft," AIAA Paper 92-2674.

19) Ng, T. T., Ong, L., Suarez, C. J. and Malcolm, G. N., "Wing Rock Suppression Using Forebody Vortex Control," AIAA Paper 91-3227.

20) Suarez, C. J., Kramer, B. R., Ayers, B. F. and Malcolm, G. N., "Forebody Vortex Control for Suppressing Wing Rock on a Highly-Swept Wing Configuration," AIAA Paper 92-2716.

21) Ng. T. T., Suarez, C. J. and Malcolm, G. N., "Forebody Vortex Control Using Slot Blowing," AIAA Paper 91-3254.

22) Gee, K.,Tavella, D. and Schiff, L. B., "Computational Optimization of a Pneumatic Forebody Flow Control Concept," AIAA Paper 91-3249-CP.

23) Gee, K., Rizk, Y. M., Murman, S. M., Lanser, W. R., Meyn, L. A. and Schiff, L. B., "Analysis of a Pneumatic Forebody Flow Control Concept About a Full Aircraft Geometry." AIAA Paper 92-2678-CP

24) Font, G. I., Celik, Z. Z. and Roberts, L., "A Numerical and Experimental Study of Tangential Jet Blowing Applied to Bodies at High Angles of Attack," AIAA Paper 91-3253-CP.

25) Ross, A. J., Jefferies, E. B. and Edwards, G. F. "Control of Forebody Vortices by Suction at the Nose of the RAE High Incidence Research Model," AGARD CP-494, October, 1990.

26) Ross, A. J., Jeffries, E. B. and Edwards, G. F., "Dynamic Tests on Large-Scale High Incidence Research Models (HIRM1) in the DRA 24-Ft Wind Tunnel with Control of Forebody Vortices by Nose Suction," DRA Tech. Report 92067, December, 1992

27) Moskovitz, C. A., Hall, R. M. and DeJarnette, F. R., "New Device for Controlling Asymmetric Flowfields on Forebodies at Large Alpha," AIAA Journal of Aircraft, Vol. 28, No. 7, July 1991.

28) Suarez, C. J., Malcolm, G. N. and Ng, T. T.,"Forebody Vortex Control with Miniature Rotatable Nose-Boom Strakes," AIAA Paper 92-0022.

29) Ng, T. T. and Malcolm, G. N., "Aerodynamic Control Using Forebody Strakes," AIAA Paper 91-0618.

30) Wurtzler, K., "Numerical Analysis of a Chined Forebody with Asymmetric Strakes," AIAA Paper 93-0051.

31) Boalbey, R. E., Ely, W. L. and Robinson, B. A., "A Sensitivity Study for Pneumatic Vortex Control on a Chined Forebody," AIAA Paper 93-0049.

32) Malcolm, G. N., "Forebody Vortex Control - A Progress Review," AIAA Paper 93-3538, AIAA 11th Applied Aerodynamics Conference, Monterey, CA, August 9-11, 1993.

33) Erickson, G. E., Hall, R. M., Banks, D. W., Del Frate, J. H., Schreiner, J. A., Hanley, R. J. and Pulley, C. T., " Experimental Investigation of the F/A-18 Vortex Flows at Subsonic Through Transonic Speeds," AIAA 89-2222.

34) Banks, D. W., "Wind-Tunnel Investigation of the Forebody Aerodynamics of a Vortex-Lift Fighter Configuration at High Angles of Attack," SAE Paper 881419.

35) Fisher, D. F., Del Frate, J. H. and Richwine, D. M., "In-Flight Flow Visualization Characteristics of the NASA F-18 High Alpha Research Vehicle at High Angles of Attack," NASA TM 4193, May 1990.

36) Fisher, D. F., Banks, D. W. and Richwine, D. M., "F-18 High Alpha Research Vehicle Surface Pressures: Initial In-Flight Results and Correlation With Flow Visualization and Wind Tunnel Data," NASA TM 101724, August 1990.

37) Bjarke, L. J., Del Frate, J. H. and Fisher, D. F., "A Summary of the Forebody High-Angle-of-Attack Aerodynamics Research on the F-18 and X-29A Aircraft," SAE Paper 921996.

38) Hulzberg, R., "Low Speed Rotary Aerodynamics of F-18 Configuration for 0° to 90° Angle of Attack - Test Results and Analysis," NASA CR 3608, August 1984.

39) National Instruments, "Data Acquisition VI Library Reference Manual", January, 1992

40) van Aken, Johannes M., "Description of the Standard Wind Tunnel Balance Program", CRINC Report 7440-3, NASA Grant NCC 2-417, April, 1988

JET BLOWING

PRESSURE (psia)	$C\mu$	MFR
20	0.0004	0.000042
30	0.0011	0.000080
40	0.0015	0.000112
50	0.0019	0.000145
60	0.0023	0.000177
70	0.0027	0.000210

SLOT BLOWING (SEGMENT A-B)

PRESSURE (psia)	$C\mu$	MFR
20	0.0007	0.000072
30	0.0016	0.000116
40	0.0022	0.000166
50	0.0029	0.000217
60	0.0035	0.000264

Table 1 - Blowing coefficient and mass flow ratio for different plenum pressures (q = 27 psf)

Yaw control power - with forebody vortex control.

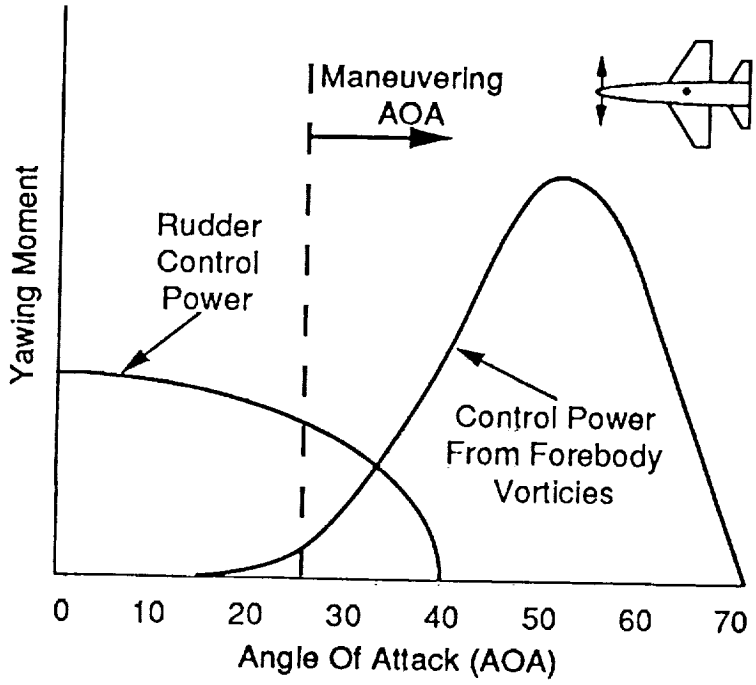

Figure 1 - Yaw control power with conventional control surfaces and with Forebody Vortex Control (FVC)

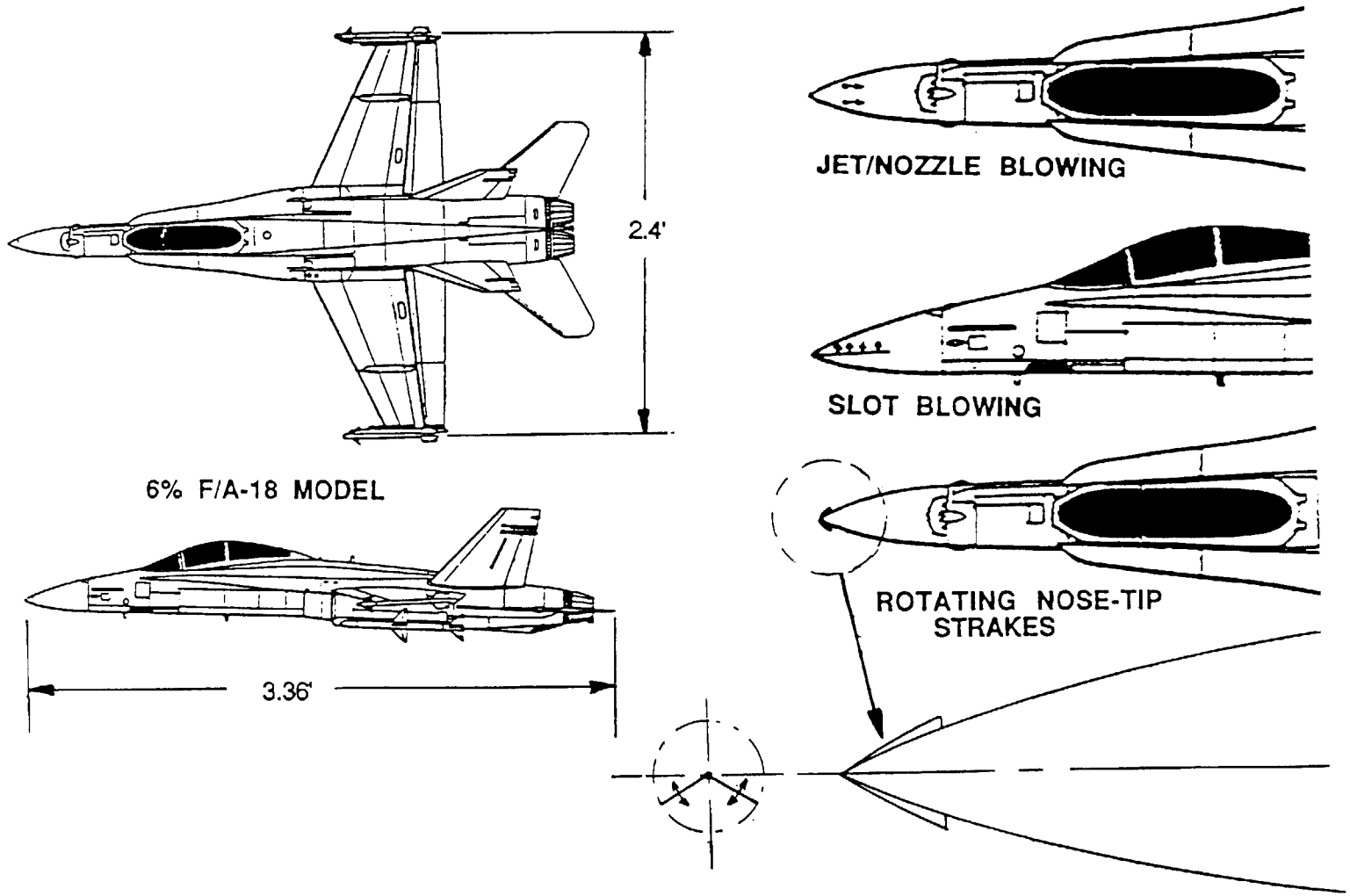

Figure 2 - Water tunnel model with different forebody vortex control techniques

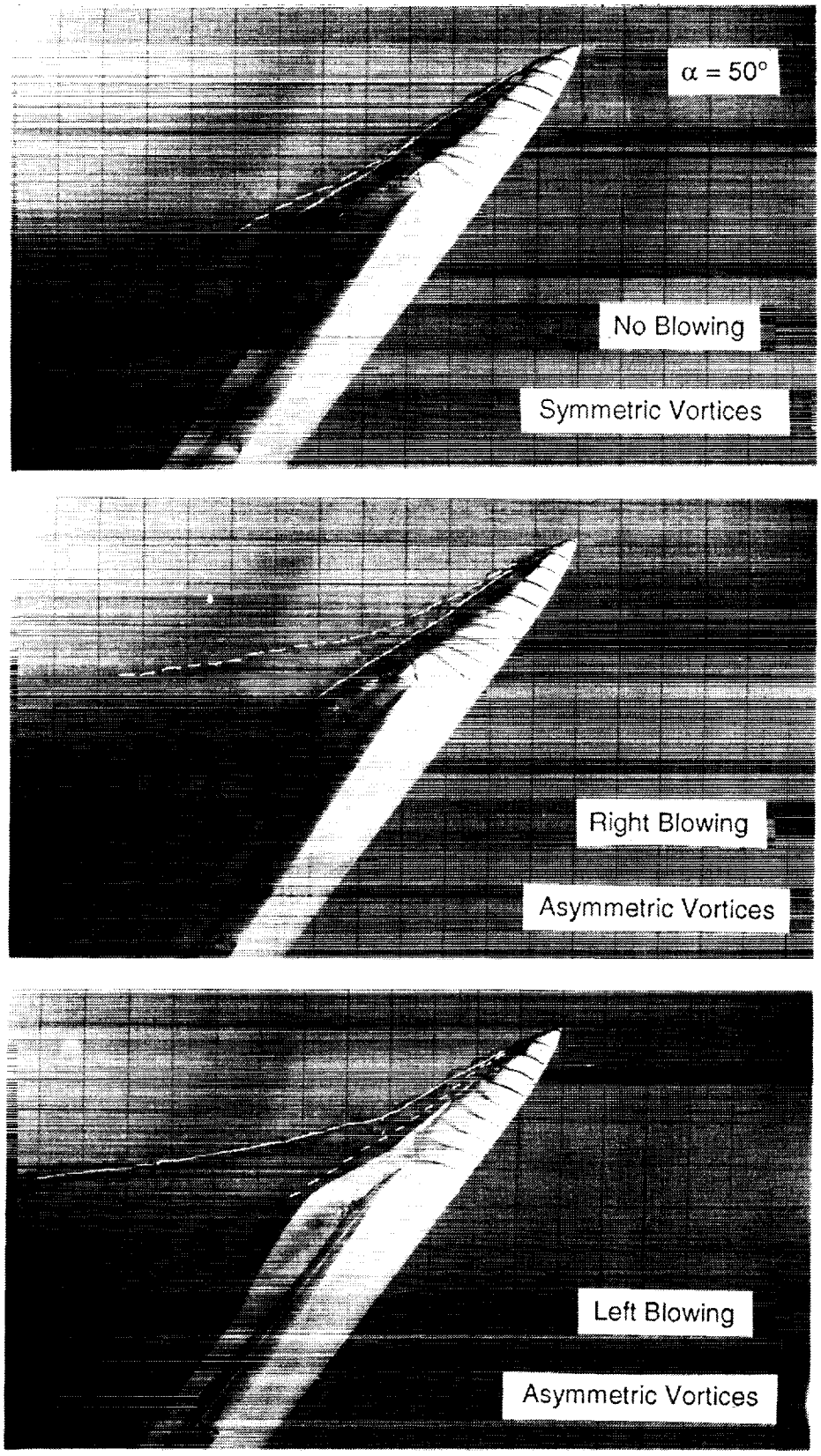

Figure 3 - **Effect of slot blowing on the forebody vortices (water tunnel test)**

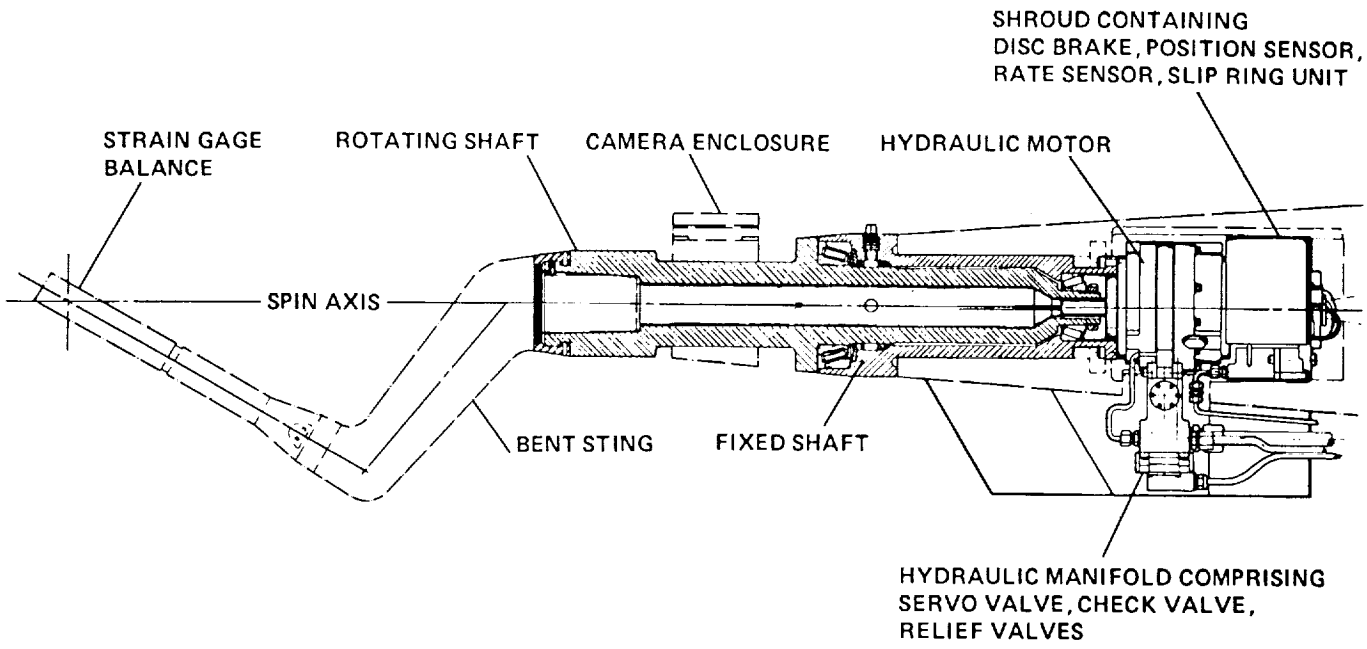

(a) Original apparatus tested in Ames 6 x 6-Ft Supersonic Wind Tunnel

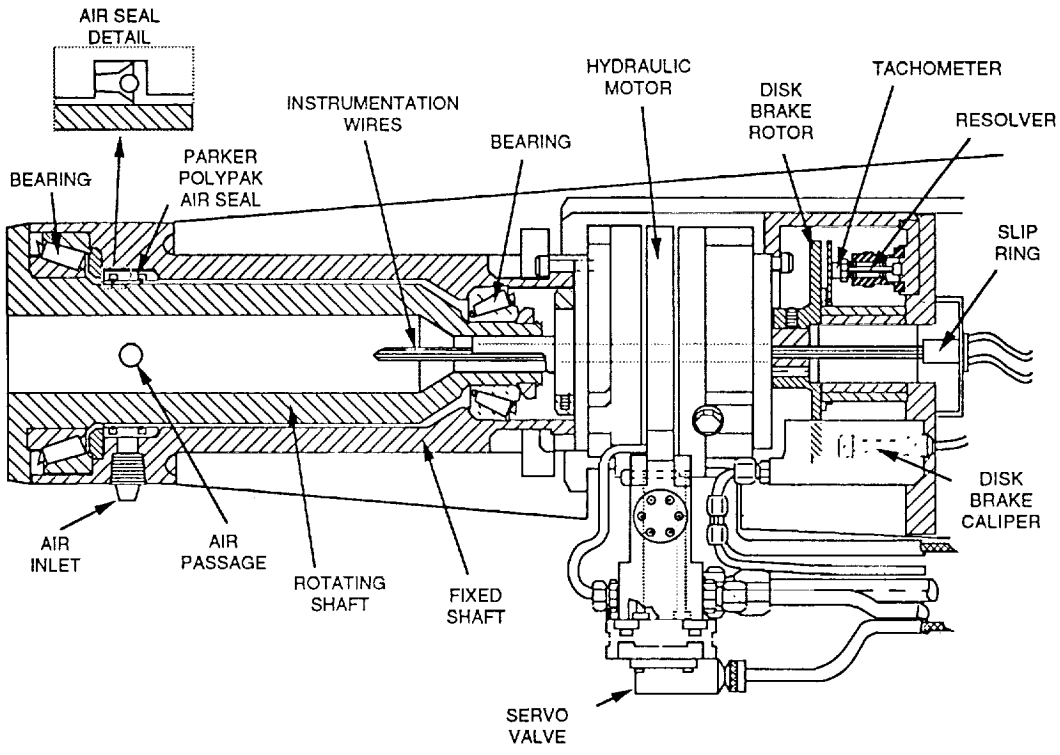

(b) Details of mechanical, hydraulic and air seal systems

Figure 4 - NASA Ames rotary-balance apparatus

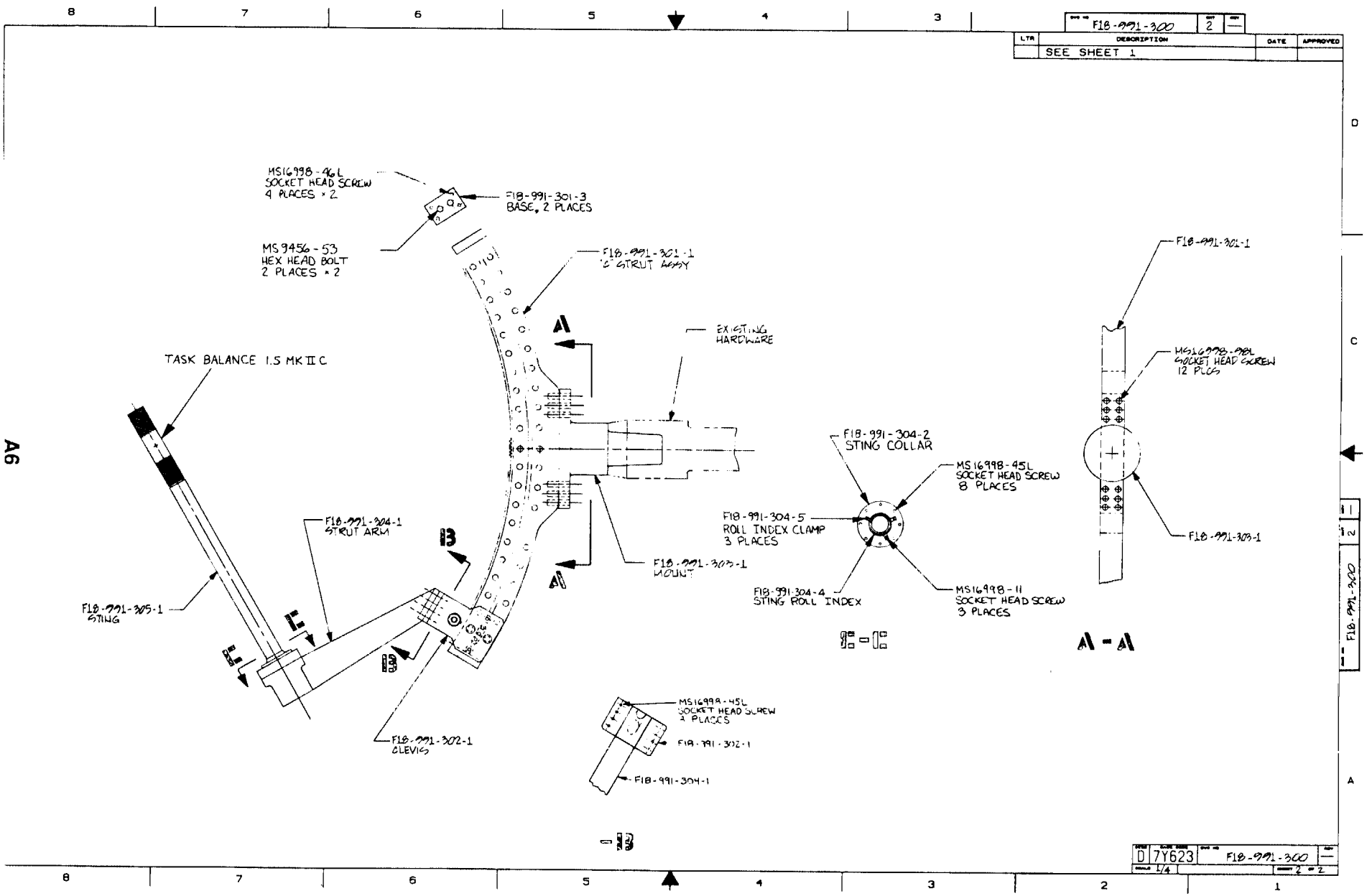

Figure 5 - New NASA Ames rotary-balance sting support hardware

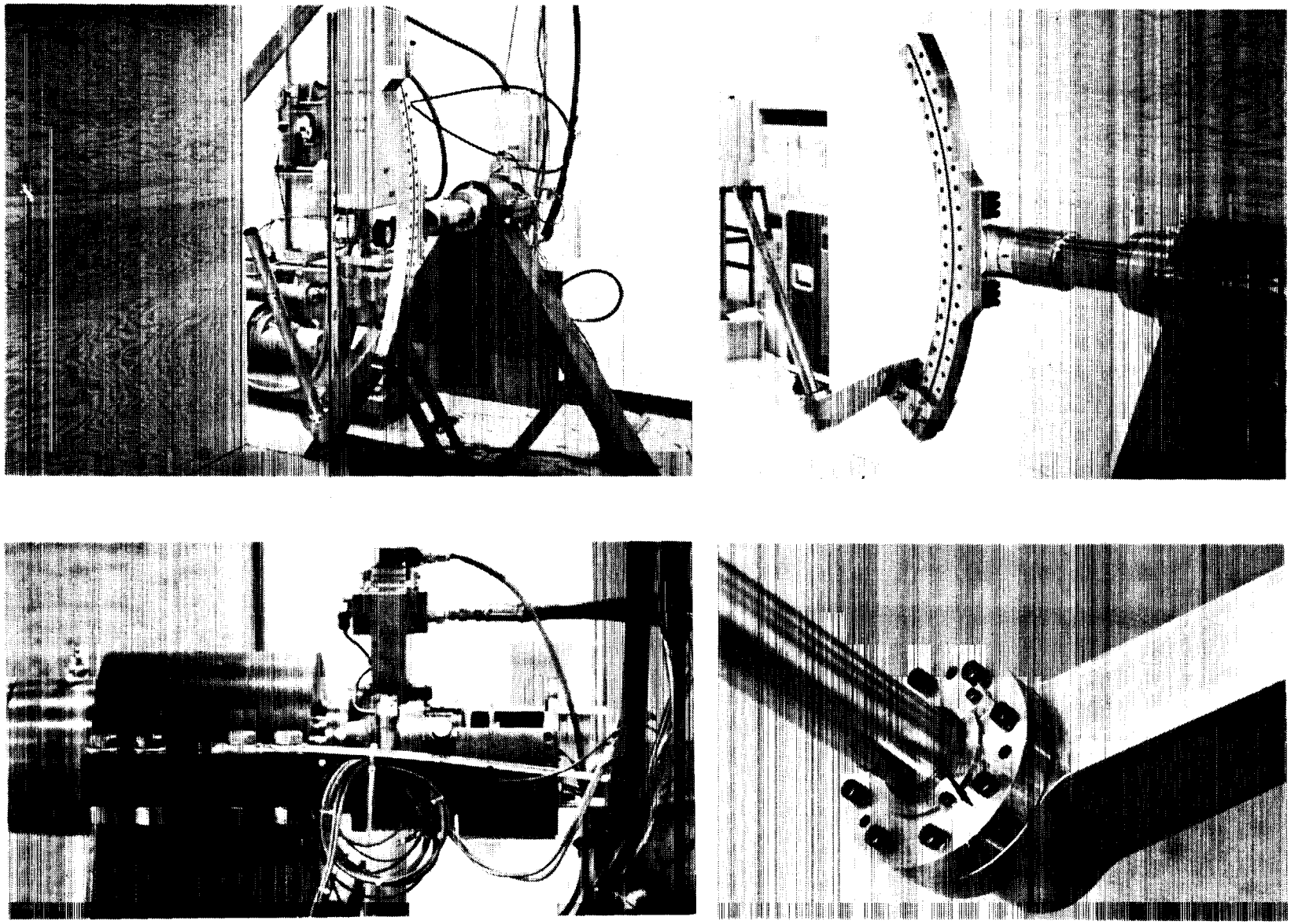

Figure 6 - Photographs of new rotary-balance hardware installed for testing in Eidetics International laboratory

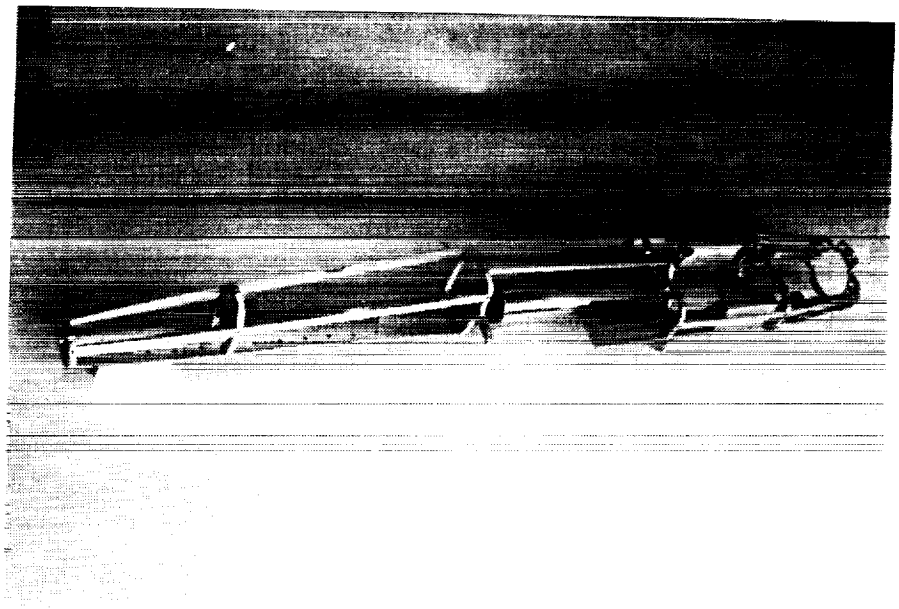

(a) Internal structural frame of model

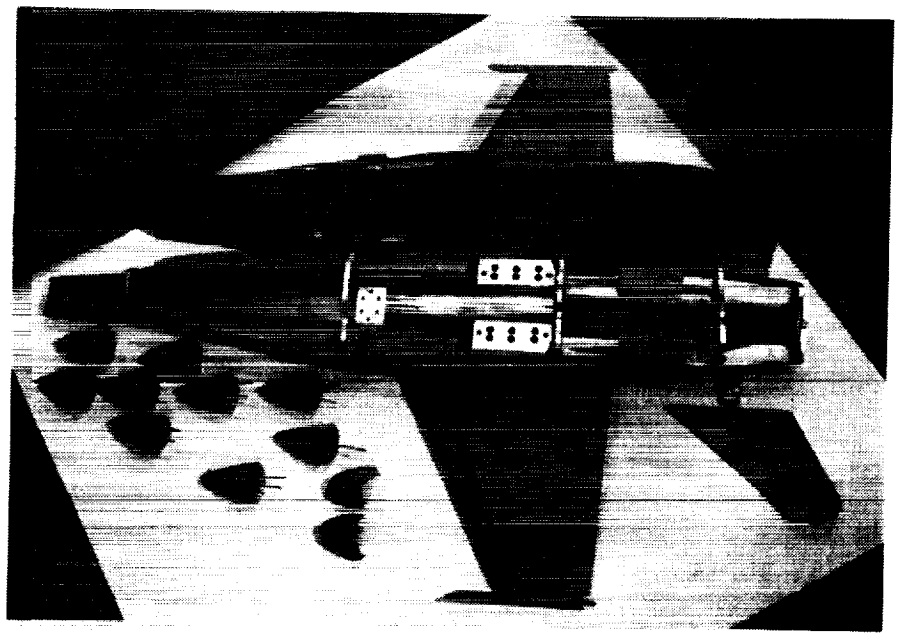

(b) Model with assorted forebody pieces

Figure 7 - Photographs of 6%-scale F/A-18 wind tunnel model

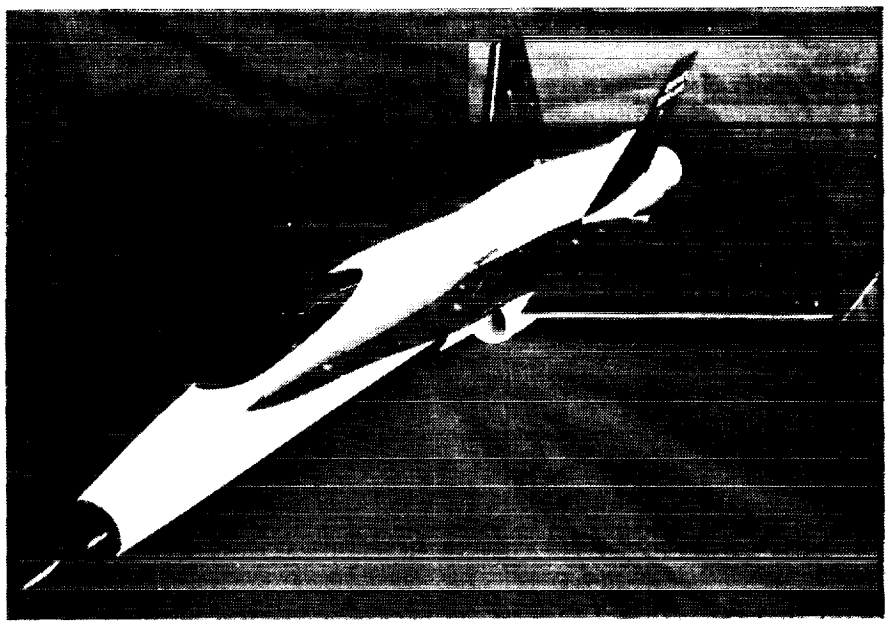

(c) Assembled model

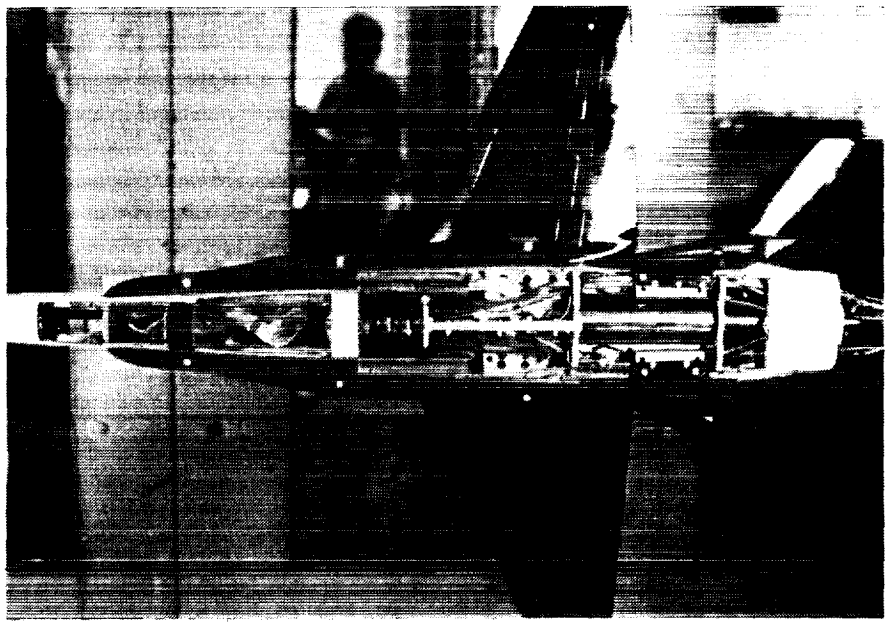

(d) Assembled model with top cover removed

Figure 7 - Concluded

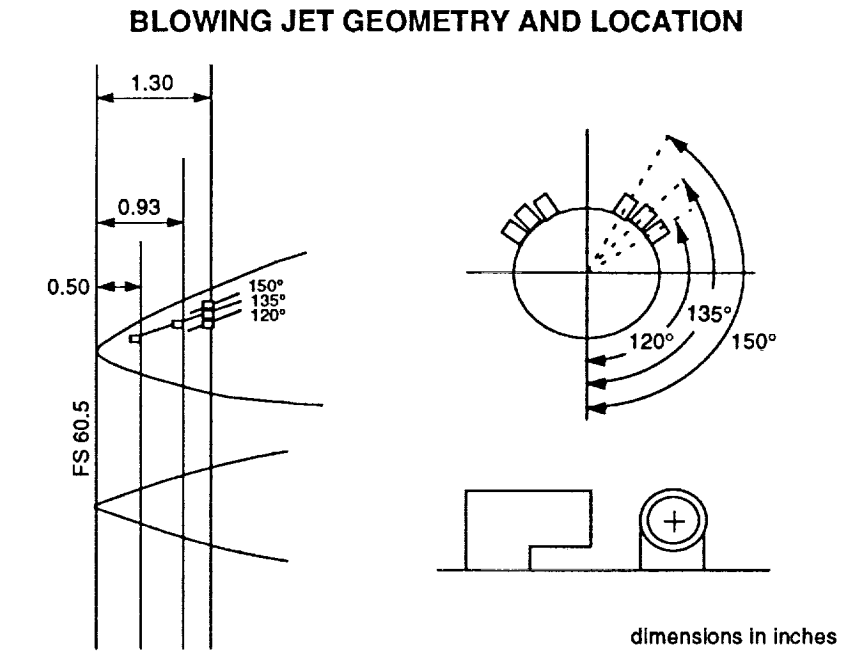

(a) Jet blowing

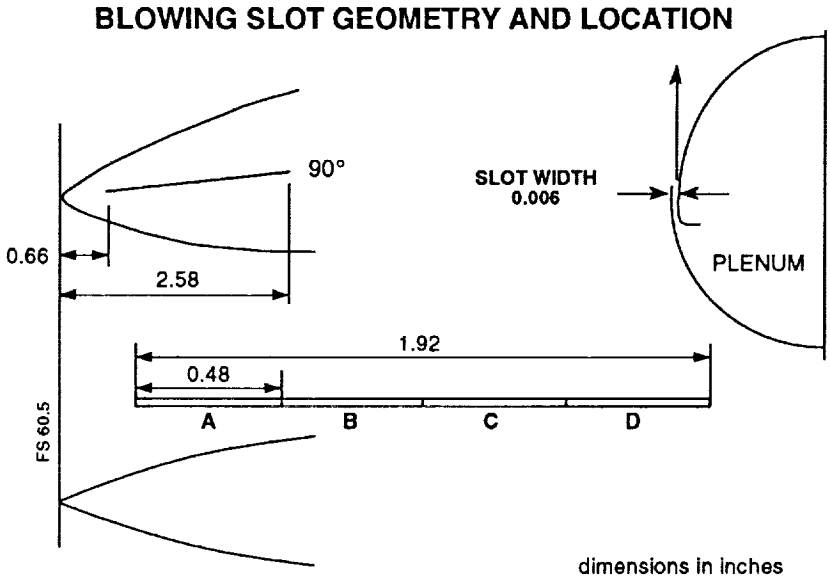

(b) Slot blowing

Figure 8 - Description of various forebody vortex control schemes

STRAKE GEOMETRY AND LOCATION

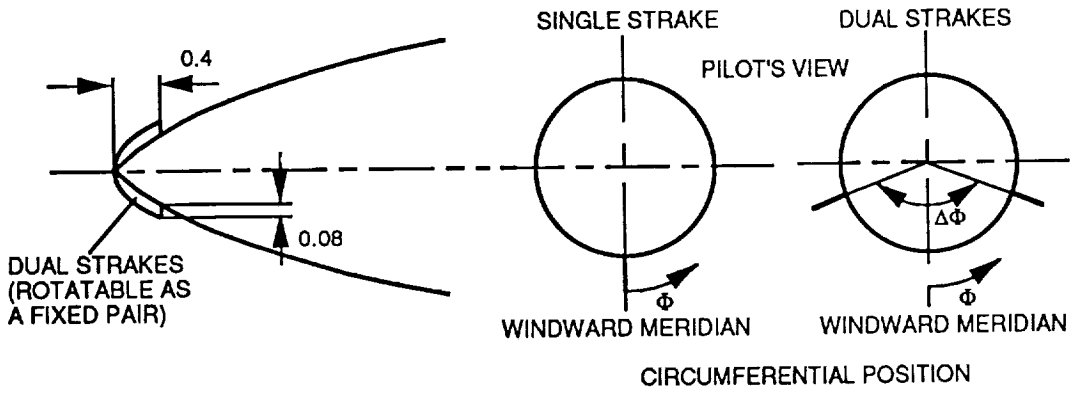

(c) Rotatable tip-strakes

VERTICAL NOSE STRAKE GEOMETRY AND LOCATION

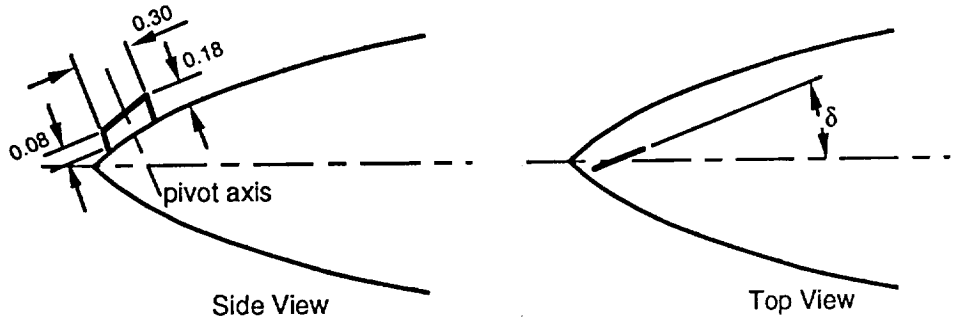

(d) Vertical nose-tip strake (Rhino-horn)

Figure 8 - Concluded

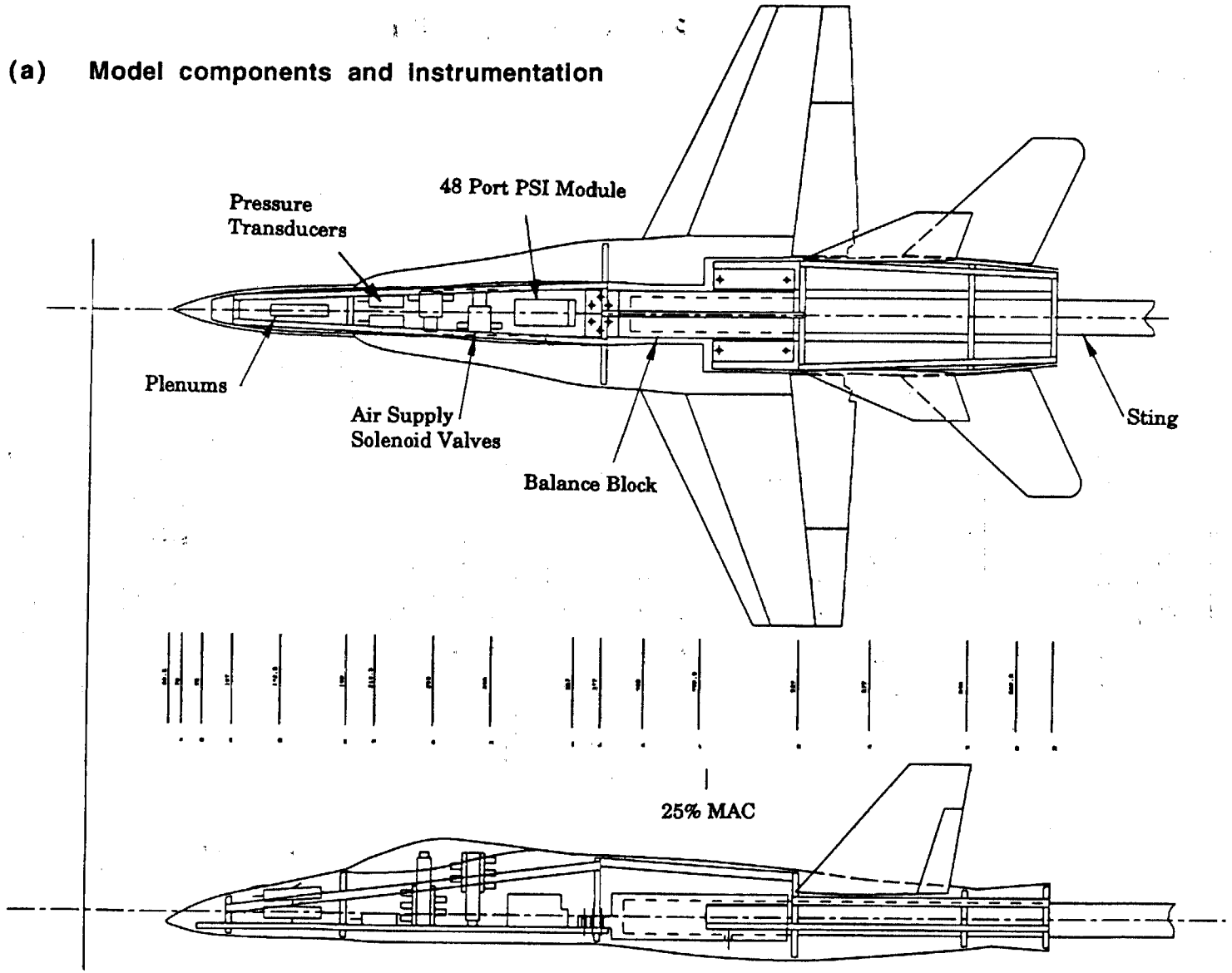

Figure 9 - 6 % F/A-18 wind tunnel model details

(b) Pressure tap locations

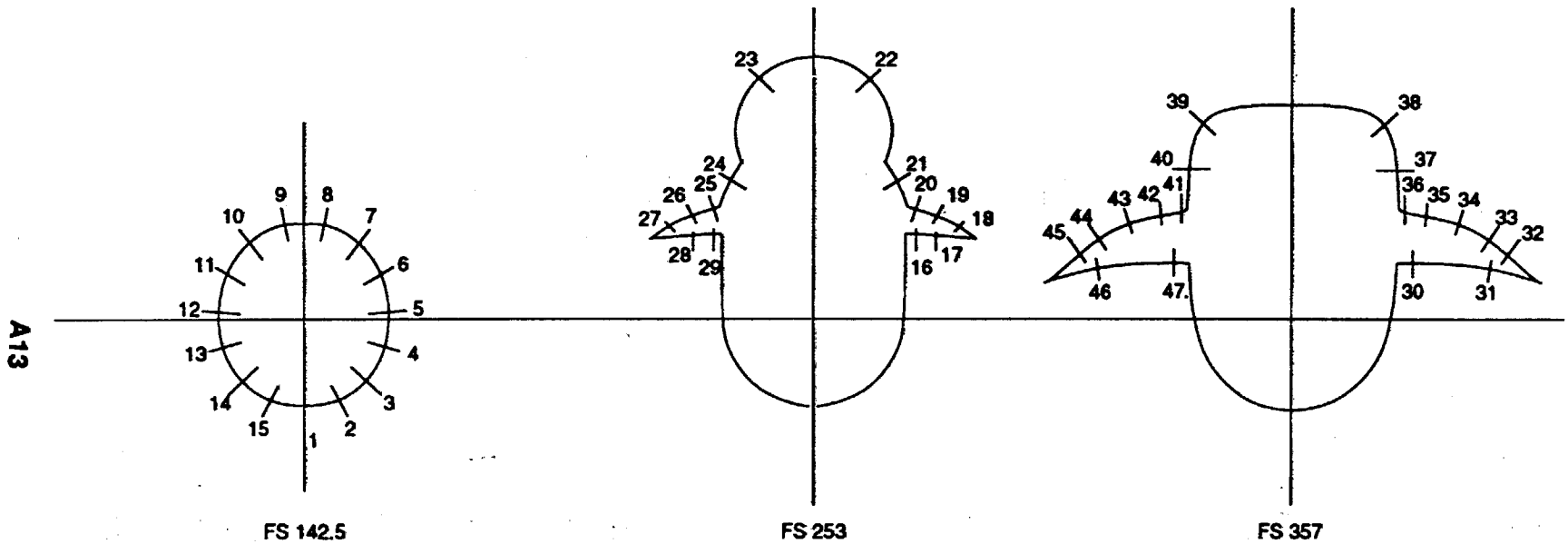

Figure 9 - Continued

F/A-18 PRESSURE TAP LOCATIONS

PORT #	FS	LOCATION	THETA	Y	Z
1	142.5	lower starboard	0	0	-1.180
2		lower starboard	24	0.0488	-1.077
3		lower starboard	45	0.818	-0.807
4		lower starboard	72	1.022	-0.33
5		upper starboard	95	1.047	0.0888
6		upper starboard	120	0.967	0.554
7		upper starboard	144	0.700	0.955
8		upper starboard	168	0.247	1.157
9		upper port	192	-0.250	1.155
10		upper port	216	-0.695	0.944
11		upper port	240	-0.953	0.542
12		upper port	265	-1.033	0.0948
13		lower port	288	-1.011	-0.325
14		lower port	315	-0.801	-0.801
15		lower port	336	-0.482	-1.075

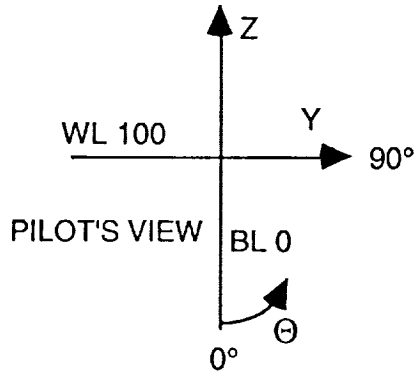

PORT #	FS	LOCATION	Y*	Y/S'	Y	Z
16	253	lower starboard	0.136	0.152		
17		lower starboard	0.401	0.45		
18		upper starboard	0.674	0.758		
19		upper starboard	0.409	0.46		
20		upper starboard	0.119	0.134		
21					-1.06	1.66
22					-0.77	2.99
23					0.77	2.99
24					1.06	1.66

Figure 9 - Continued

25		upper port	0.119	0.134		
26		upper port	0.409	0.46		
27		upper port	0.674	0.758		
28		lower port	0.401	0.45		
29		lower port	0.136	0.152		
30	357	lower starboard	0.214	0.123		
31		lower starboard	1.201	0.691		
32		upper starboard	1.448	0.883		
33		upper starboard	1.195	0.689		
34		upper starboard	0.788	0.454		
35		upper starboard	0.374	0.215		
36		upper starboard	0.08	0.046		
37					-1.36	1.91
38					-1.13	2.52
39					1.13	2.52
40					1.36	1.91
41		upper port	0.08	0.046		
42		upper port	0.374	0.215		
43		upper port	0.788	0.454		
44		upper port	1.195	0.689		
45		upper port	1.448	0.883		
46		lower port	1.201	0.691		
47		lower port	0.214	0.123		

Y* is 6% scale from inboard edge of LEX

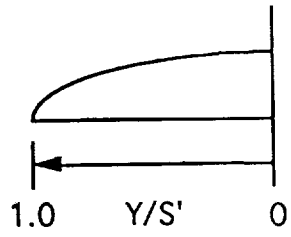

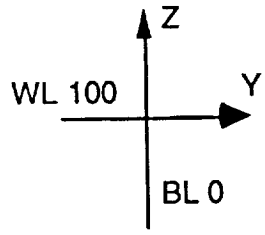

PILOT'S VIEW

Figure 9 - Continued

(c) Endevco pressure transducer locations

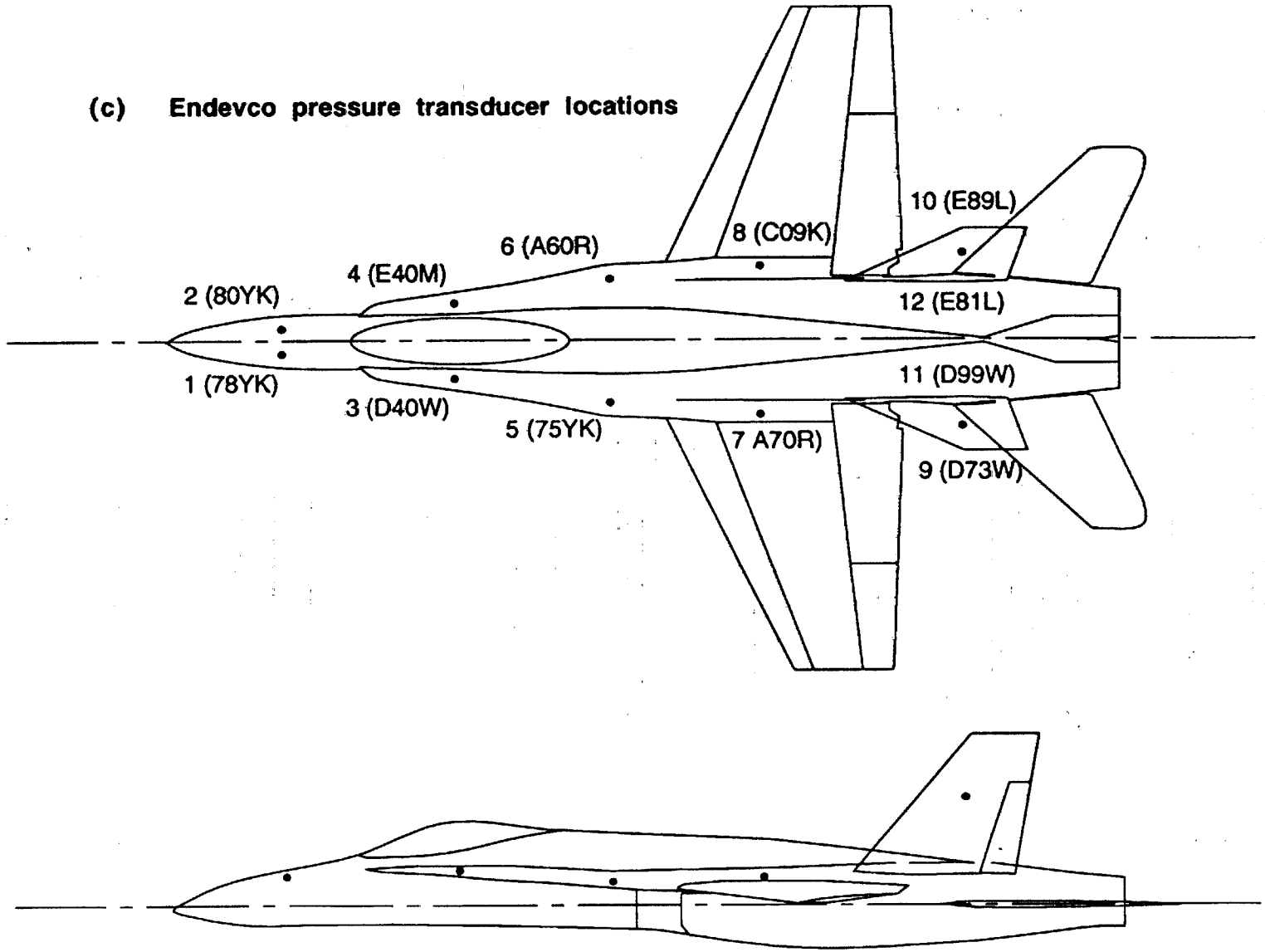

Figure 9 - Continued

F/A-18 ENDEVCO SENSOR LOCATION

END. #	FS	LOCATION	THETA	Y/S'	BL
2	142.5+	upper starboard	135		
1		upper port	225		
4	253+	upper starboard		0.5	
3		upper port		0.5	
6	357+	upper starboard		0.7	
5		upper port		0.7	
8	470	over wing 0.5Cr			54.2
7					-54.2

END. #	LOCATION
9, 10, 11, 12	Vertical Tail 45% chord 60% span Inboard and outboard of both tails

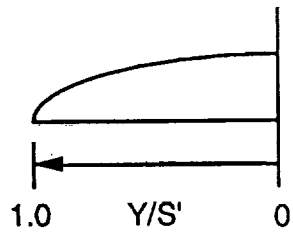

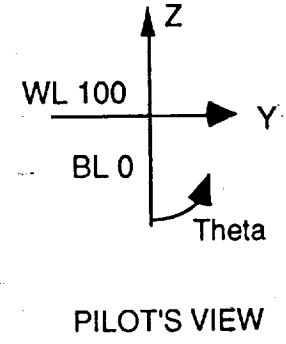

Figure 9 - Concluded

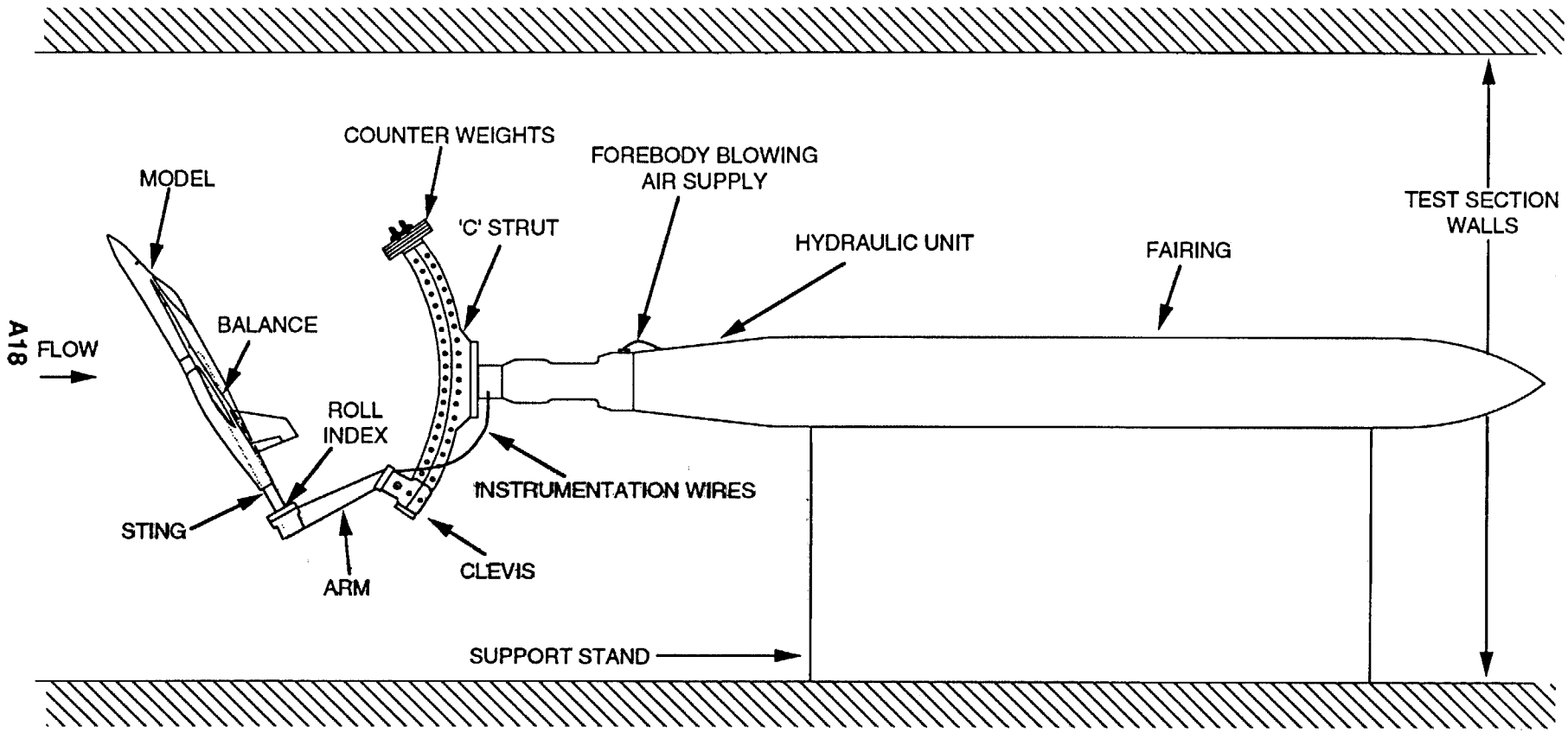

Figure 10 - Drawing of new rotary-balance apparatus installed in Ames 7 x 10-ft wind tunnel

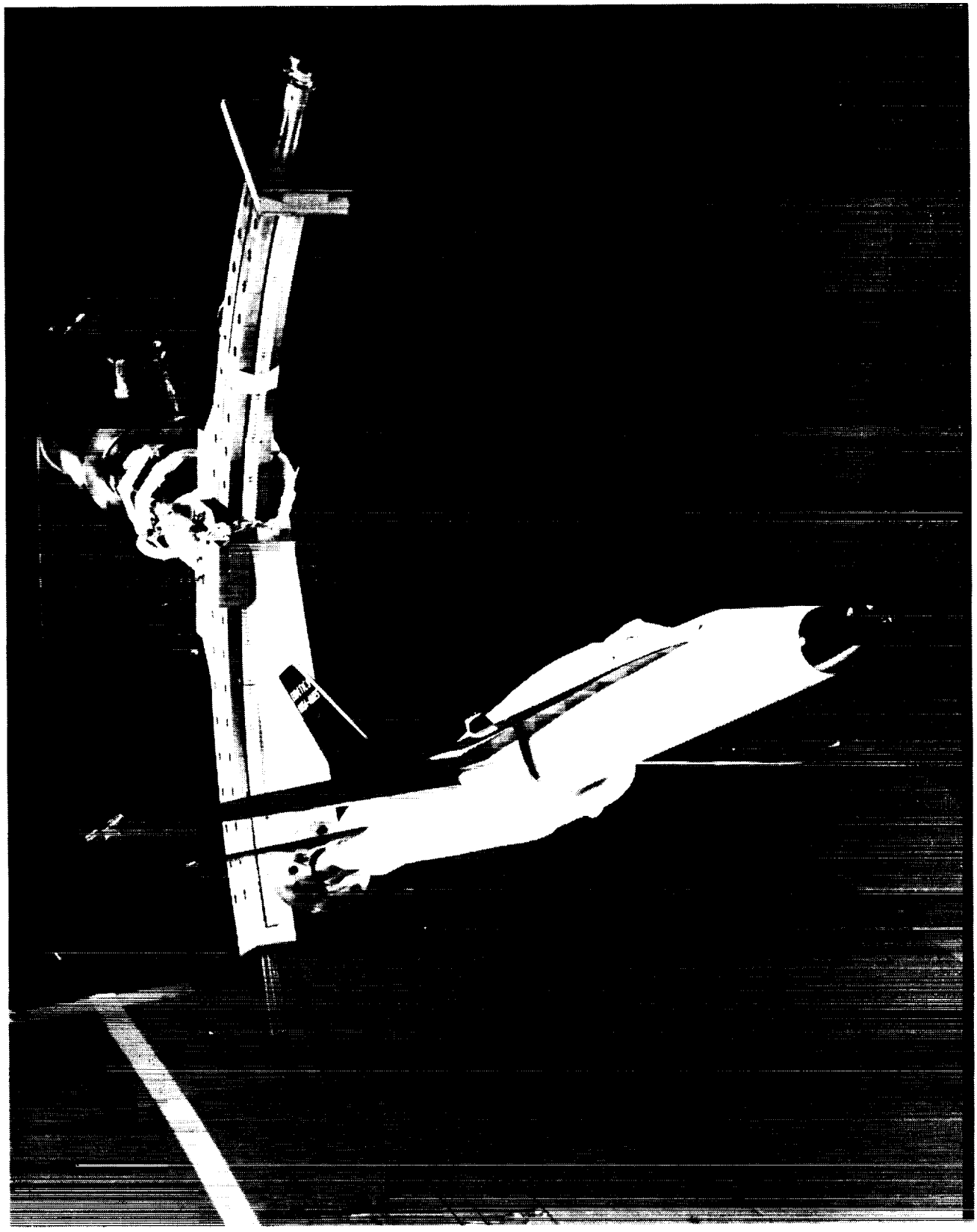

Figure 11 - Photographs of F/A-18 model installed on rotary-balance apparatus in Ames 7 x 10-ft wind tunnel

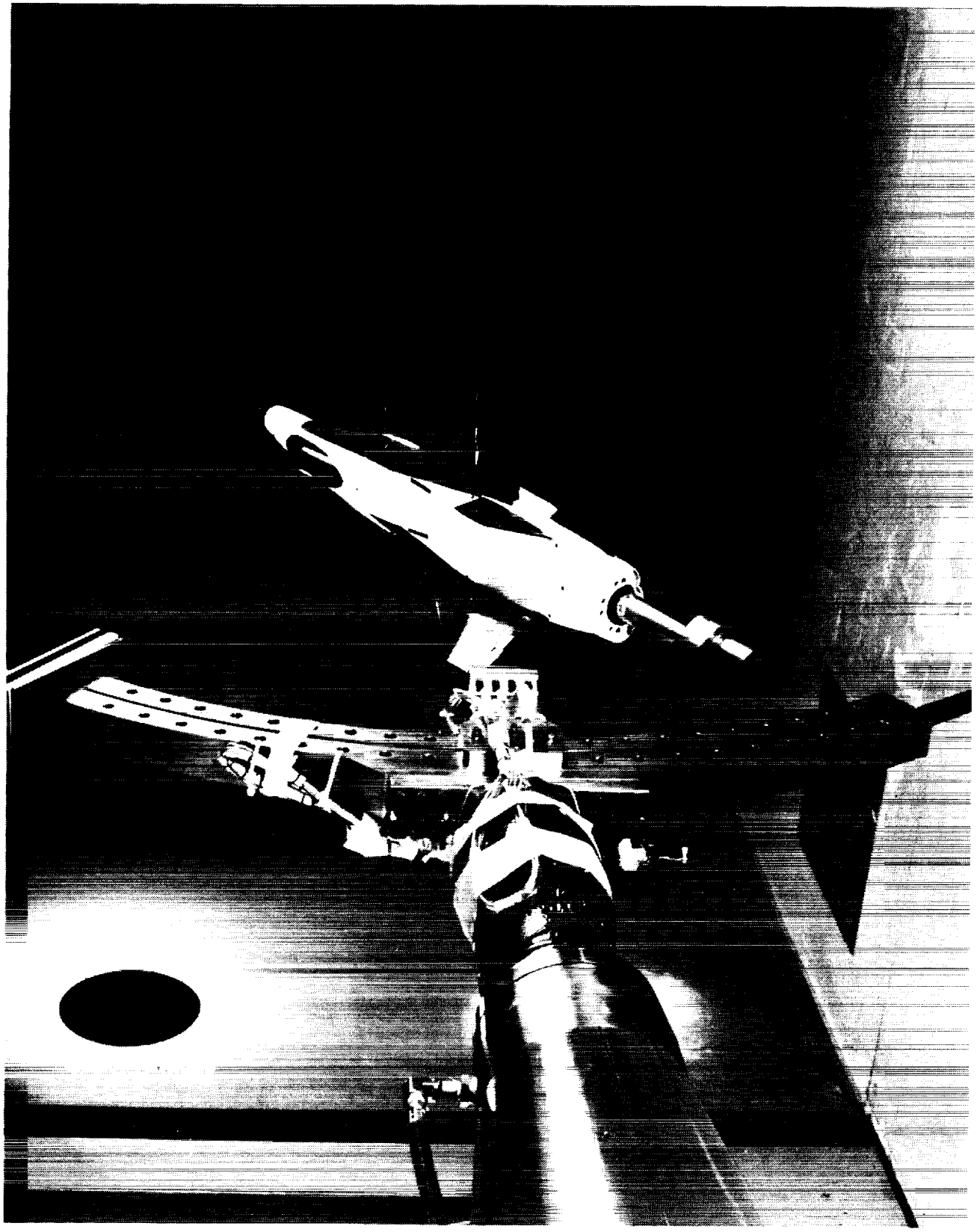

Figure 11 - Concluded

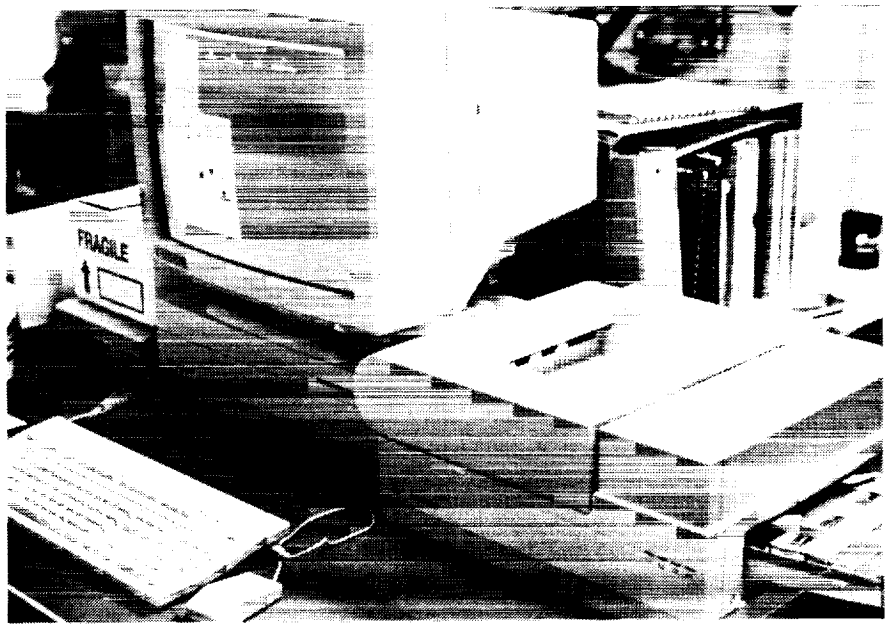

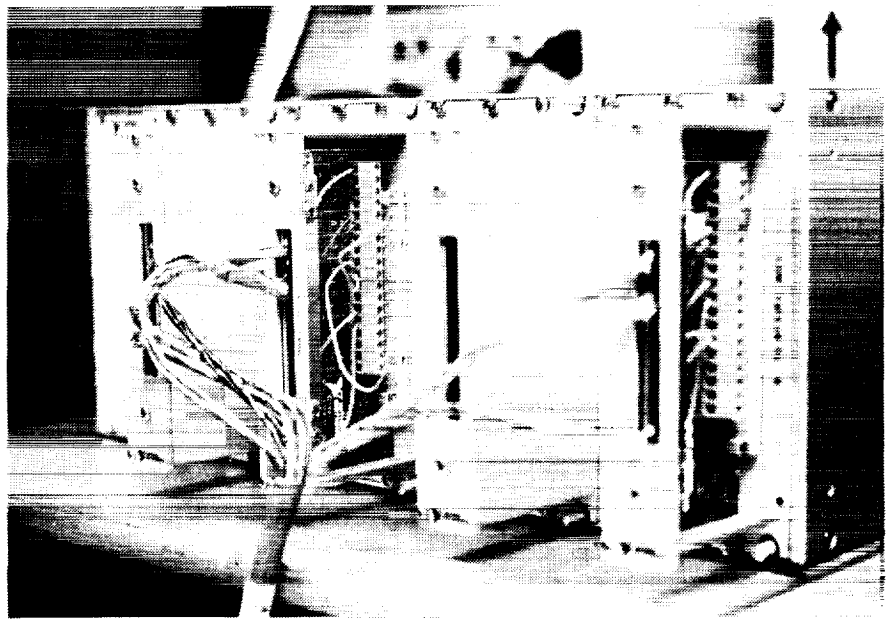

(a) Photographs of Macintosh-based data acquisition system

Fig. 12 - Macintosh-based data acquisition

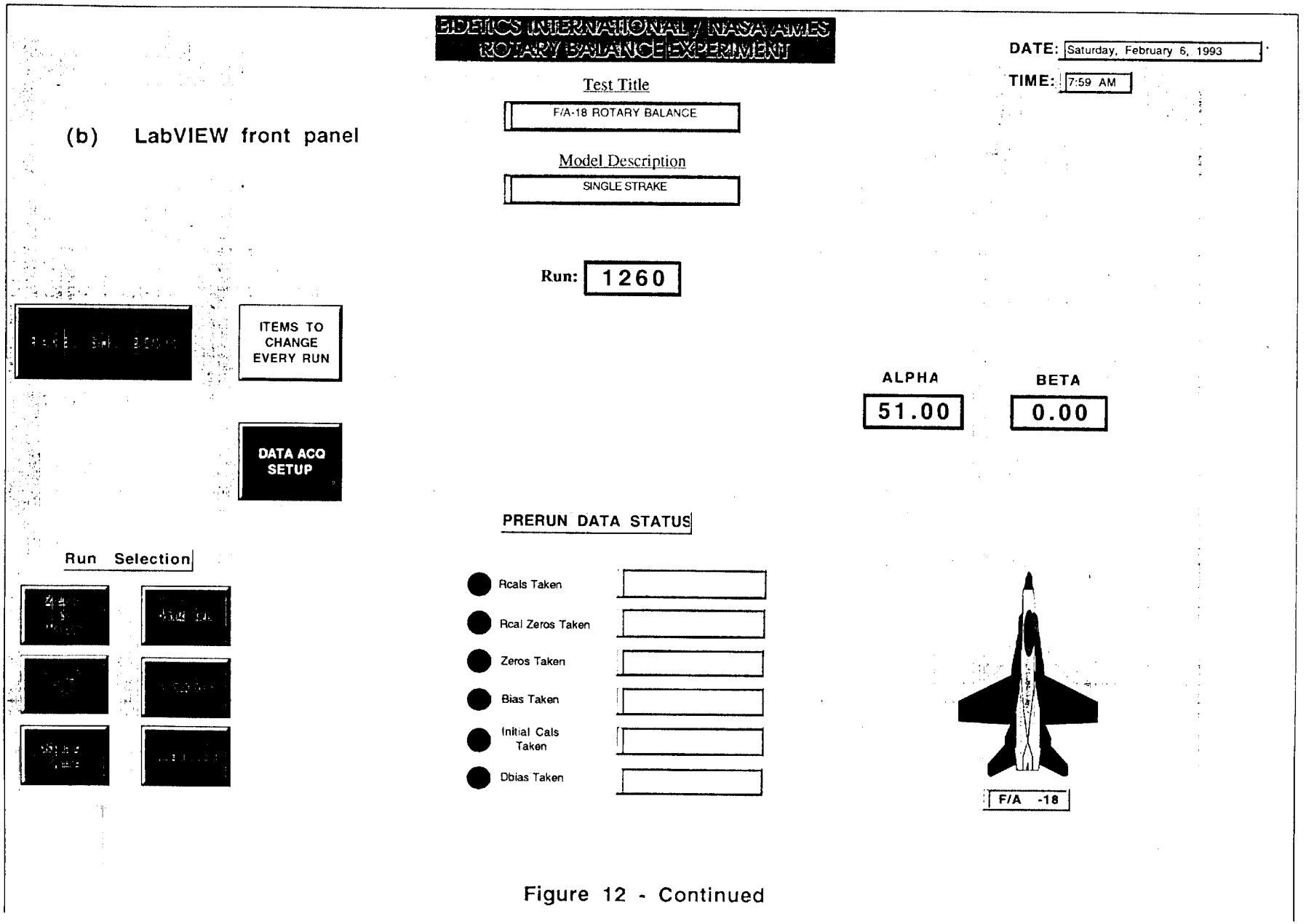

(b) LabVIEW front panel

Figure 12 - Continued

(c) Front panel diagram

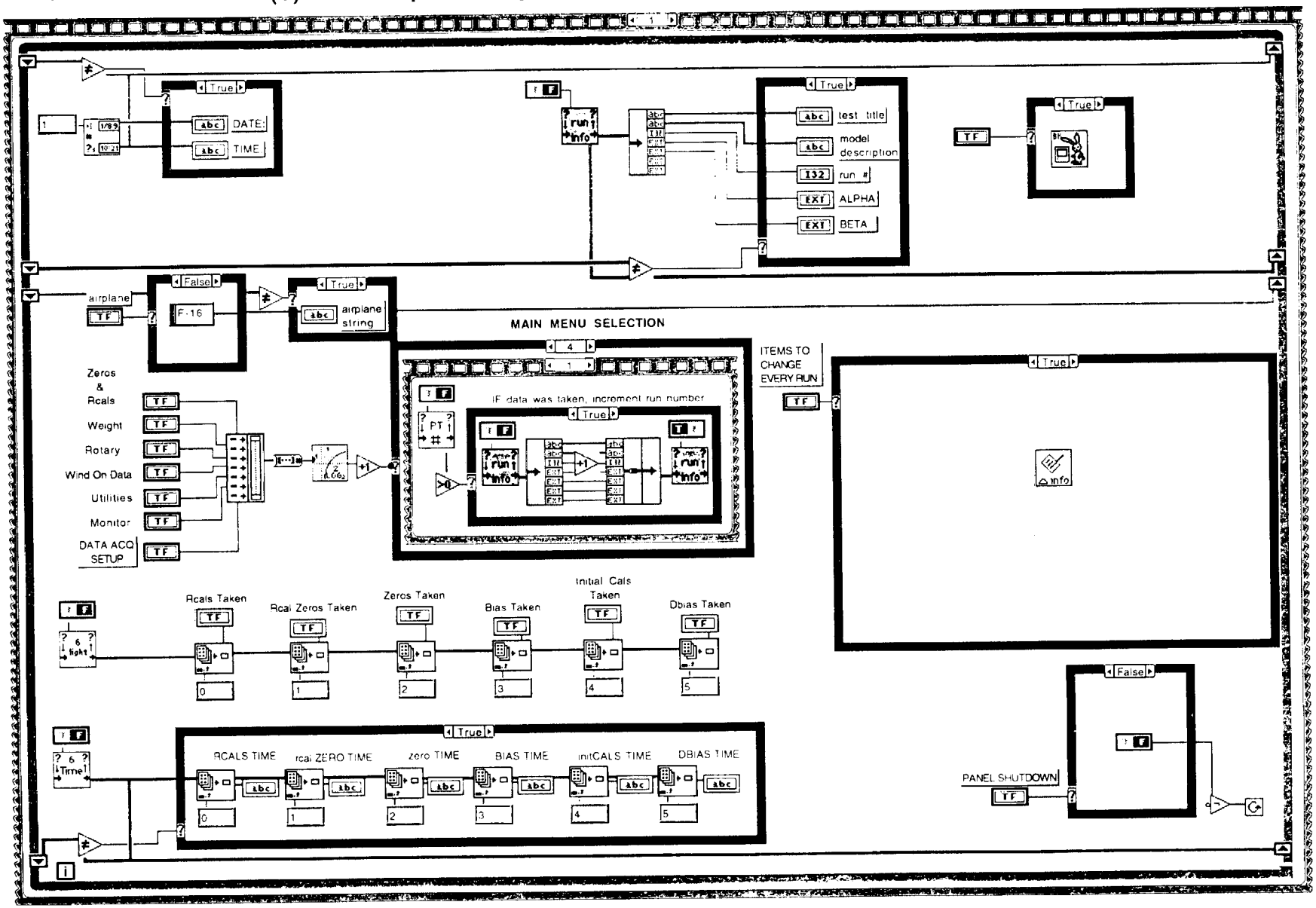

Figure 12 - Continued

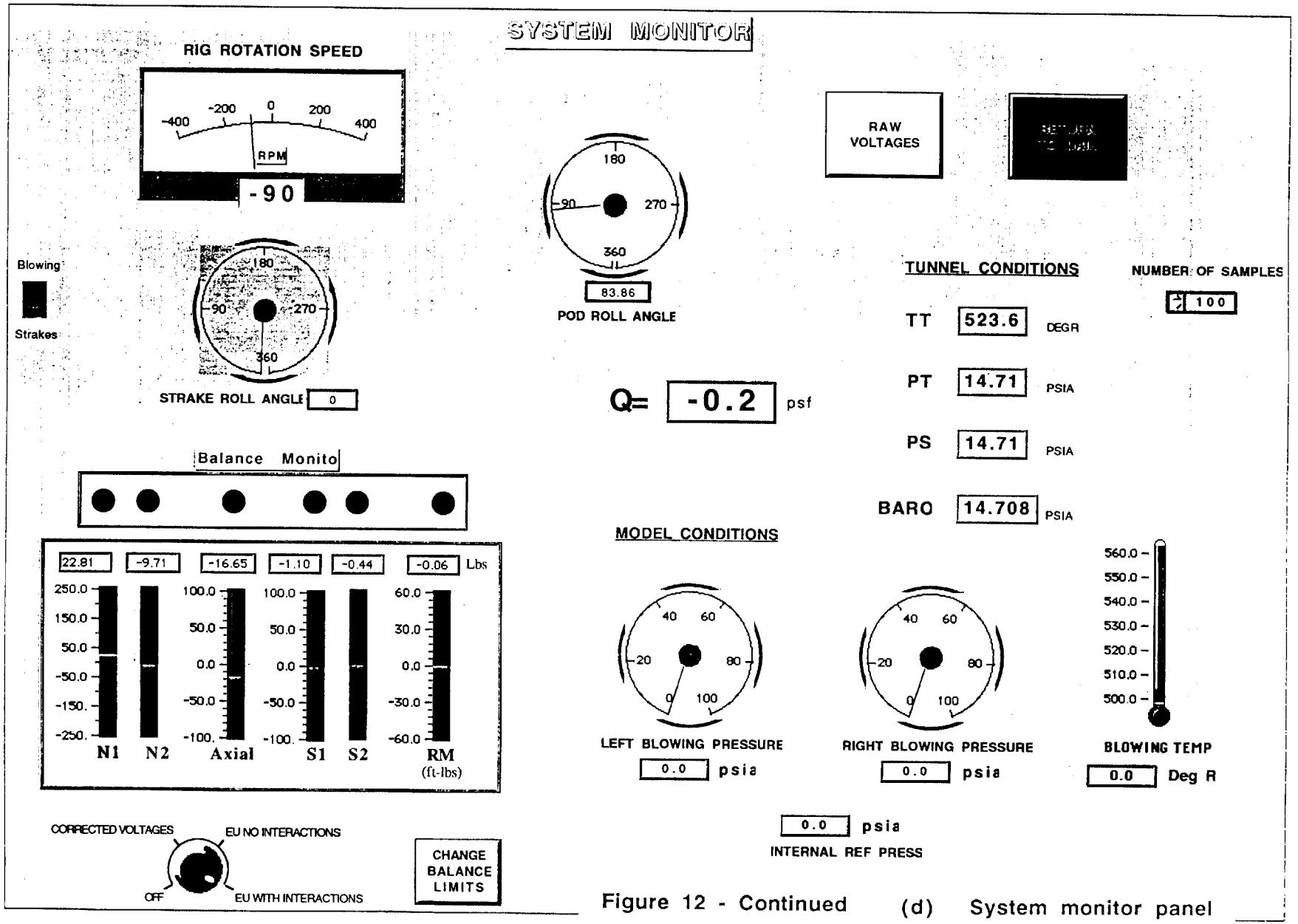

Figure 12 - Continued (d) System monitor panel

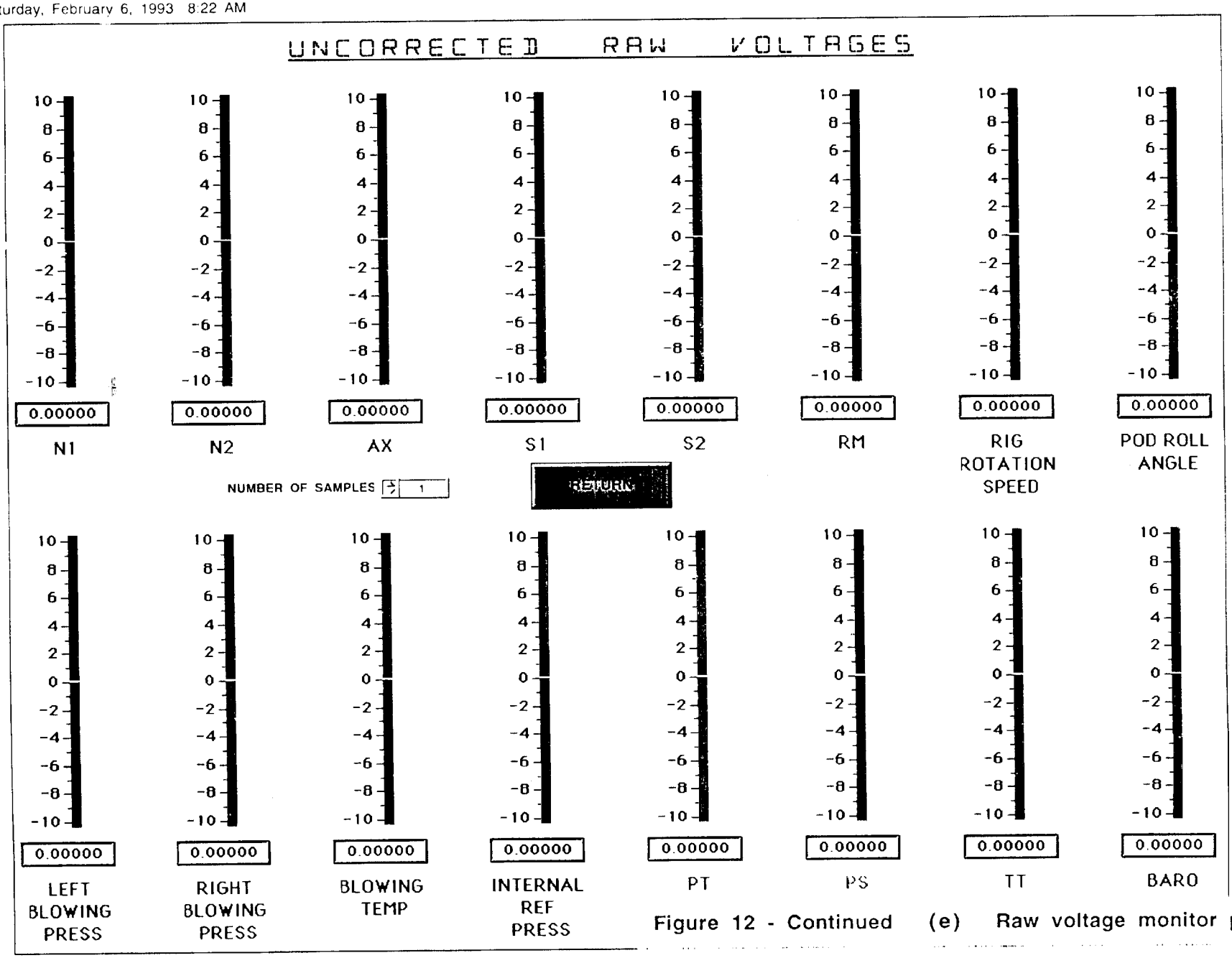

Figure 12 - Continued (e) Raw voltage monitor pane

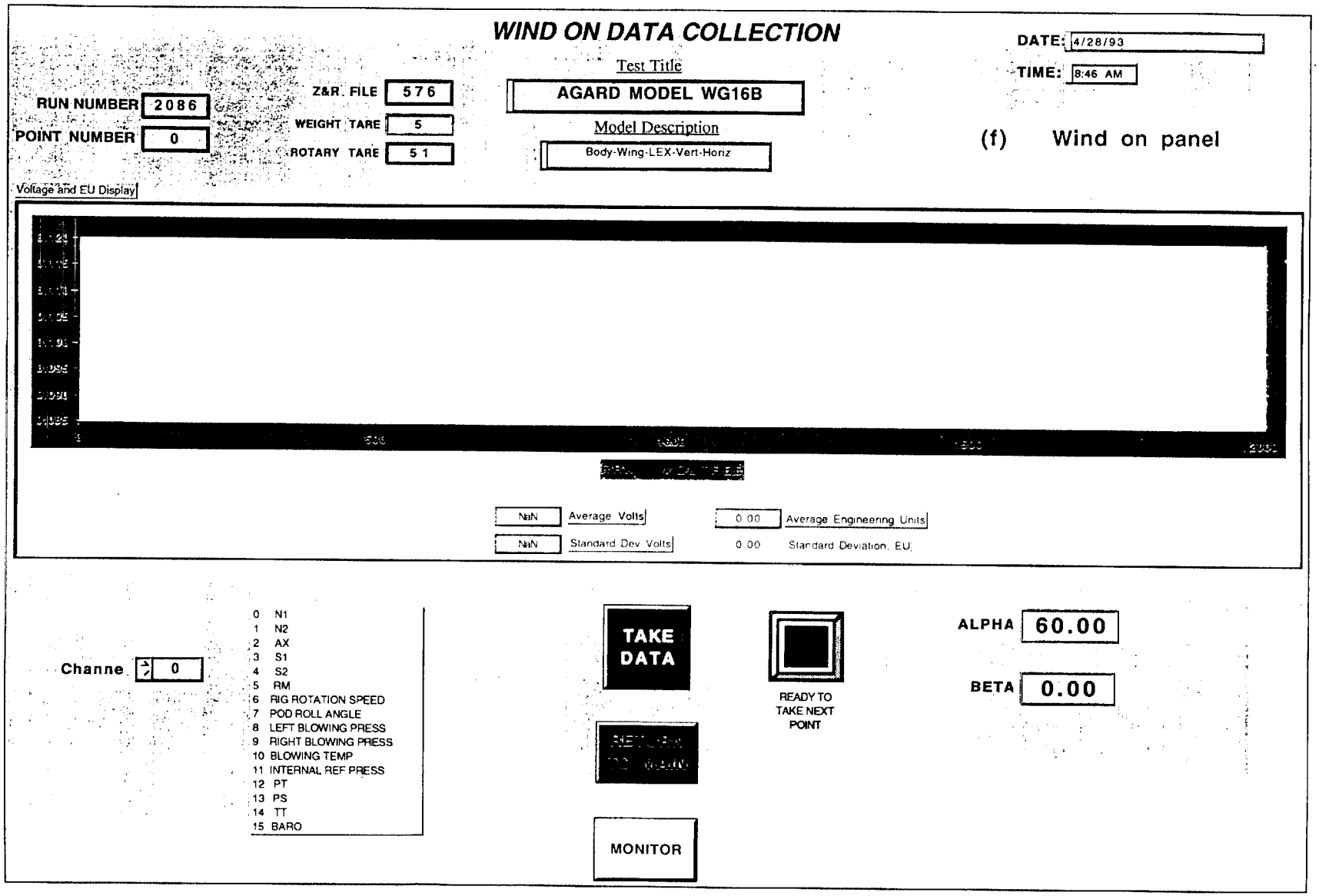

Figure 12 - Continued

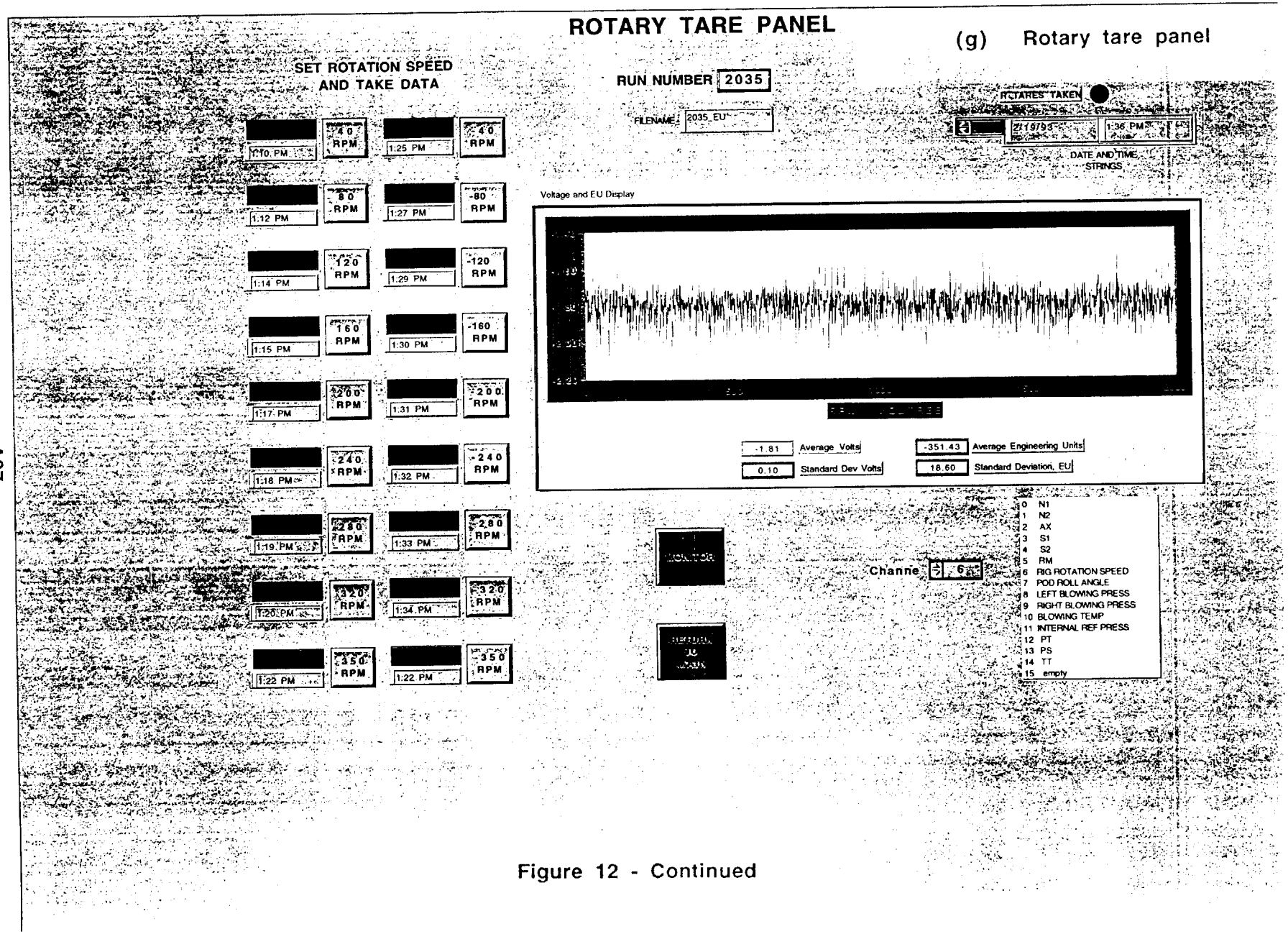

(g) Rotary tare panel

Figure 12 - Continued

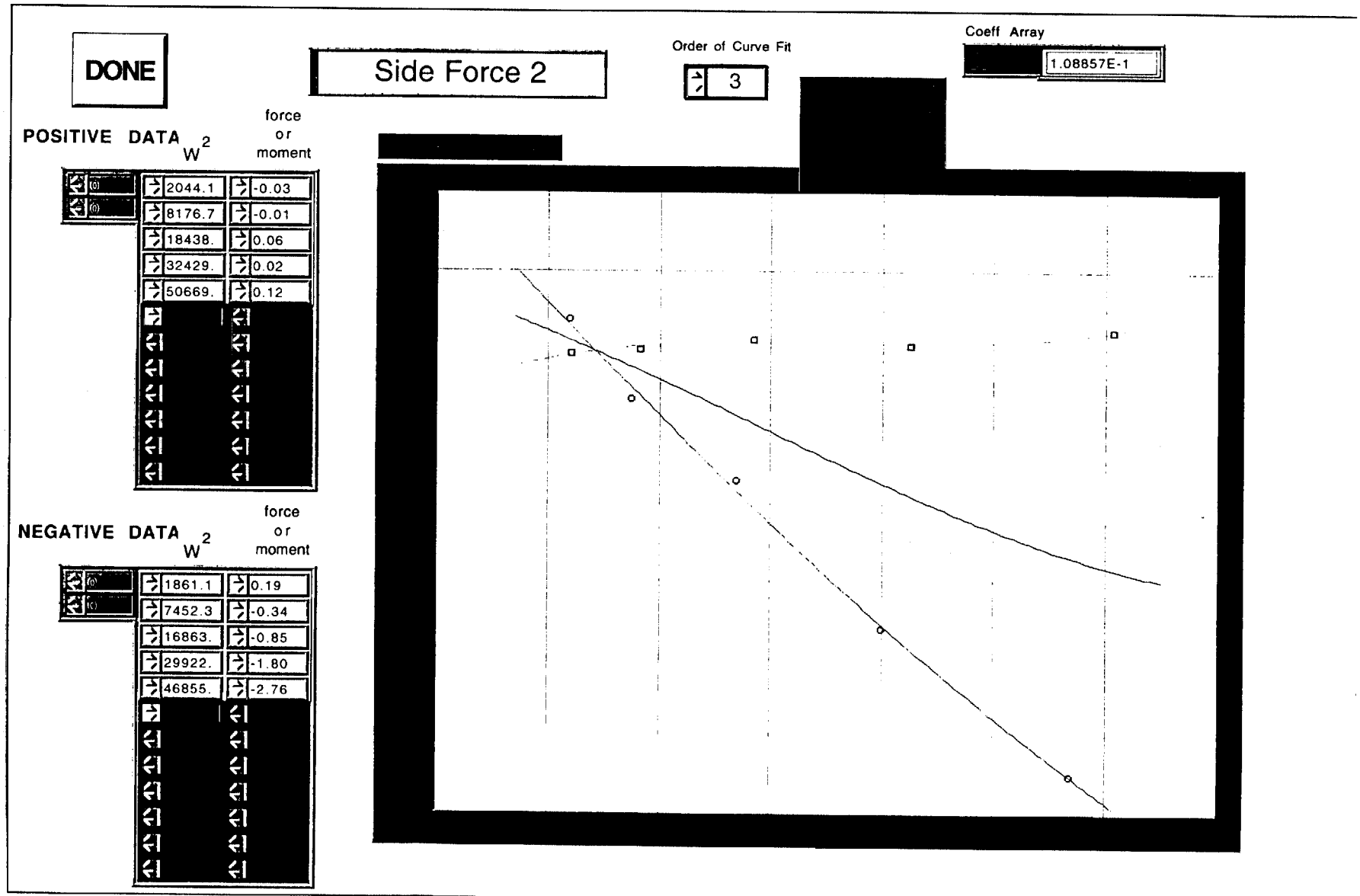

Figure 12 - Continued (h) Rotary tare curve fit panel

Reduce Weight Tare
Tuesday, January 5, 1993 4:41 PM
Front Panel

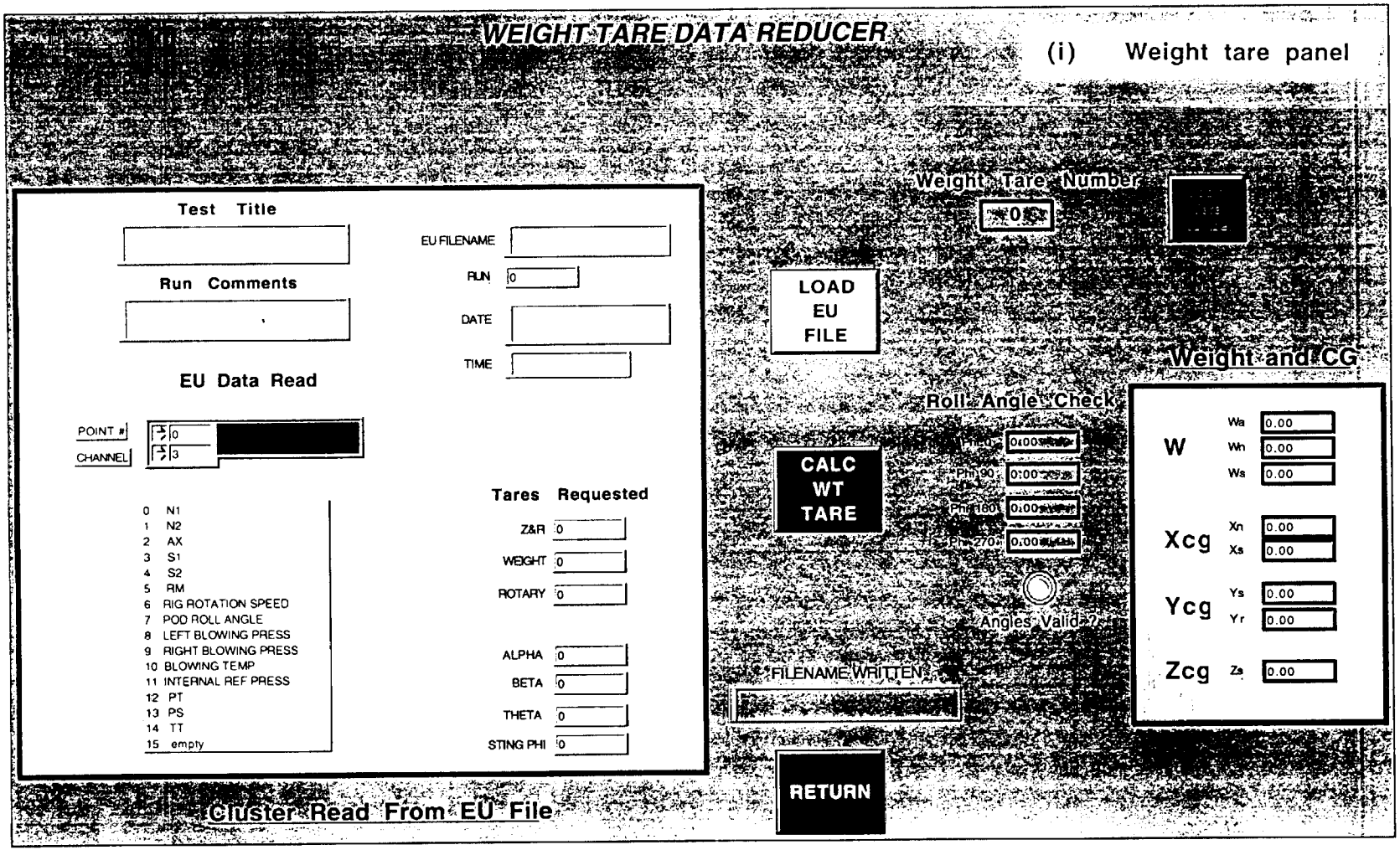

A29

Figure 12 - Continued

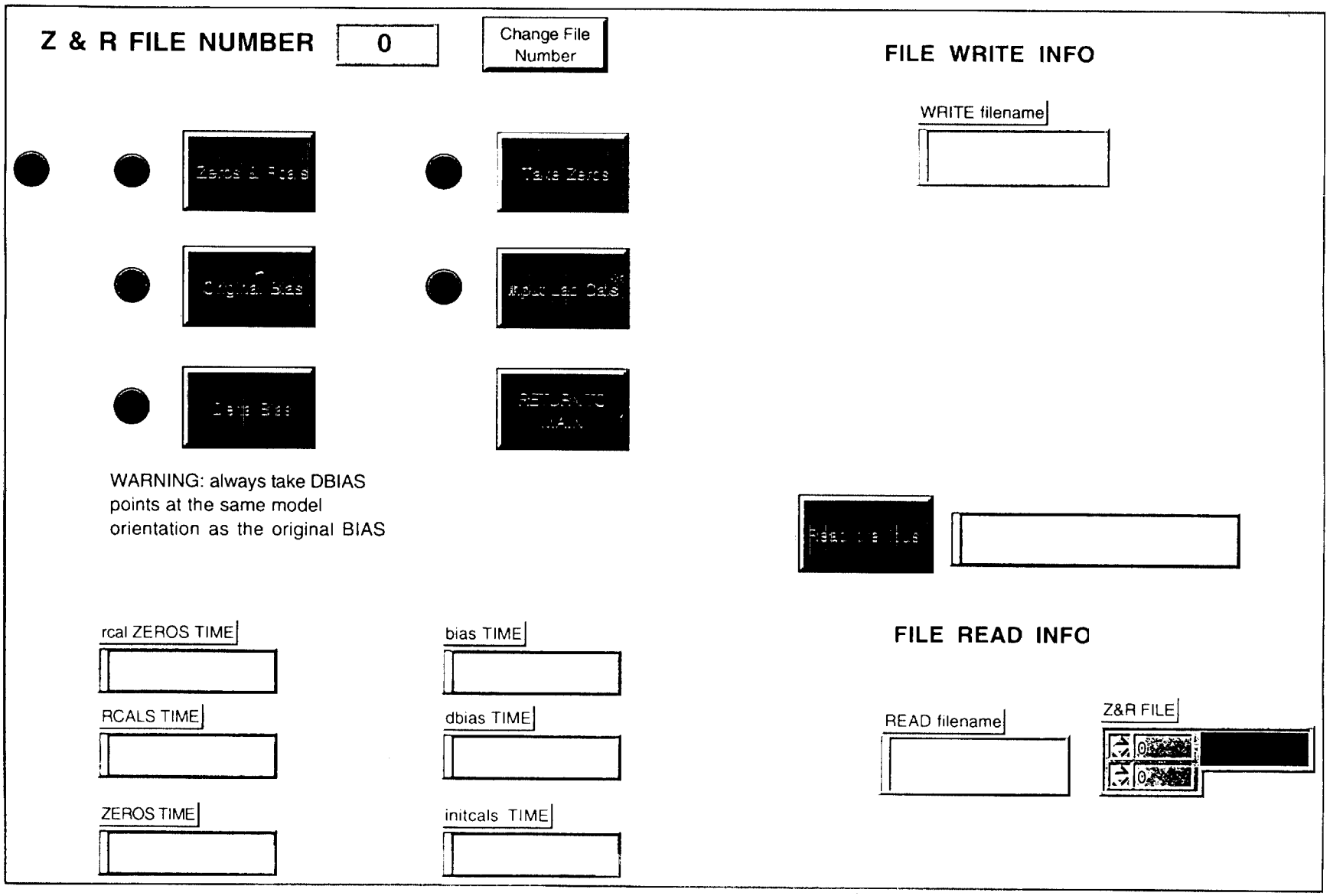

A30

Figure 12 - Concluded (j) Zero and Rcal panel

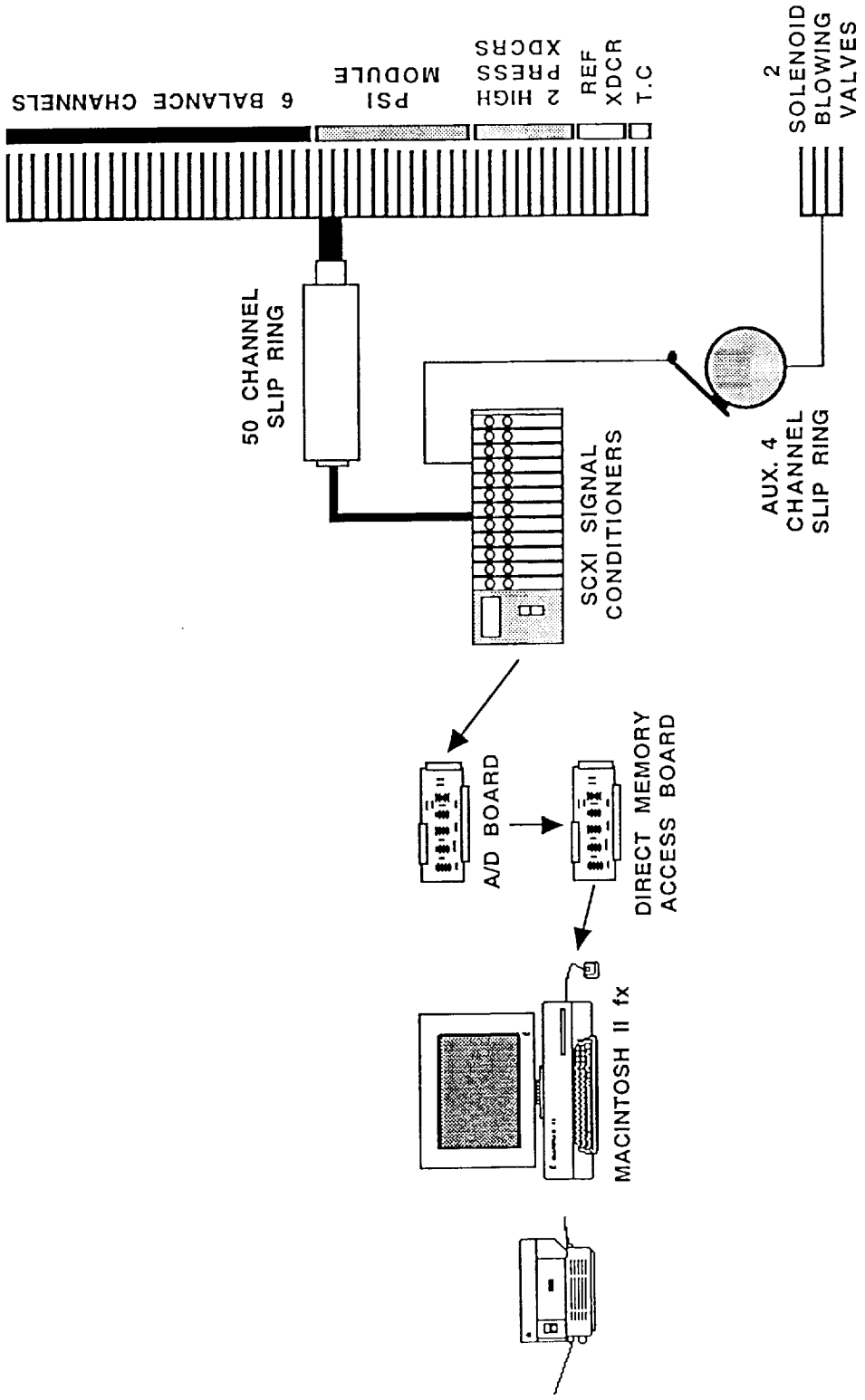

Figure 13 - Schematic of data acquistion and reduction system

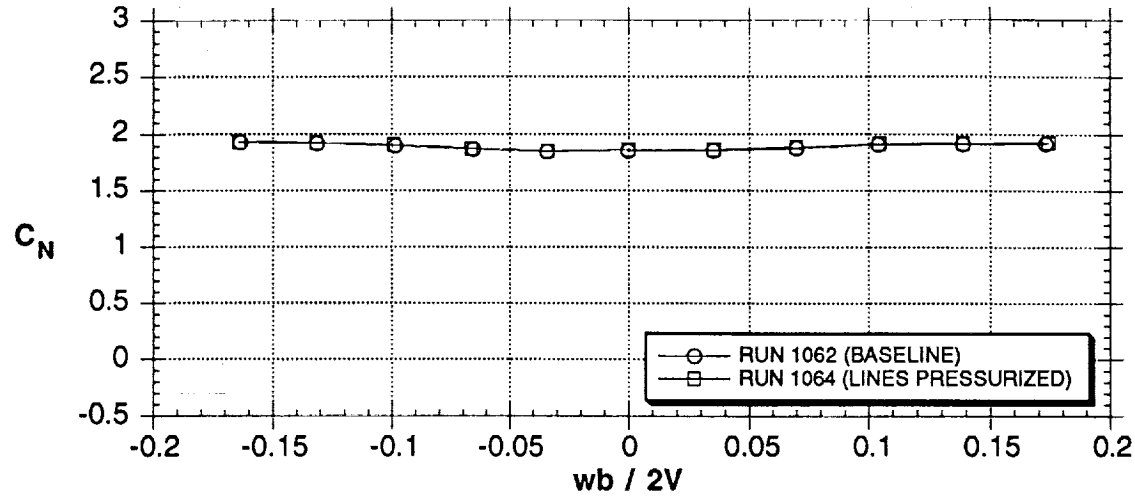

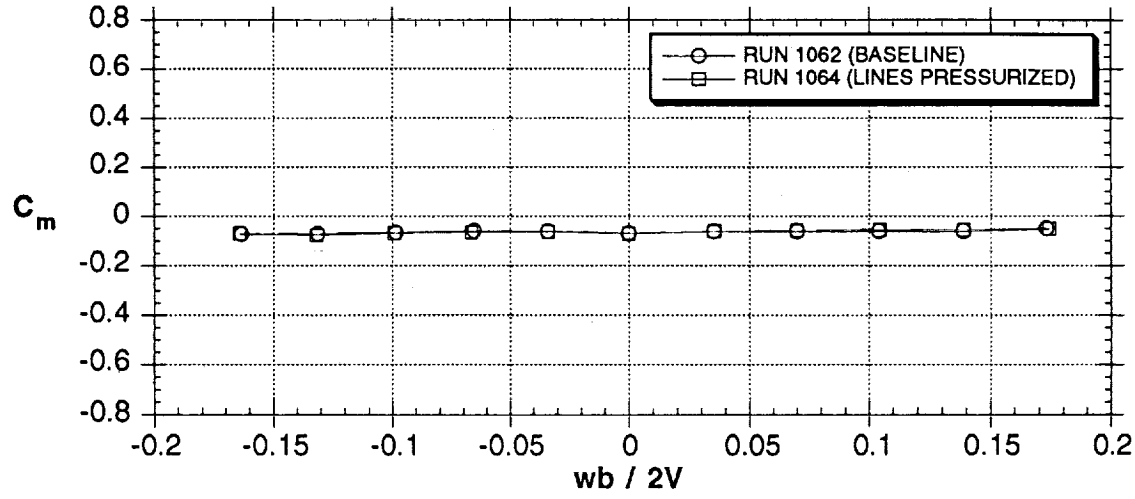

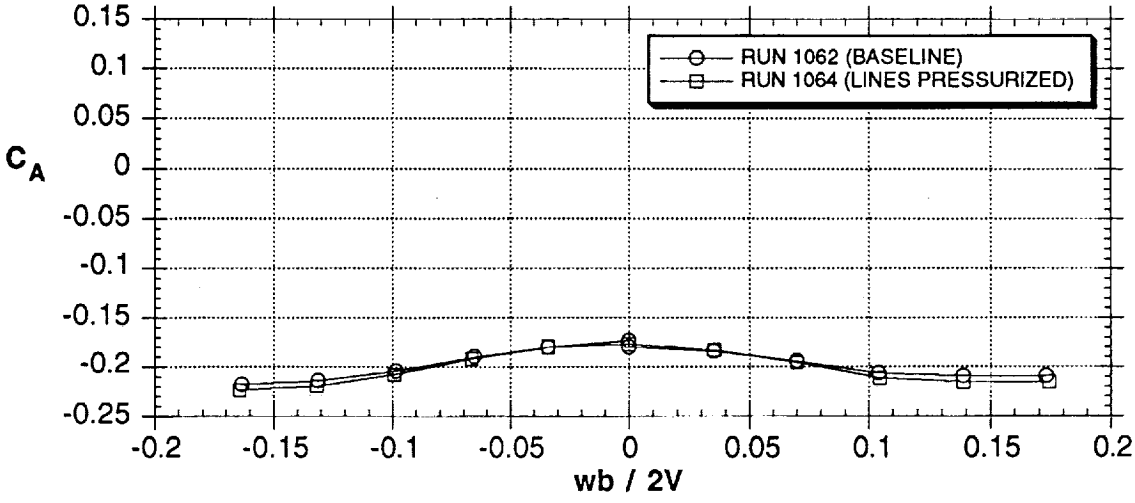

Figure 14 - Effects of pressurized air line on force and moments

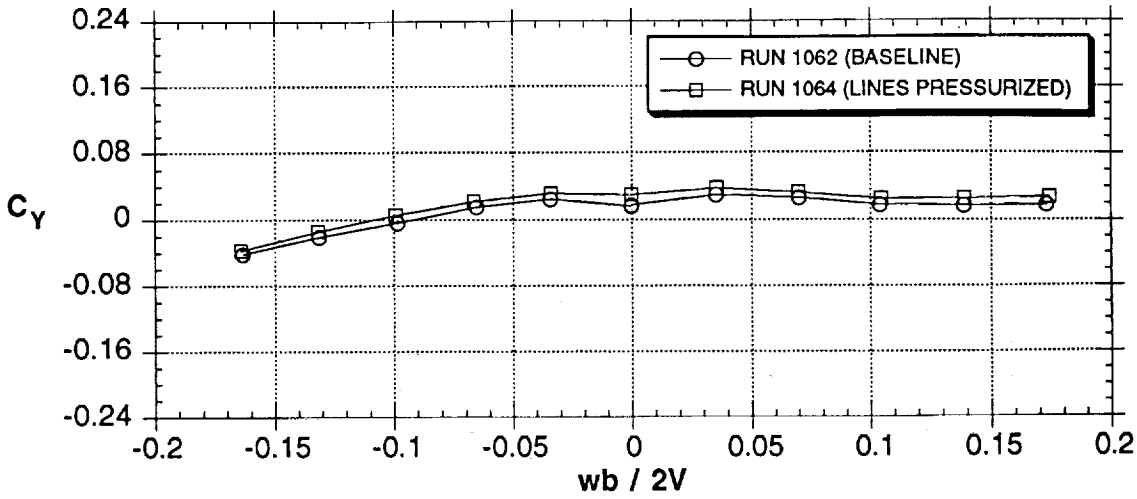

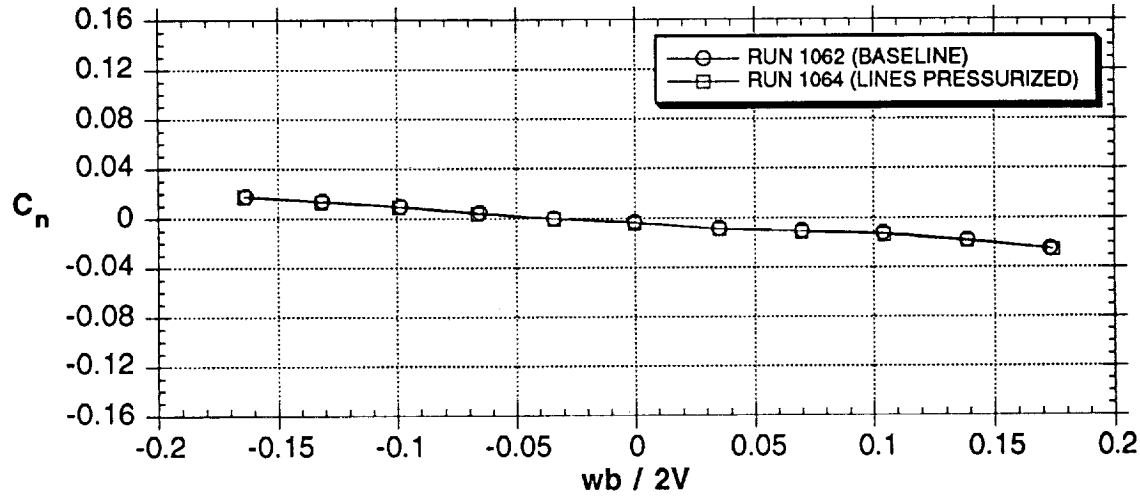

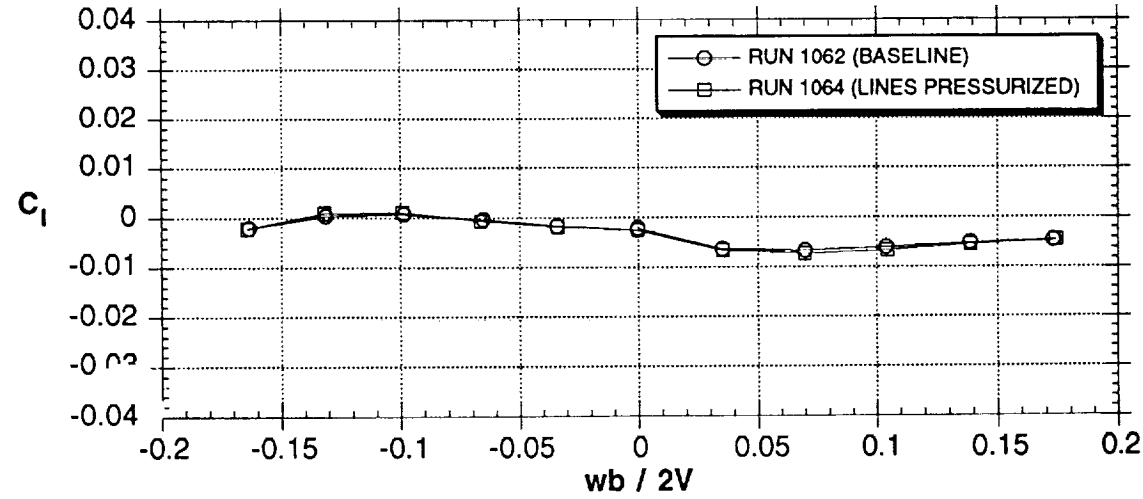

Figure 14 - Concluded

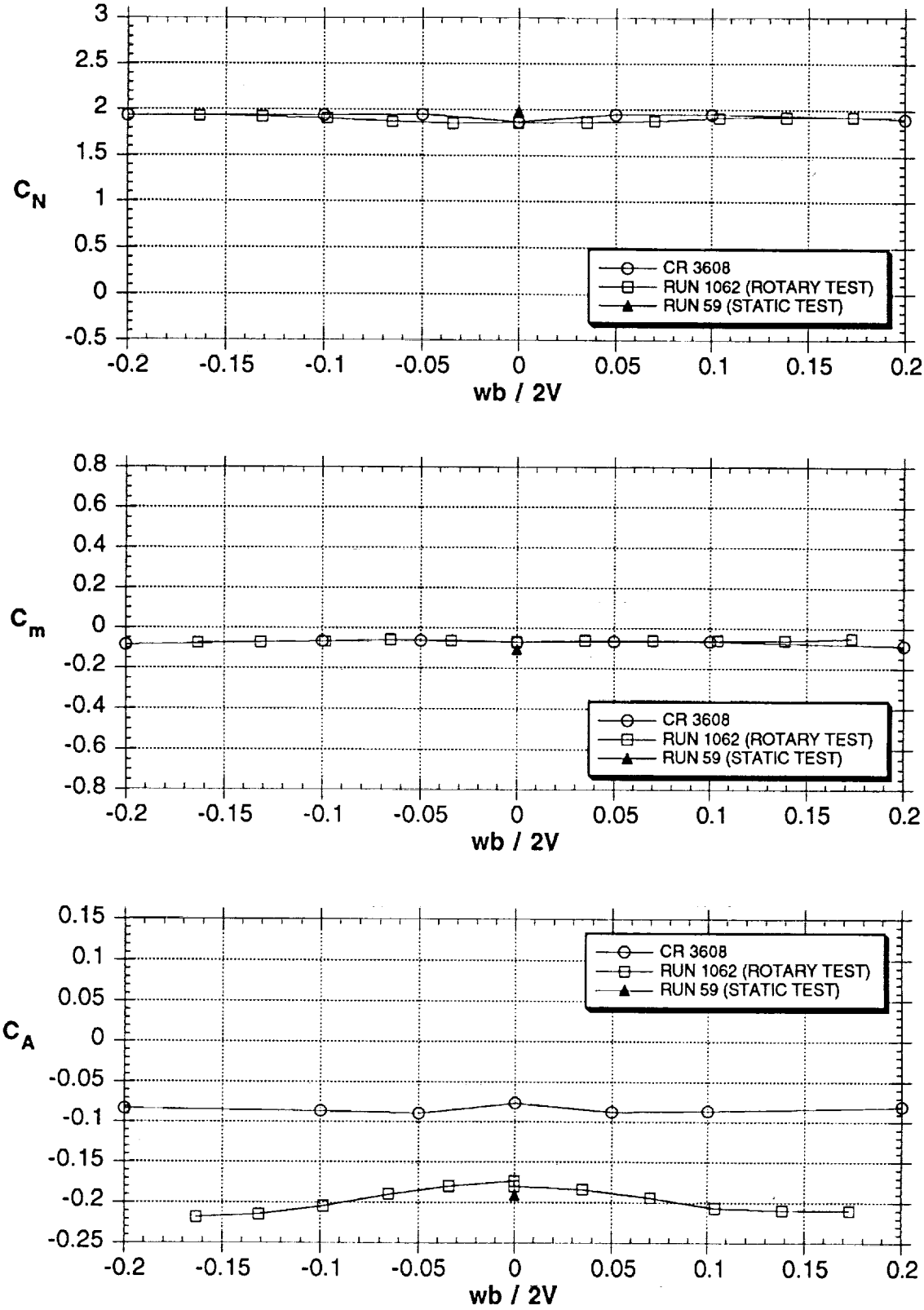

Figure 15 - Comparison of data from Eidetics static test and zero-rotation rotary-balance data from Eidetics and NASA CR 3608 (Ref. 38), α = 30°

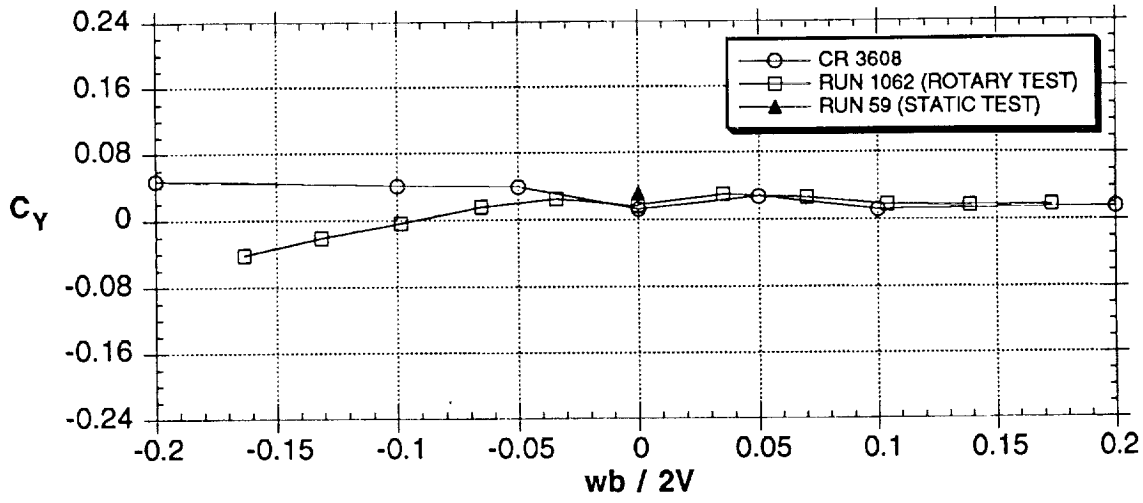

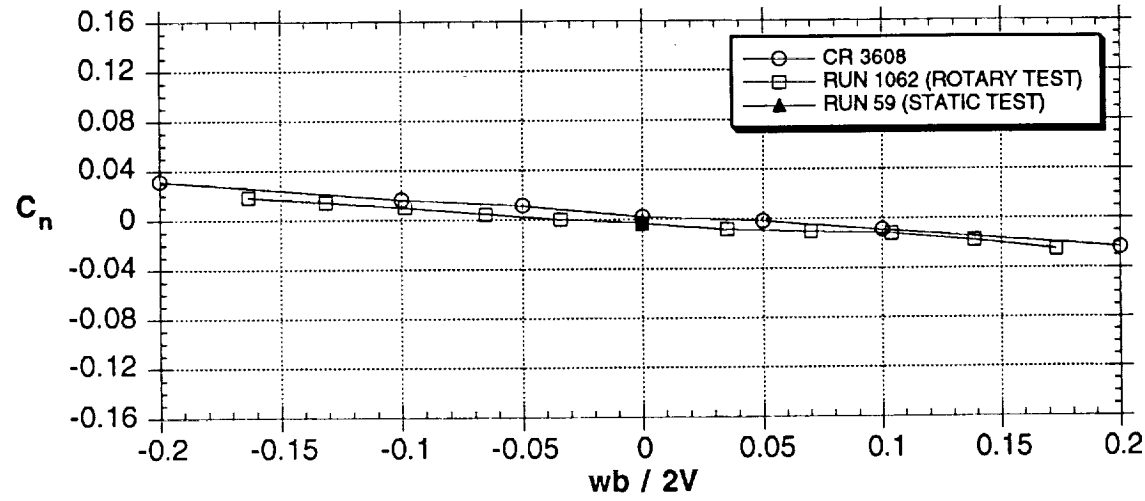

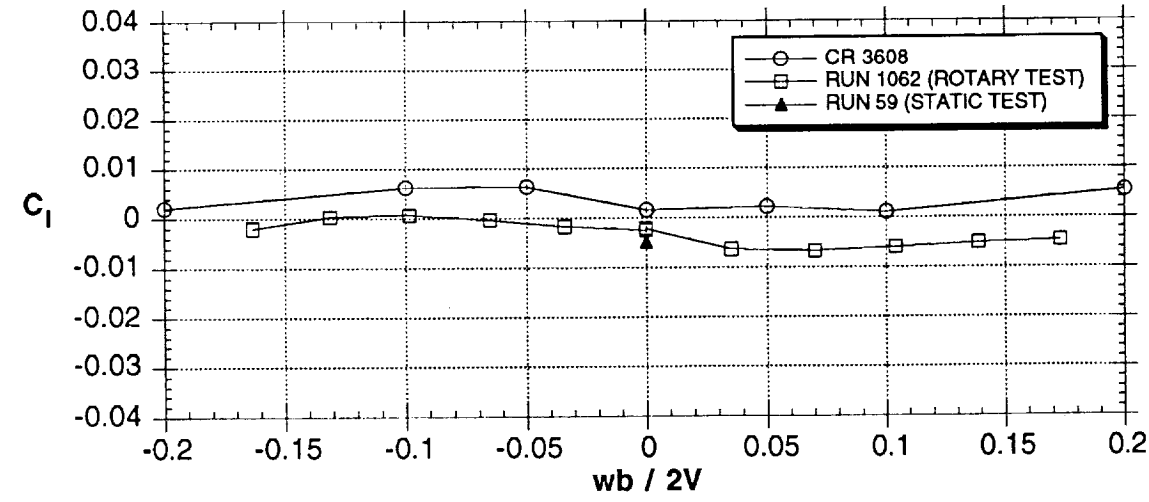

Figure 15 - Concluded

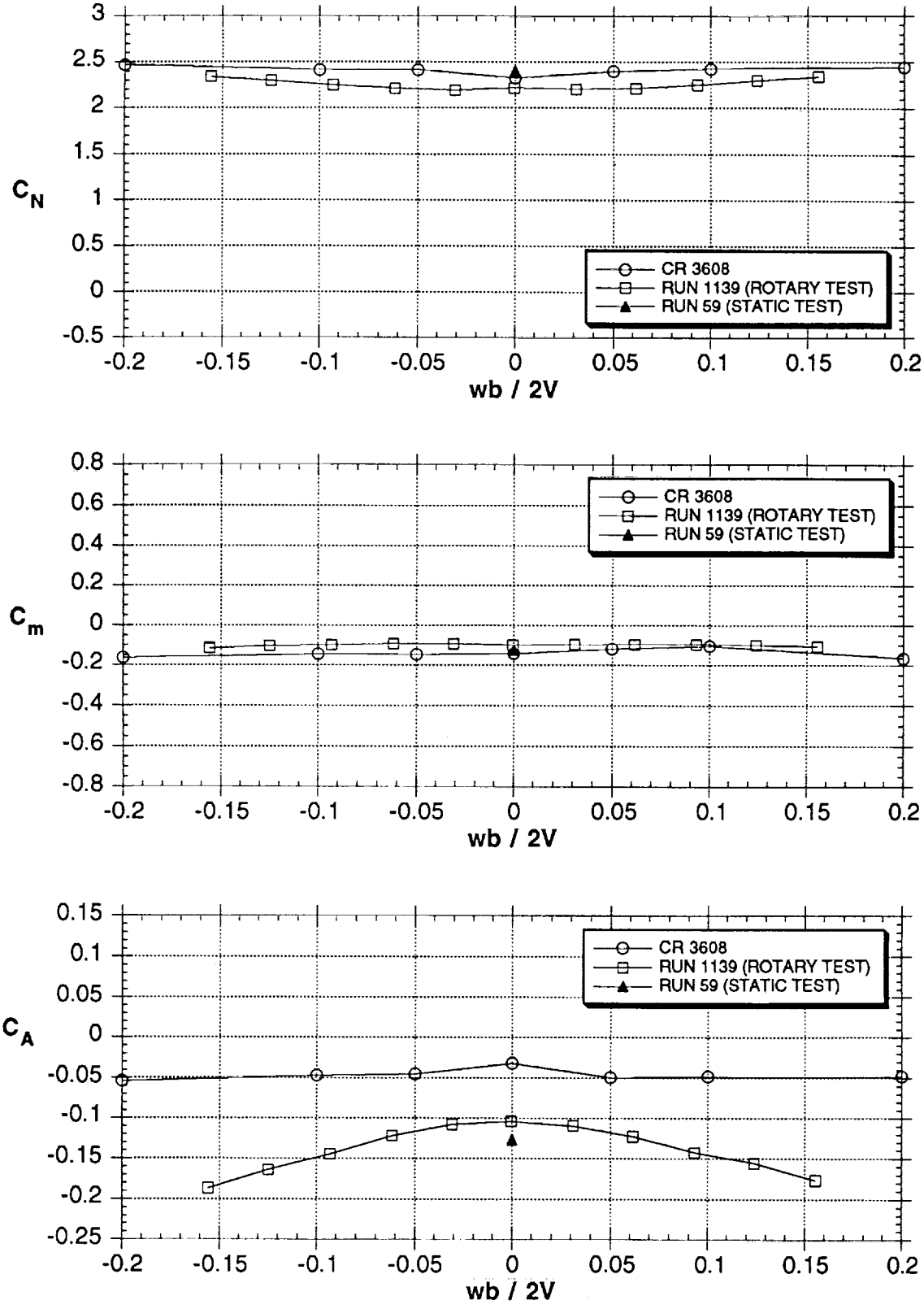

Figure 16 - Comparison of data from Eidetics static test and zero-rotation rotary-balance data from Eidetics and NASA CR 3608 (Ref. 38), α = 45°

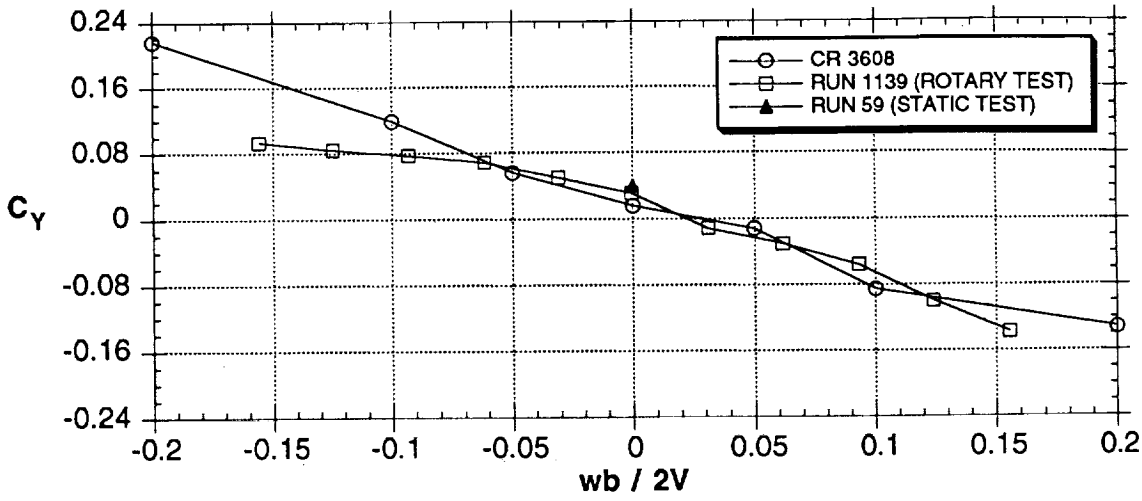

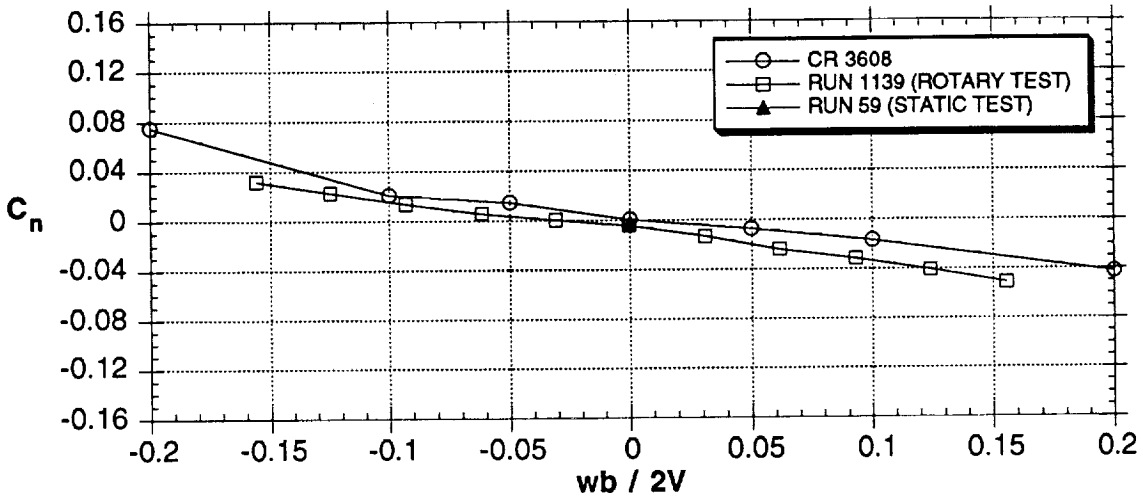

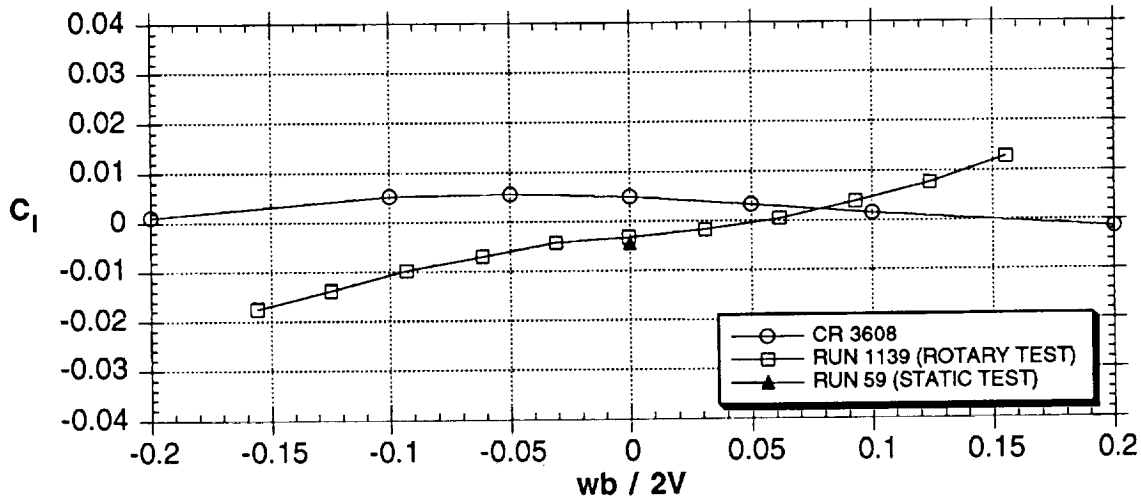

Figure 16- Concluded

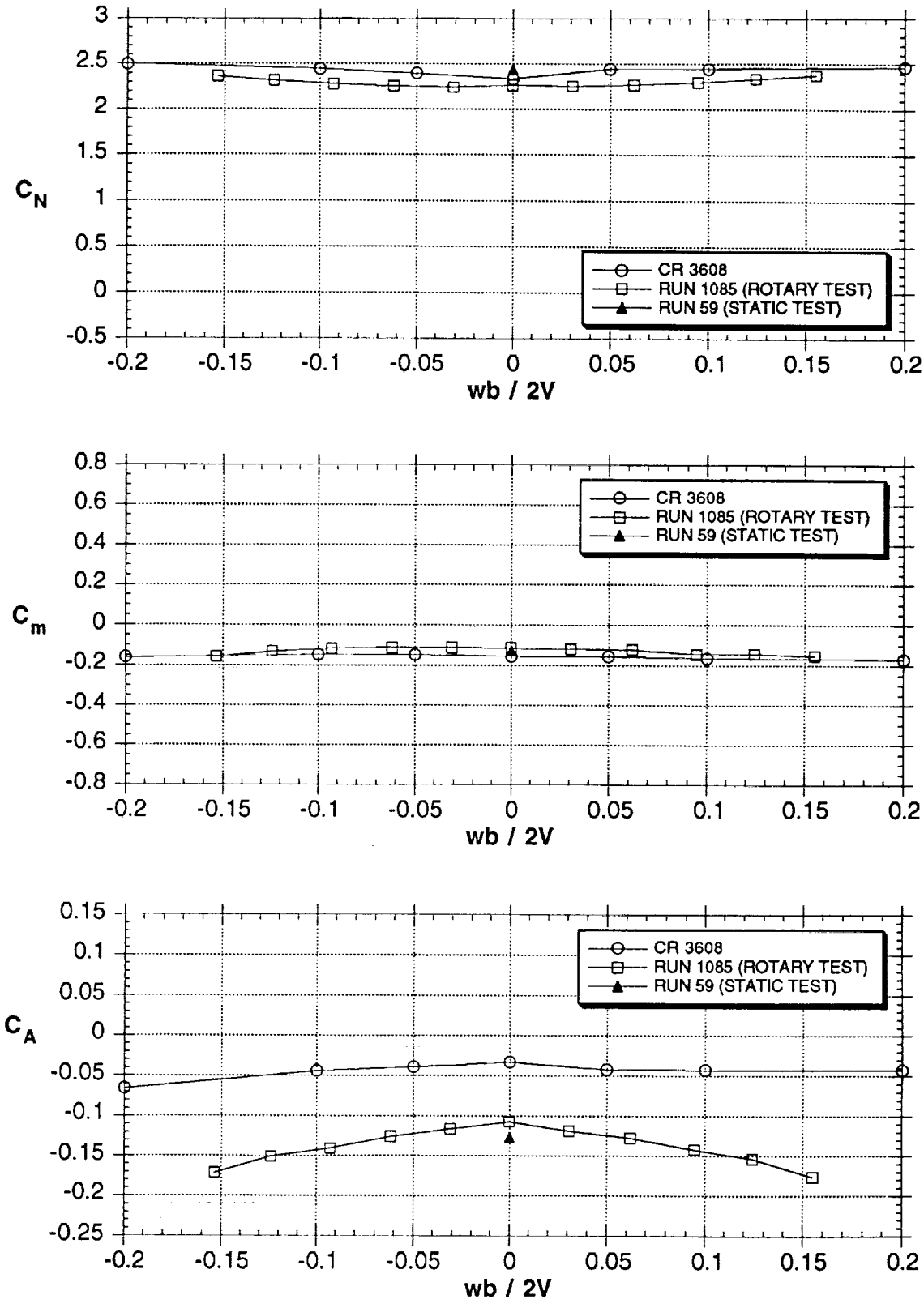

Figure 17 - Comparison of data from Eidetics static test and zero-rotation rotary-balance data from Eidetics and NASA CR 3608 (Ref. 38), α = 50(51)°

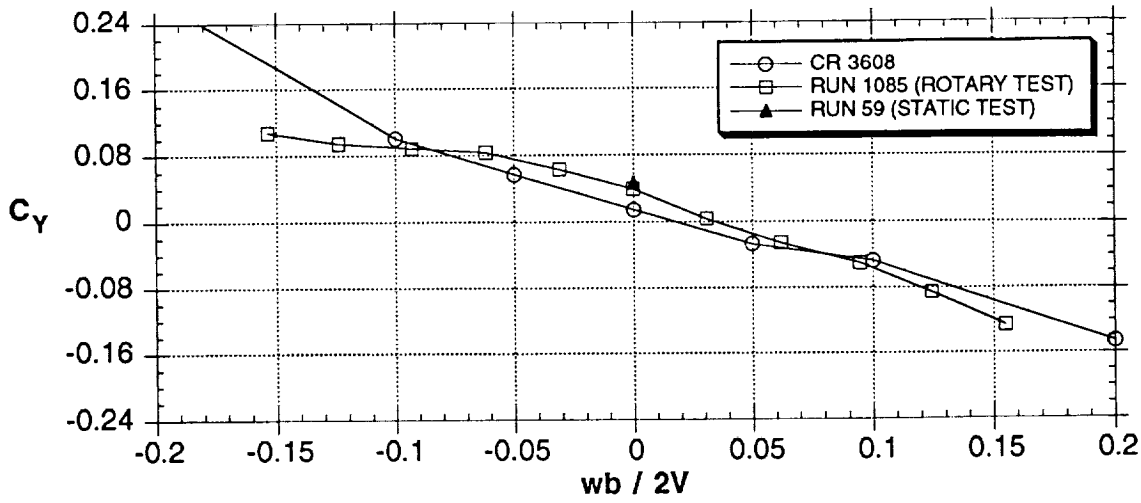

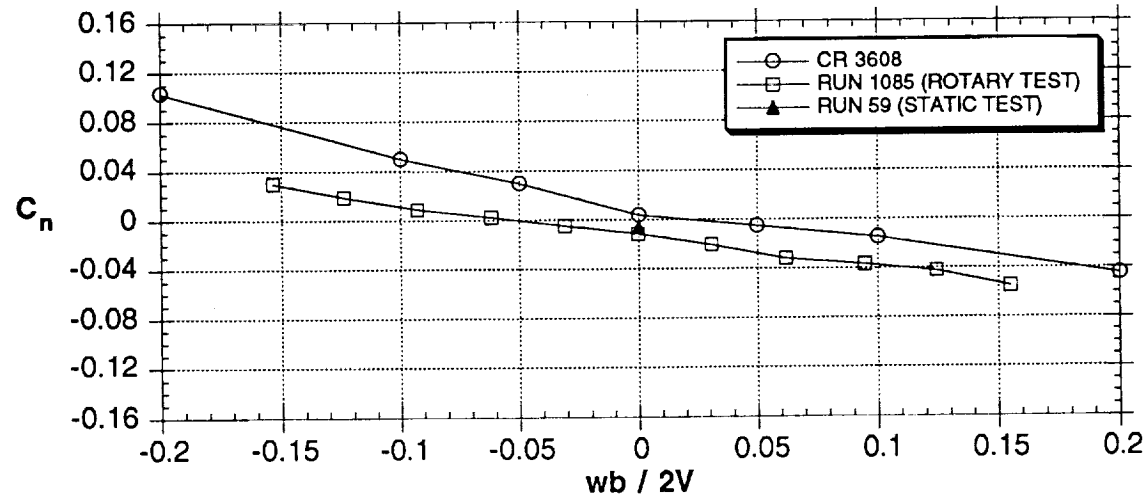

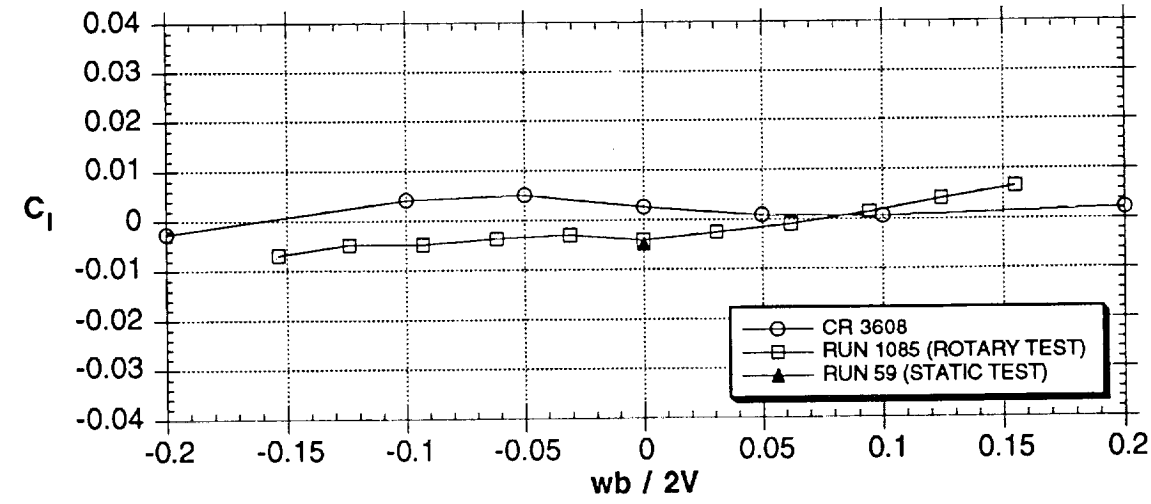

Figure 17 - Concluded

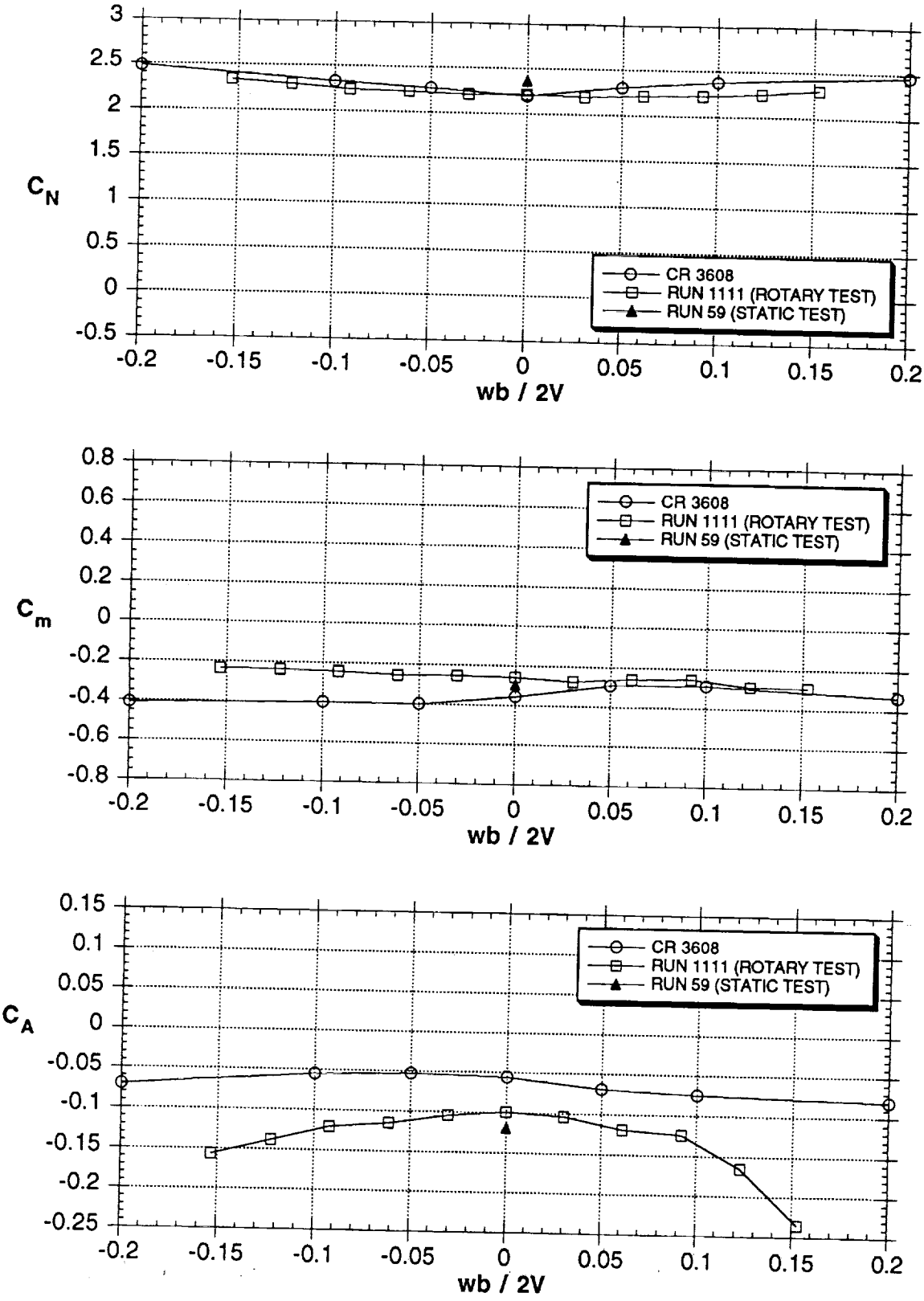

Figure 18 - Comparison of data from Eidetics static test and zero-rotation rotary-balance data from Eidetics and NASA CR 3608 (Ref. 38), $\alpha = 60°$

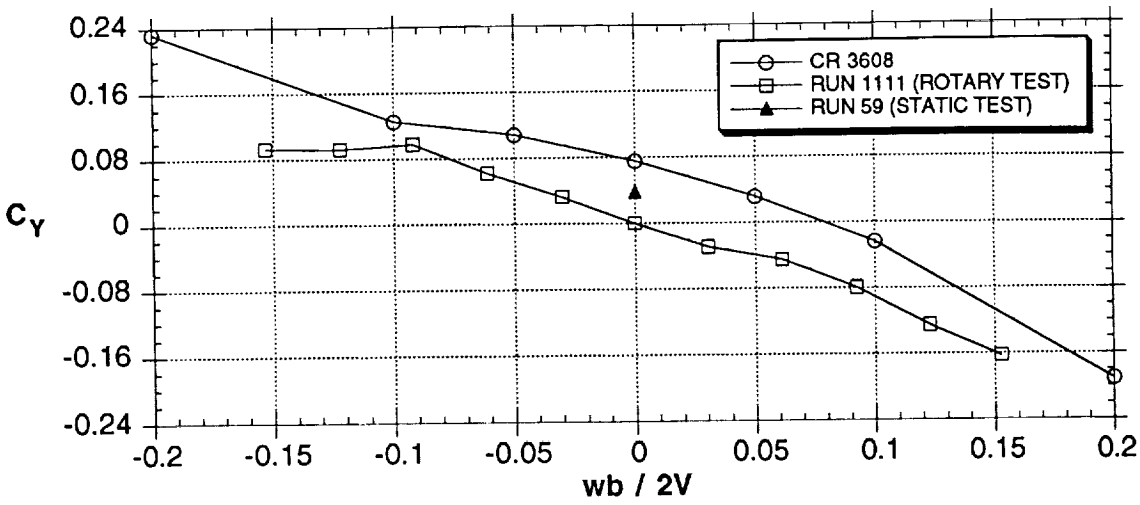

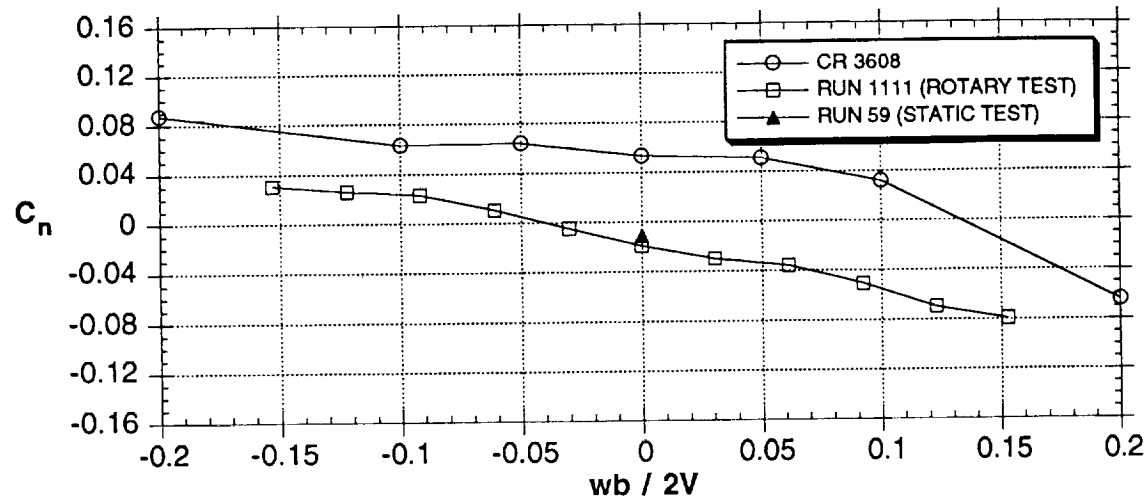

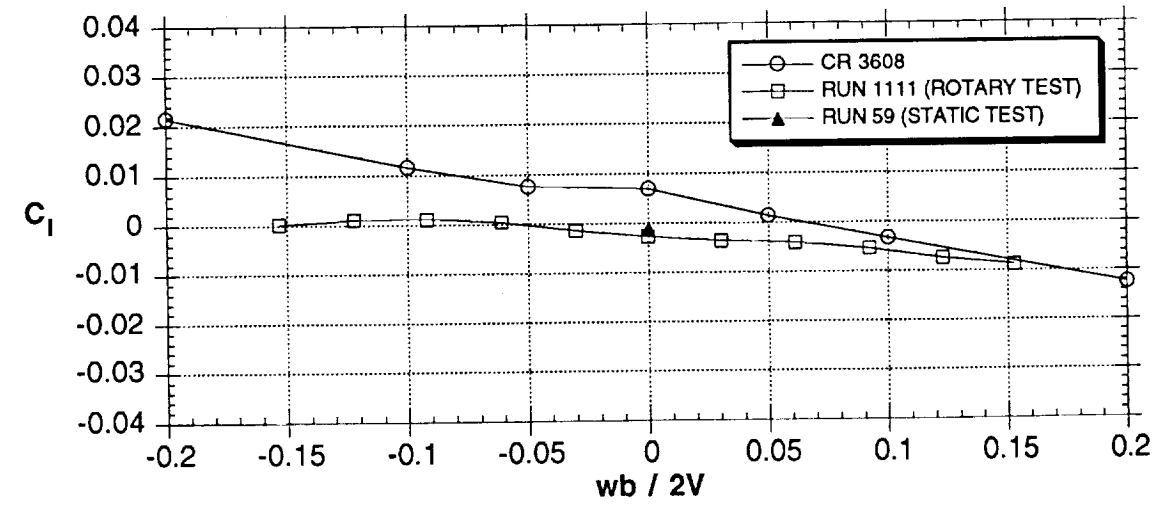

Figure 18 - Concluded

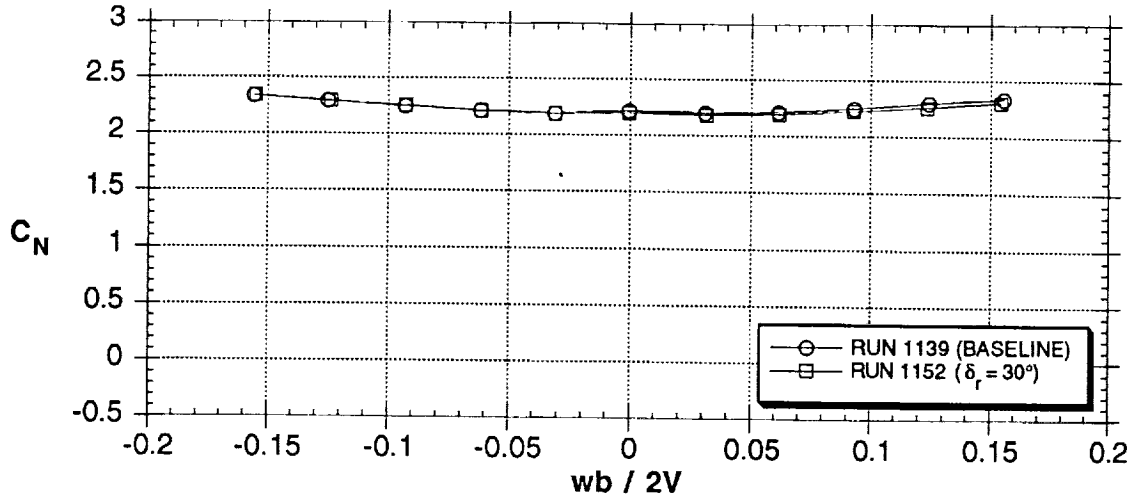

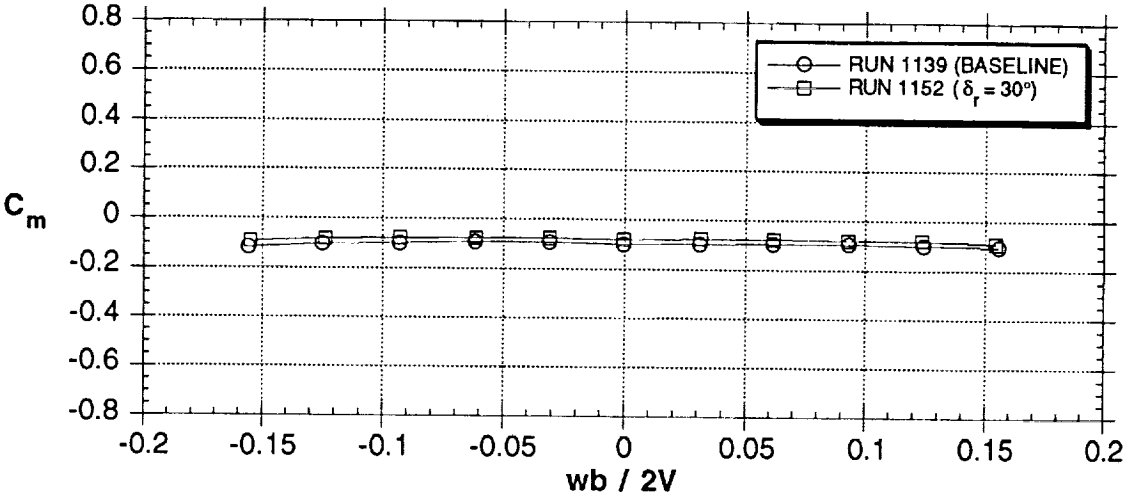

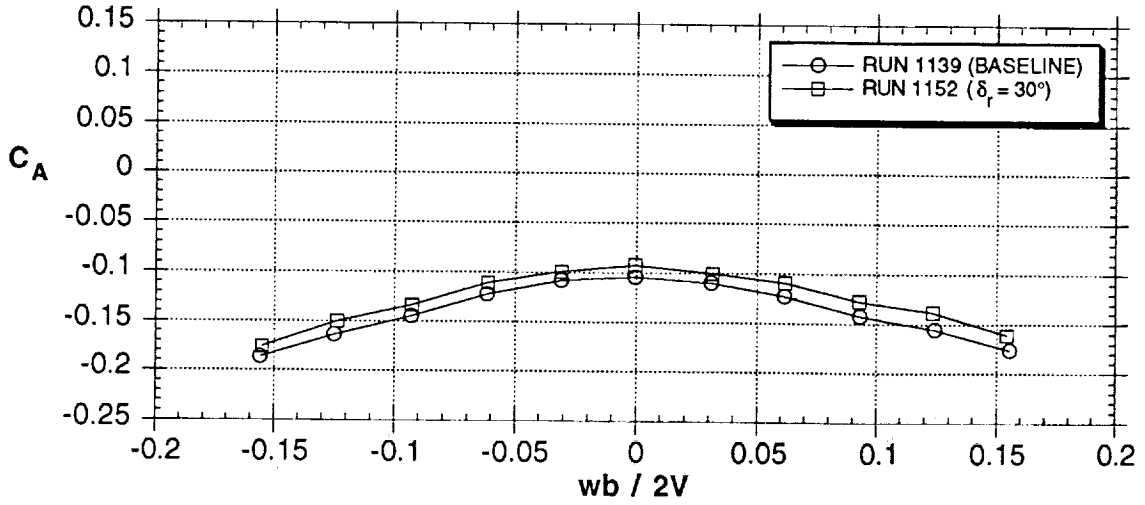

Figure 19 - Effect of 30° rudder deflection, α = 45°

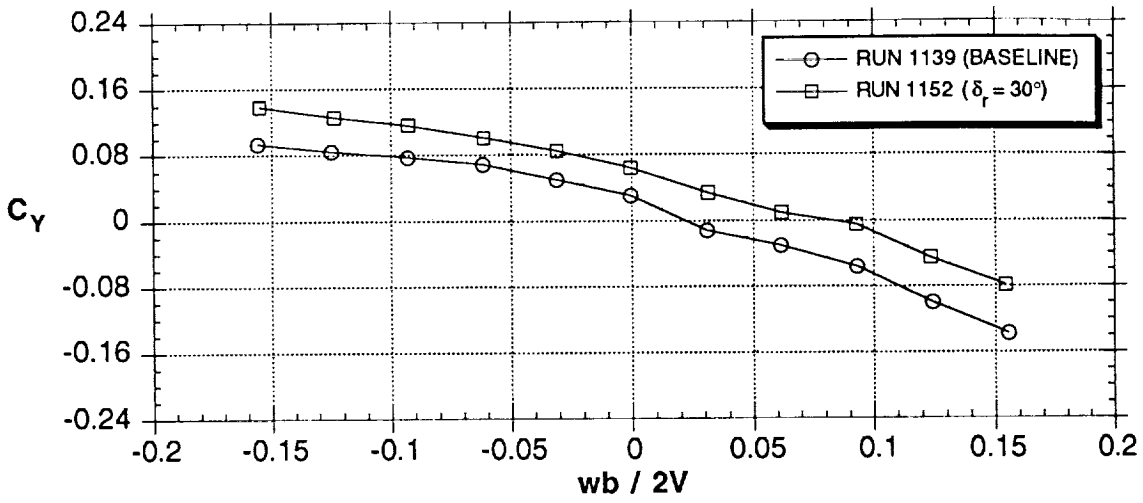

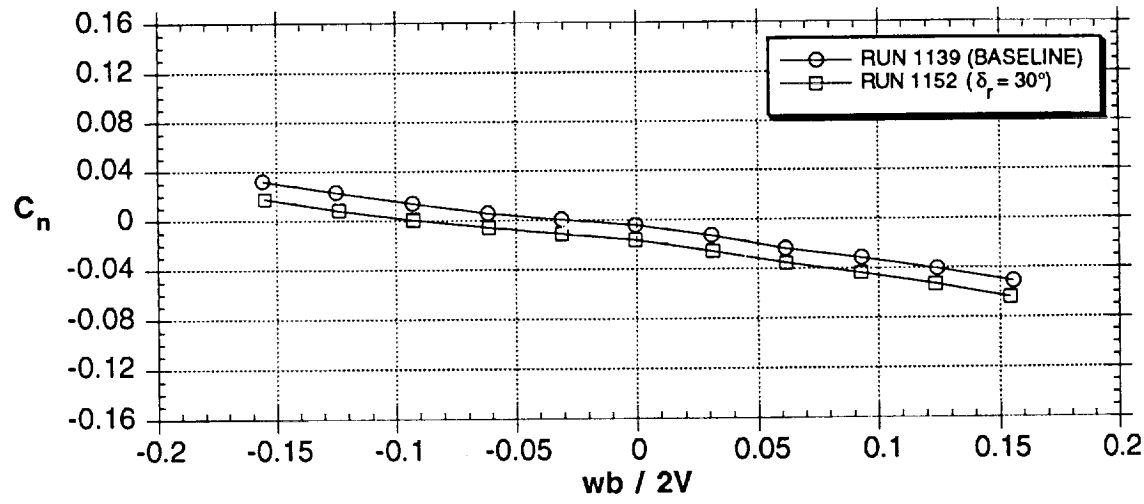

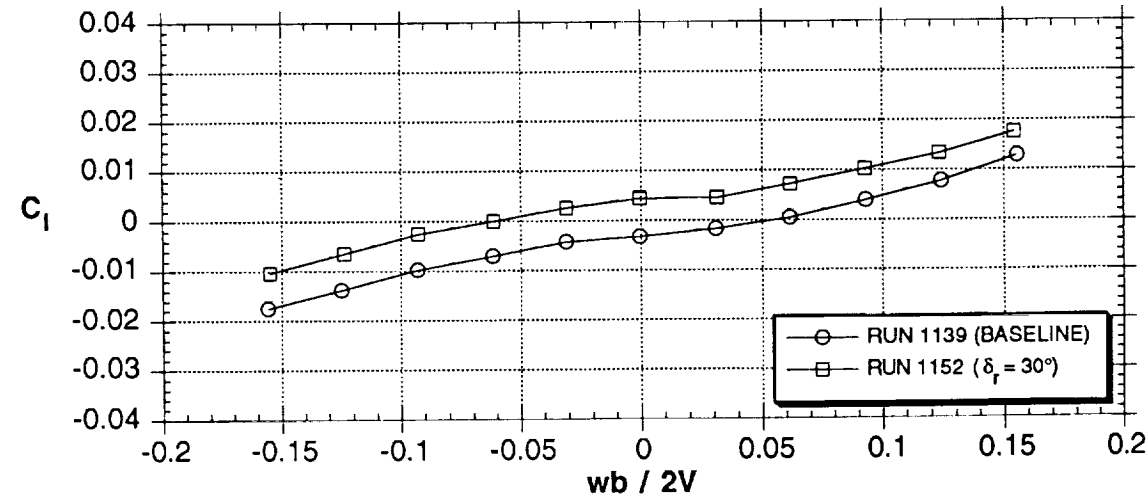

Figure 19 - Concluded

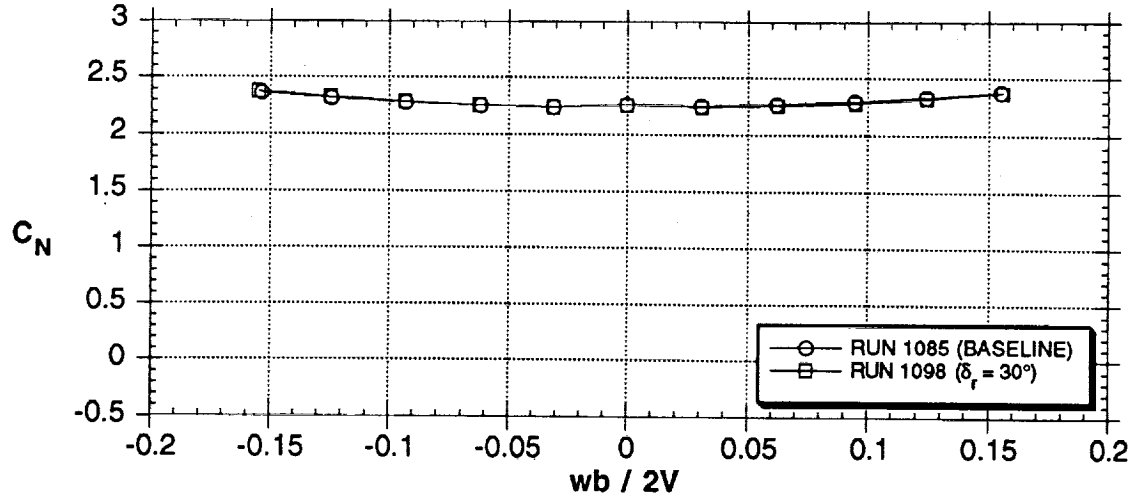

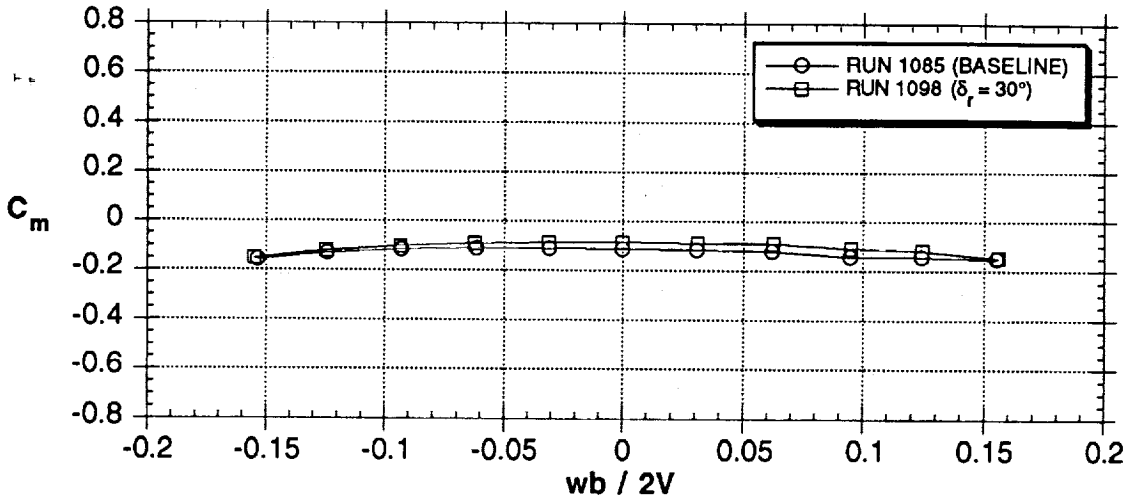

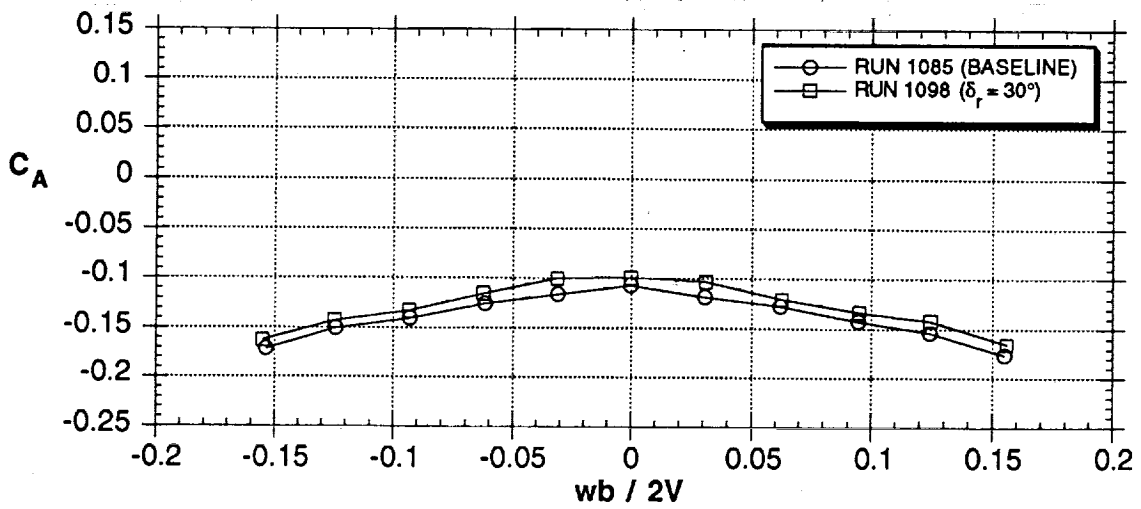

Figure 20 - Effect of 30° rudder deflection, α = 51°

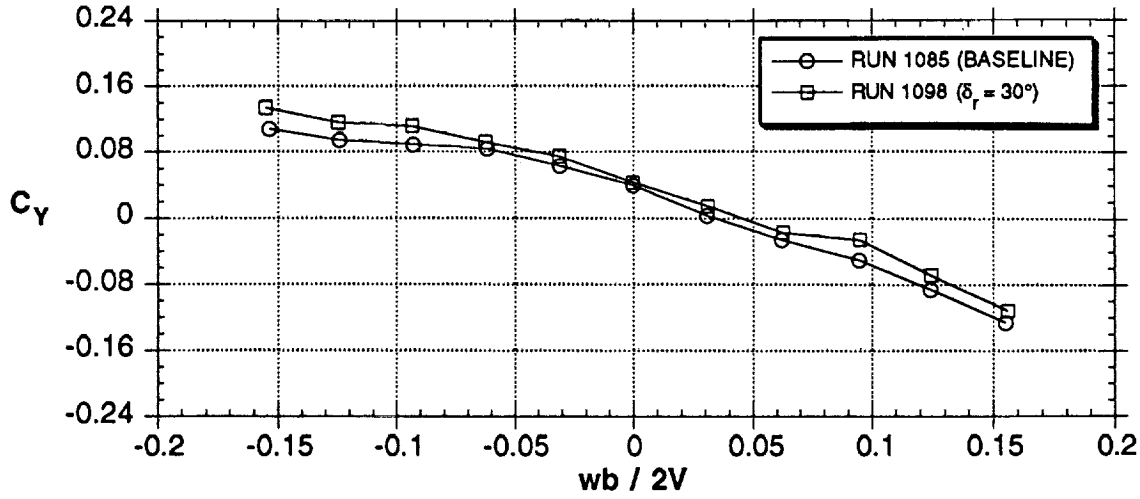

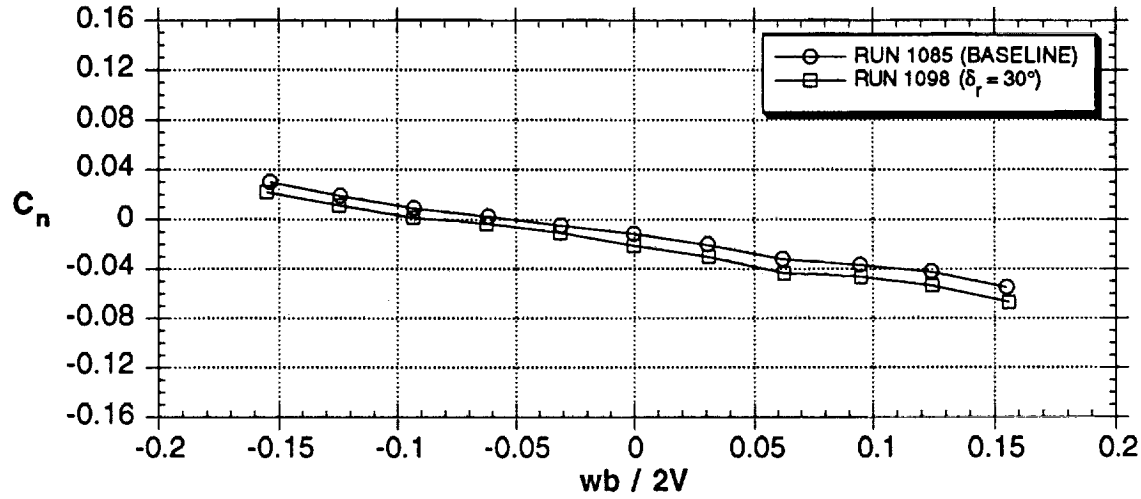

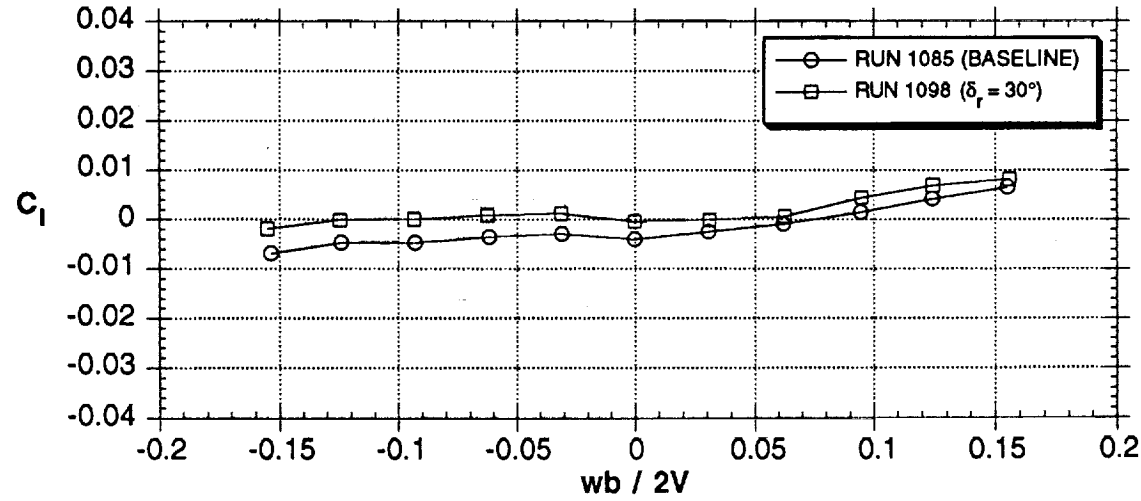

Figure 20 - Concluded

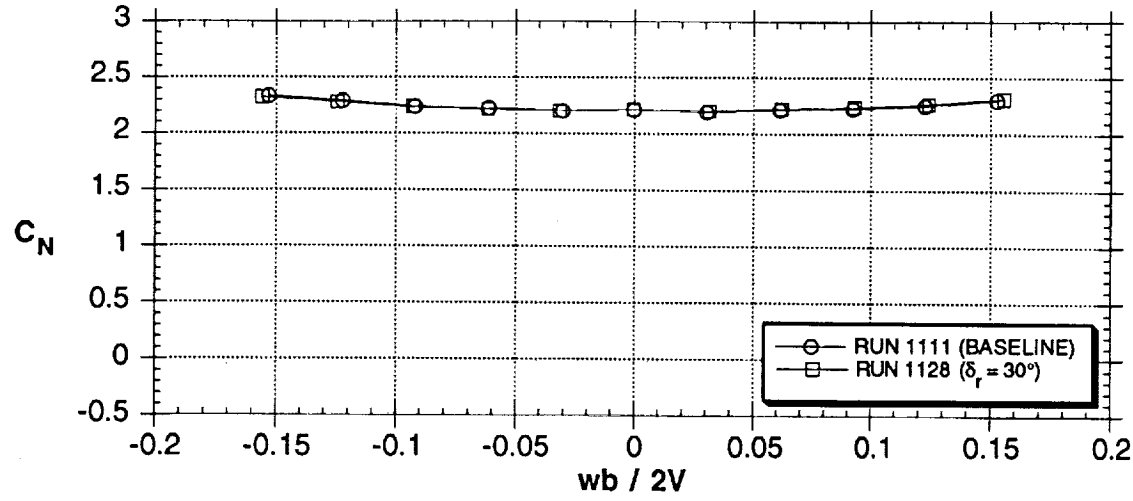

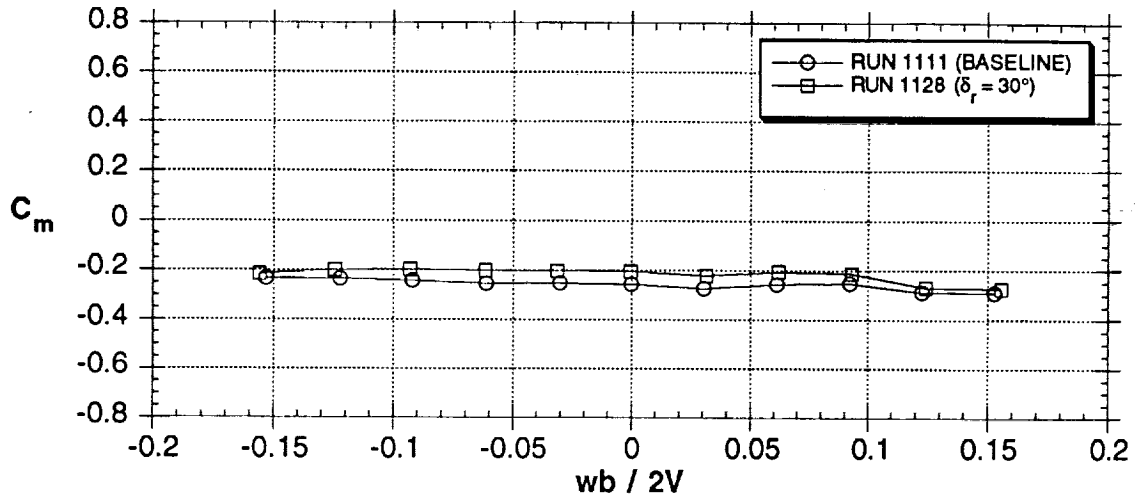

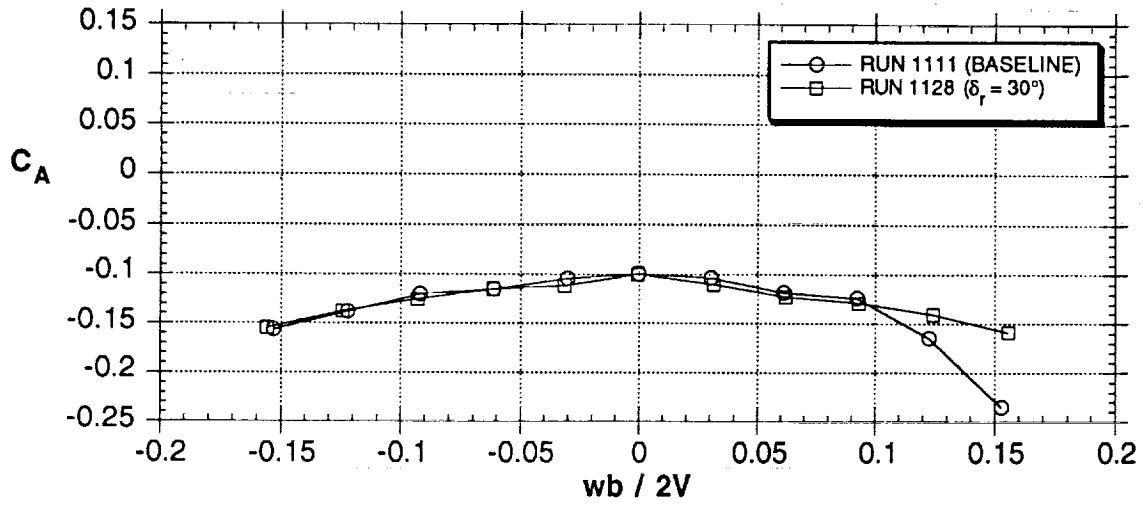

Figure 21 - Effect of 30° rudder deflection, α = 60°

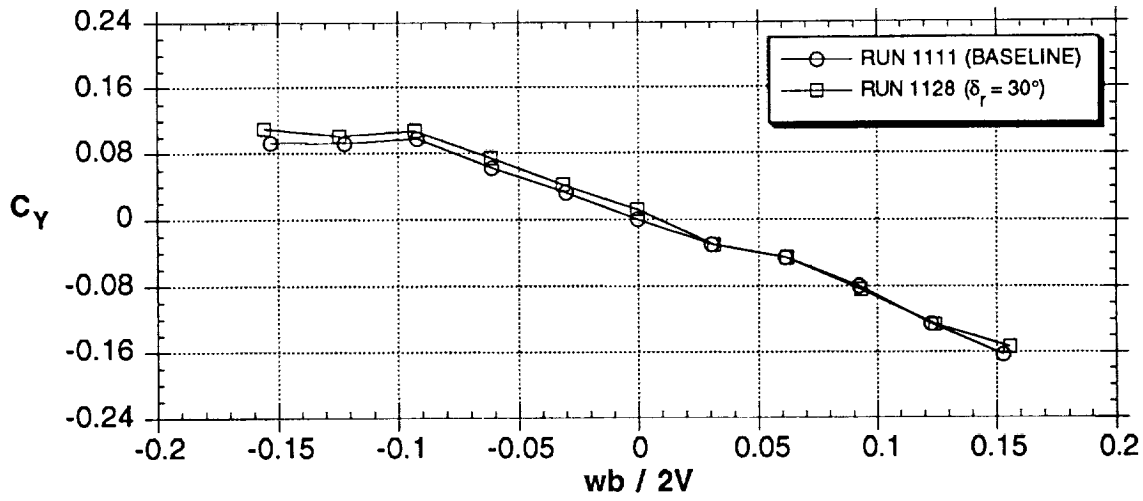

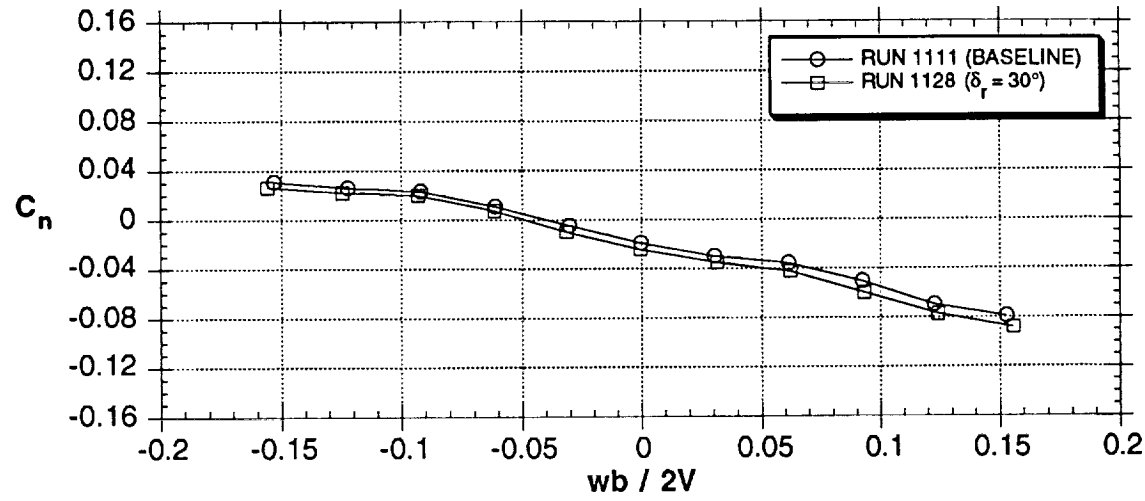

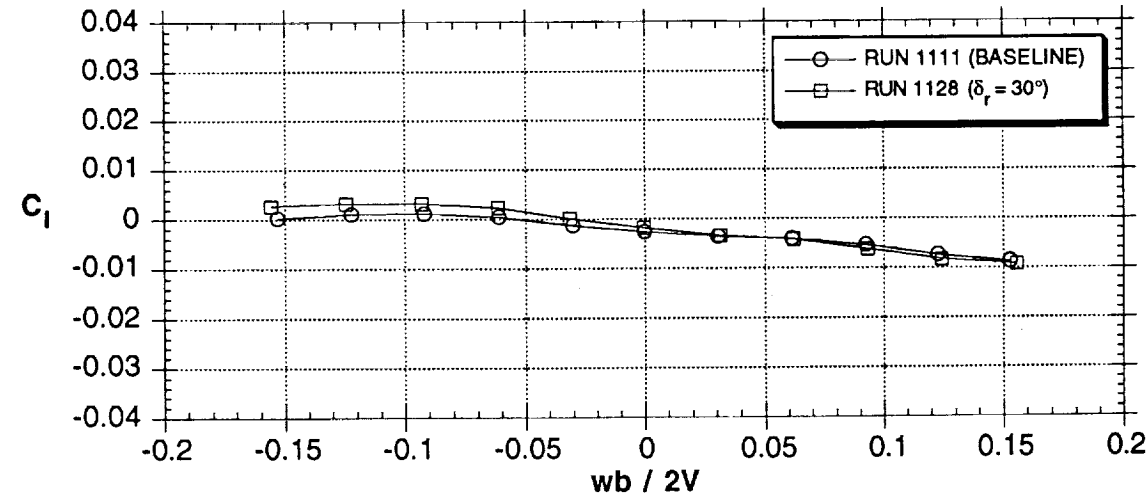

Figure 21 - Concluded

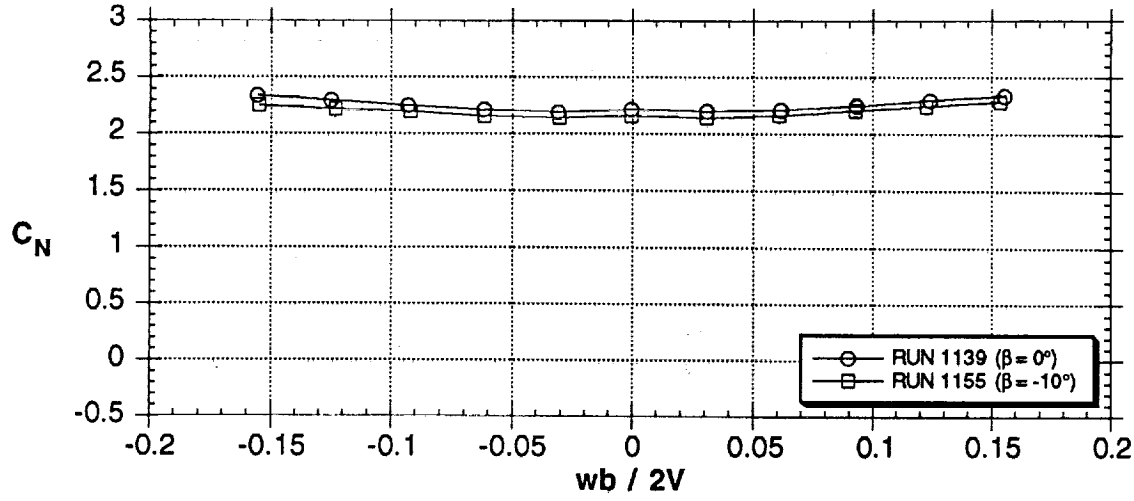

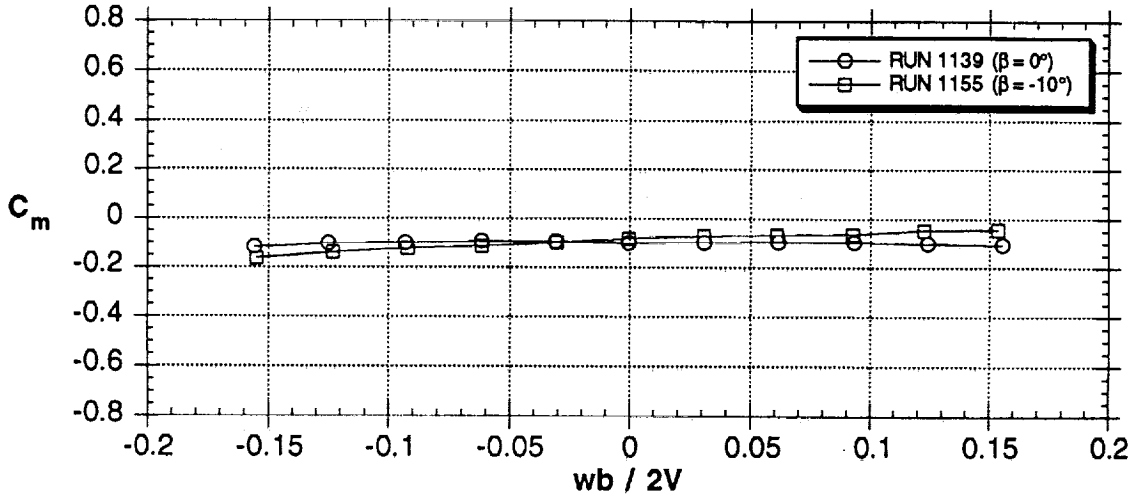

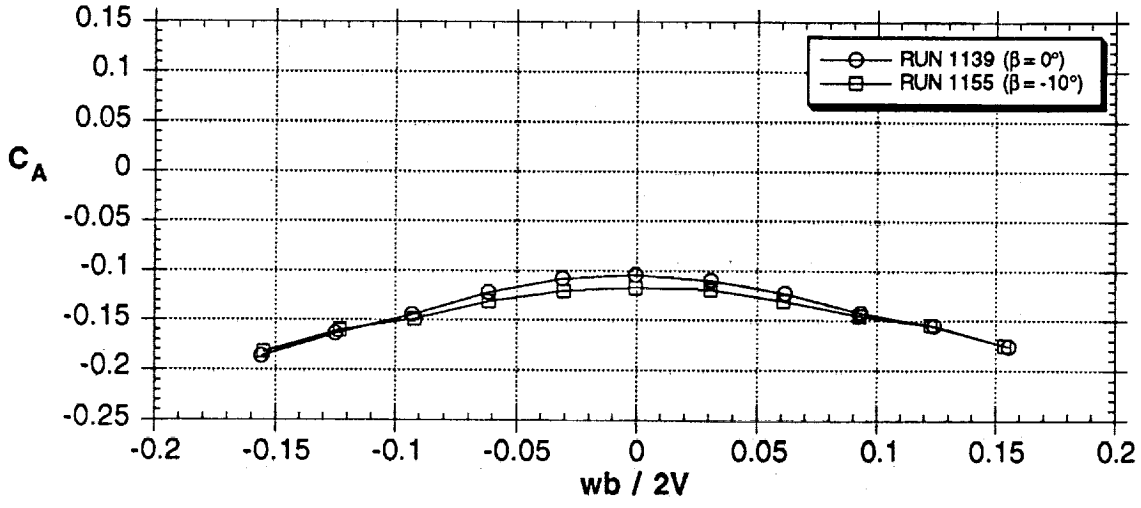

Figure 22 - Effect of sideslip angle of β = -10°, α = 45°

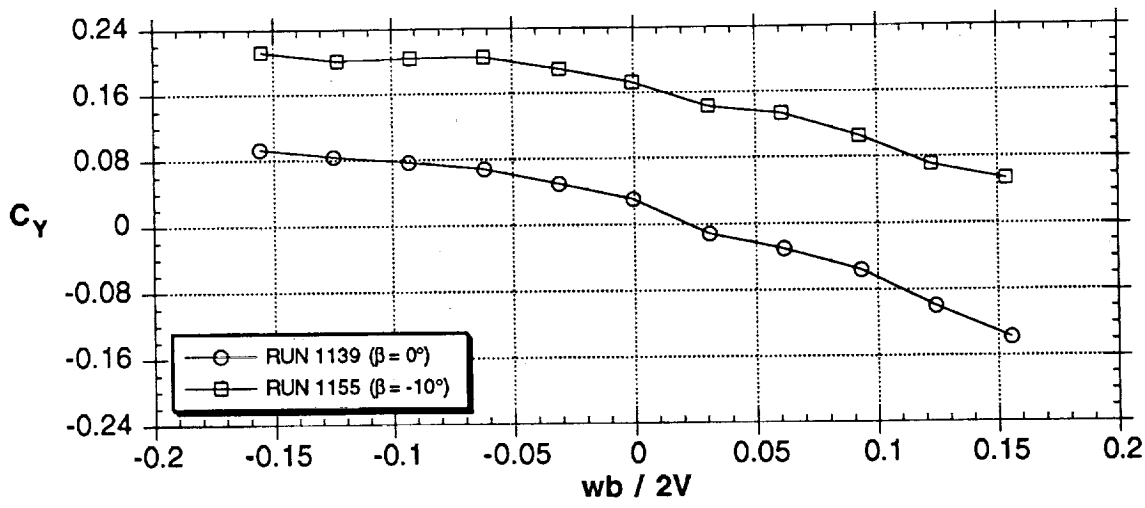

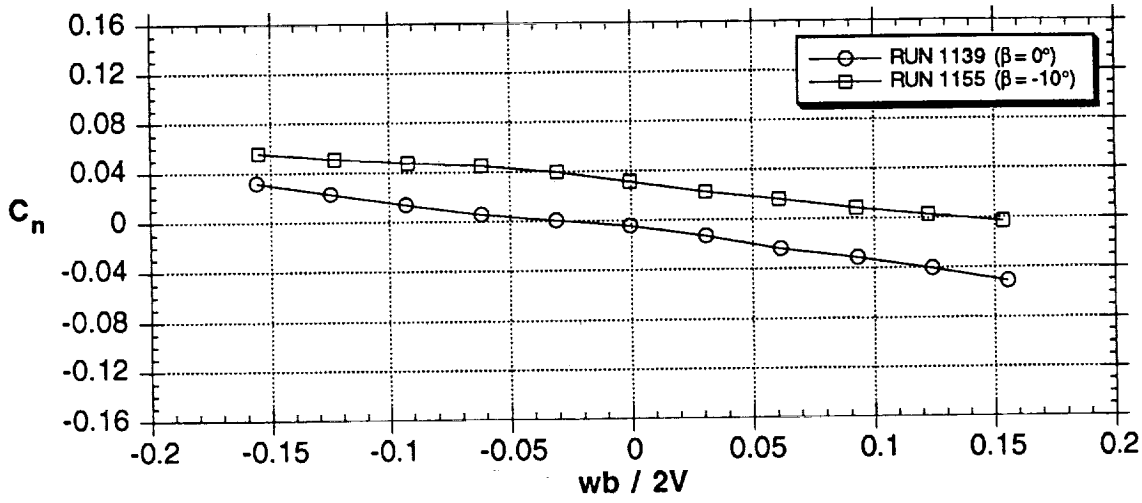

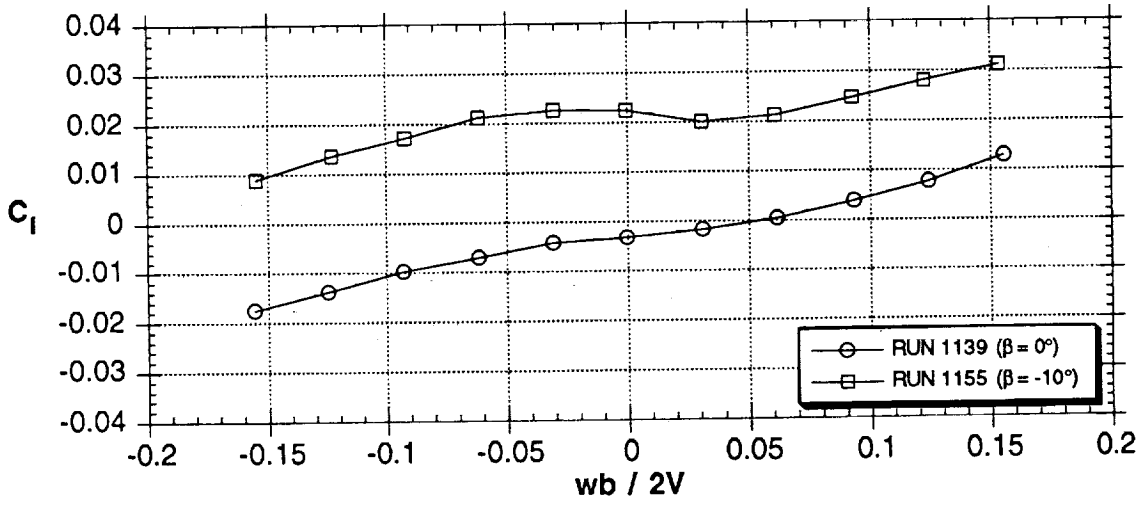

Figure 22 - Concluded

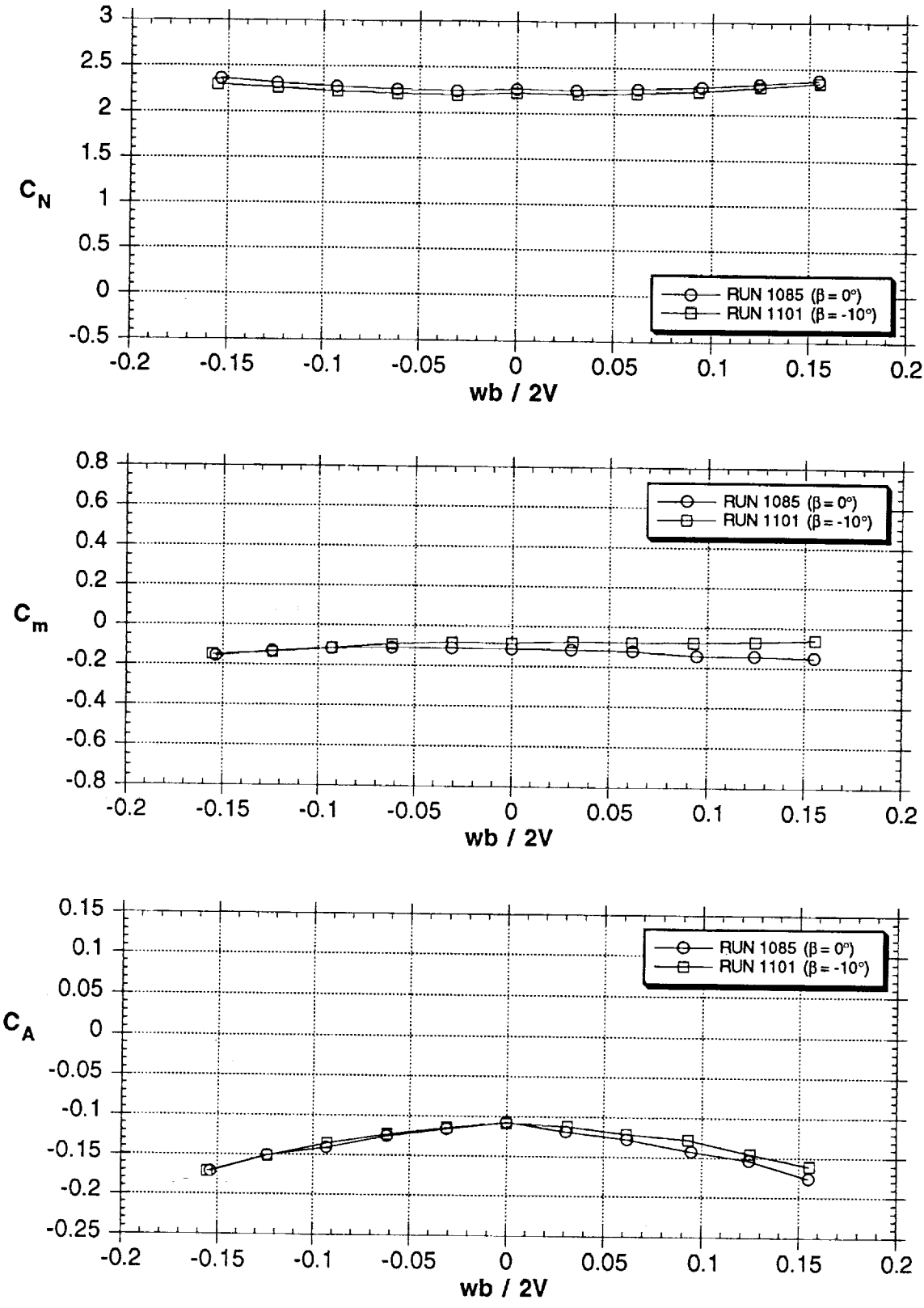

Figure 23 - Effect of sideslip angle of β = -10°, α = 51°

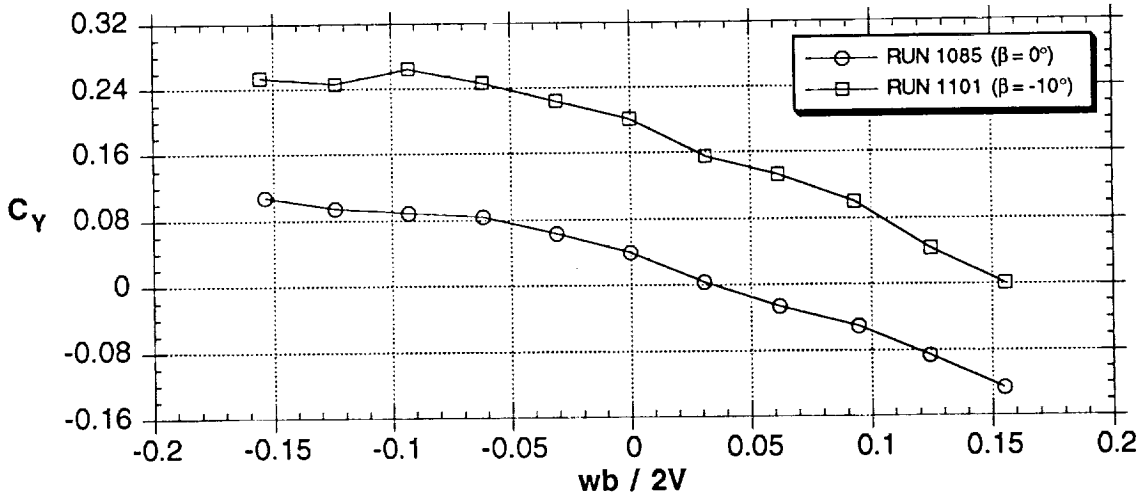

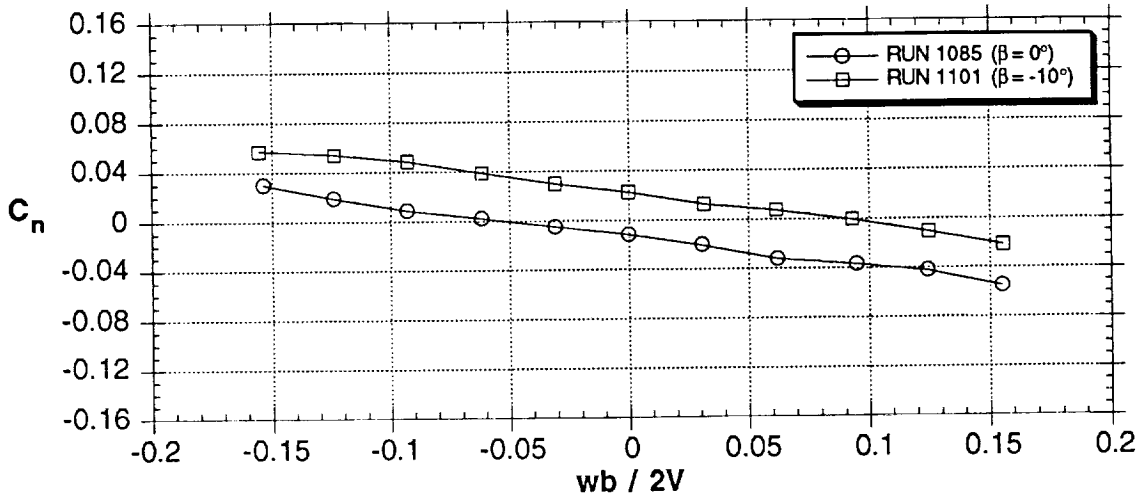

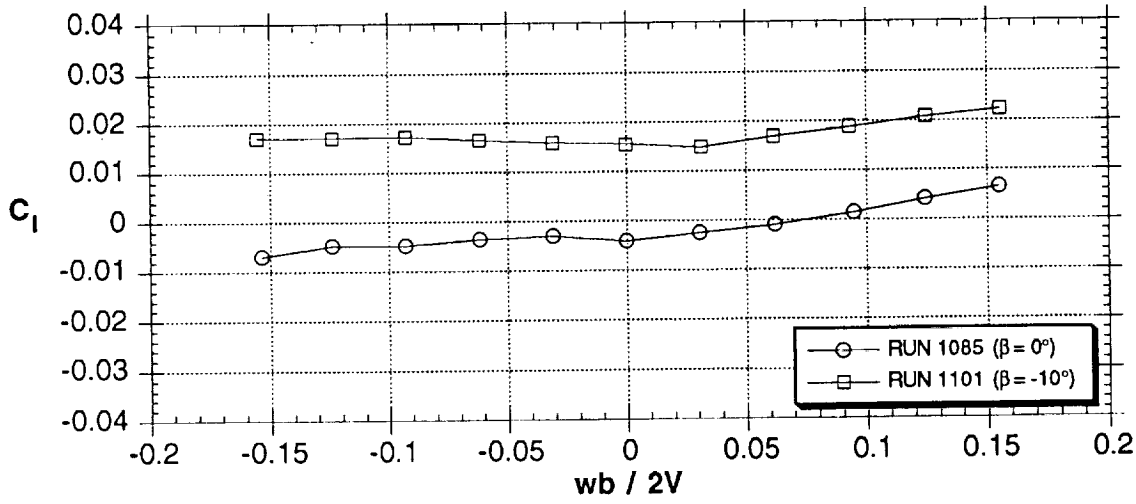

Figure 23 - Concluded

C-2.

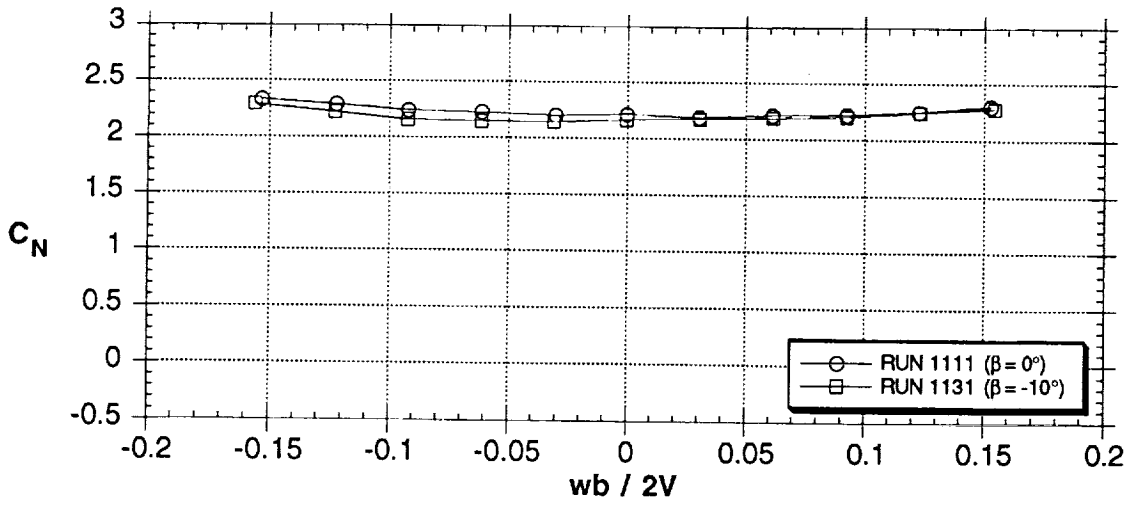

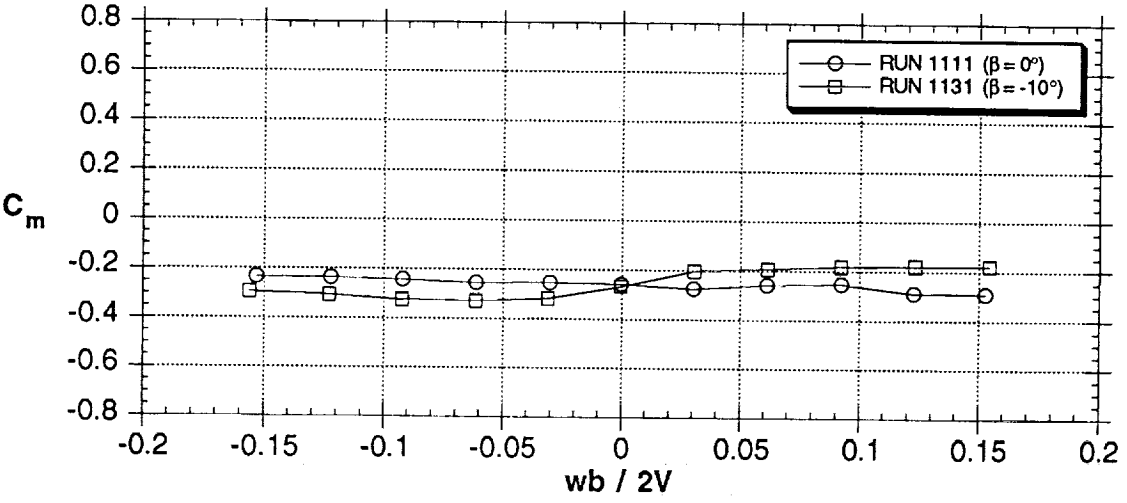

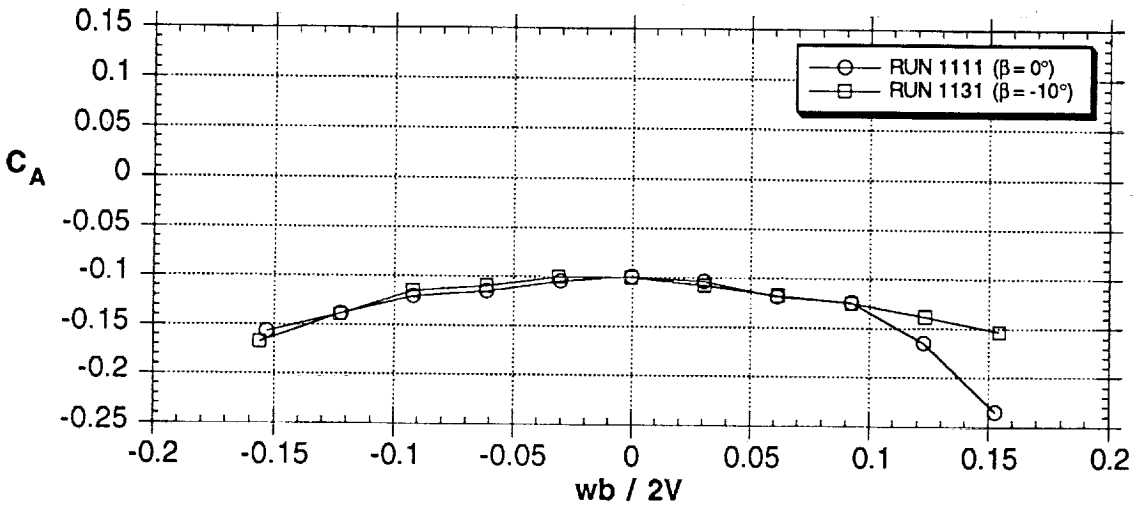

Figure 24 - Effect of sideslip angle of β = -10°, α = 60°

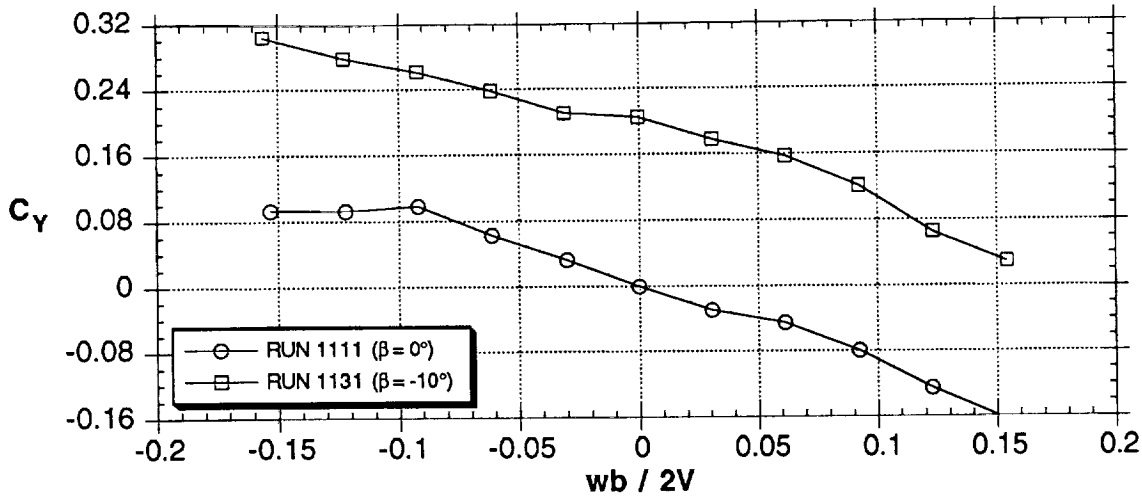

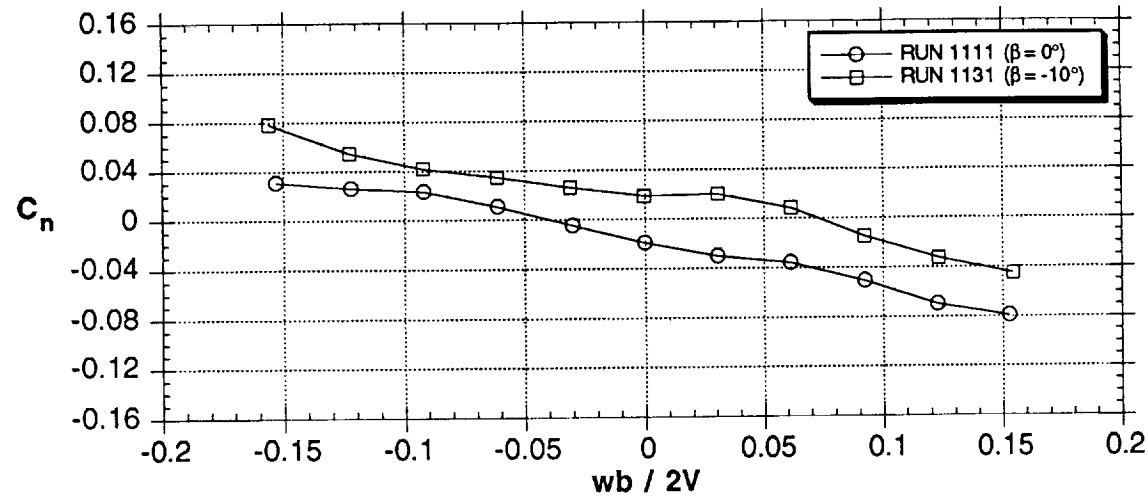

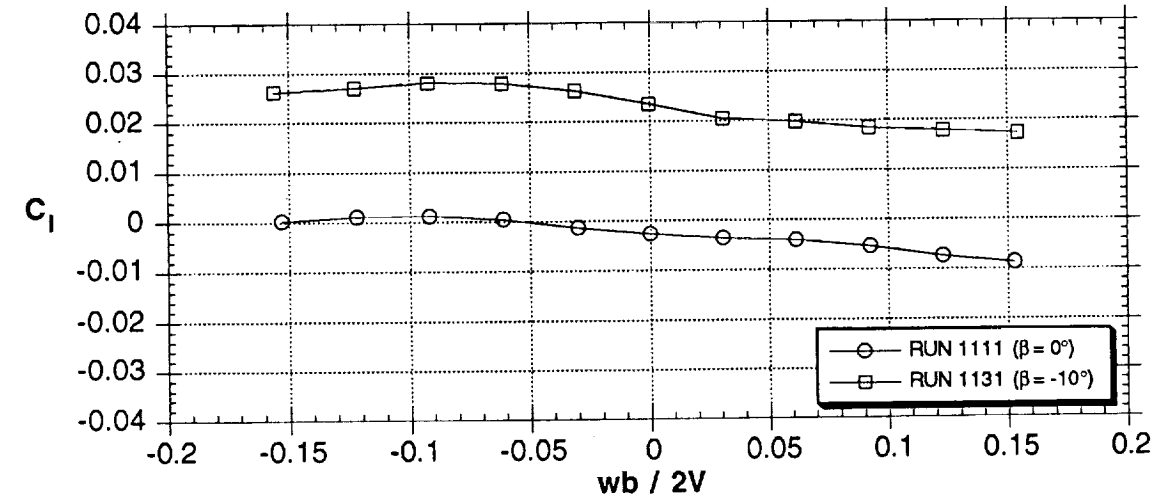

Figure 24 - Concluded

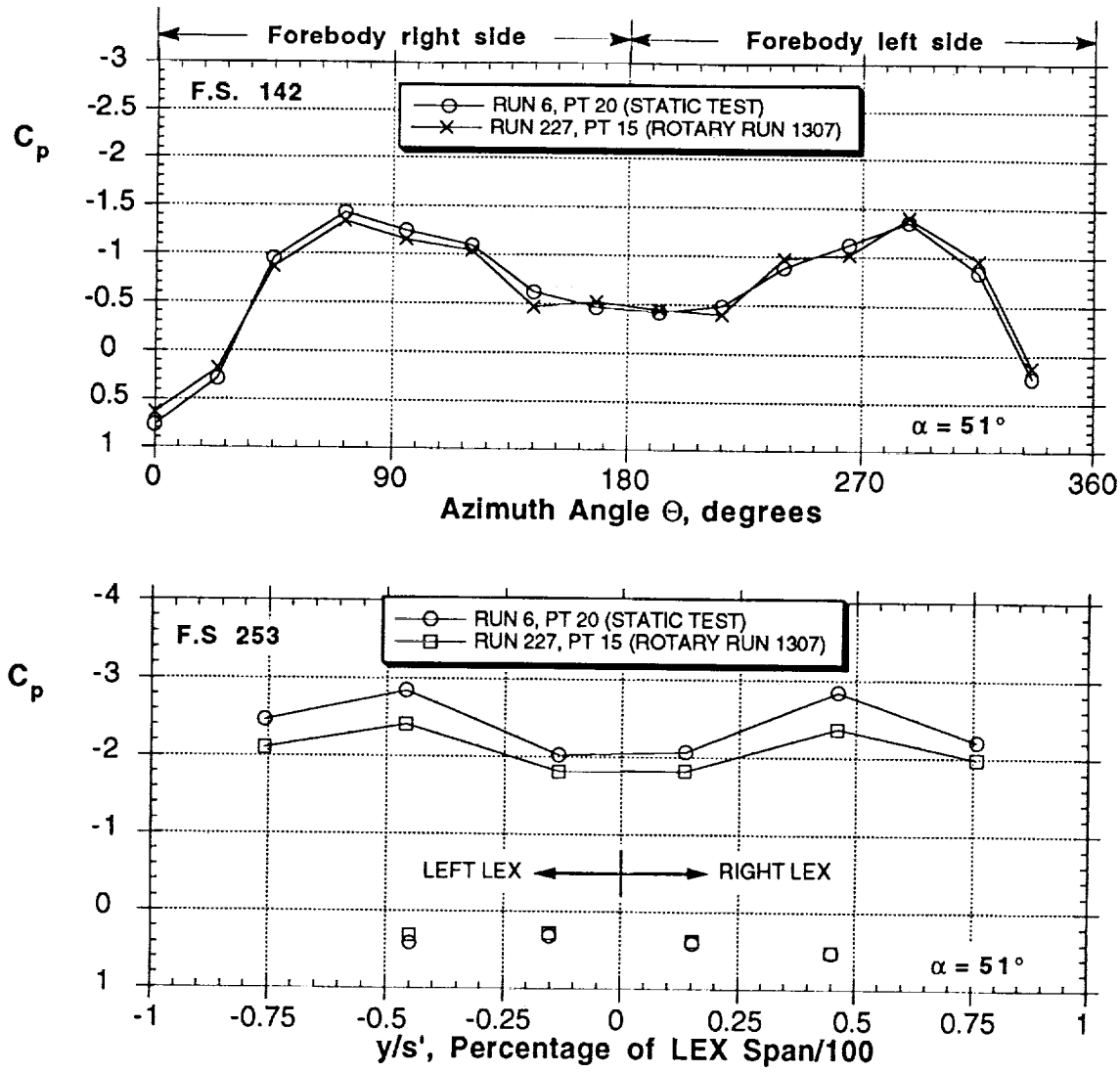

(a) Comparison to static test

Figure 25 - Baseline pressure distribution on the forebody and LEX at 51° AOA

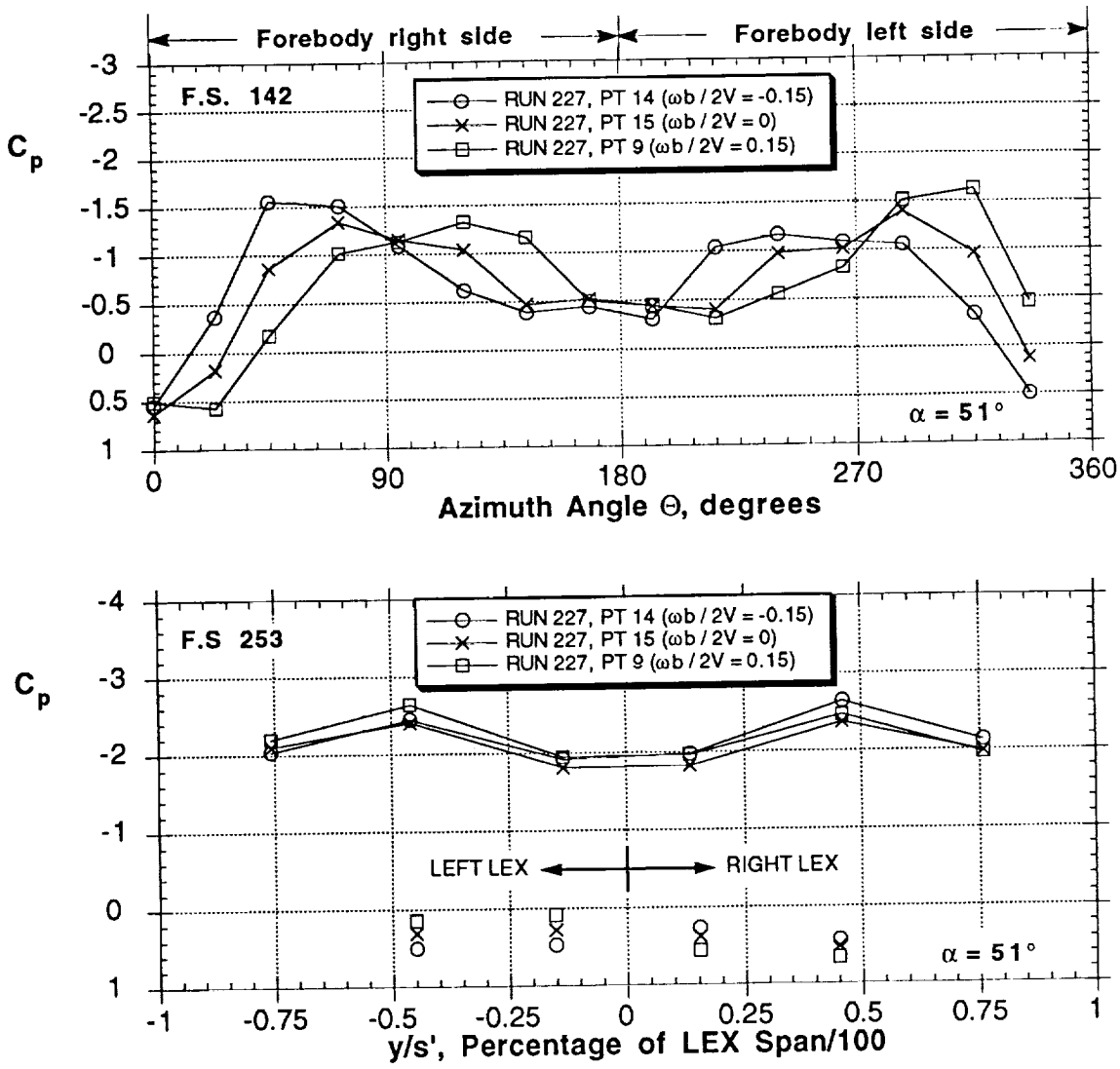

(b) Effect of rotary flow field

Figure 25 - Concluded

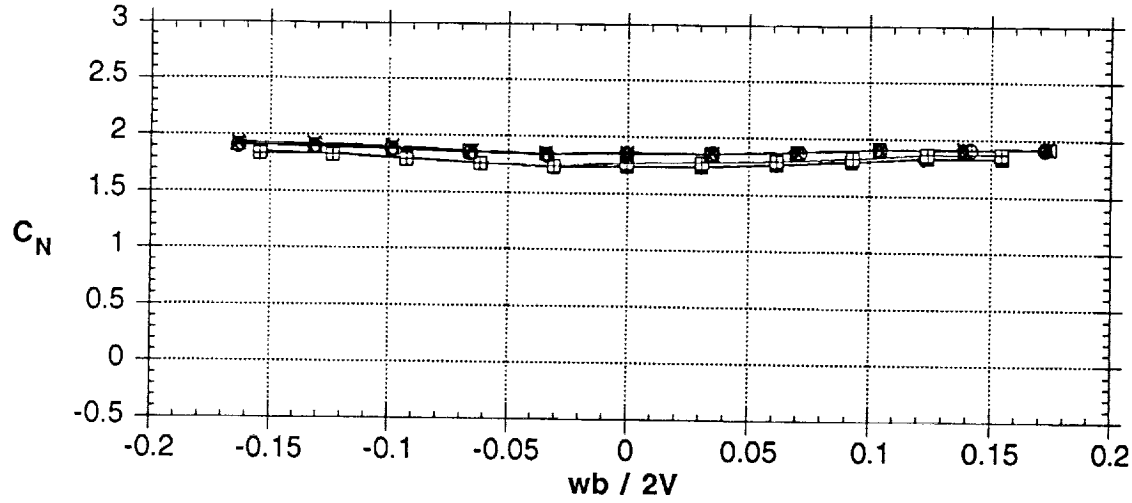

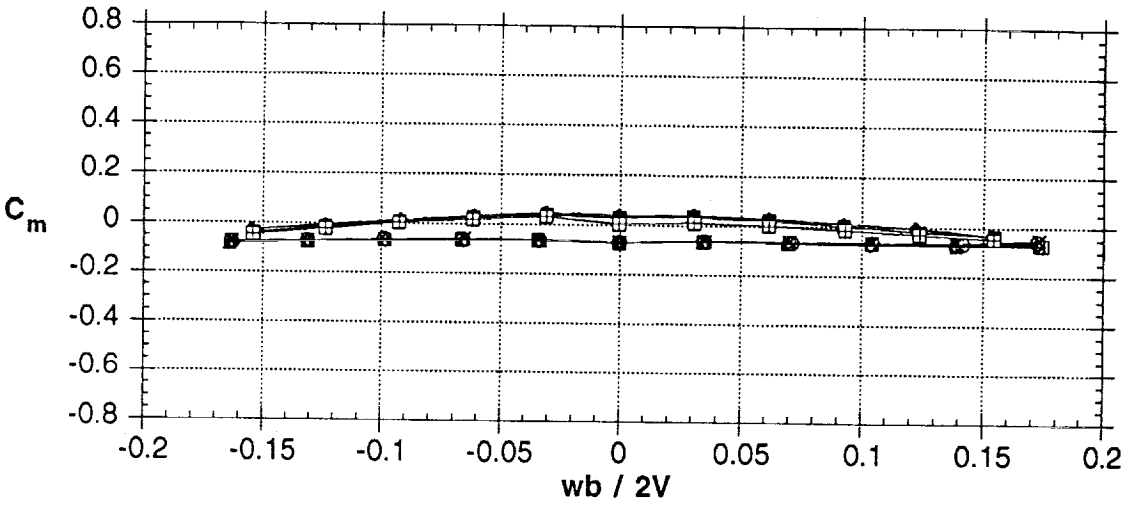

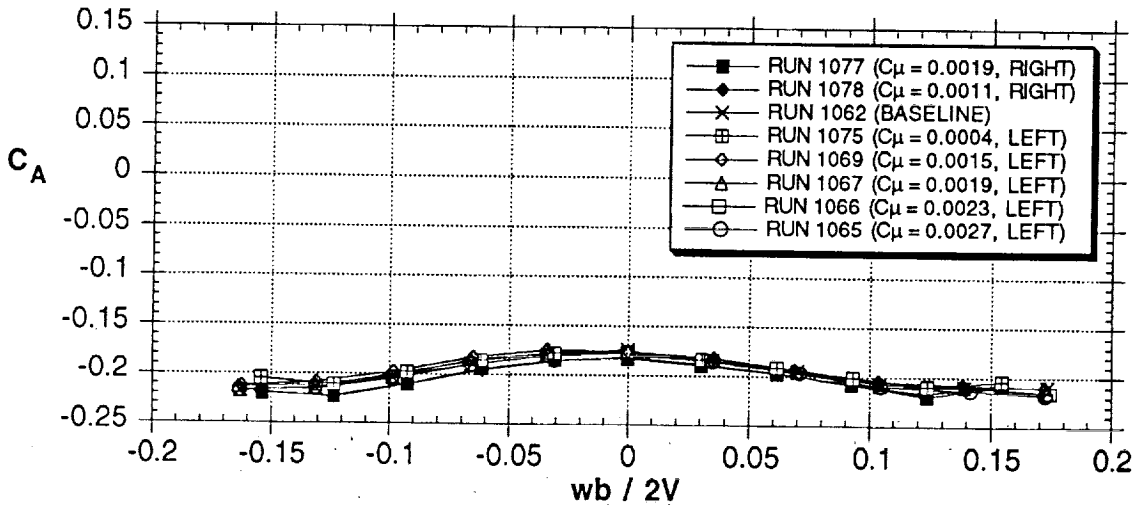

Figure 26 - Effects of NOSE 4 - 60° INBOARD blowing jet at 30° AOA

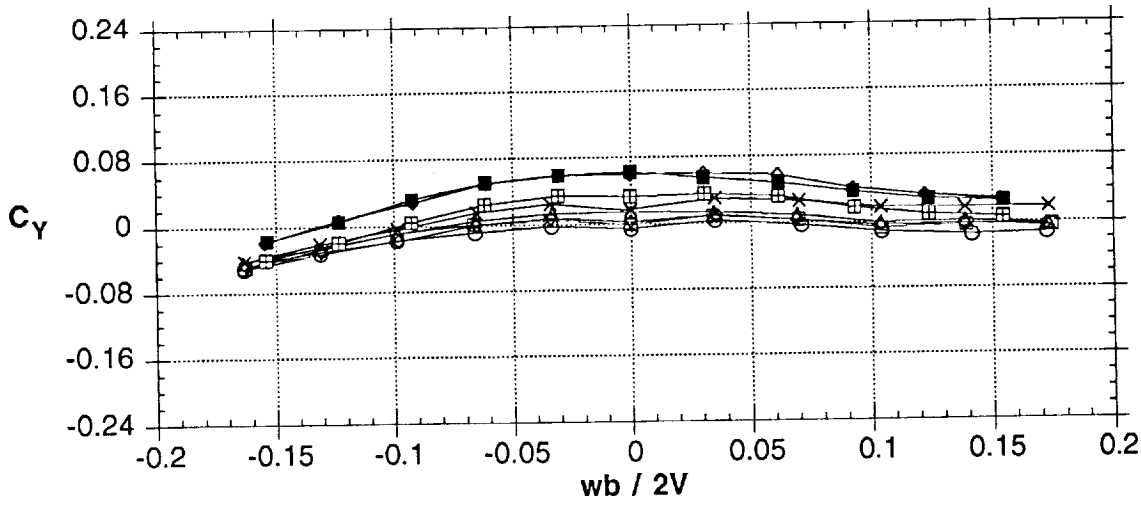

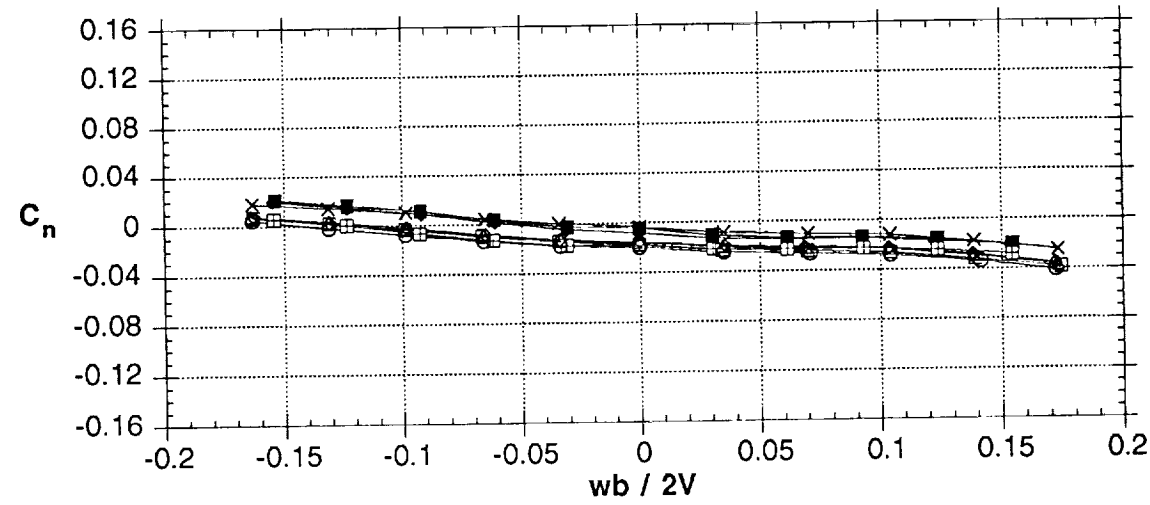

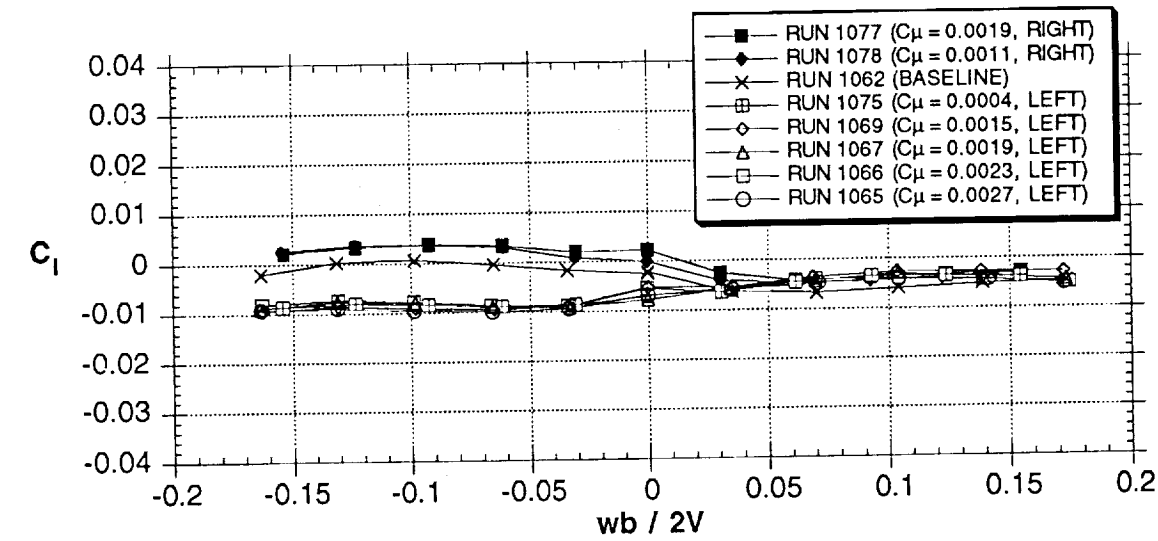

Figure 26 - Concluded

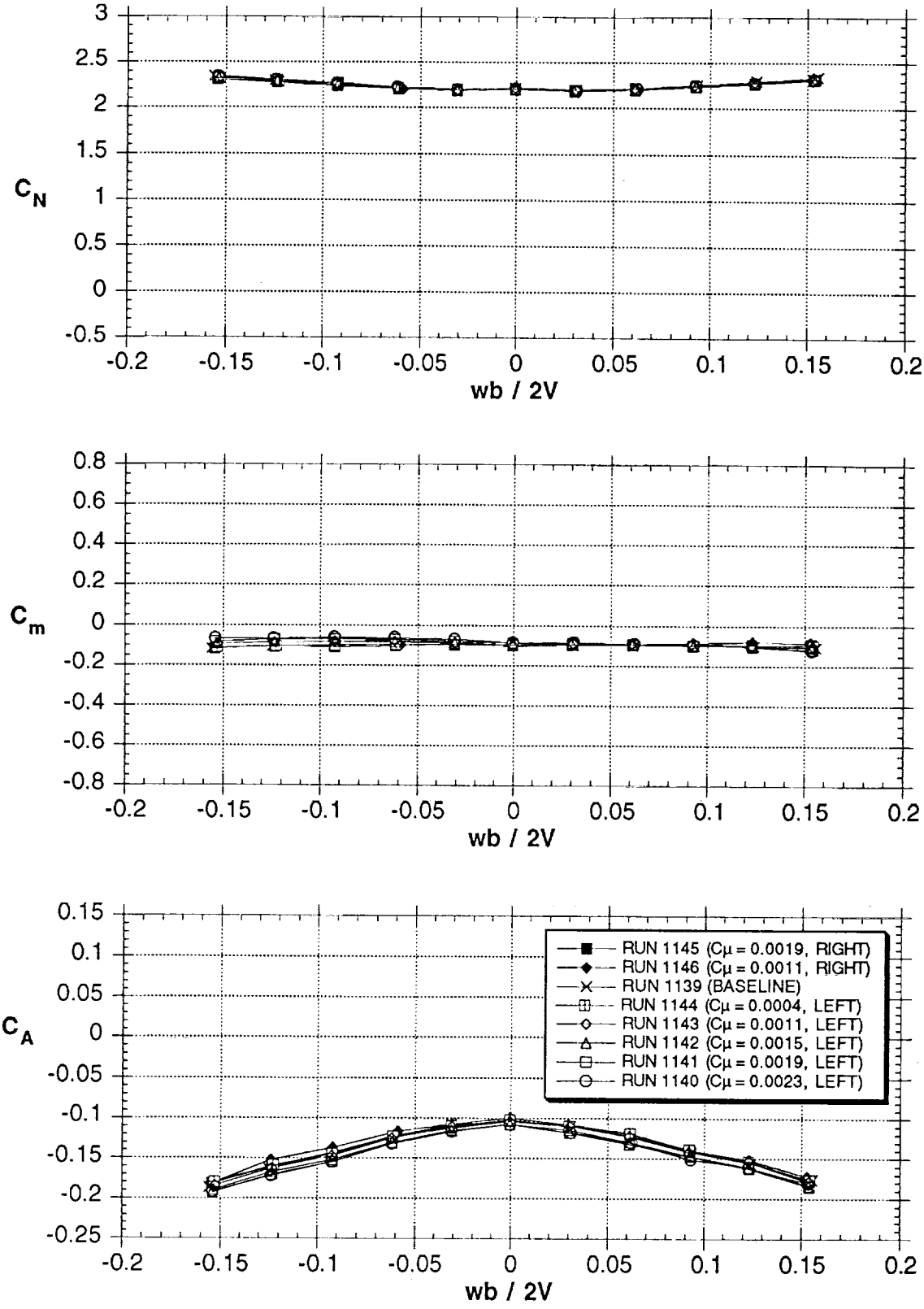

Figure 27 - Effects of NOSE 4 - 60° INBOARD blowing jet at 45° AOA

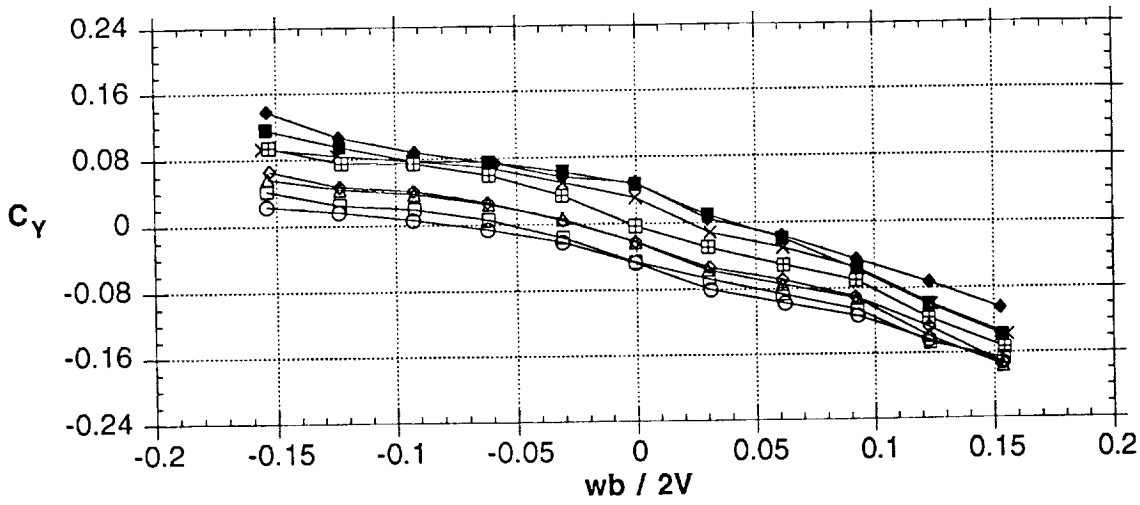

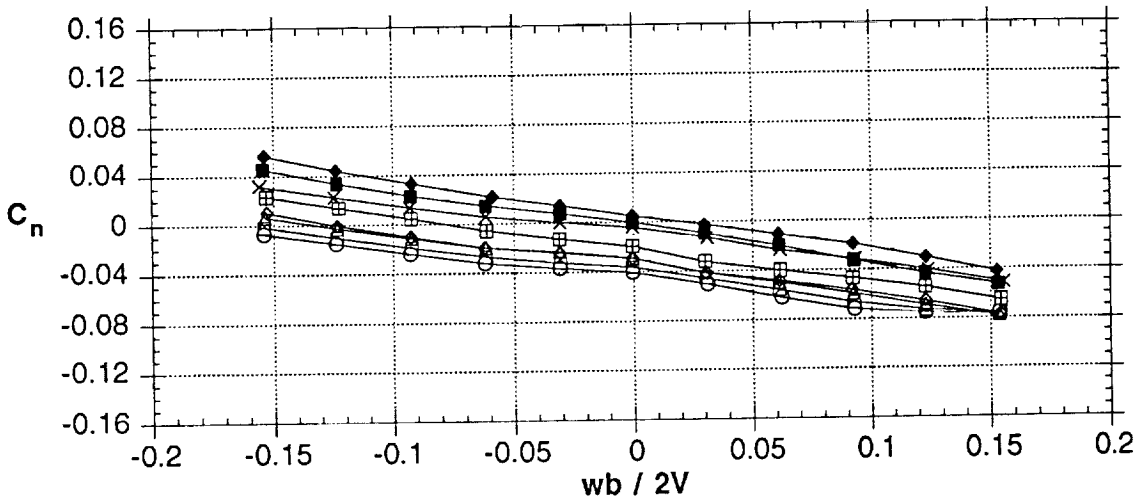

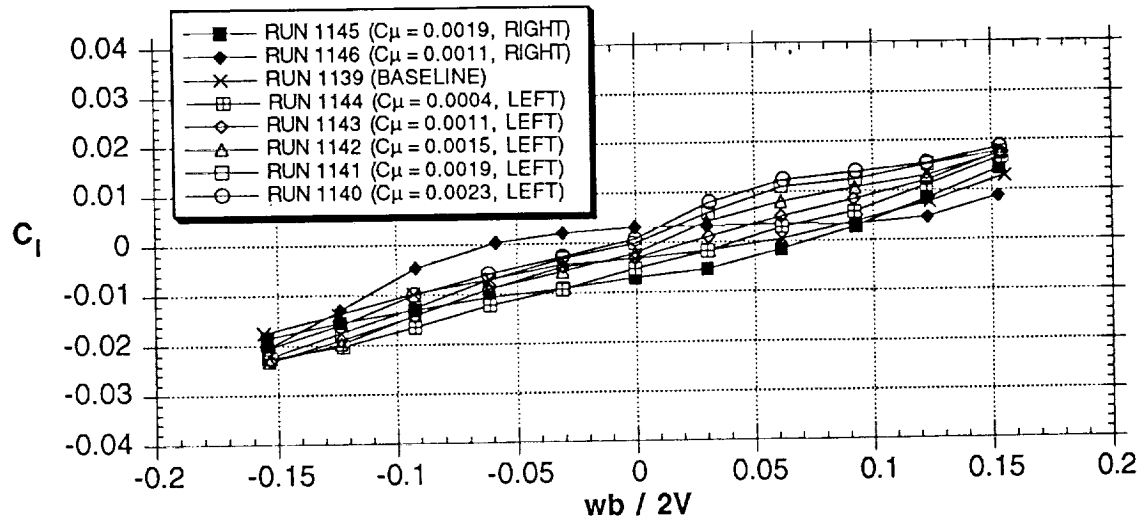

Figure 27 - Concluded

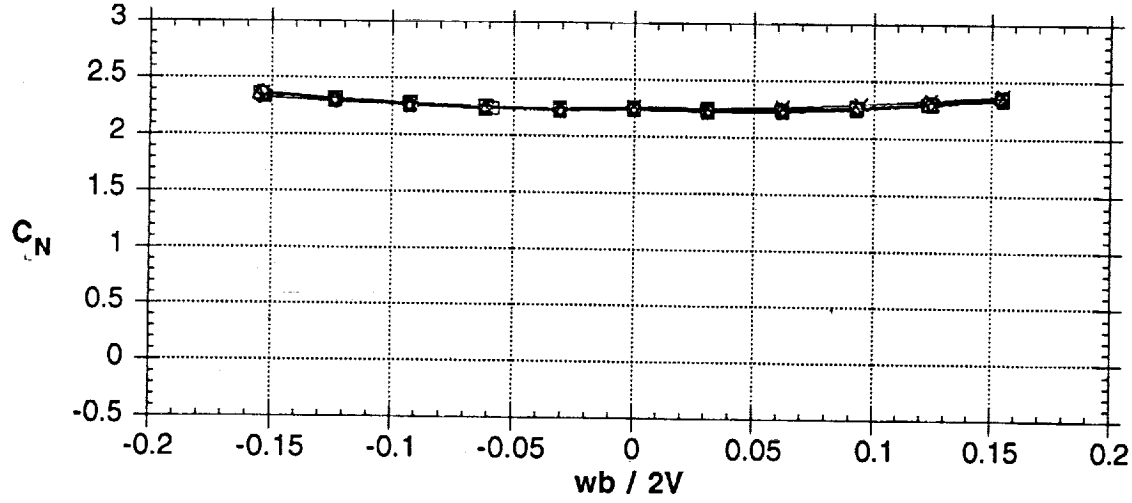

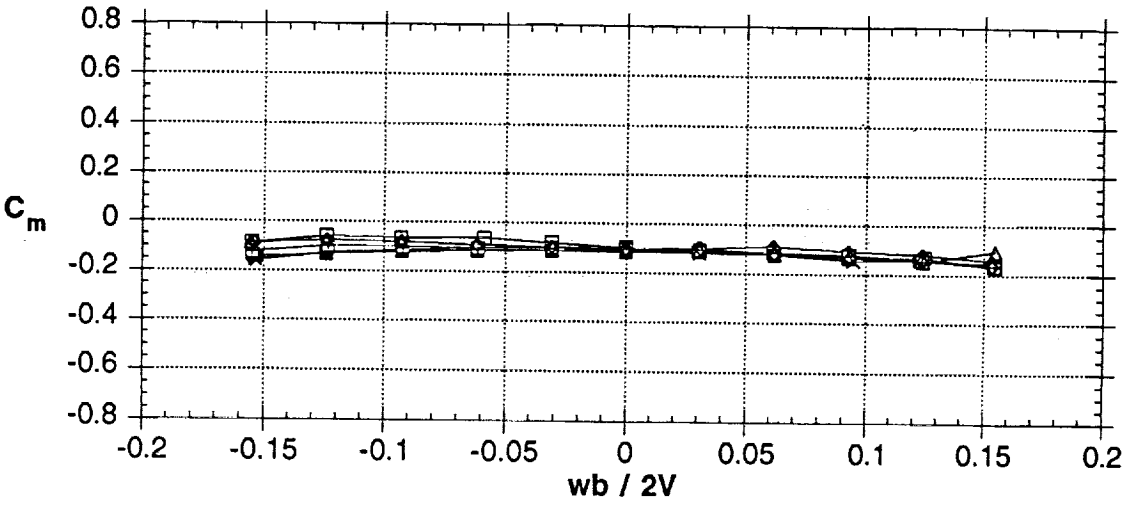

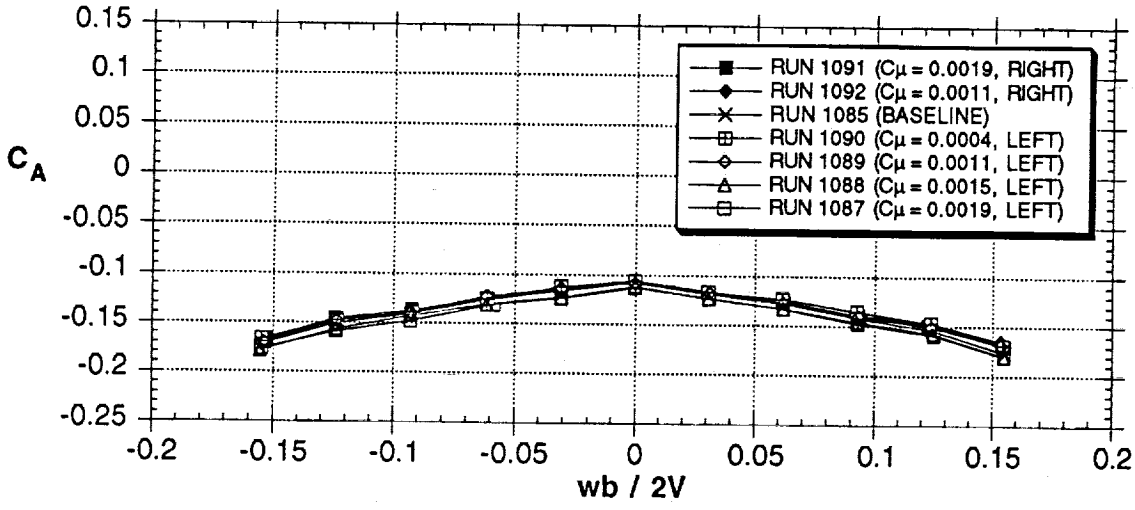

Figure 28 - Effects of NOSE 4 - 60° INBOARD blowing jet at 51° AOA

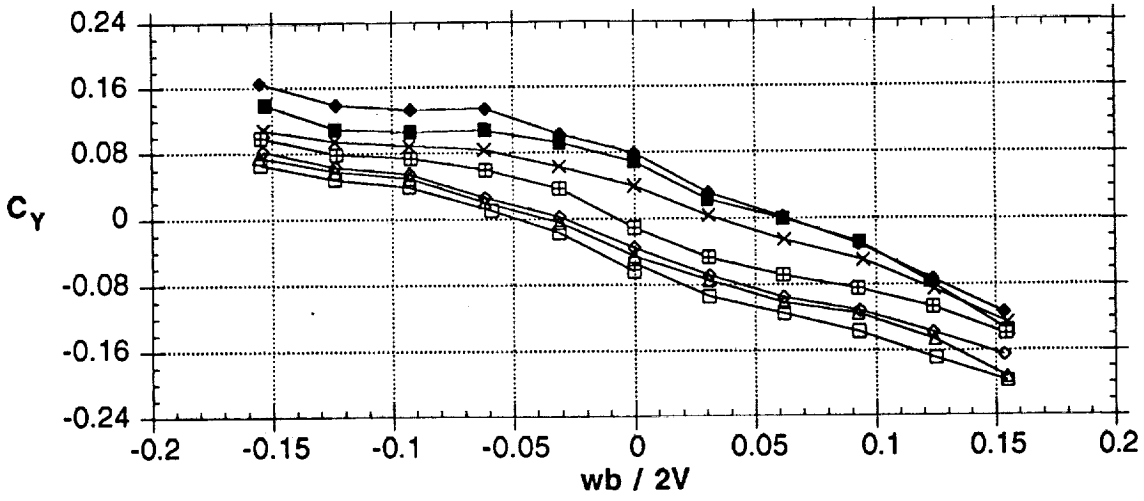

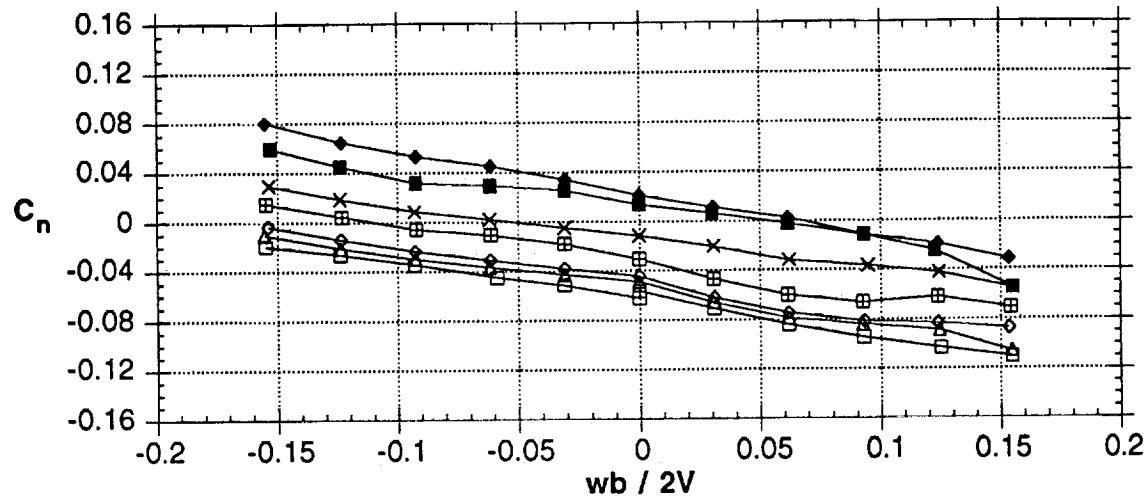

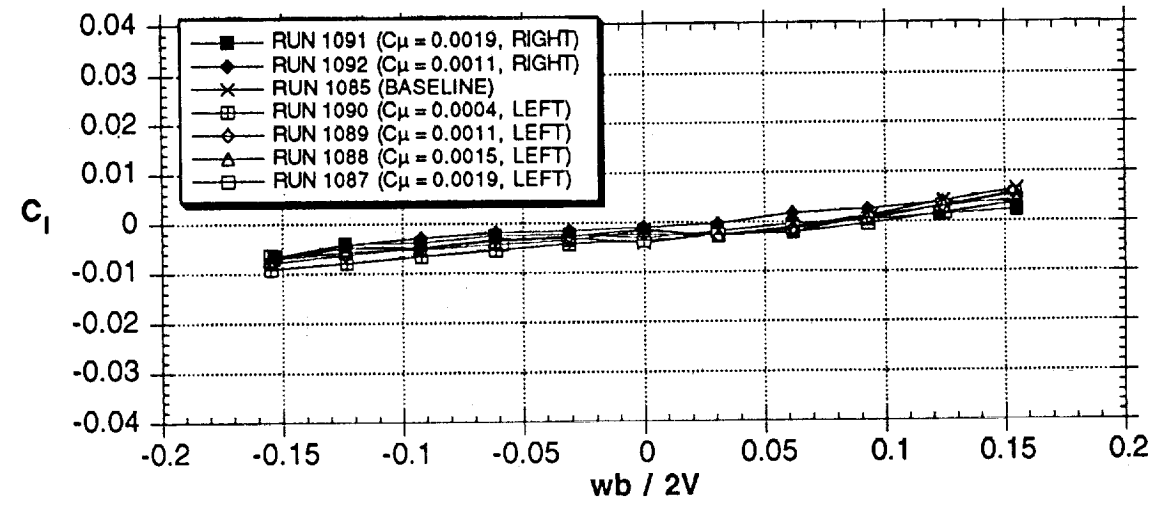

Figure 28 - Concluded

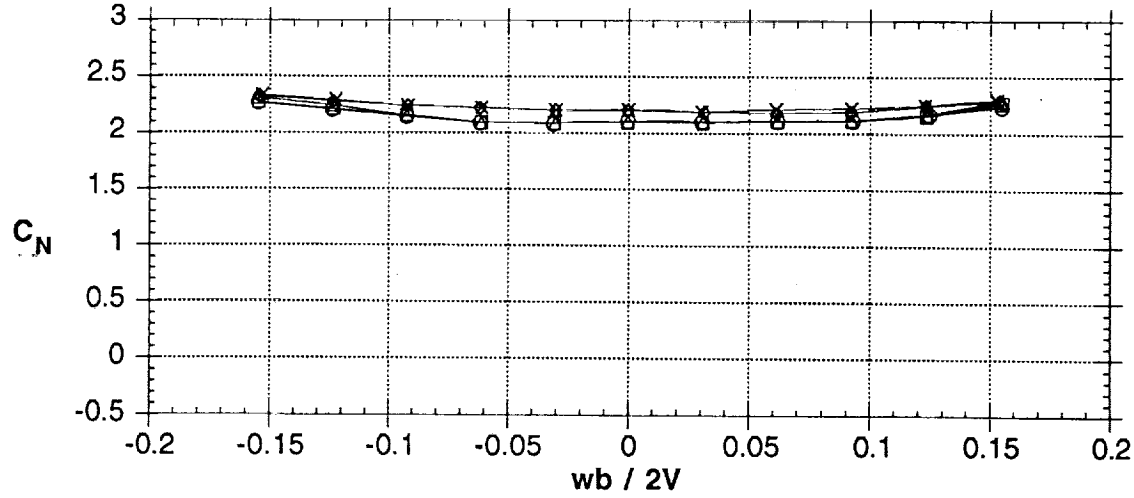

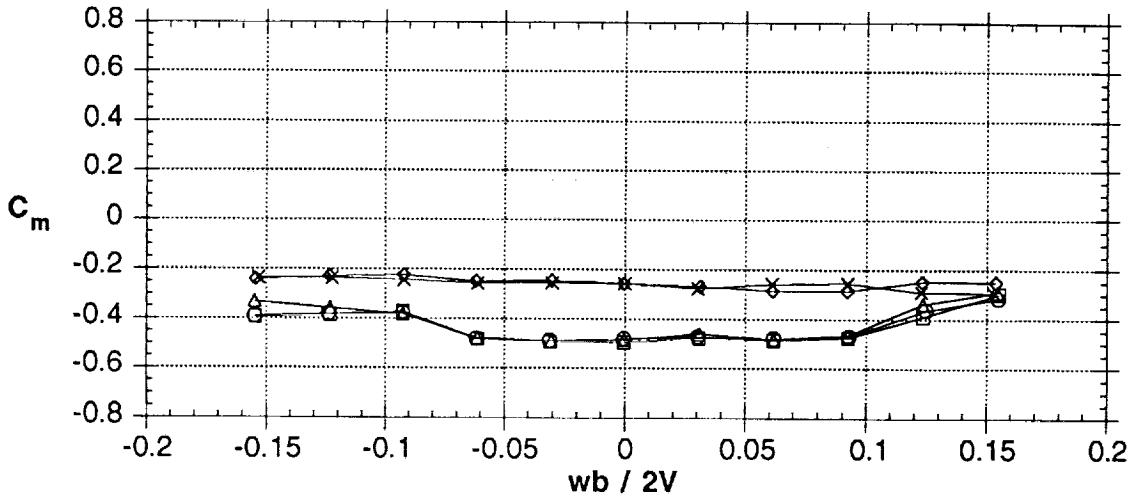

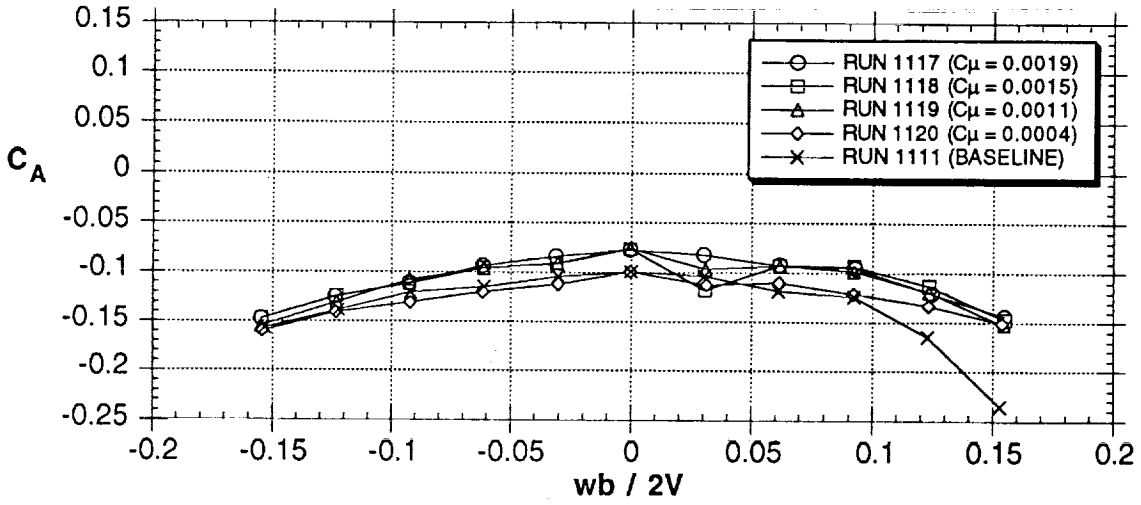

(a) Right side jet

Figure 29 - Effects of NOSE 4 - 60° INBOARD blowing jet at 60° AOA

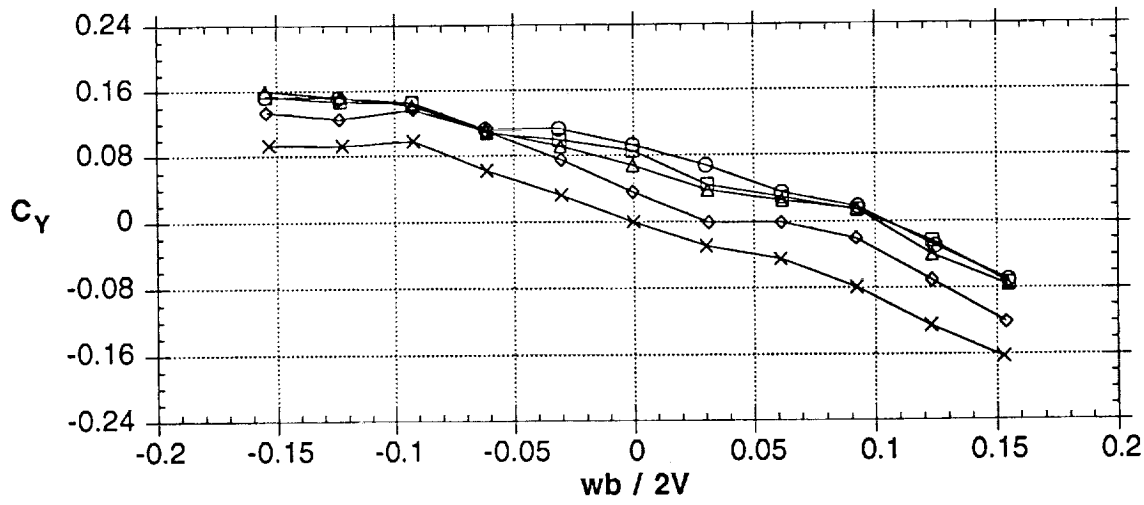

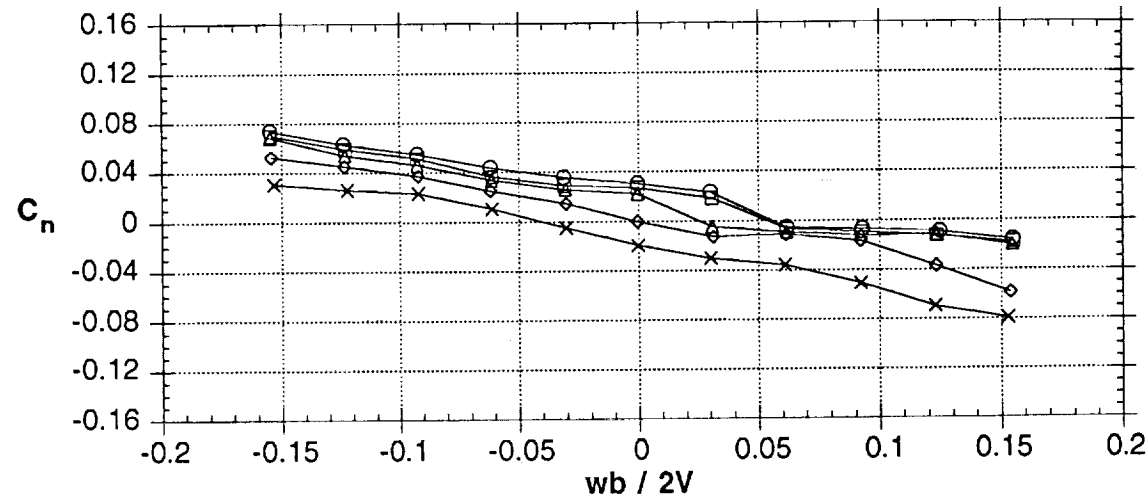

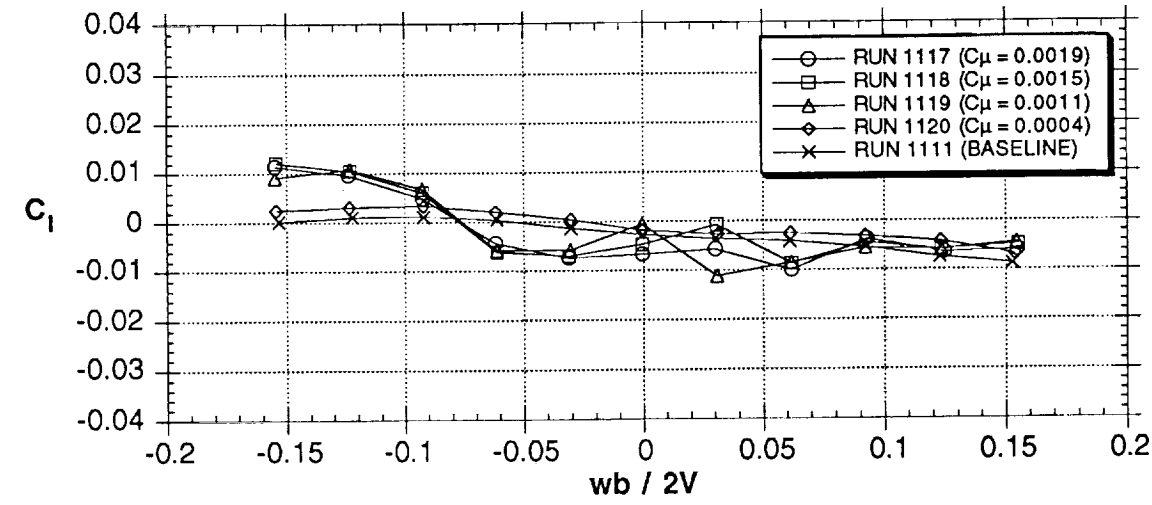

(a) Right side jet

Figure 29 - Continued

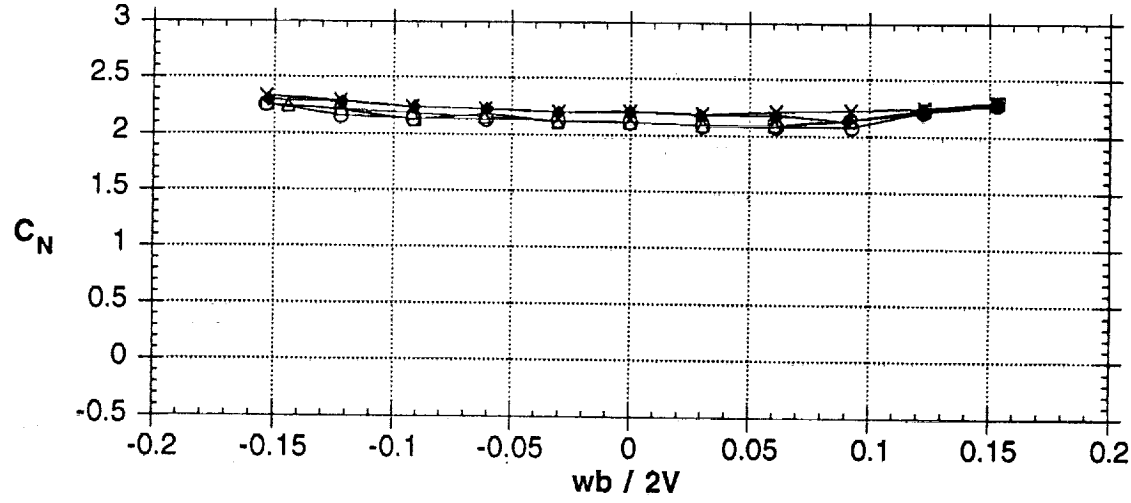

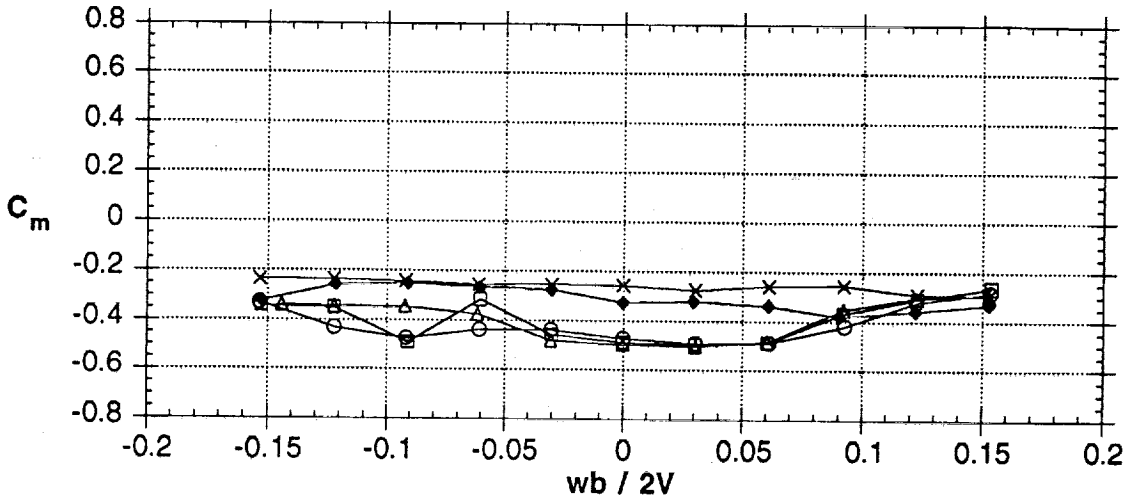

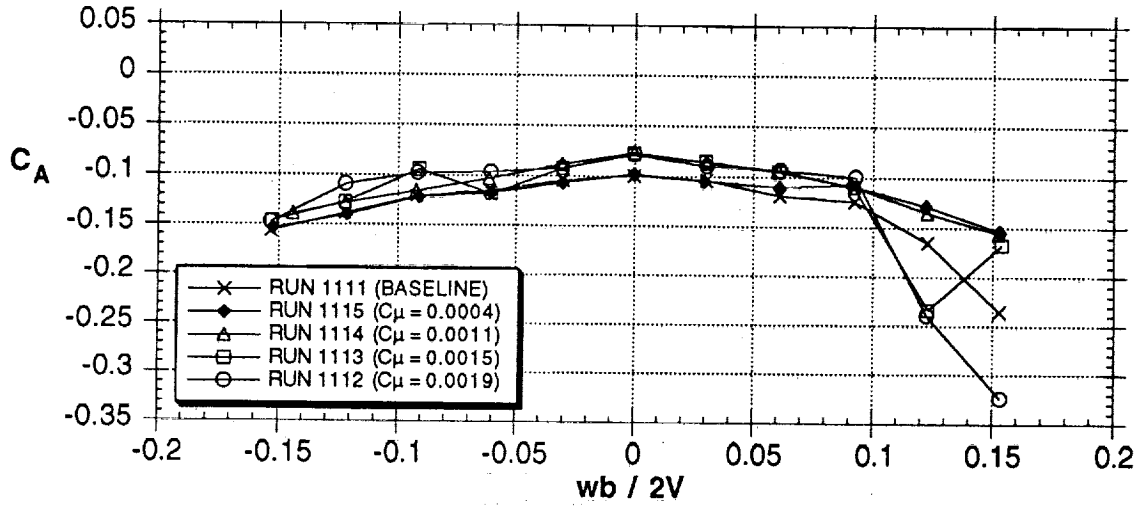

(b) Left side jet

Figure 29 - Continued

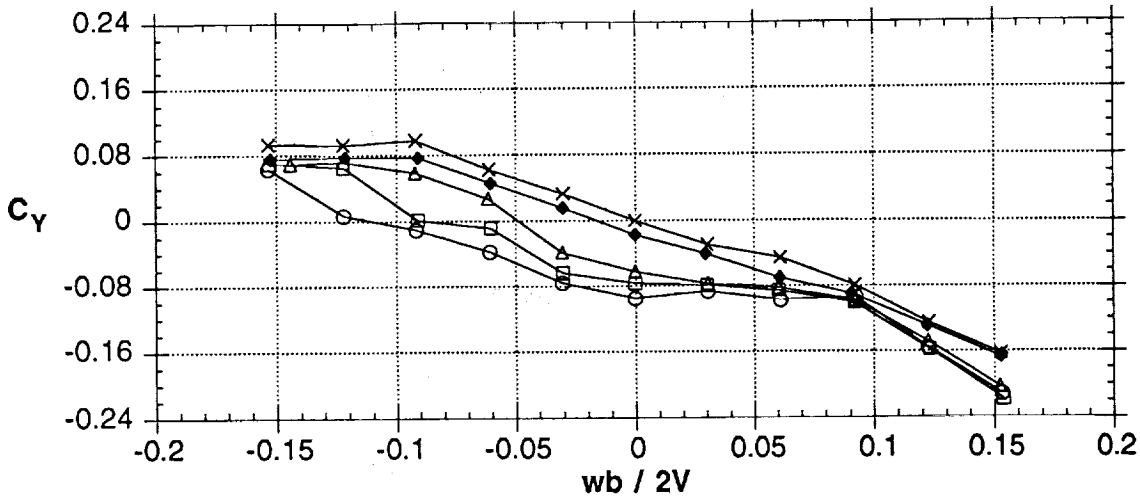

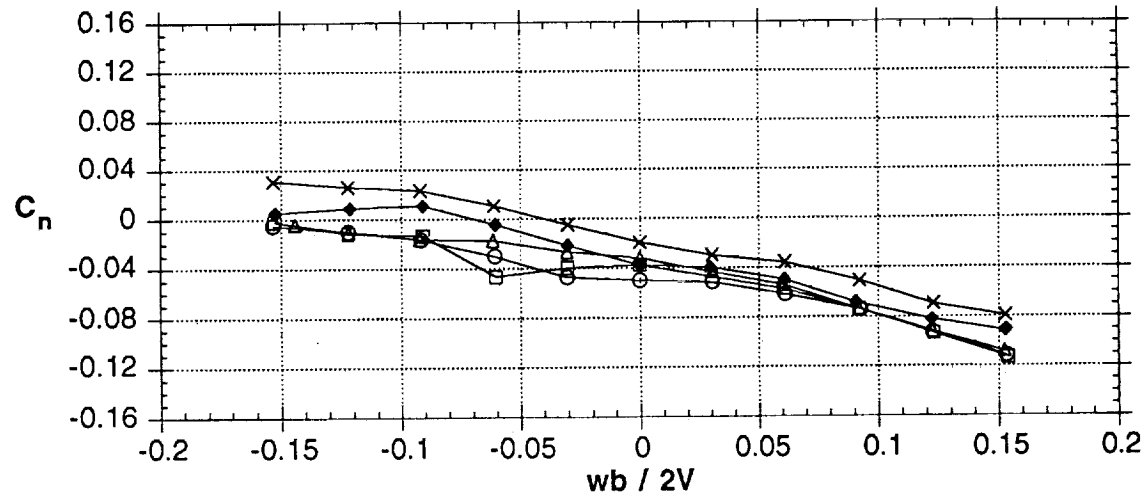

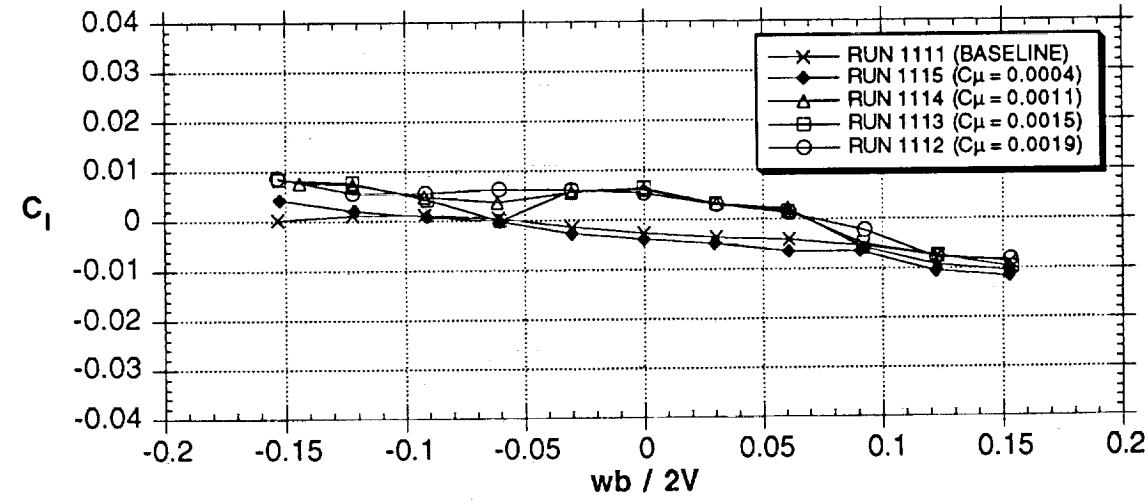

(b) Left side jet

Figure 29 - Concluded

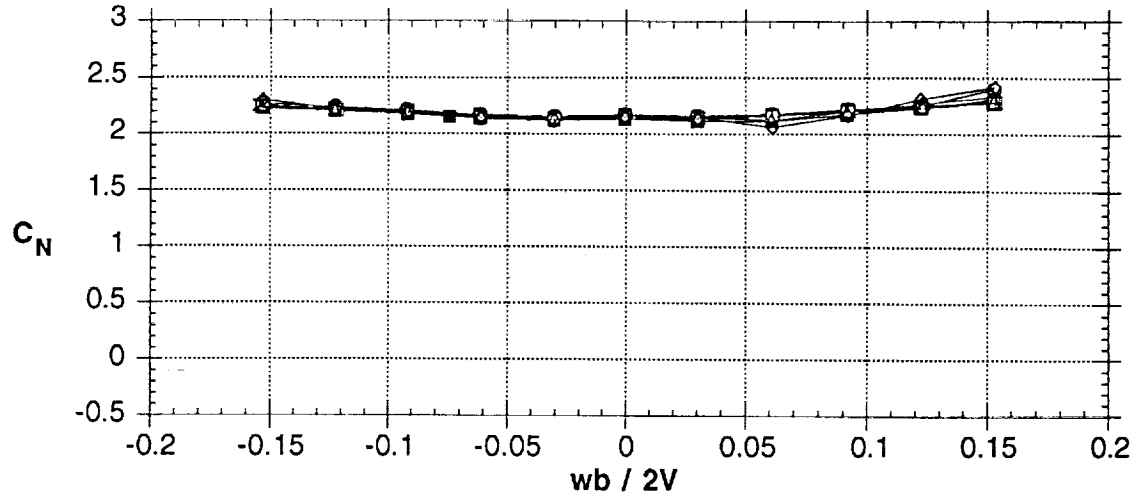

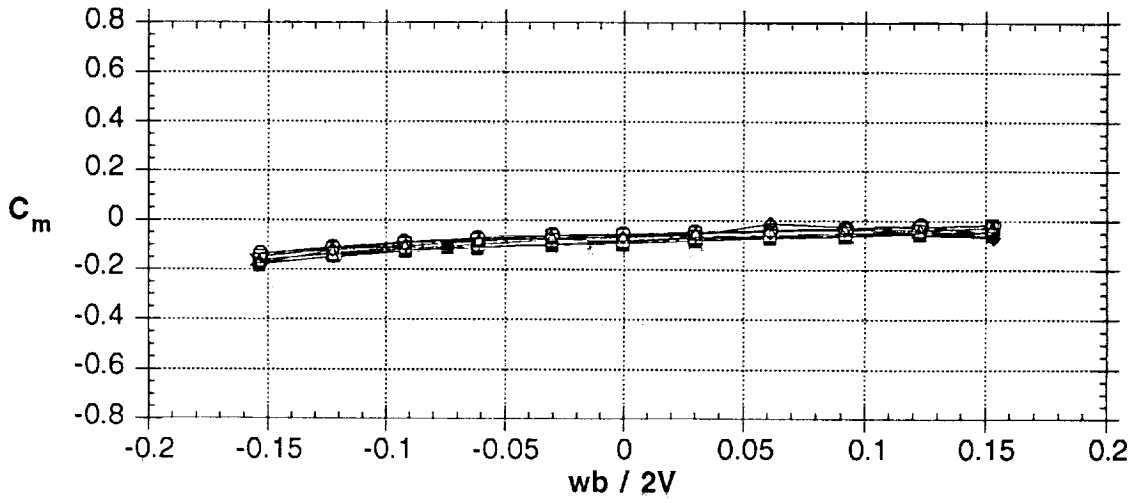

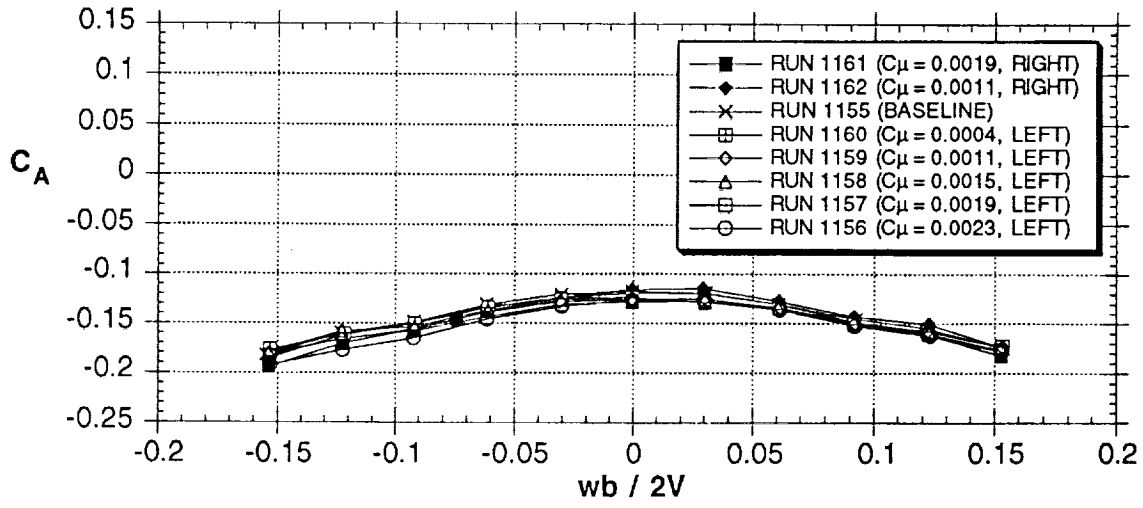

Figure 30 - Effects of NOSE 4 - 60° INBOARD blowing jet with sideslip angle of β = -10° at 45° AOA

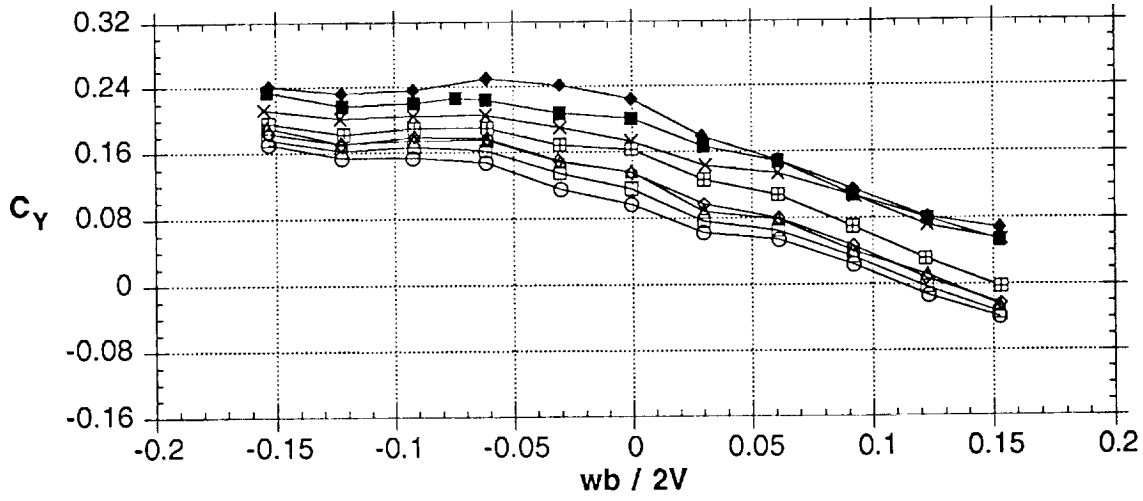

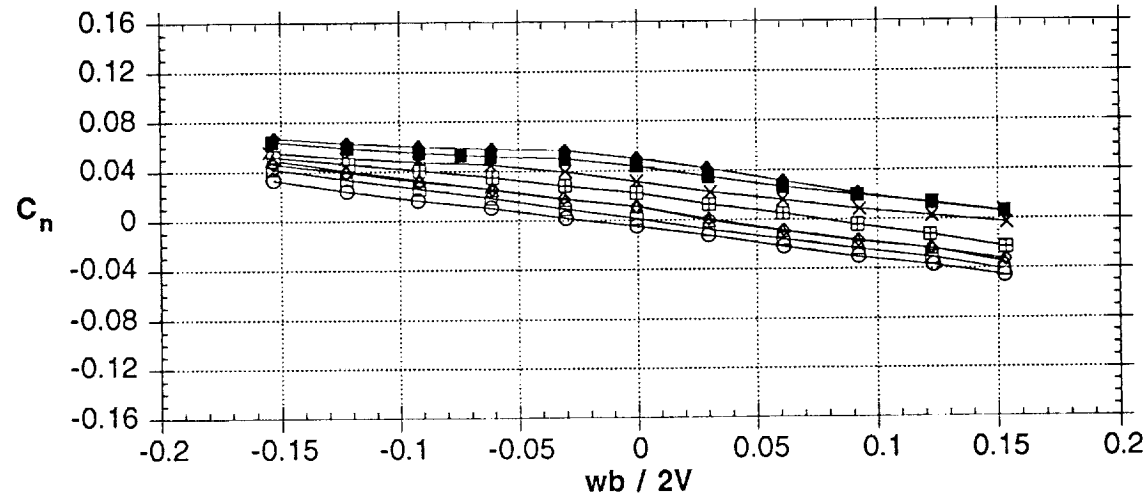

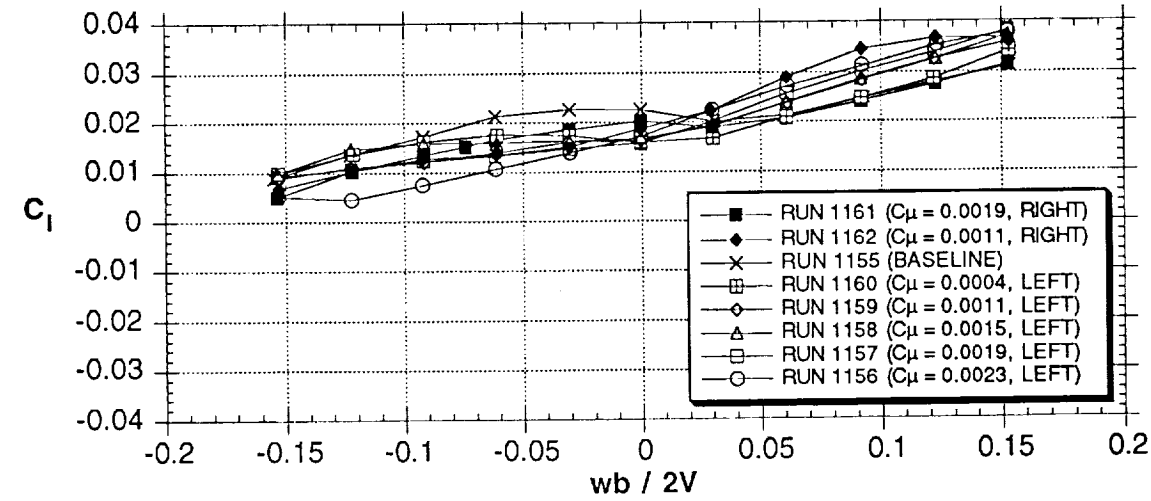

Figure 30 - Concluded

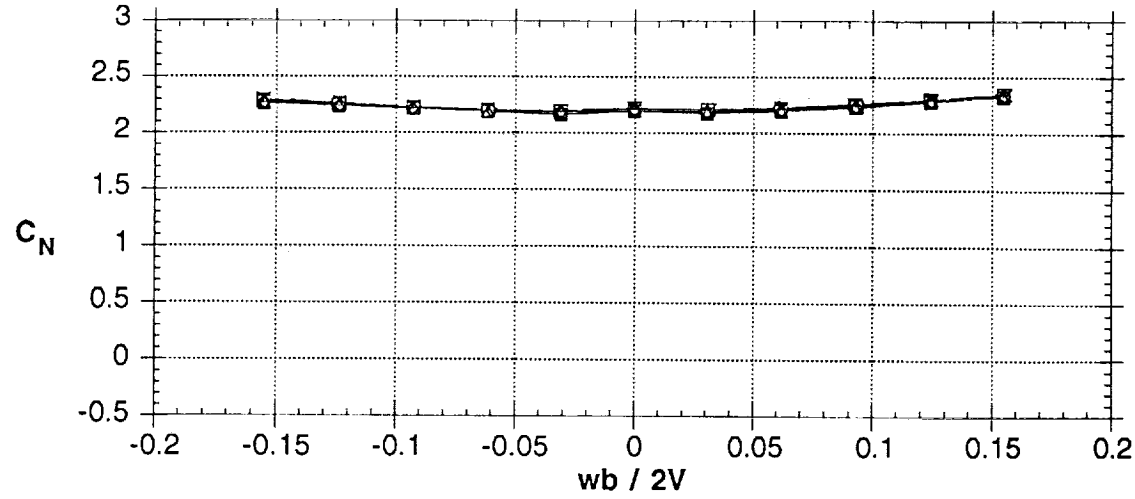

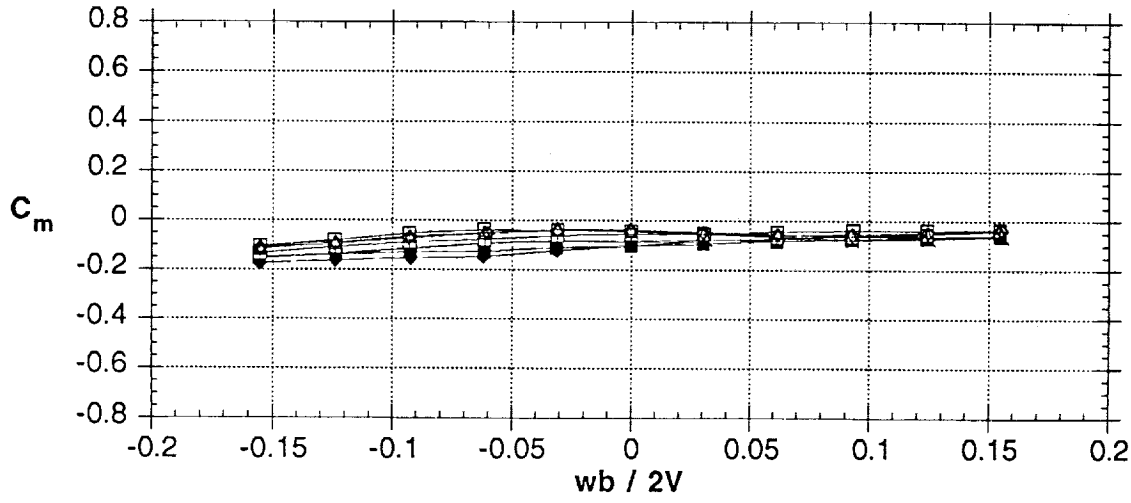

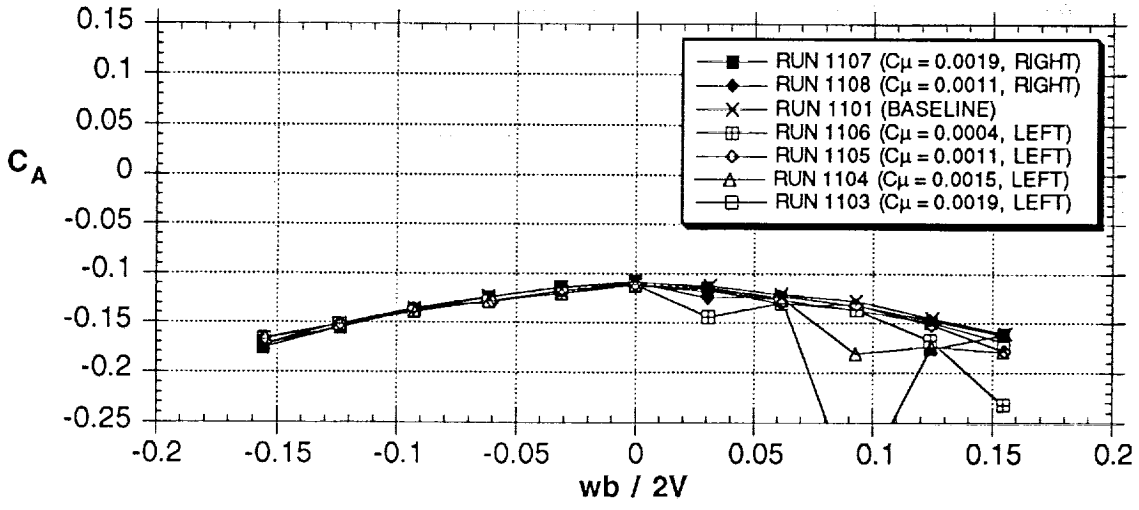

Figure 31 - Effects of NOSE 4 - 60° INBOARD blowing jet with sideslip angle of β = -10° at 51° AOA

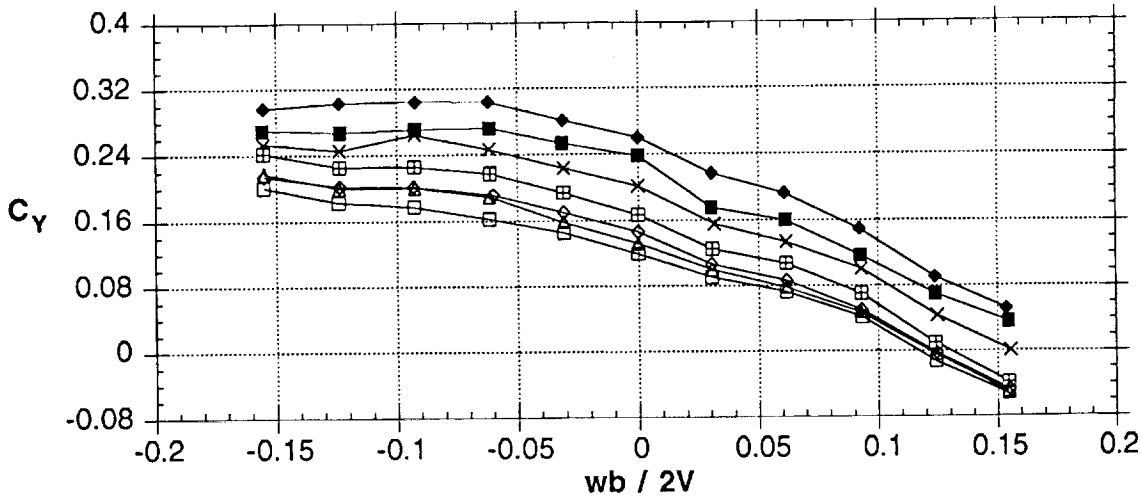

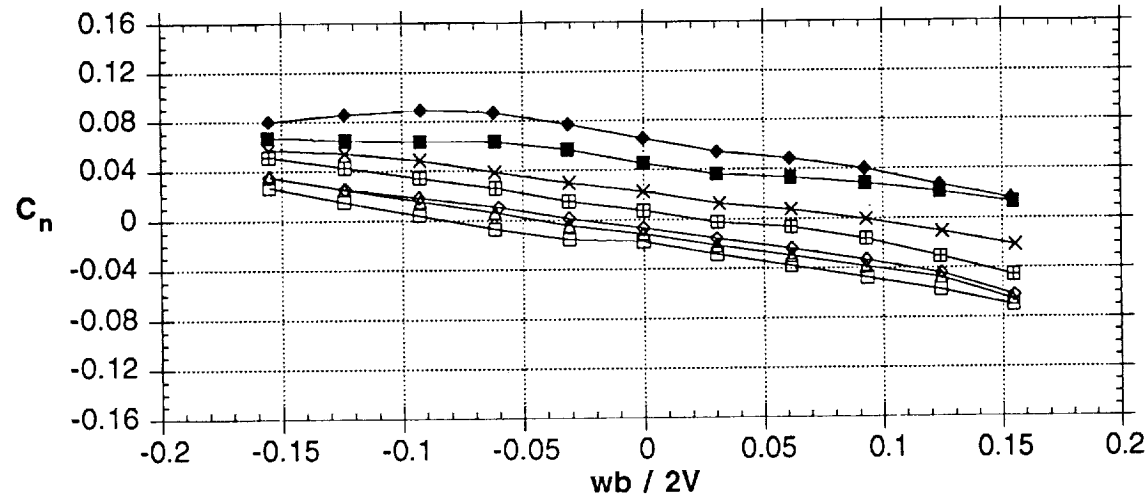

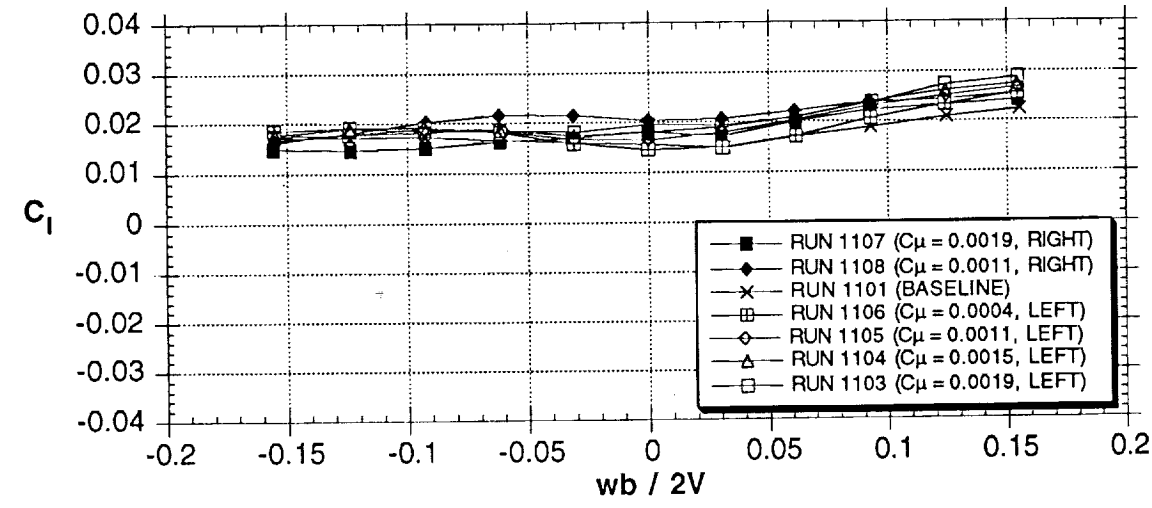

Figure 31 - Concluded

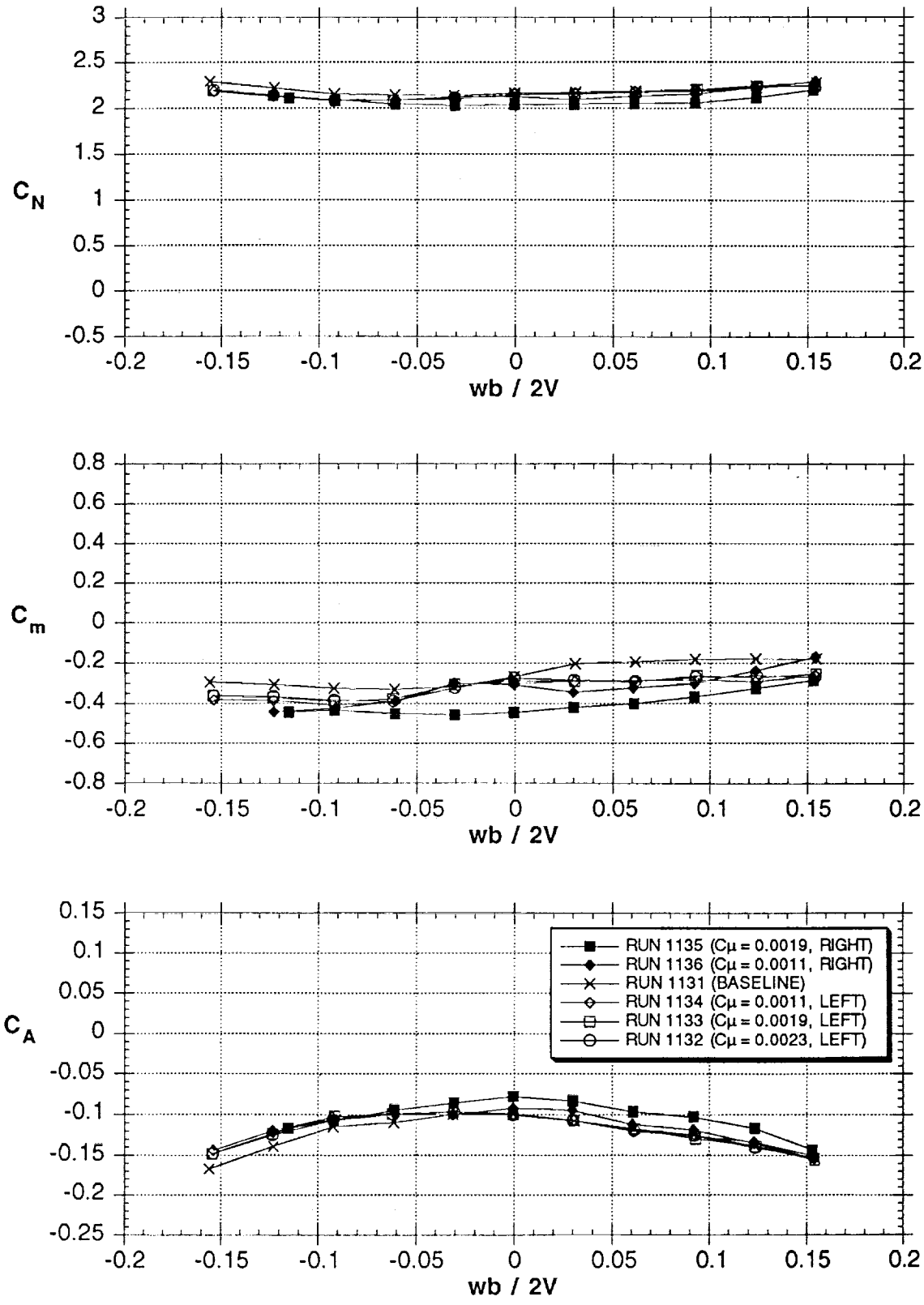

Figure 32 - Effects of NOSE 4 - 60° INBOARD blowing jet with sideslip angle of β = -10° at 60° AOA

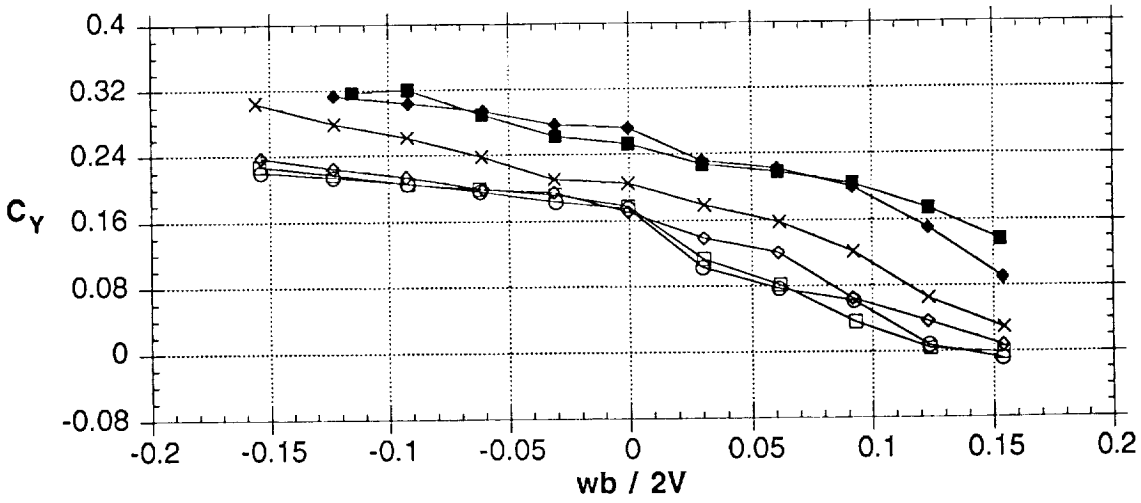

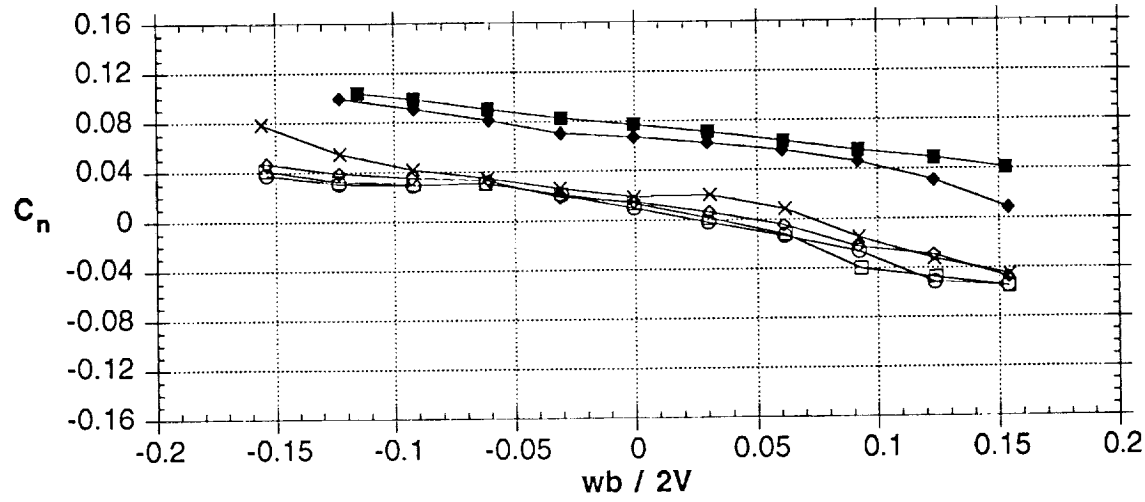

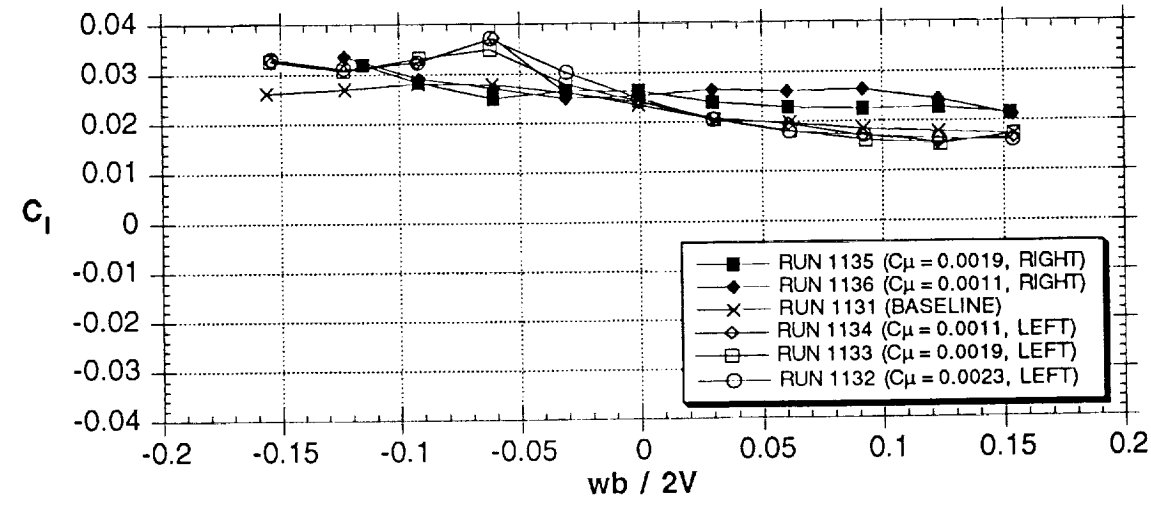

Figure 32 - Concluded

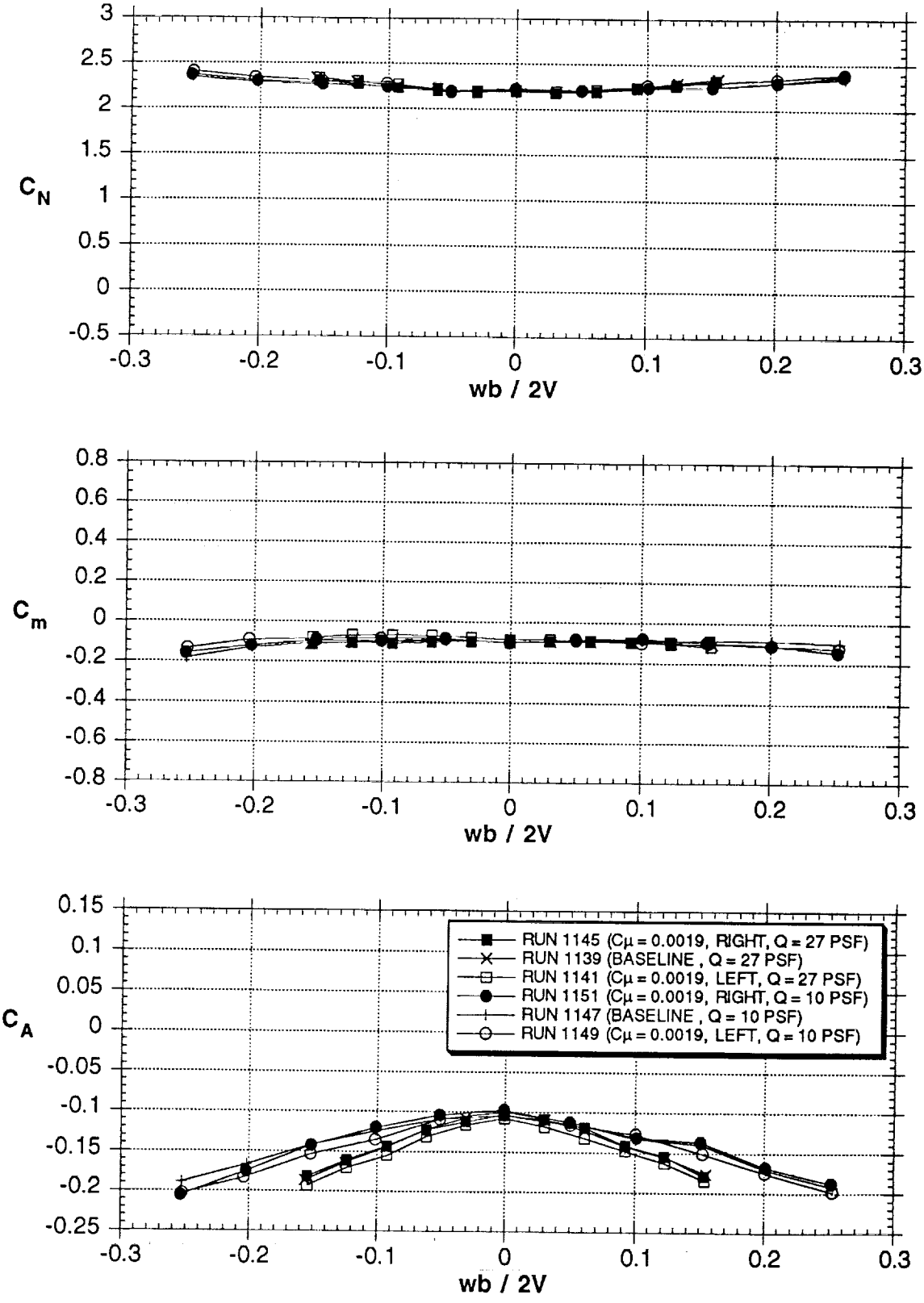

Figure 33 - Effects of Reynolds number with NOSE 4 - 60° INBOARD blowing jet, Q=27 psf ($Rn=0.636 \times 10^6$) and Q=10 psf ($Rn=0.387 \times 10^6$), 45° AOA

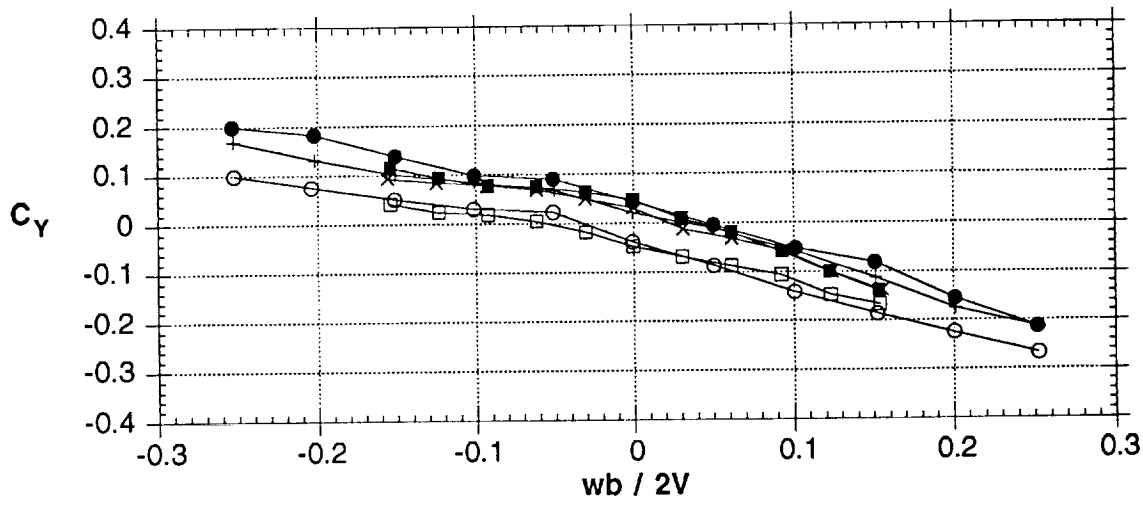

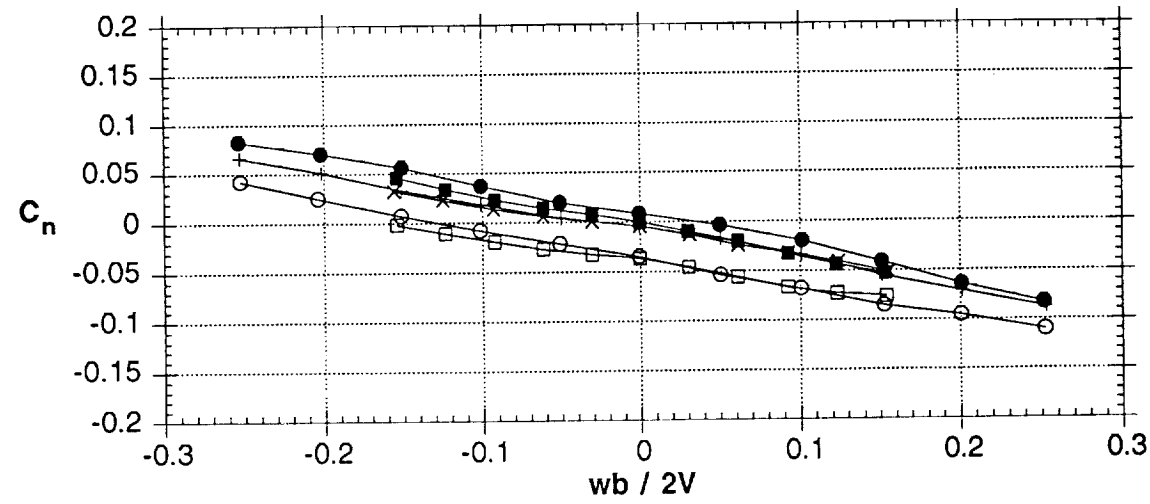

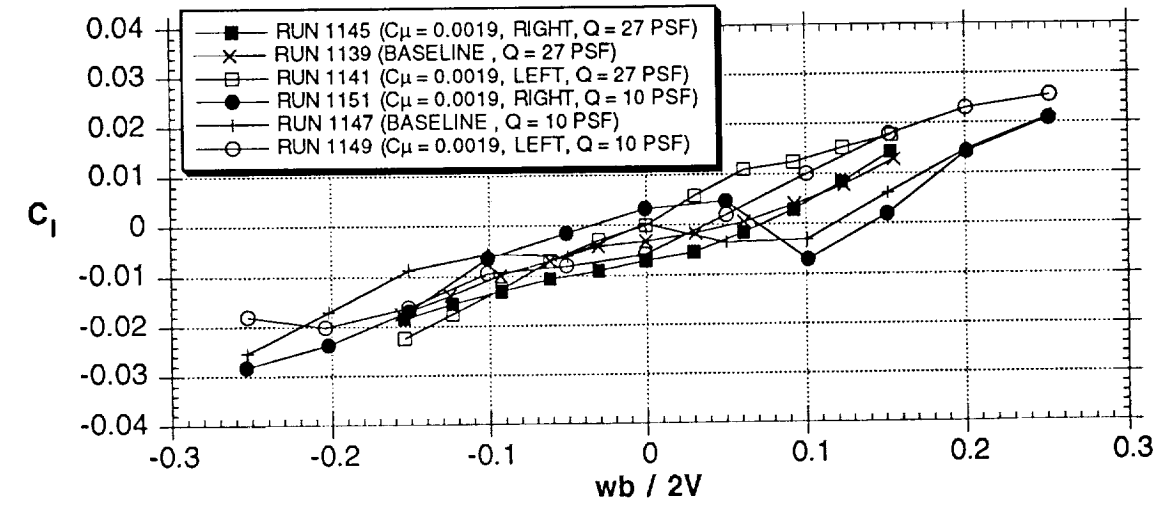

Figure 33 - Concluded

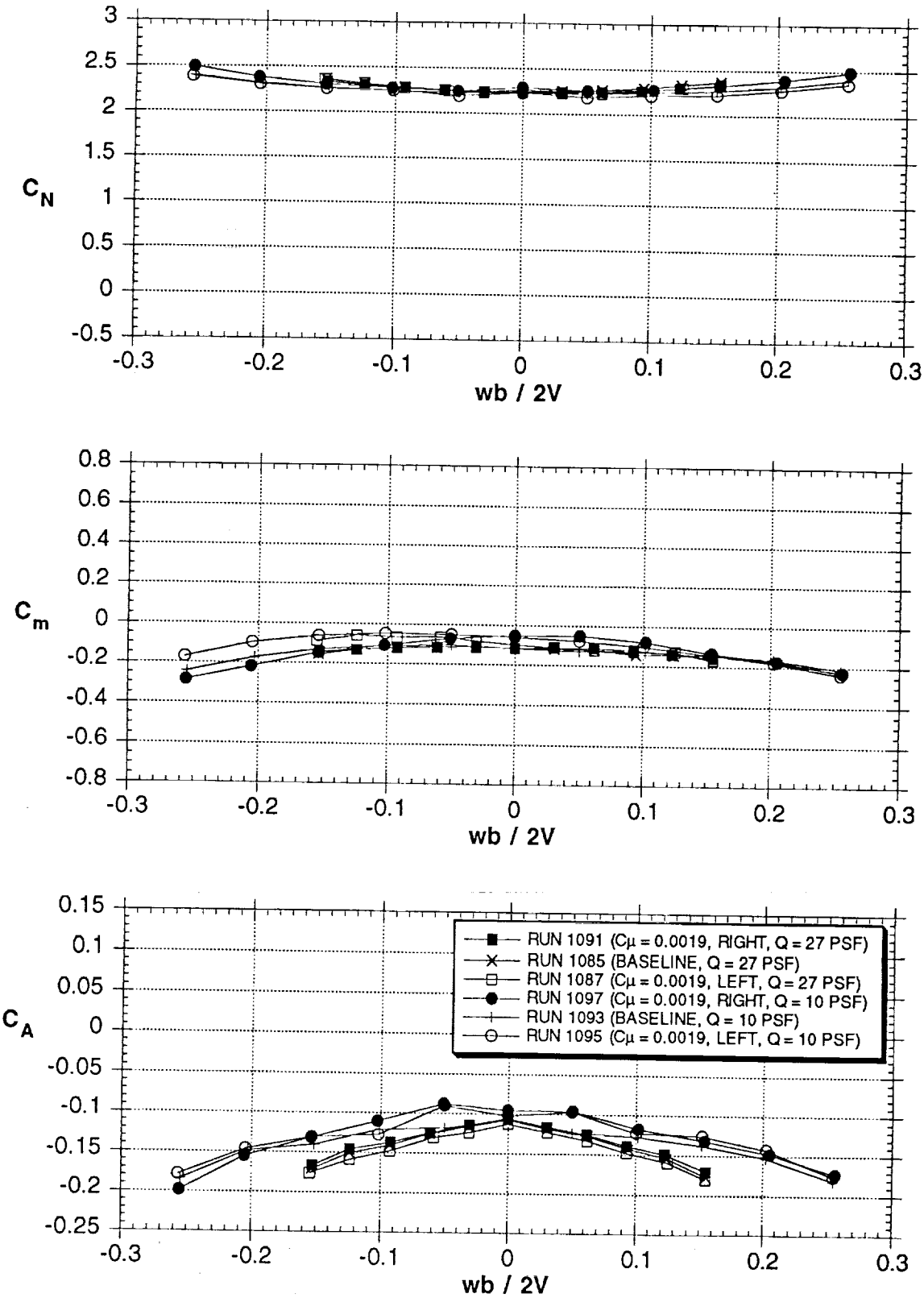

Figure 34 - Effects of Reynolds number with NOSE 4 - 60° INBOARD blowing jet, Q=27 psf (Rn=0.636x10^6) and Q=10 psf (Rn=0.387x10^6), 51° AOA

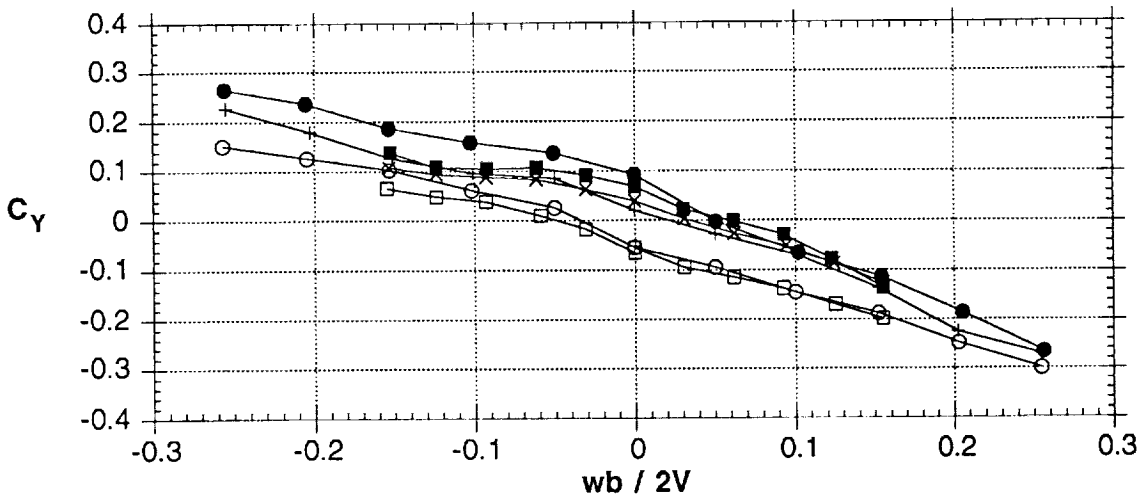

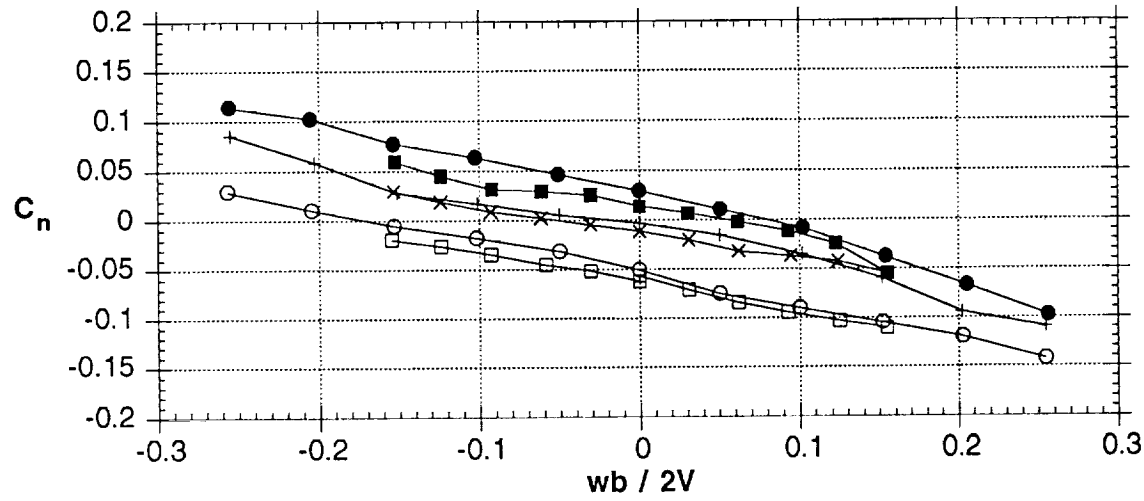

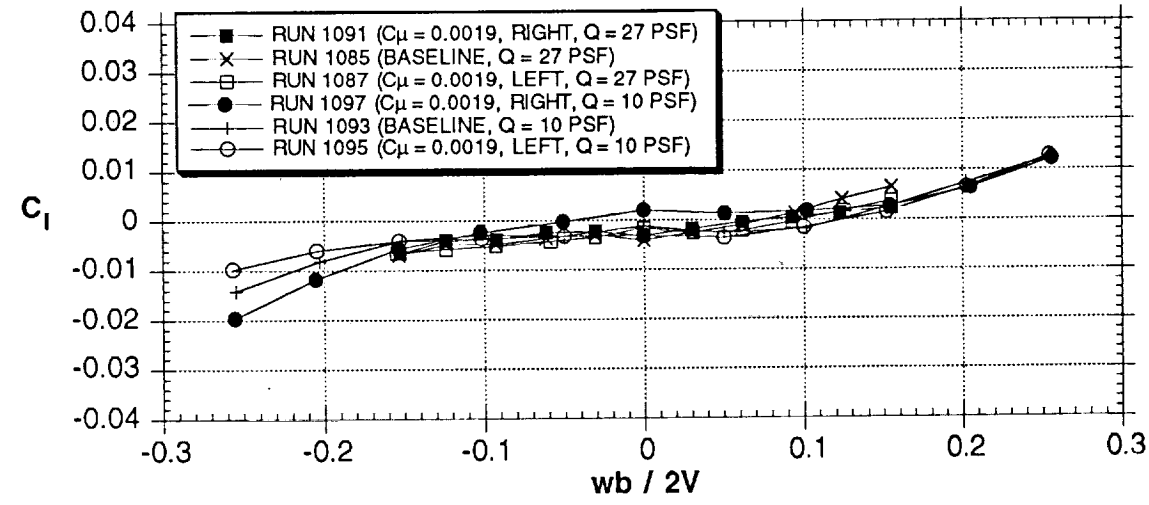

Figure 34 - Concluded

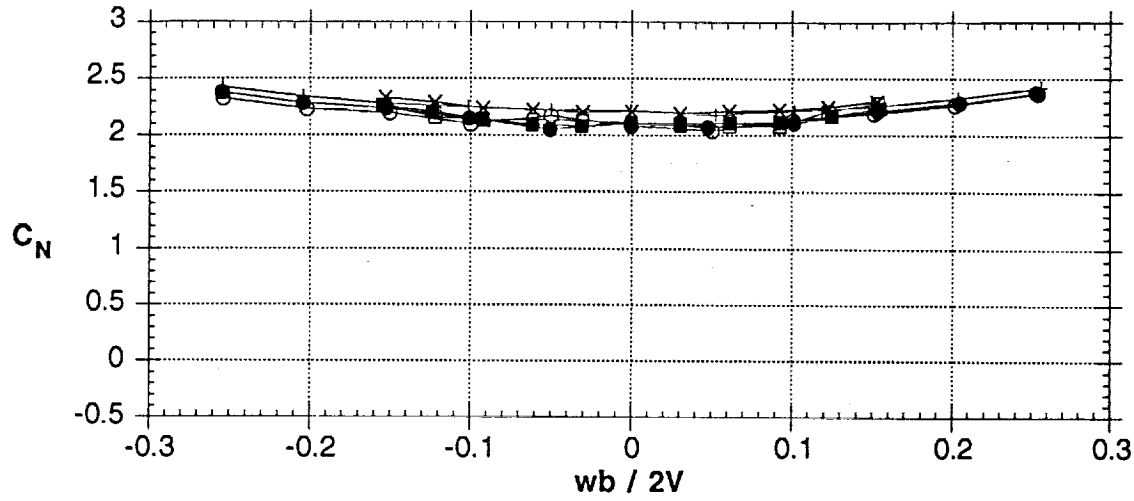

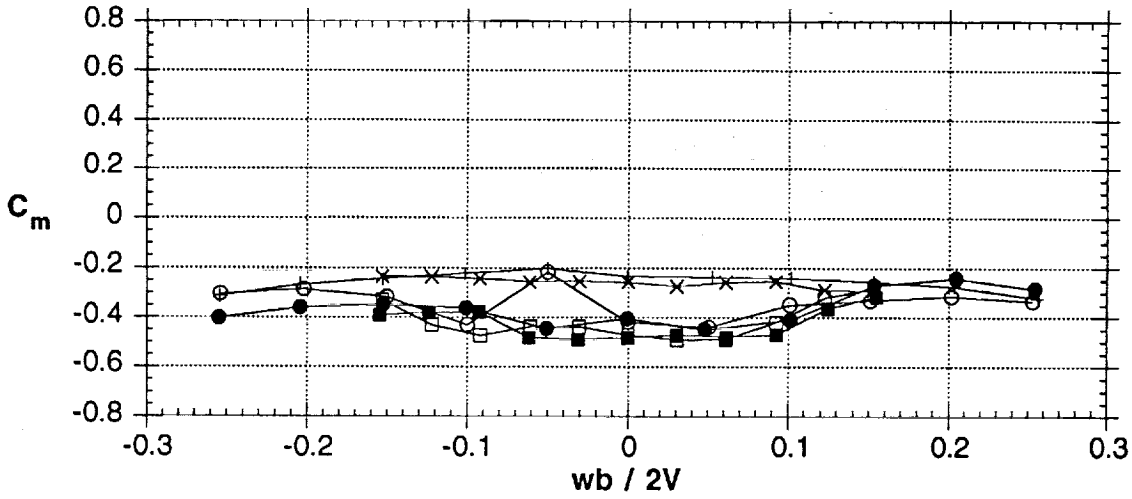

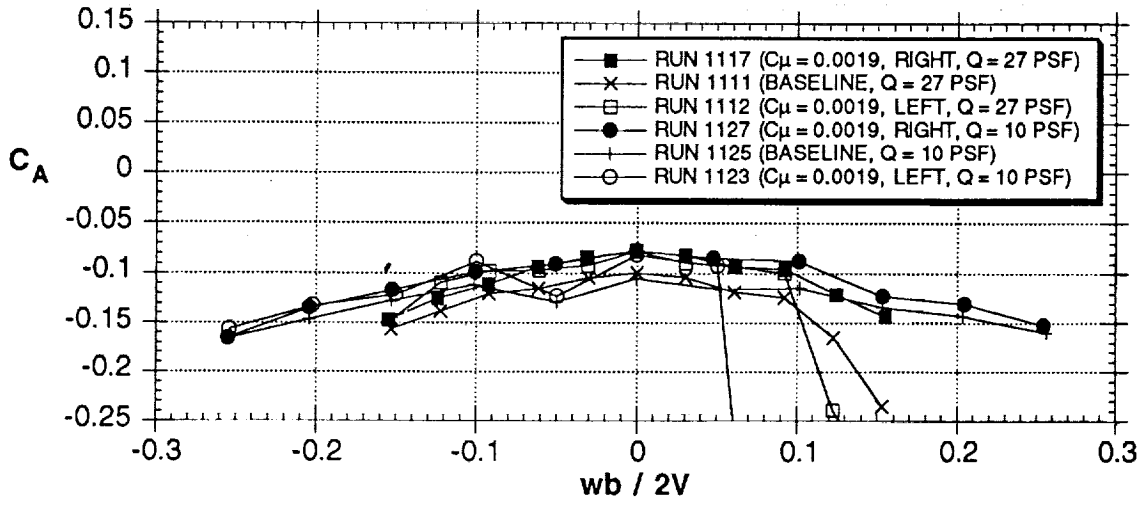

Figure 35 - Effects of Reynolds number with NOSE 4 - 60° INBOARD blowing jet, Q=27 psf ($Rn=0.636 \times 10^6$) and Q=10 psf ($Rn=0.387 \times 10^6$), 60° AOA

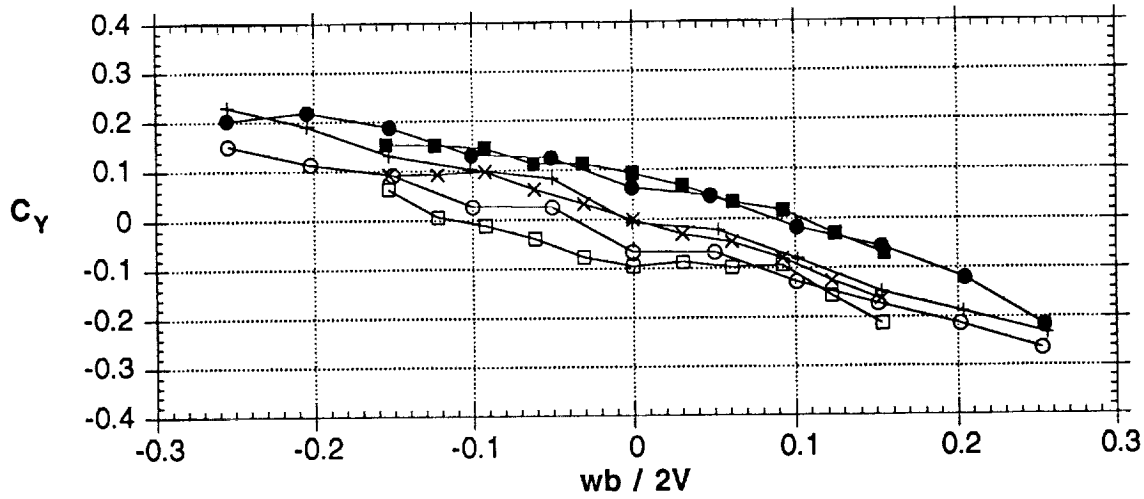

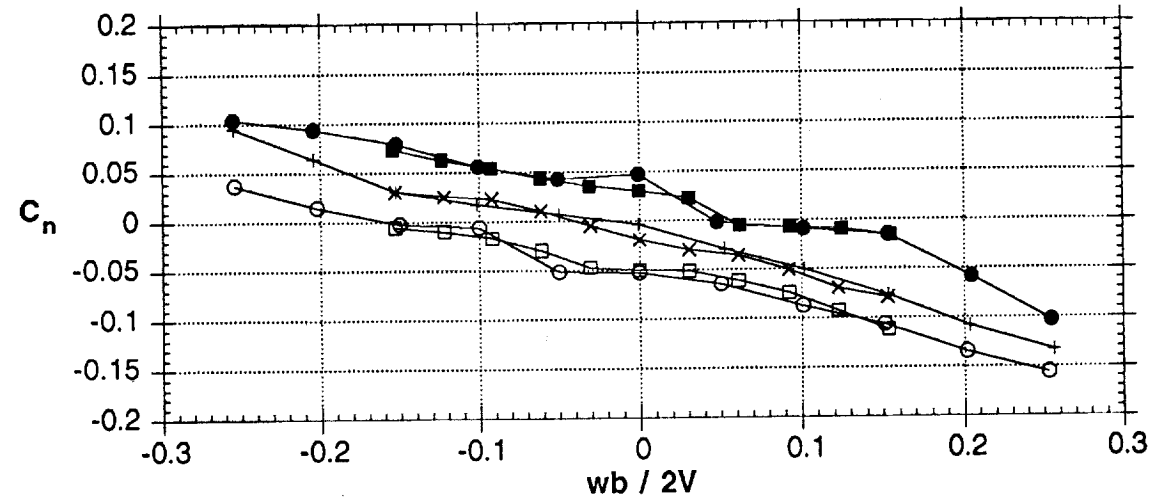

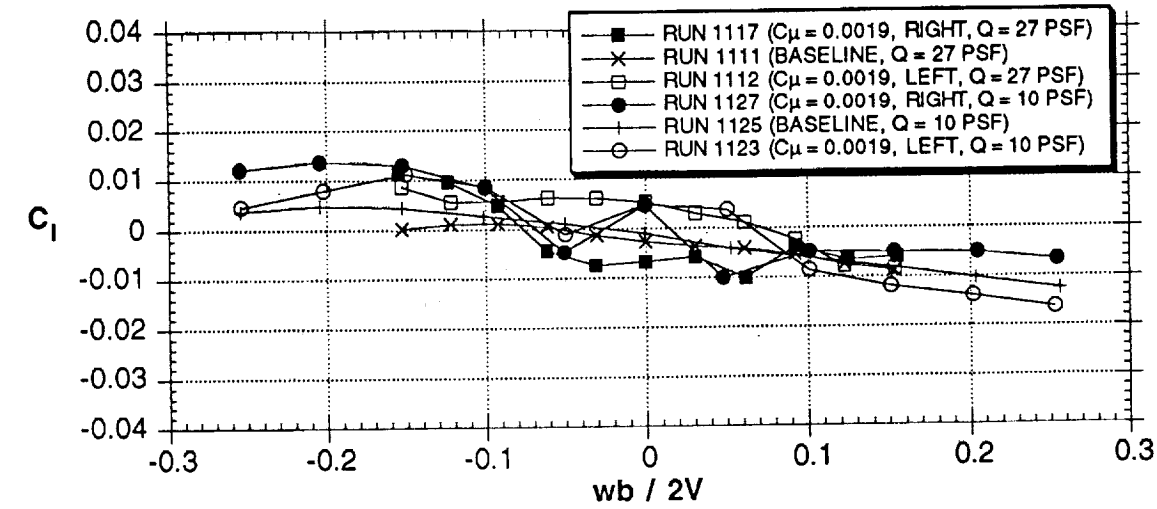

Figure 35 - Concluded

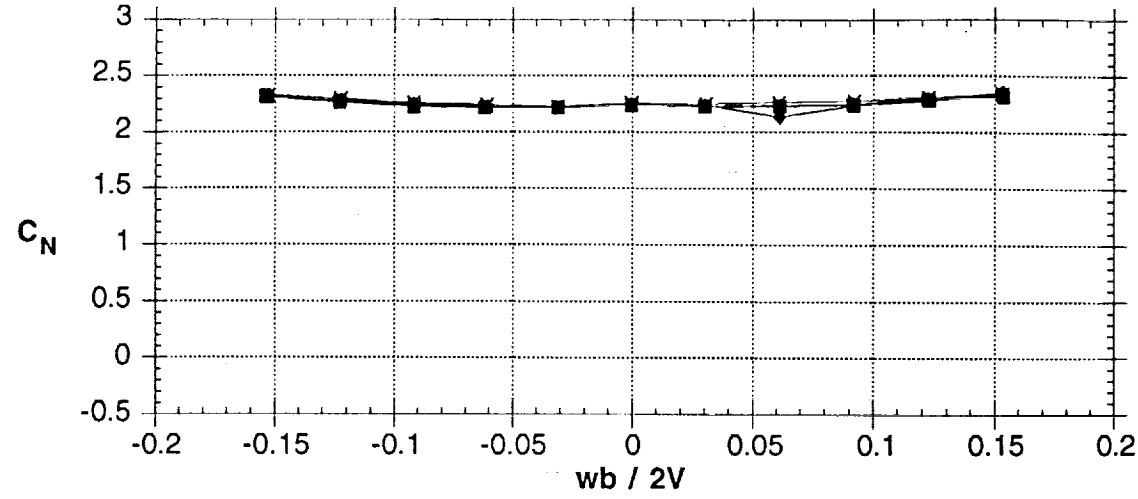

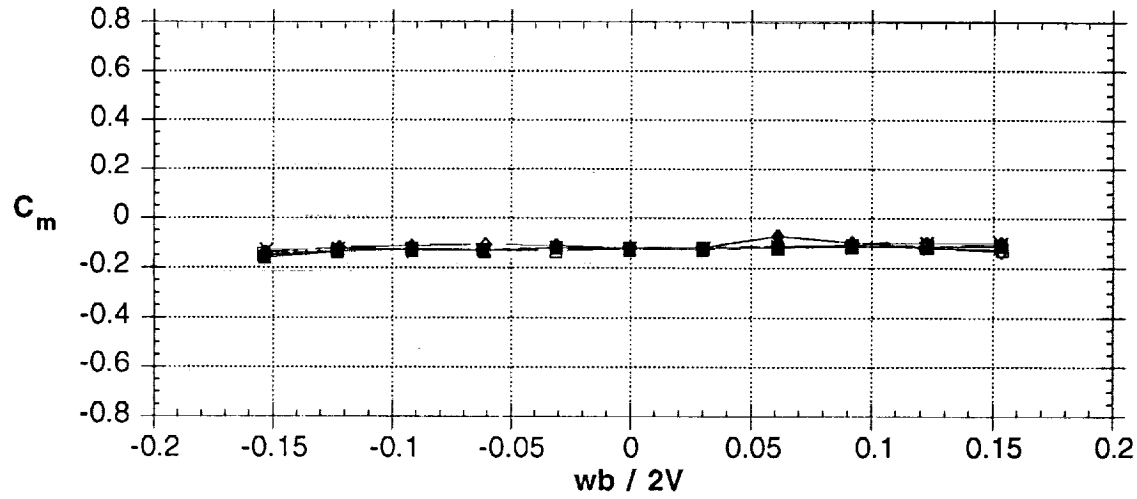

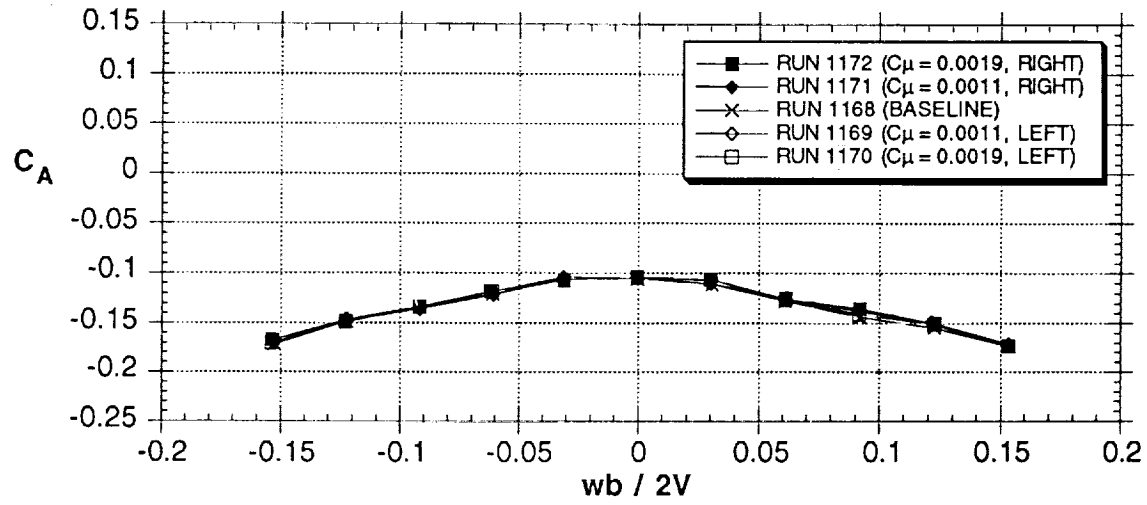

Figure 36 - Effects of NOSE 6 (flush mounted NOSE 4 - 60° INBOARD) blowing jet, 51° AOA

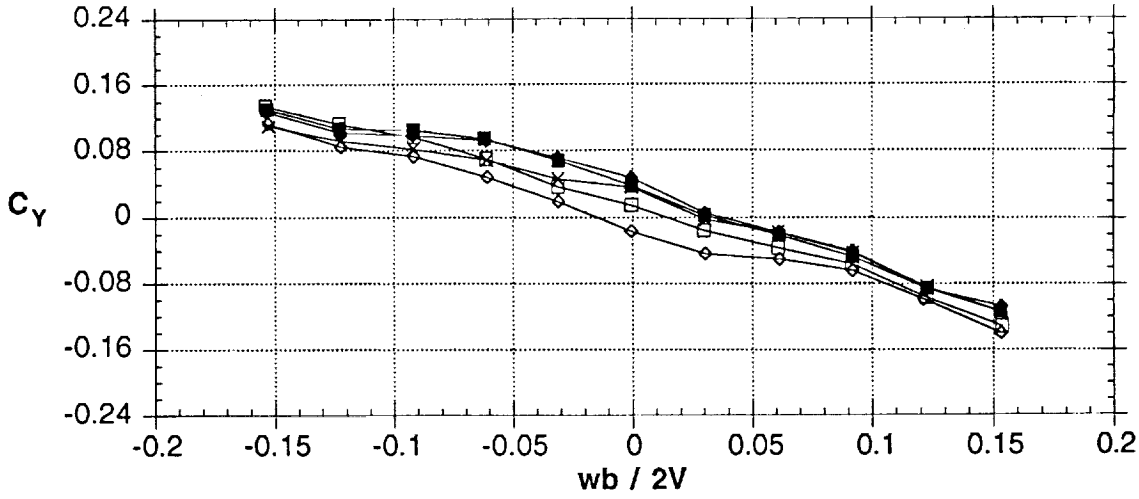

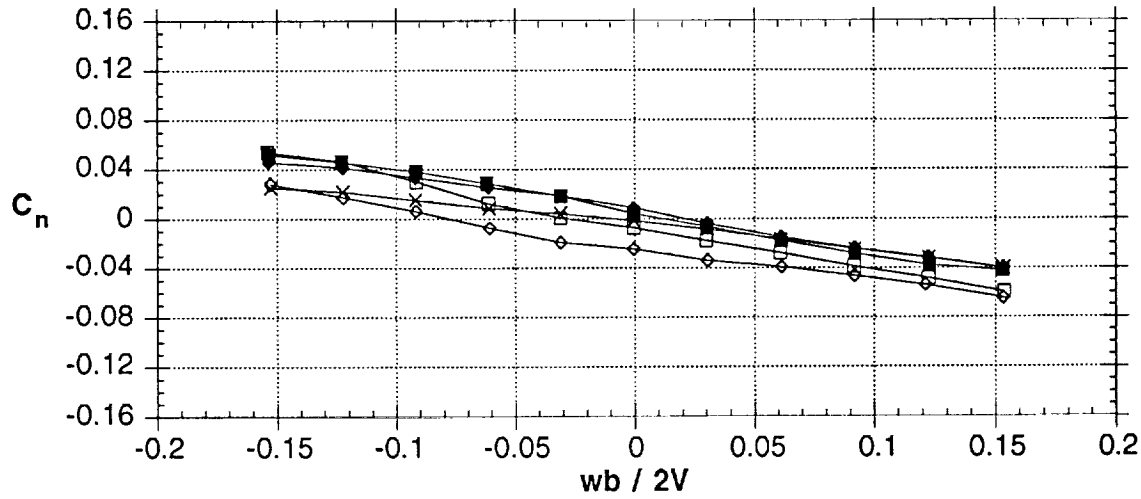

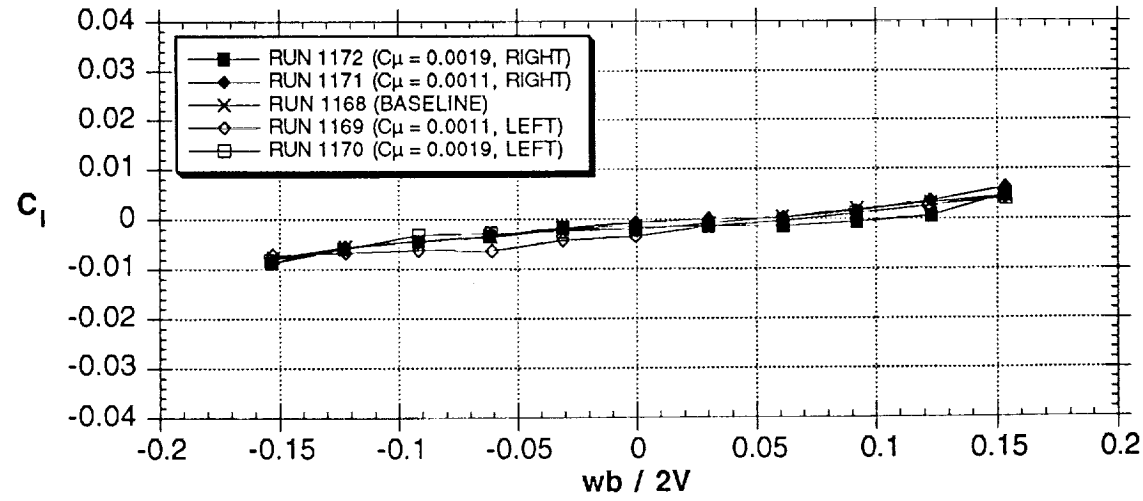

Figure 36 - Concluded

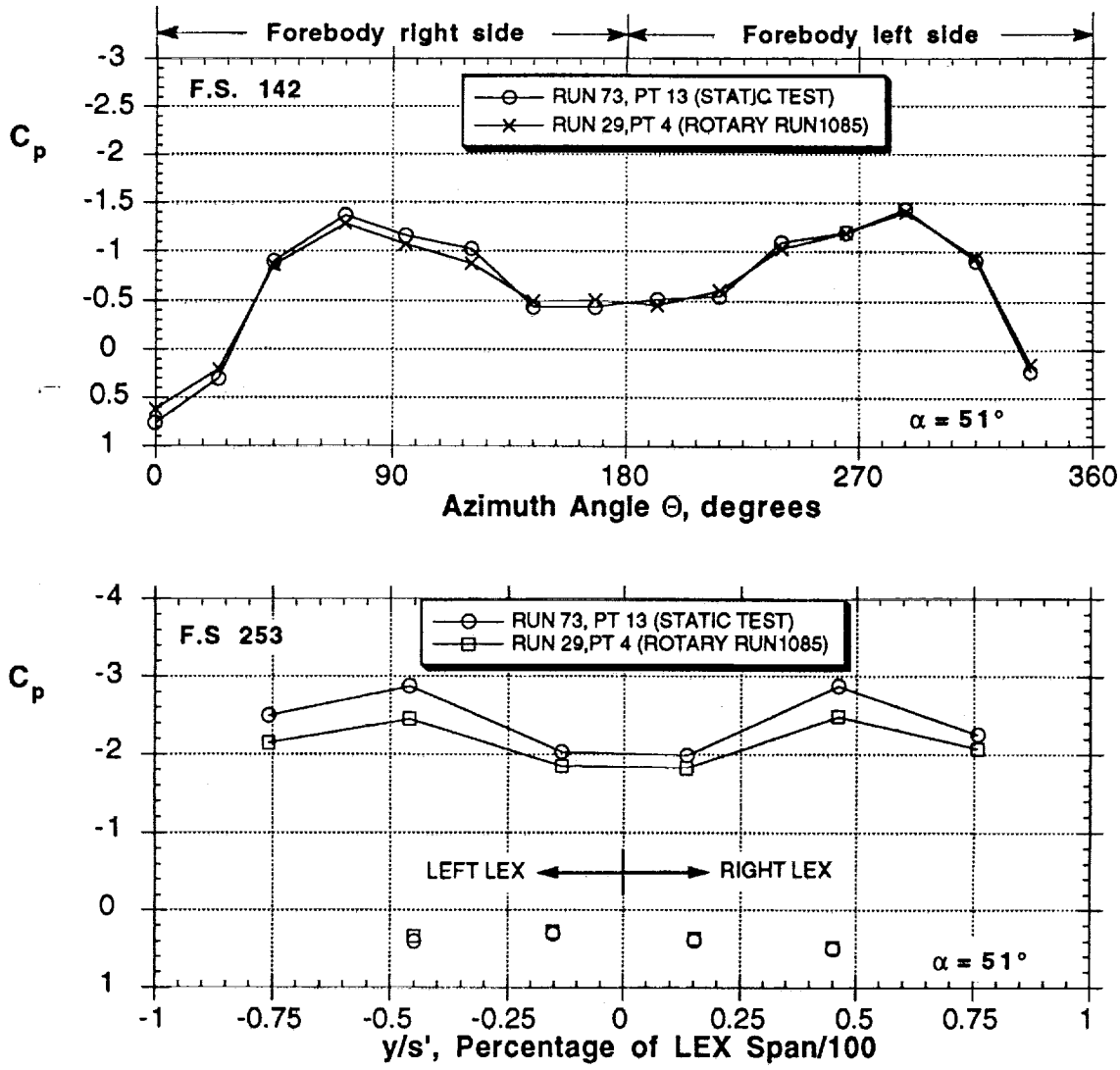

(a) Comparison to static test

Figure 37 - Nose 4-60° jet blowing pressure distribution at 51° AOA

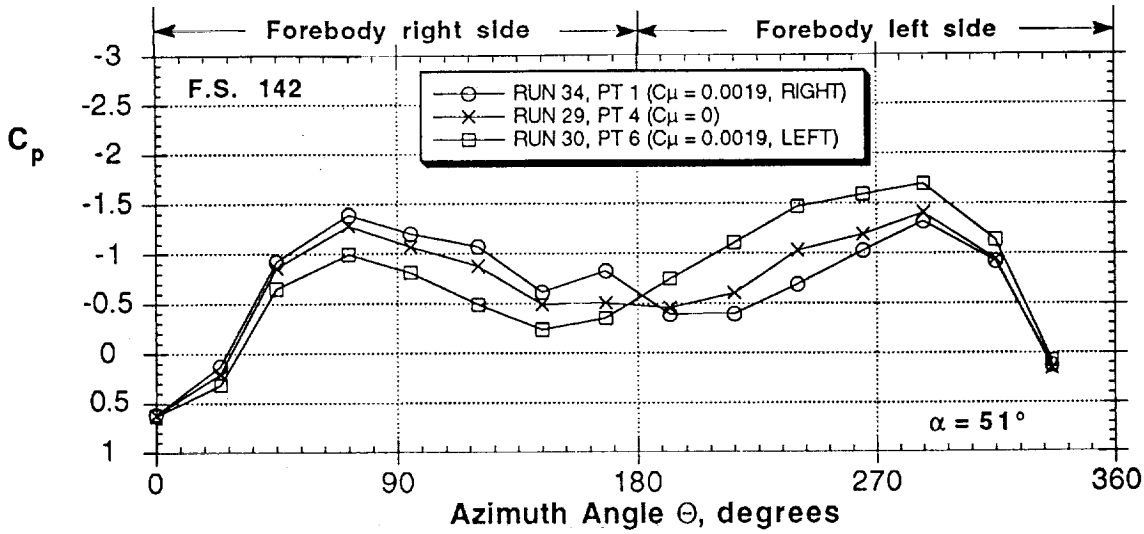

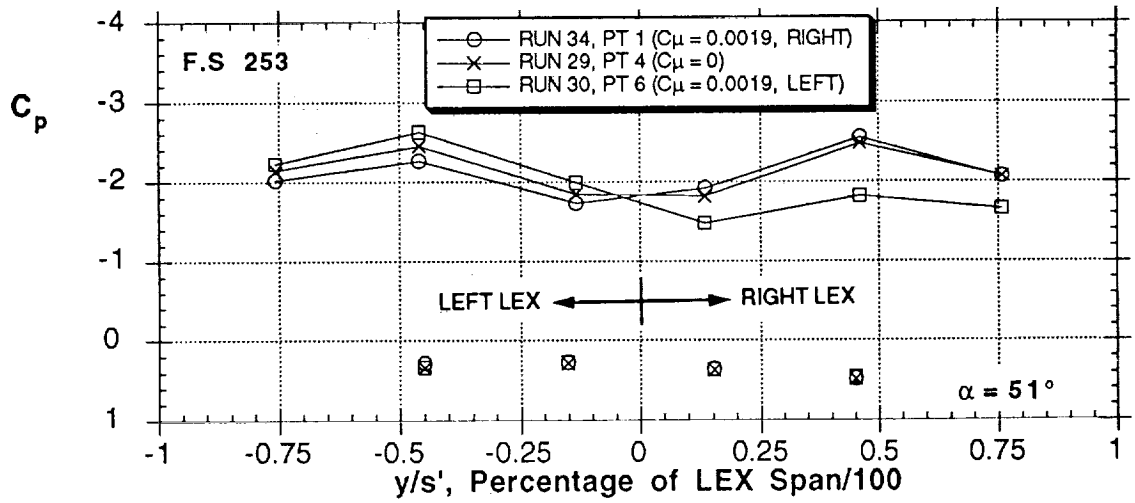

(b) Effect of Cμ, ωb/2V = 0

Figure 37 - Continued

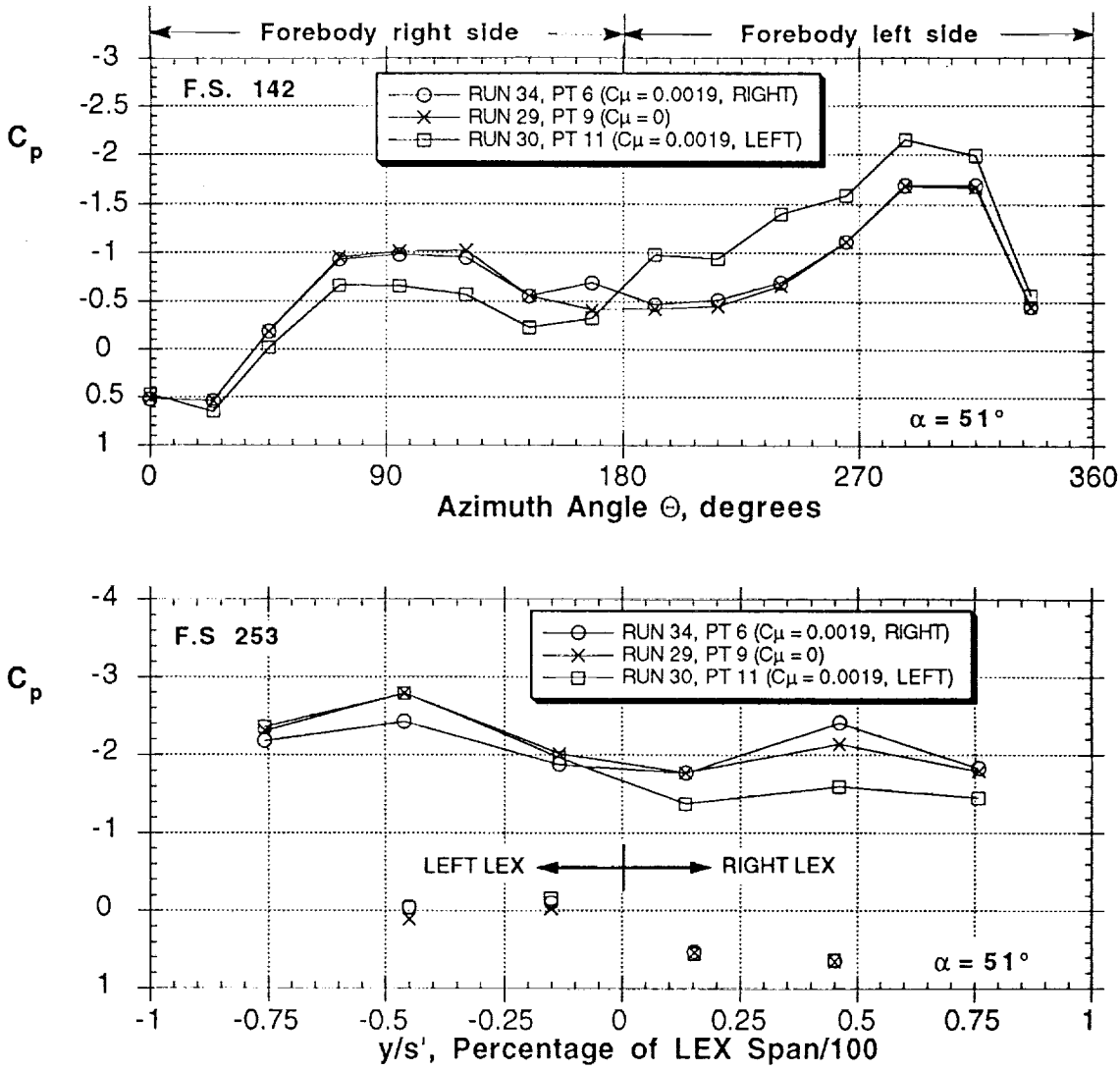

(c) Effect of Cμ, ωb/2V = 0.15

Figure 37 - Continued

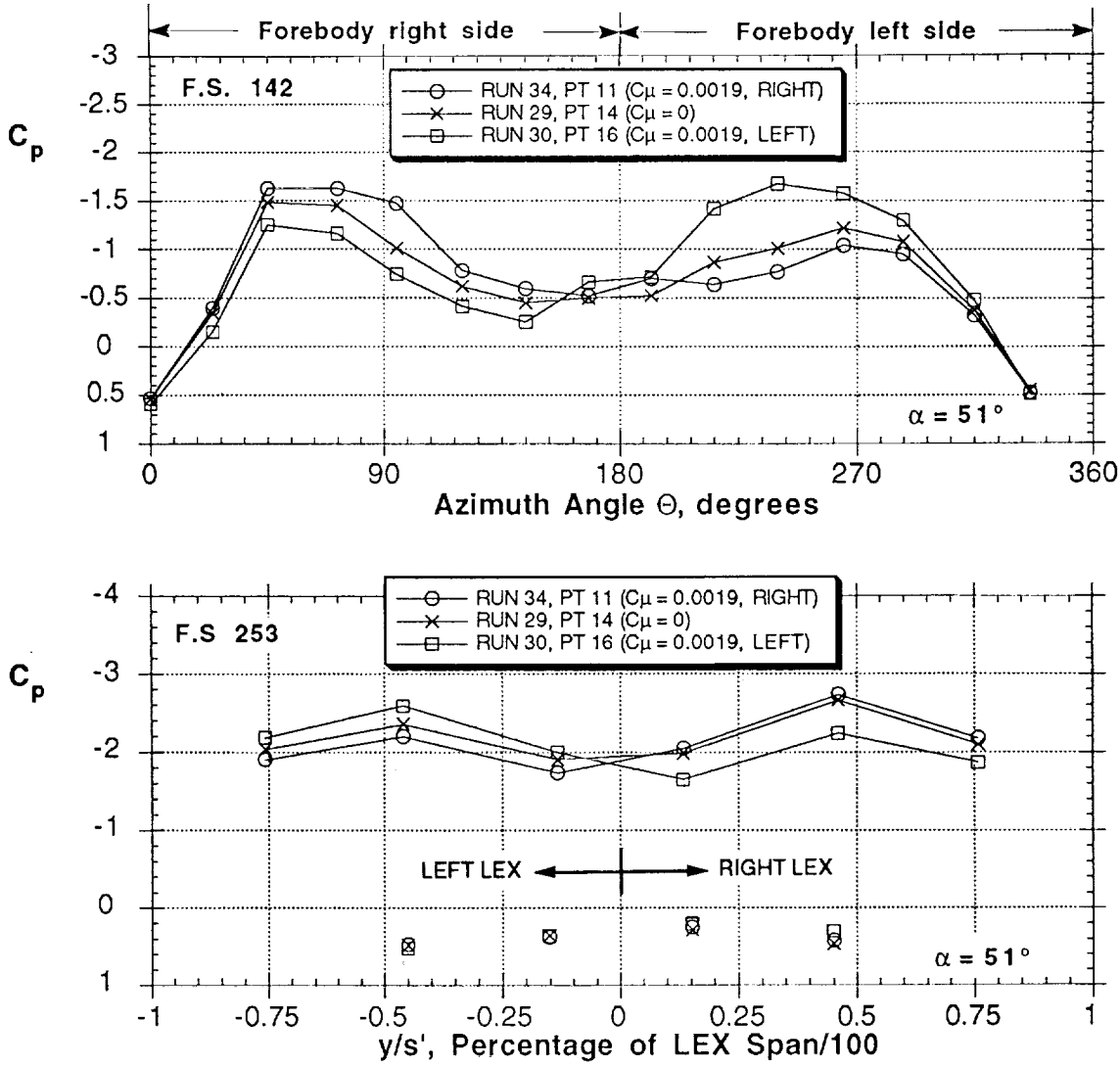

(d) Effect of Cμ, ωb/2V = -0.15

Figure 37 - Continued

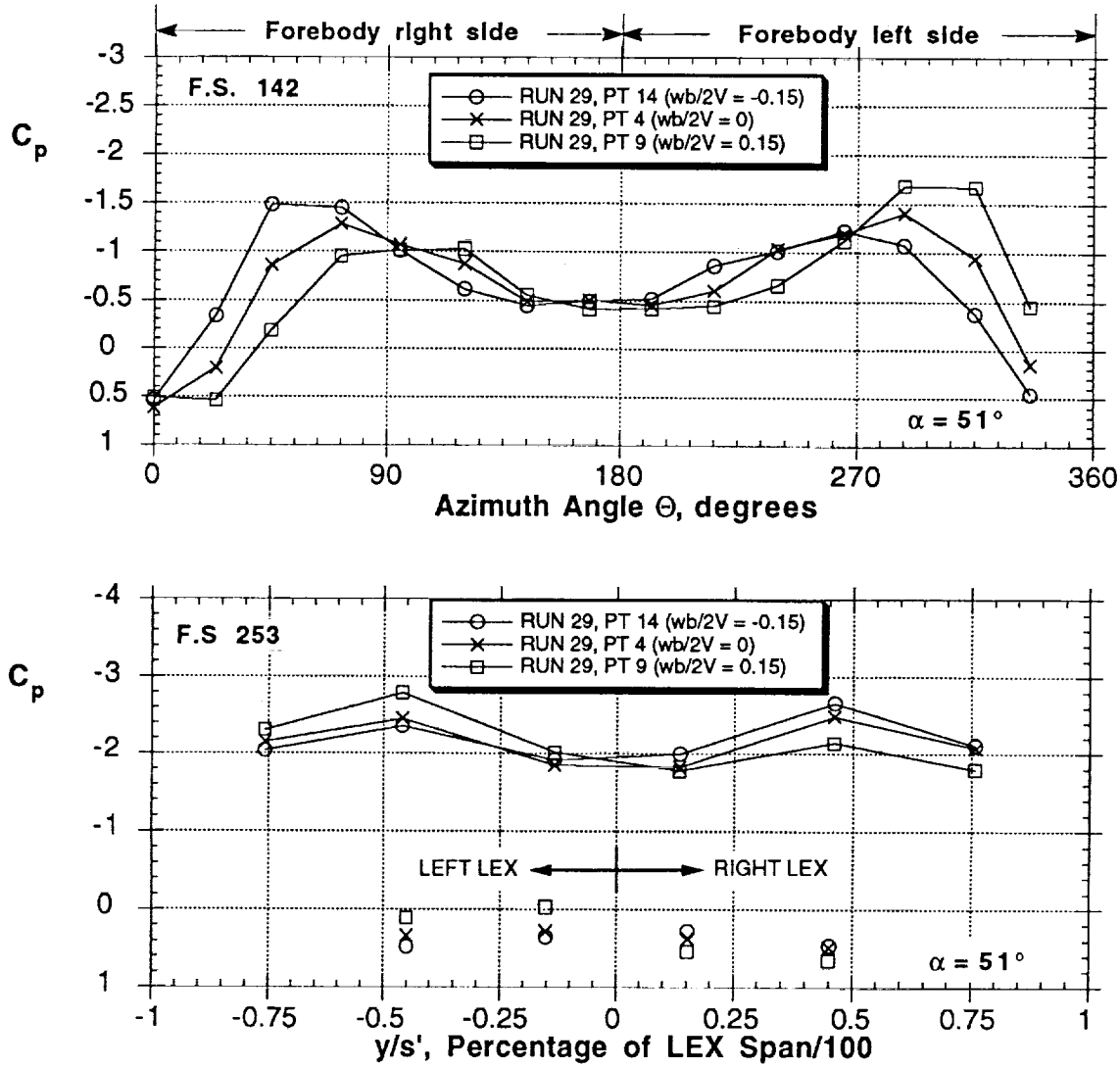

(e) Effect of ωb/2V, Cμ = 0

Figure 37 - Continued

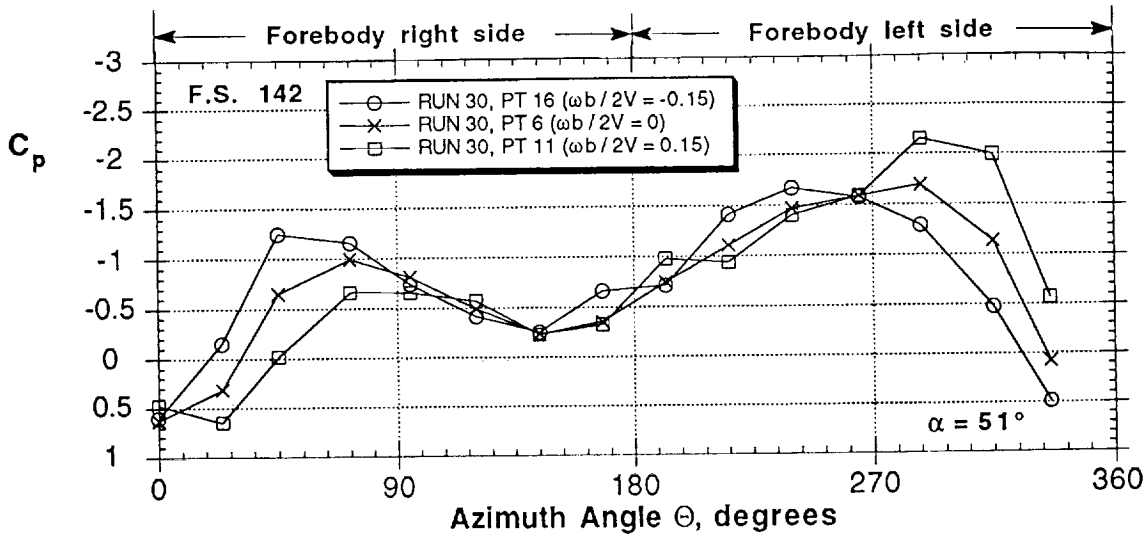

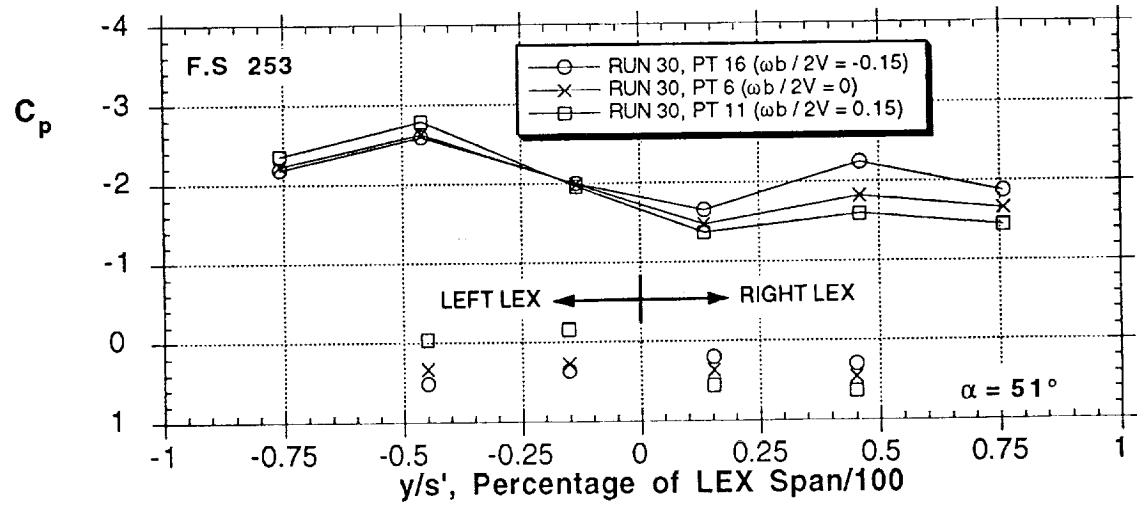

(f) Effect of ωb/2V, Cμ = 0.0019, left

Figure 37 - Continued

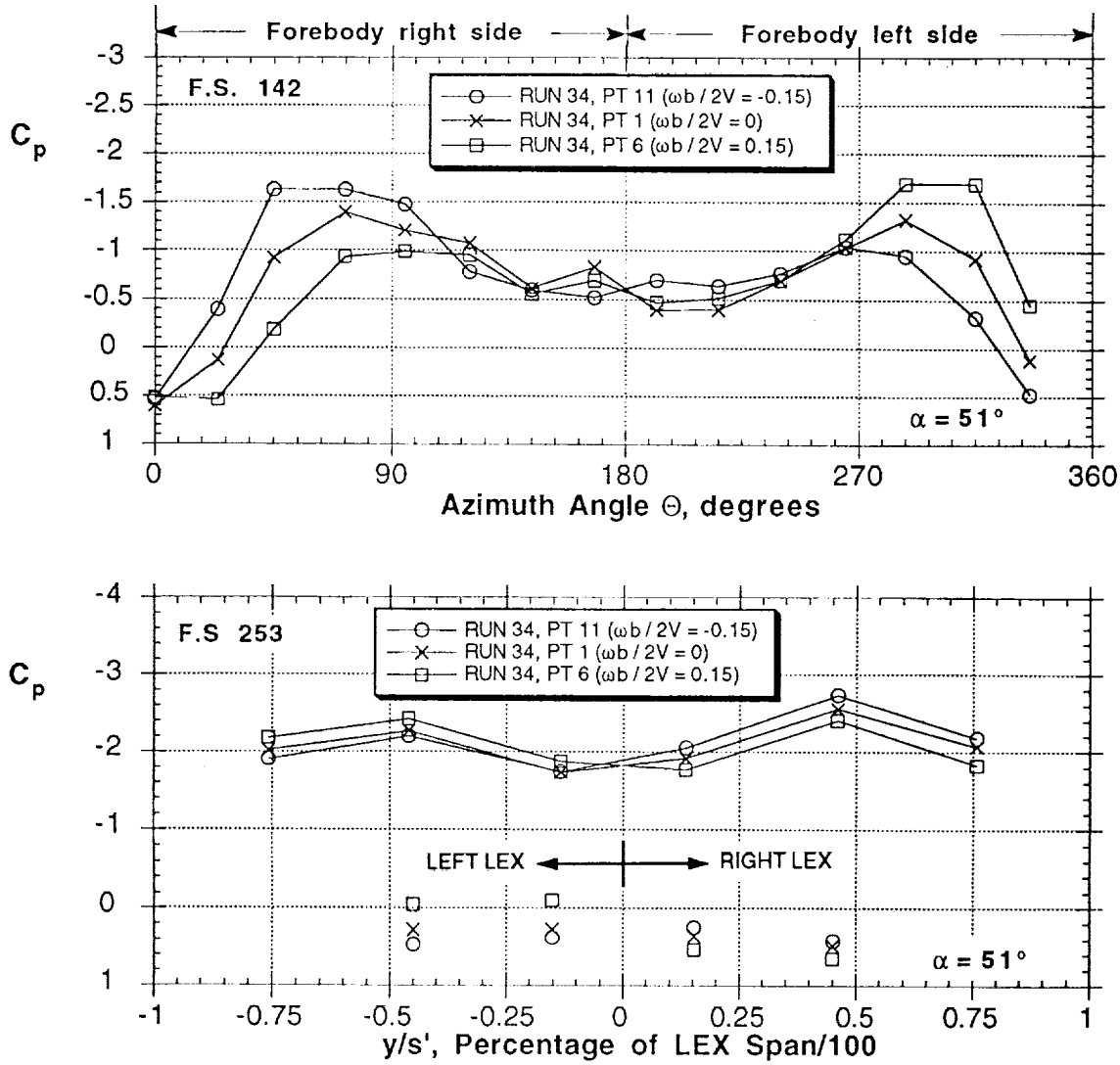

(g) Effect of ωb/2V, Cμ = 0.0019, right

Figure 37 - Concluded

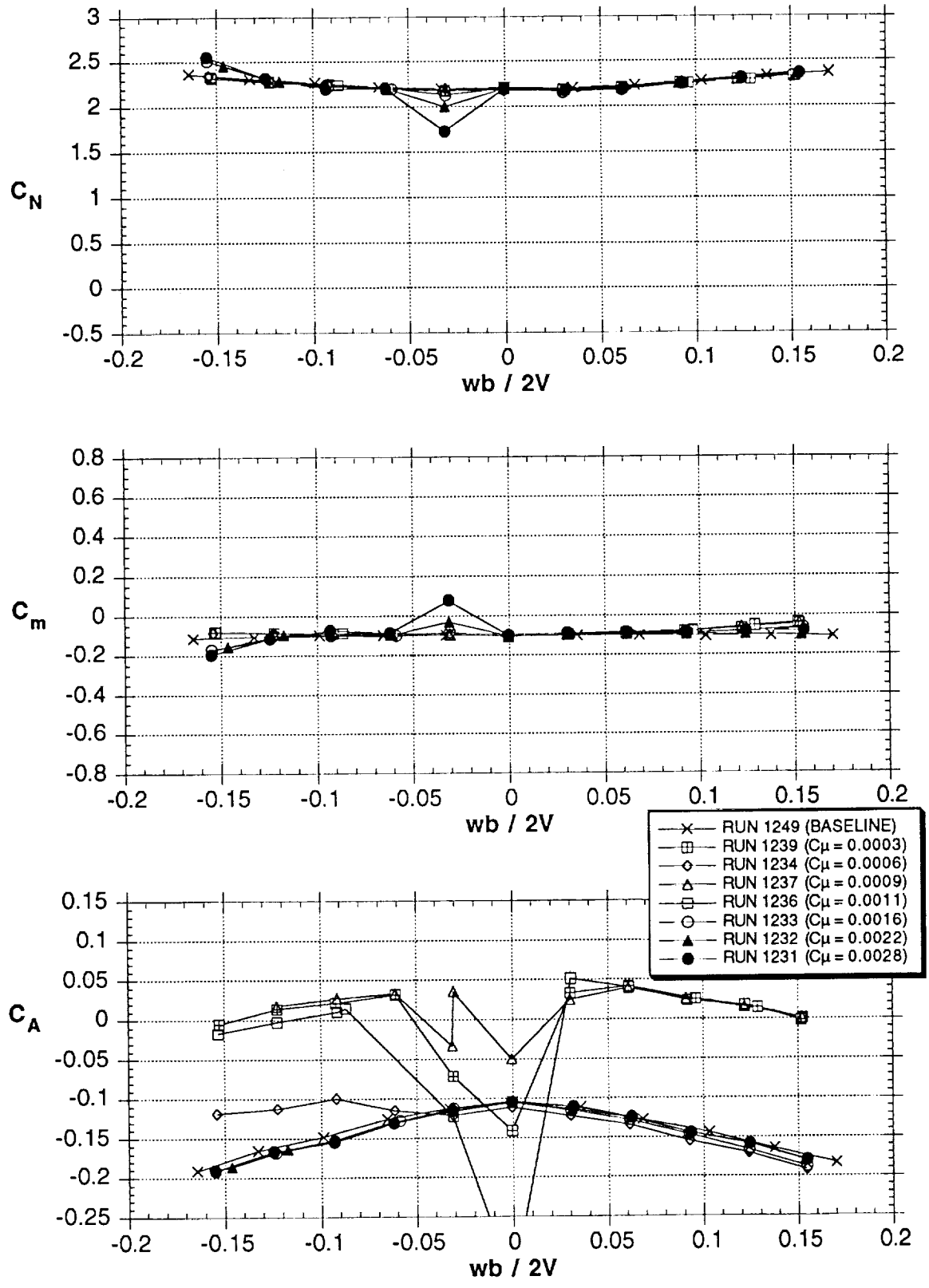

(a) left side slot

Figure 38 - Effects of SLOT AB blowing slot at 45° AOA

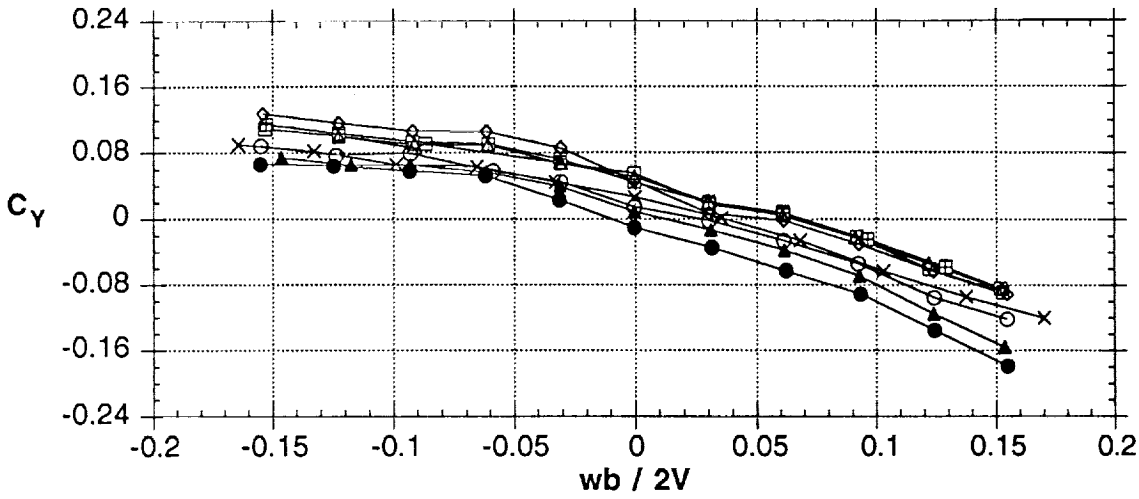

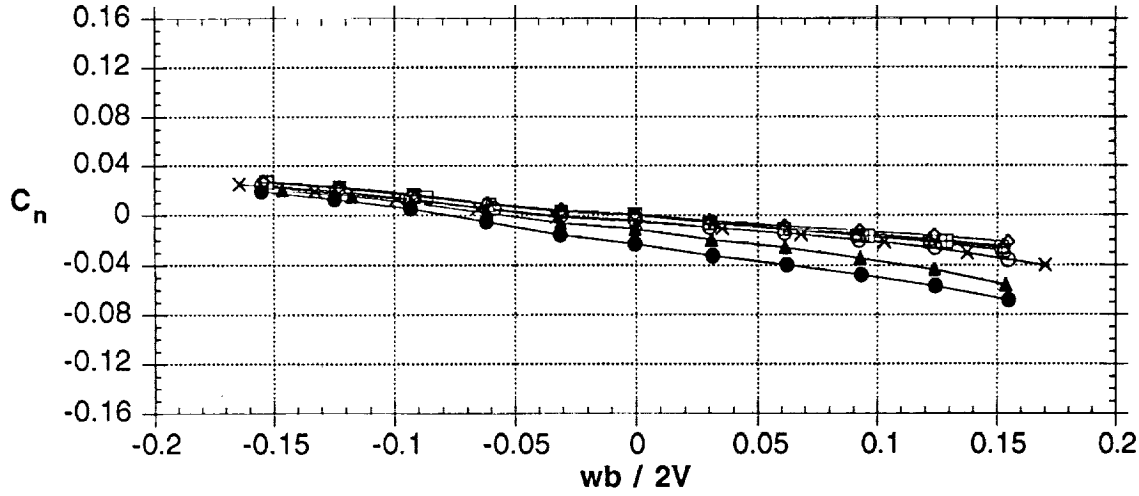

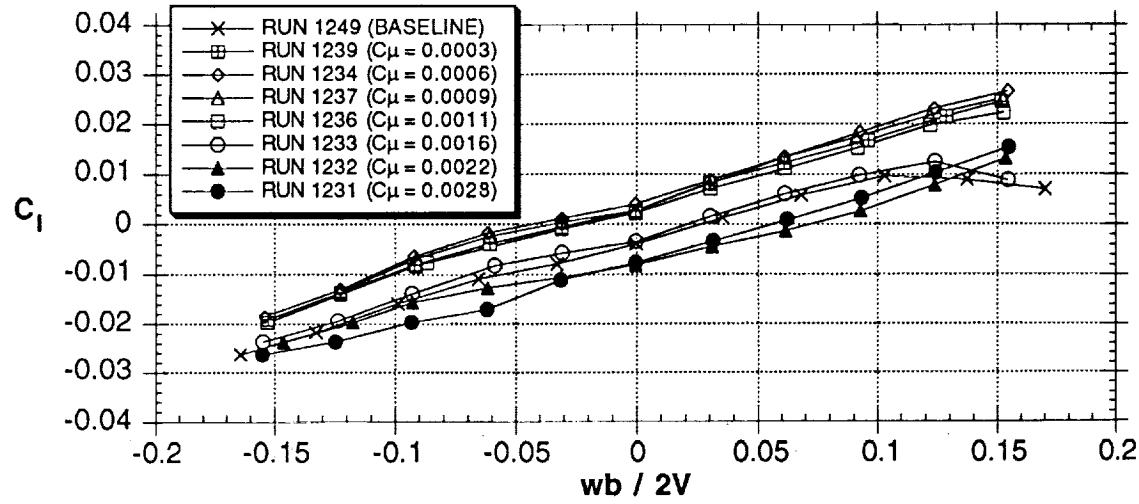

(a) left side slot

Figure 38 - Continued

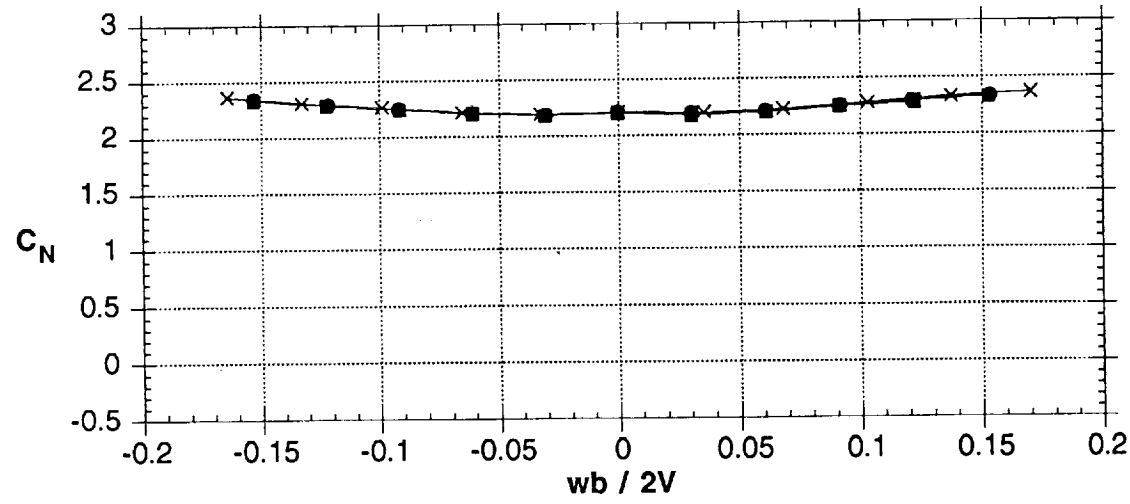

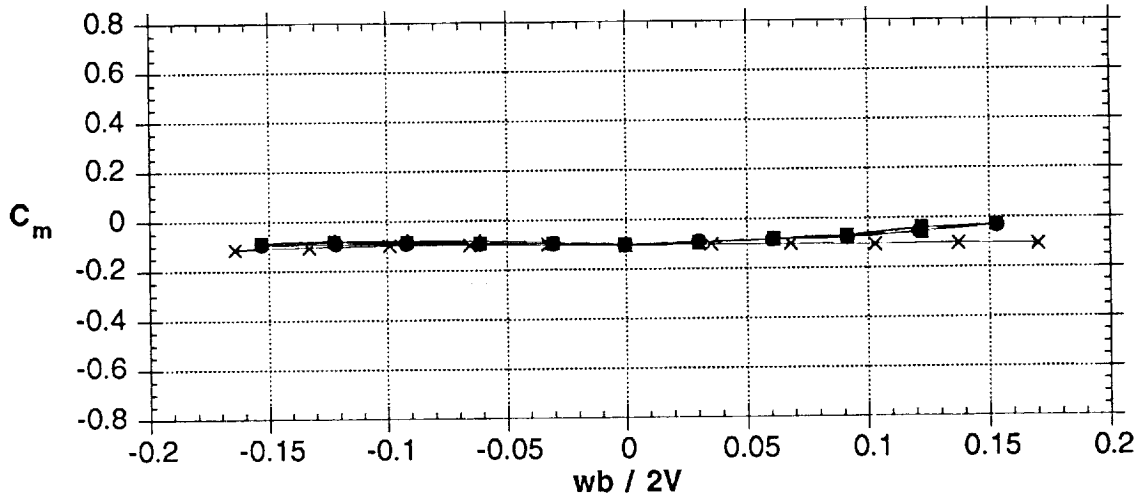

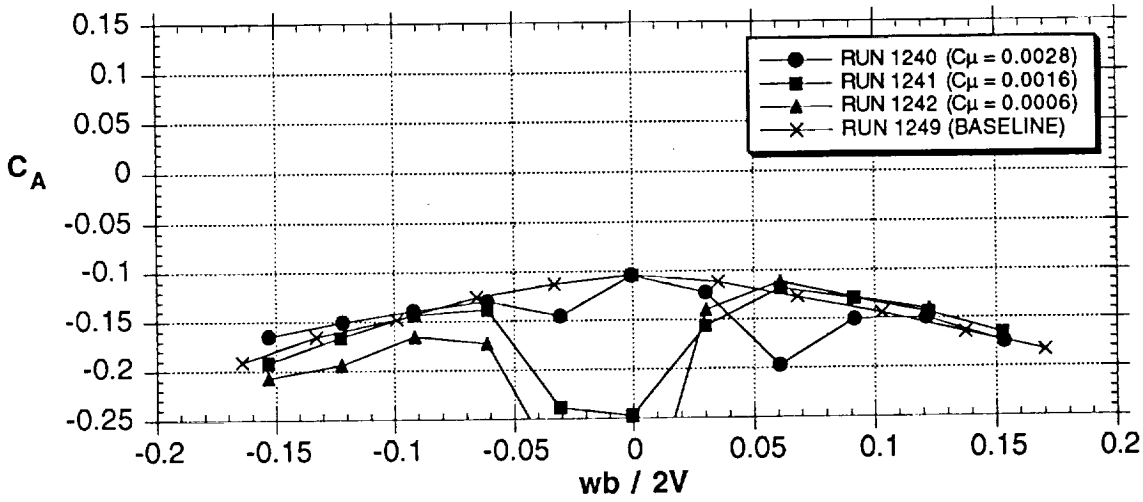

(b) right side slot

Figure 38 - Continued

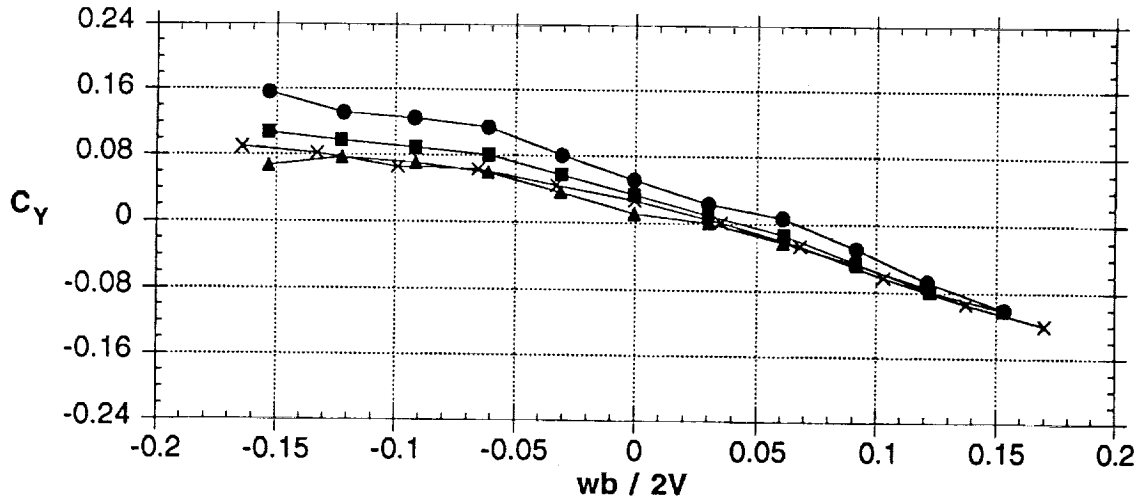

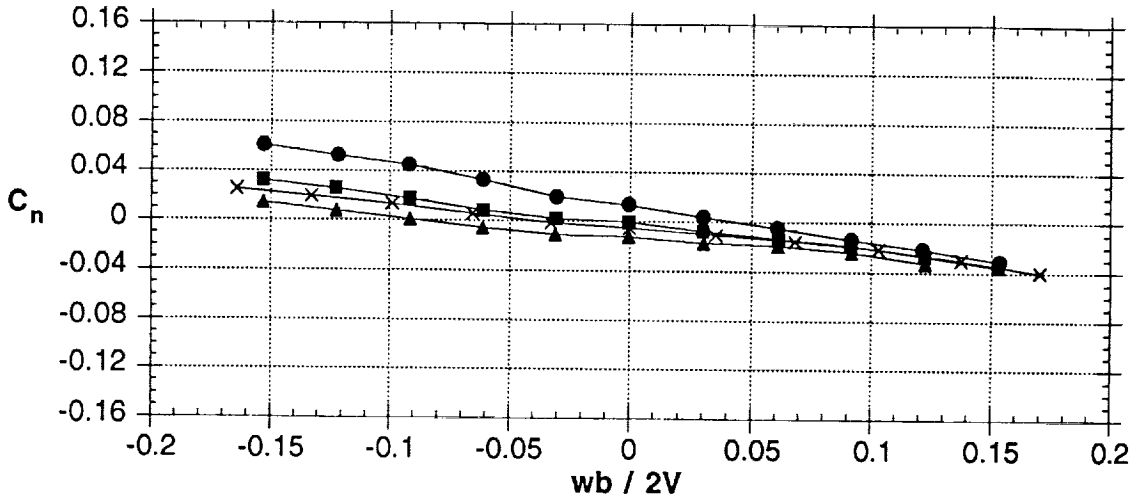

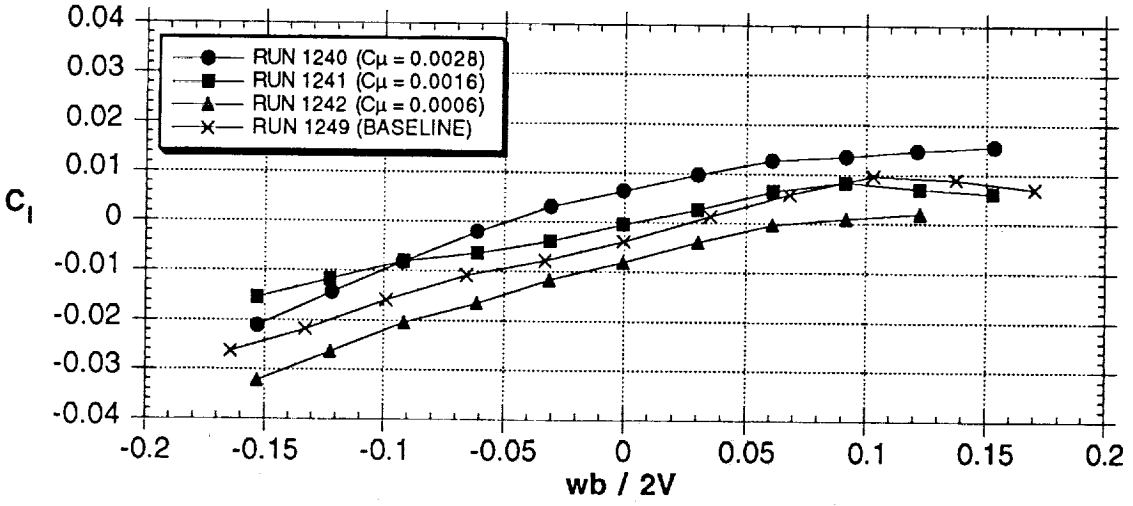

(b) right side slot

Figure 38 - Concluded

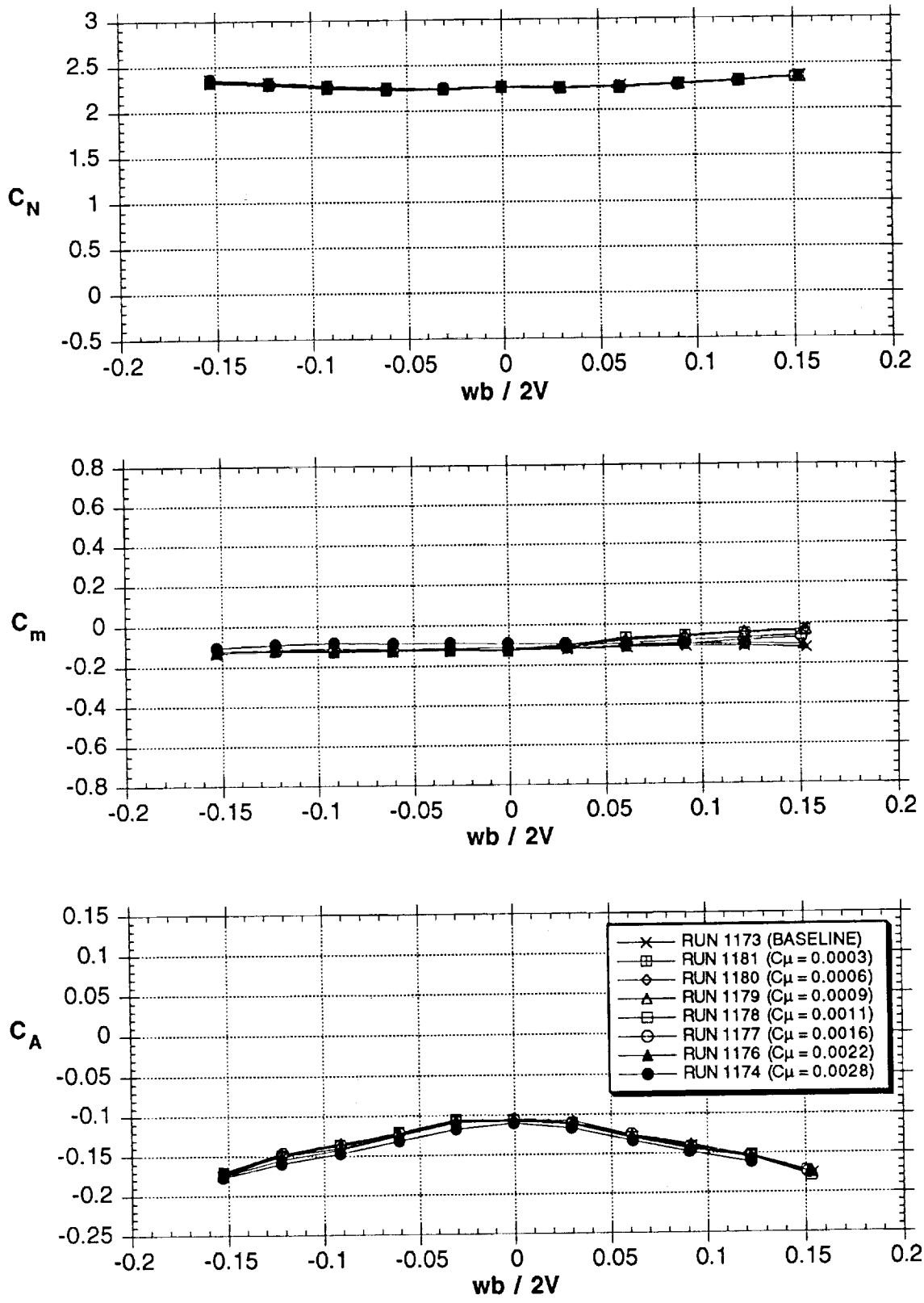

(a) left side slot

Figure 39 - Effects of SLOT AB blowing slot at 51° AOA

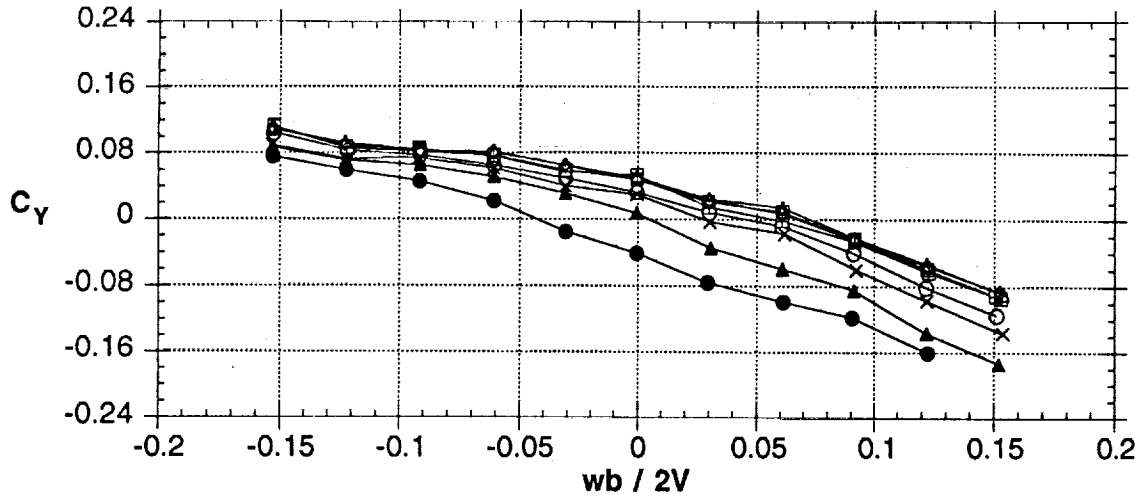

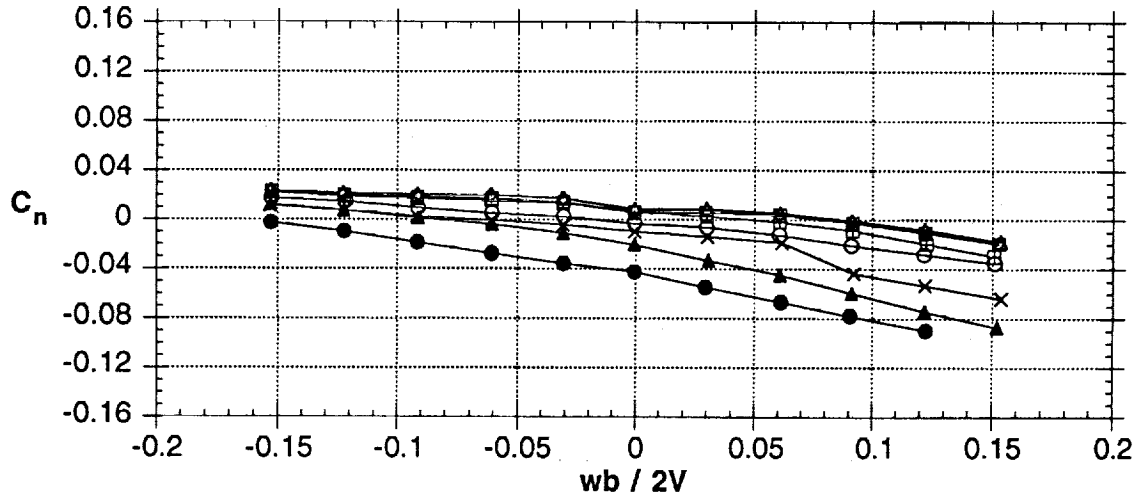

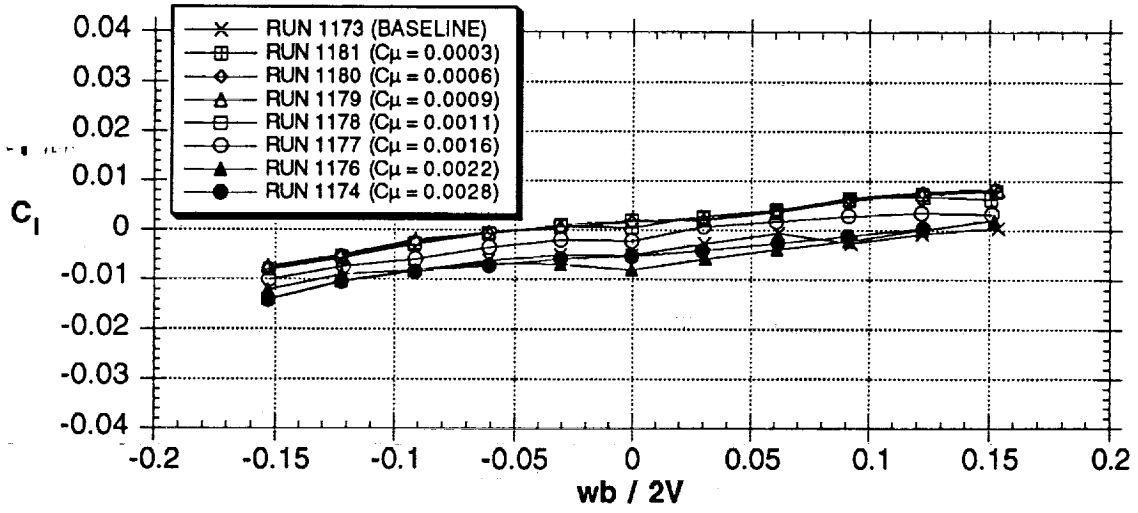

(a) left side slot

Figure 39 - Continued

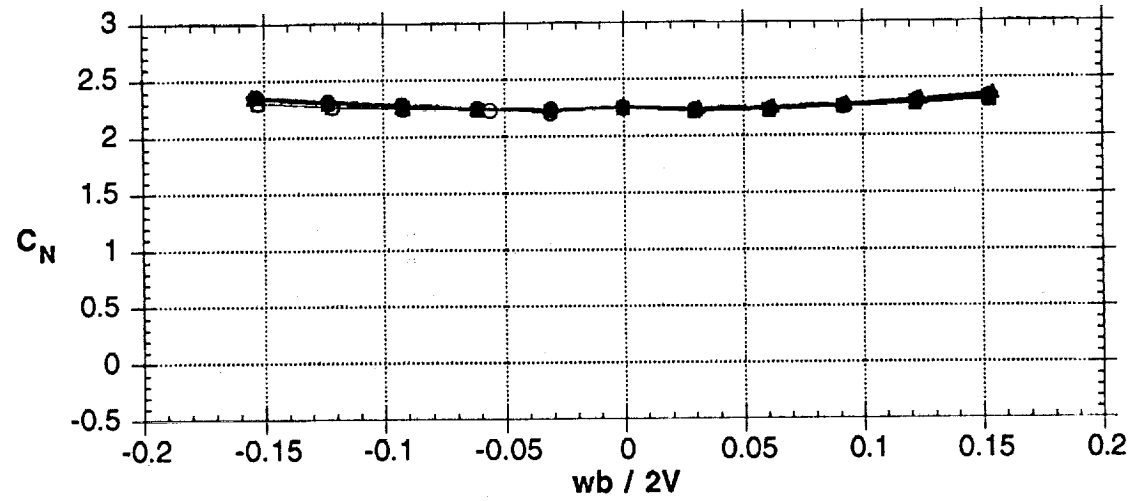

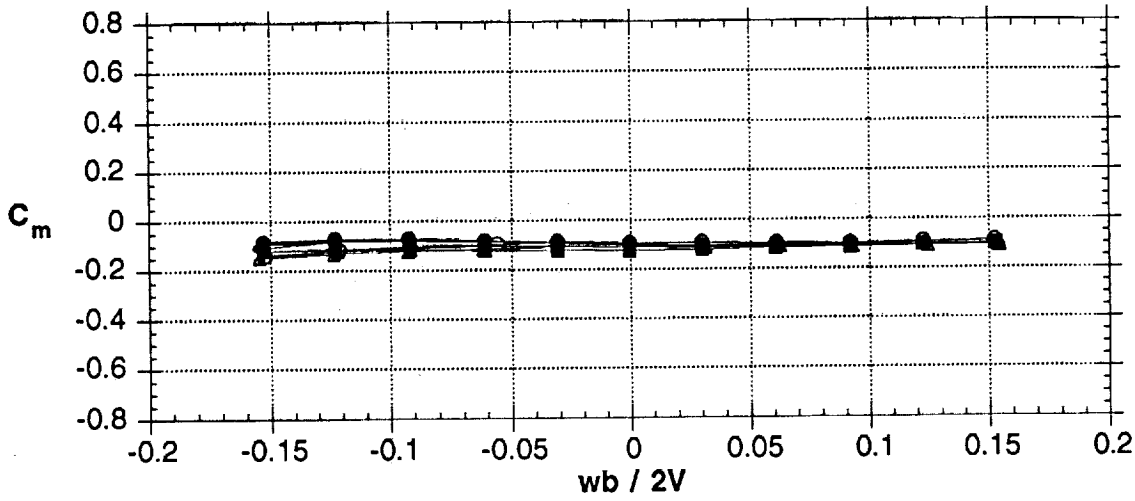

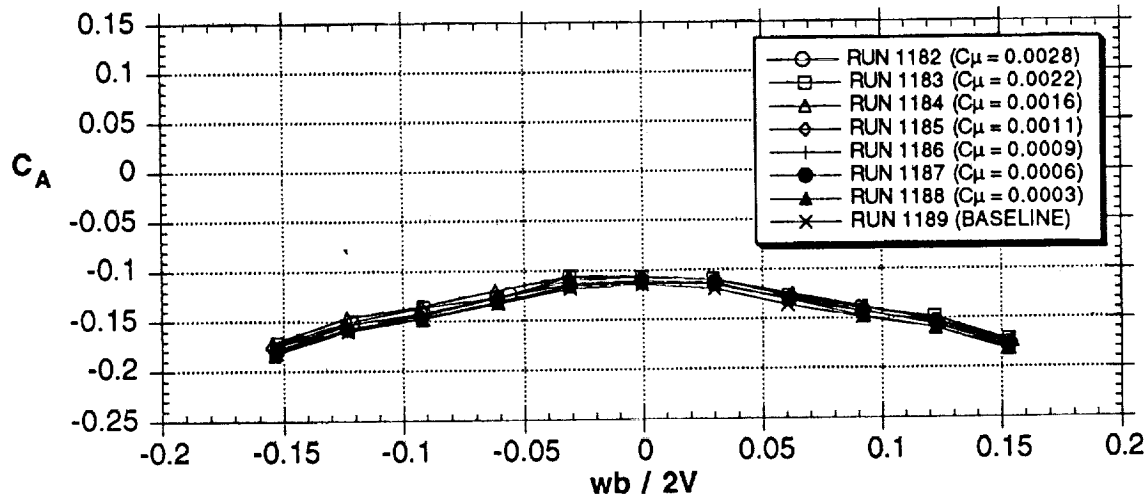

(b) right side slot

Figure 39 - Continued

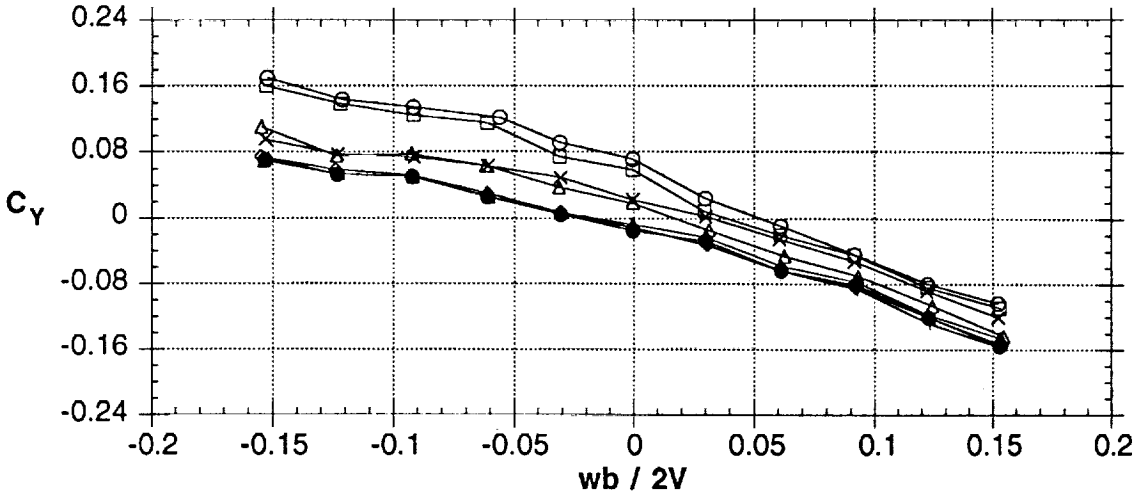

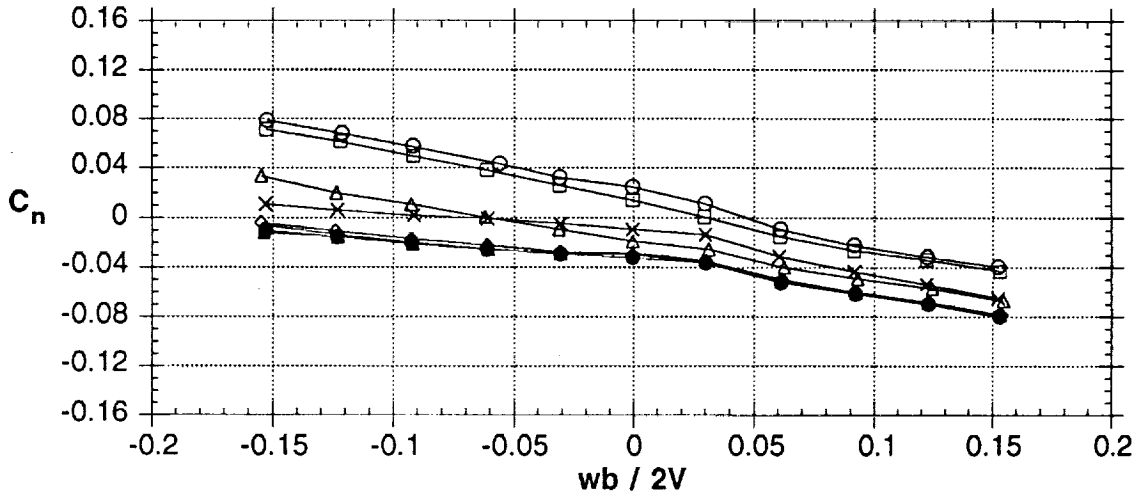

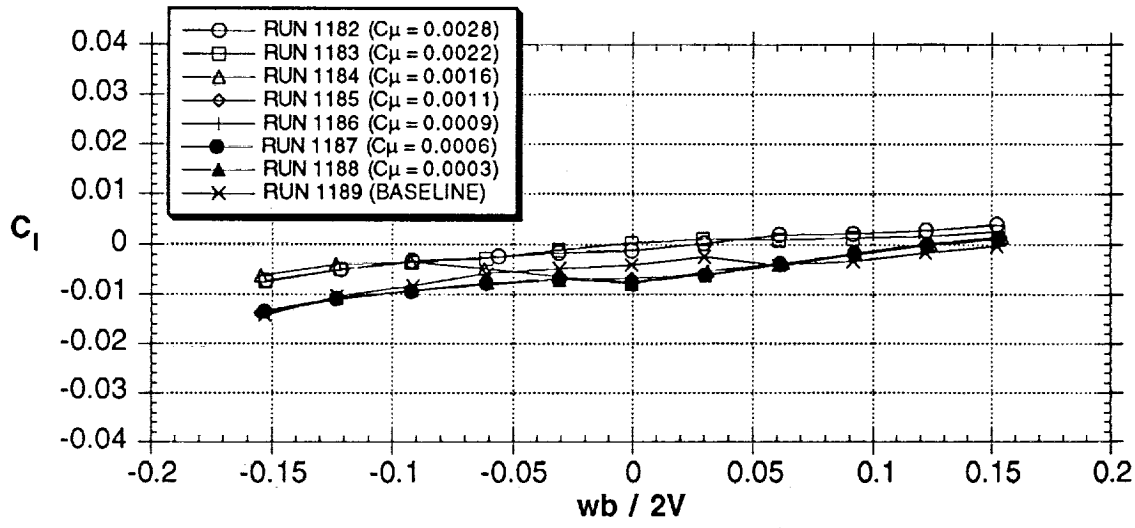

(b) right side slot

Figure 39 - Concluded

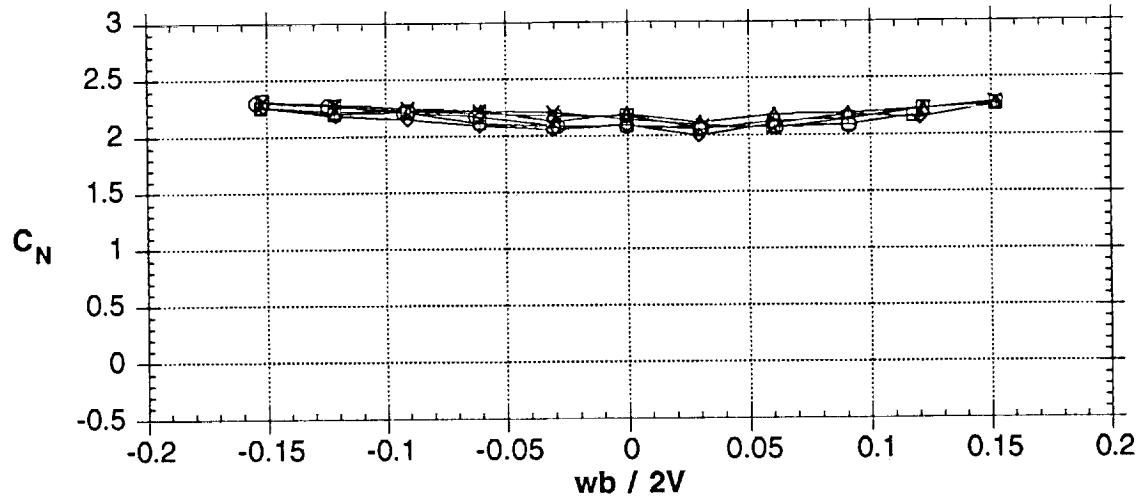

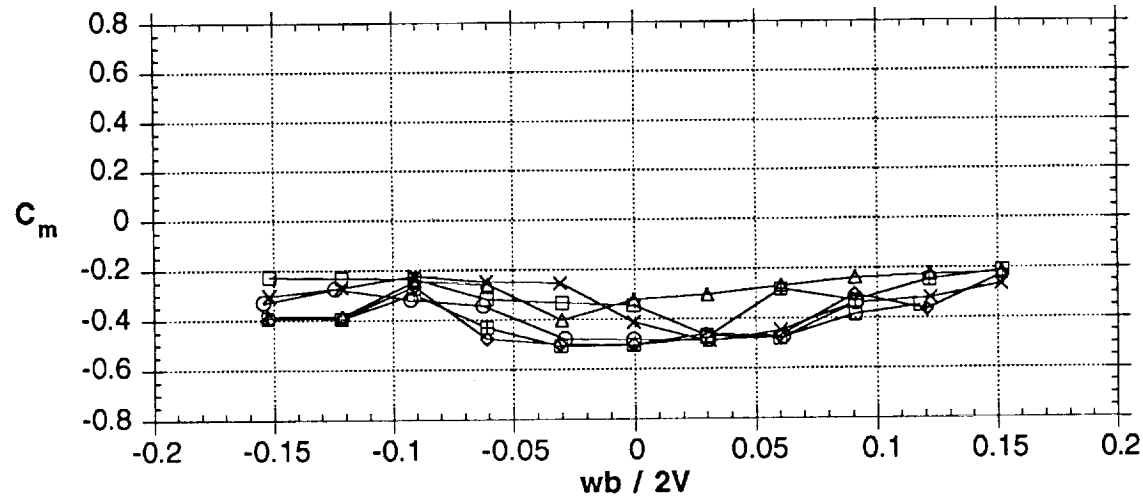

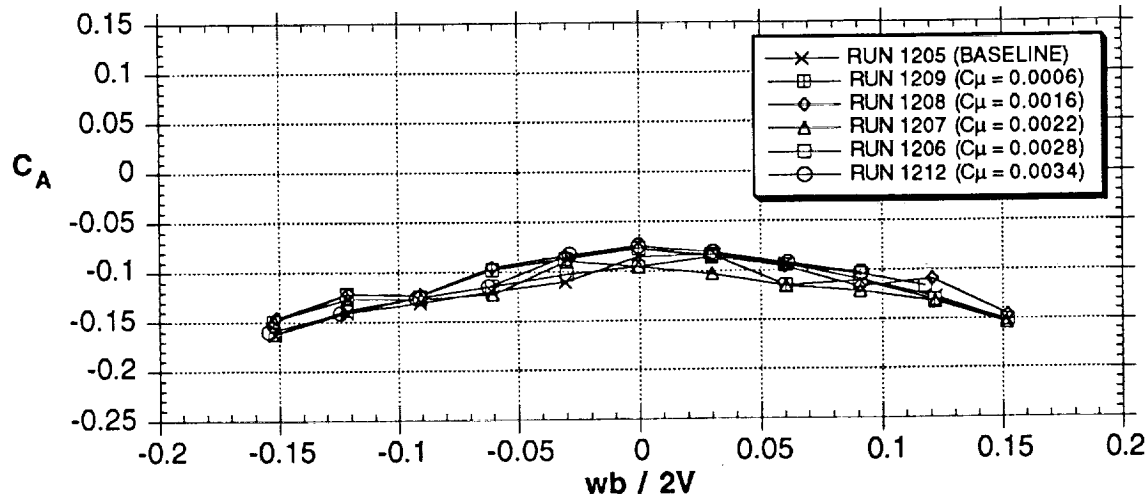

(a) left side slot

Figure 40 - Effects of SLOT AB blowing slot at 60° AOA

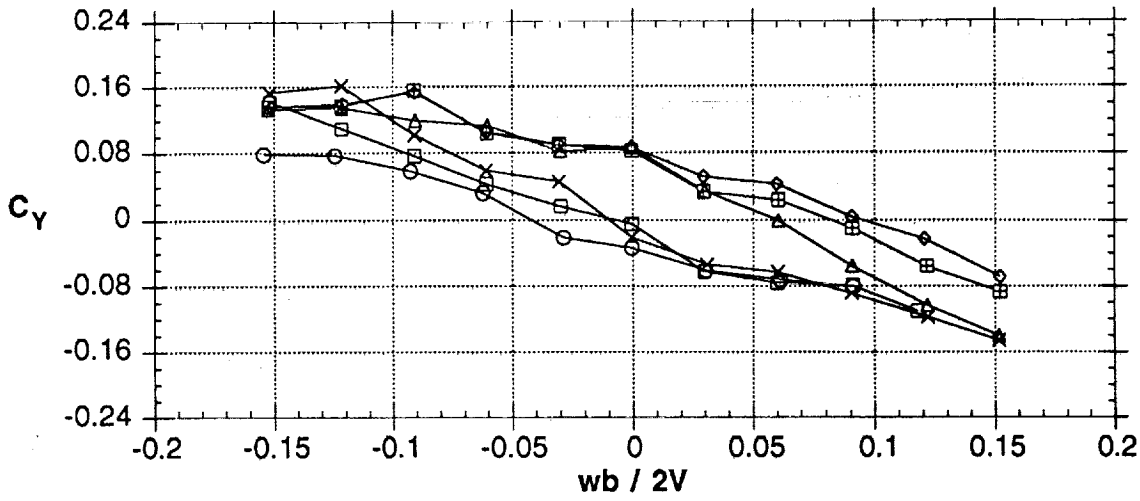

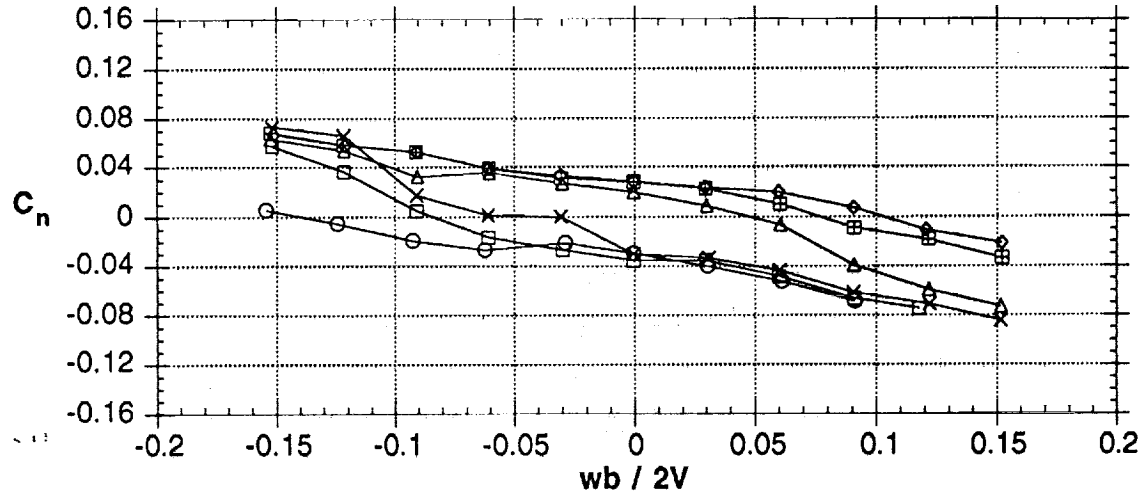

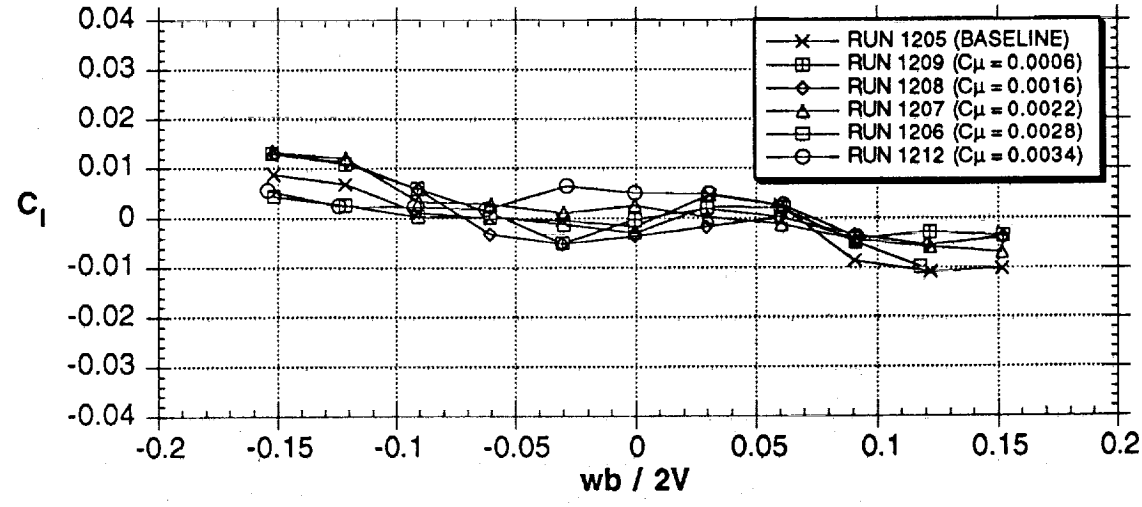

(a) left side slot

Figure 40 - Continued

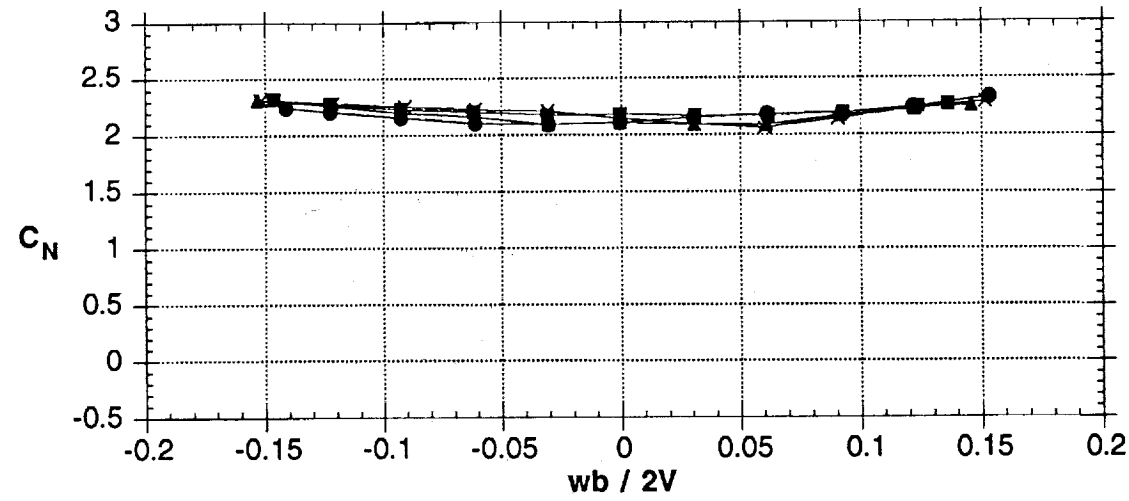

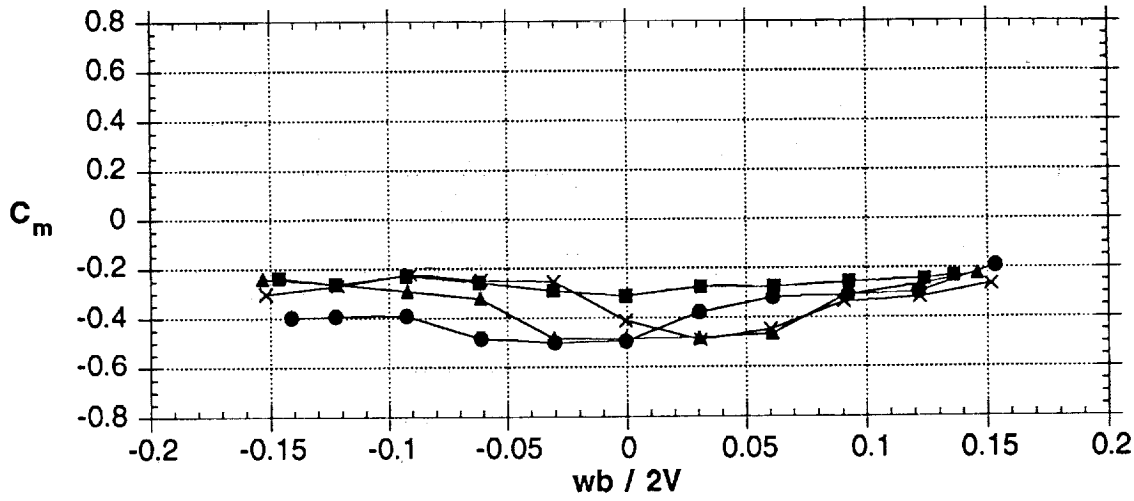

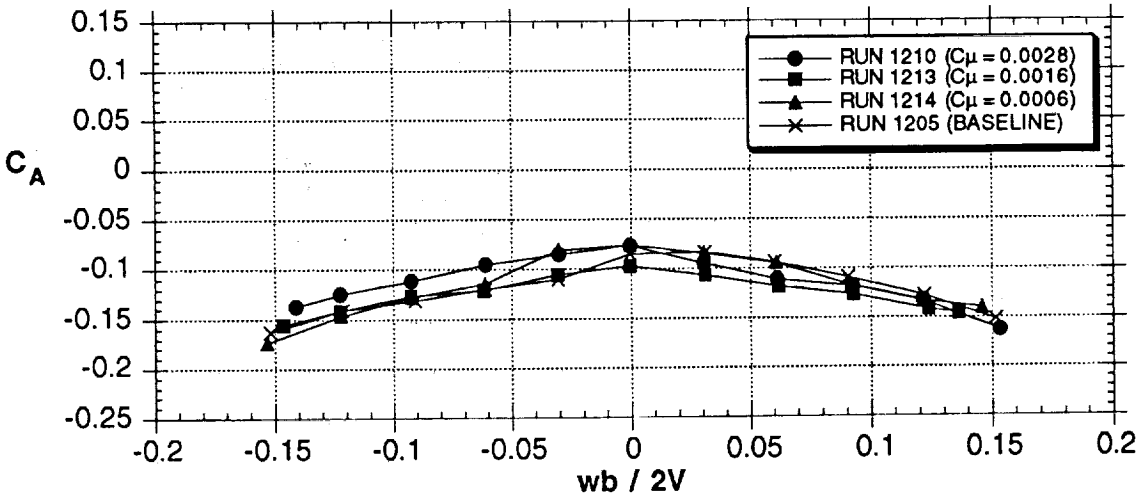

(b) right side slot

Figure 40 - Continued

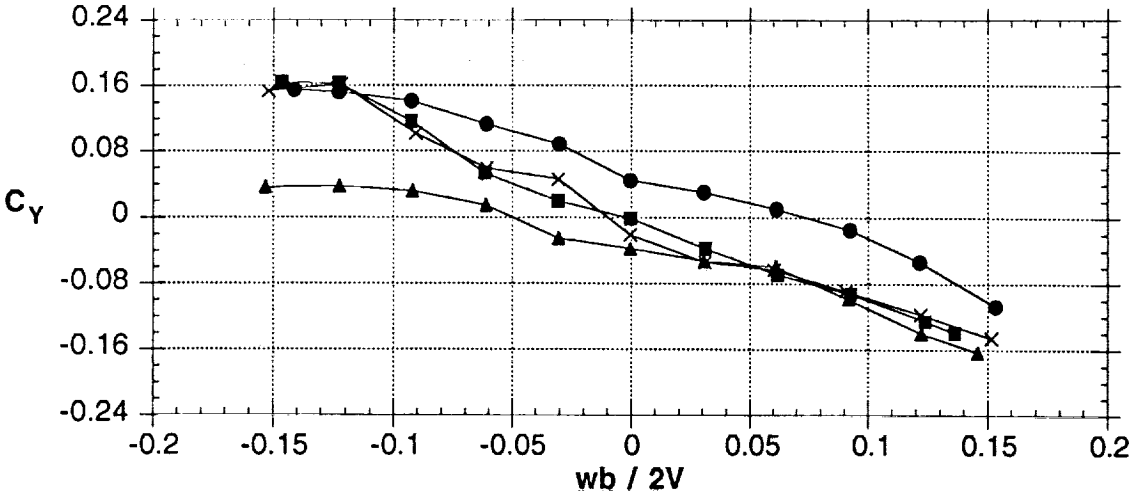

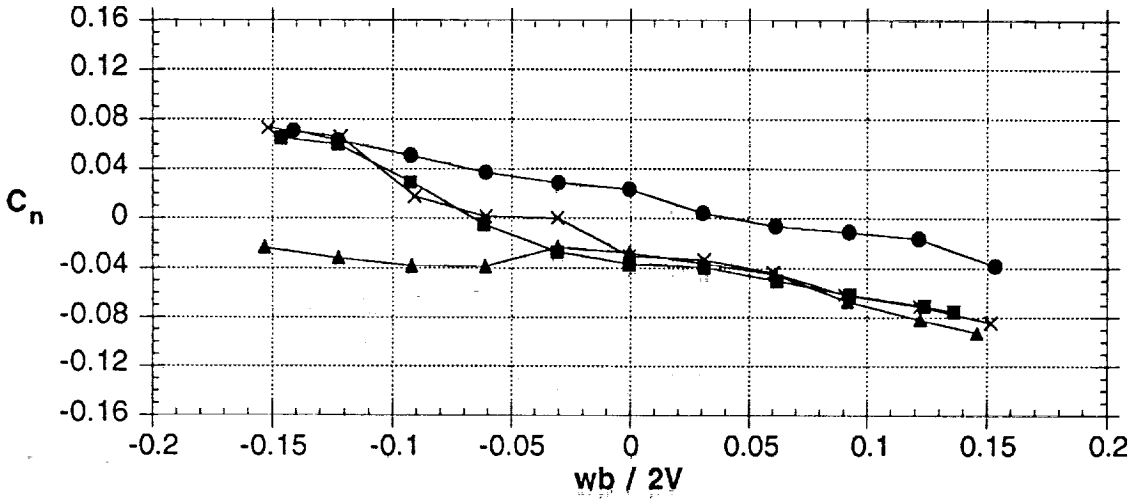

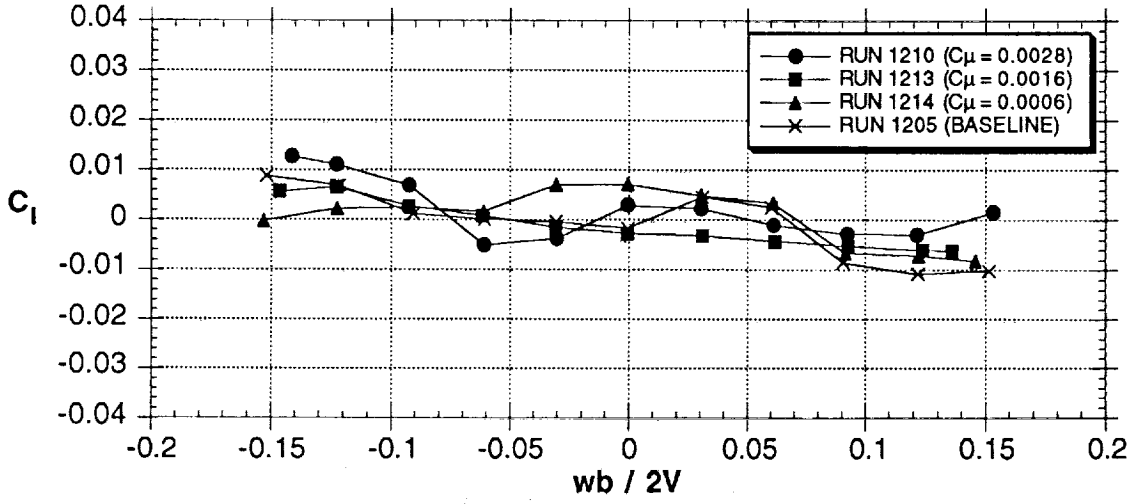

(b) right side slot

Figure 40 - Concluded

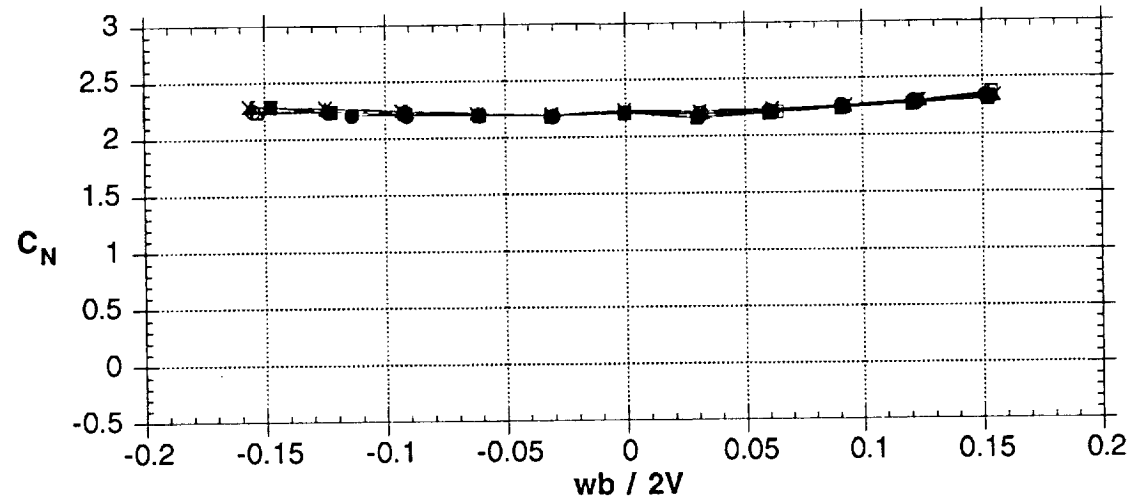

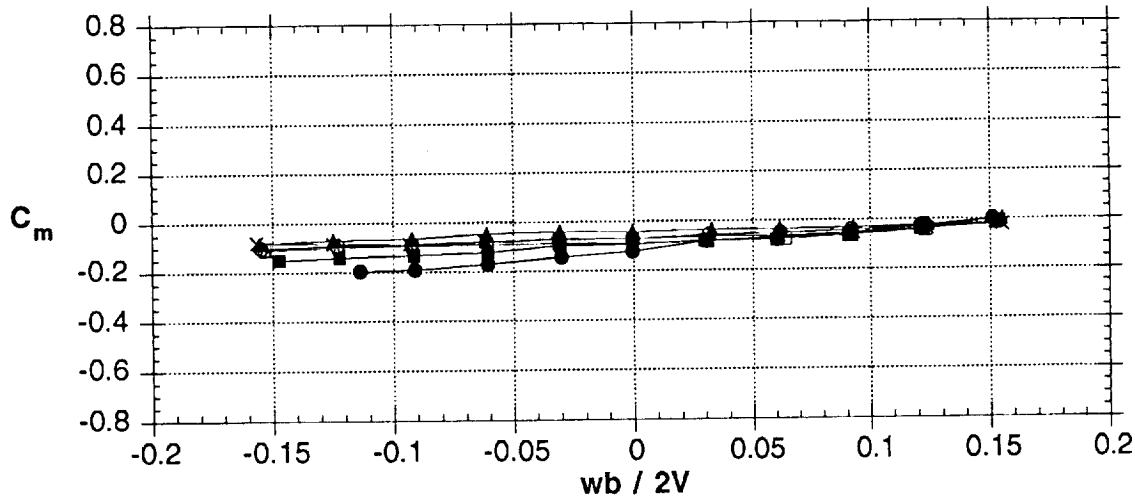

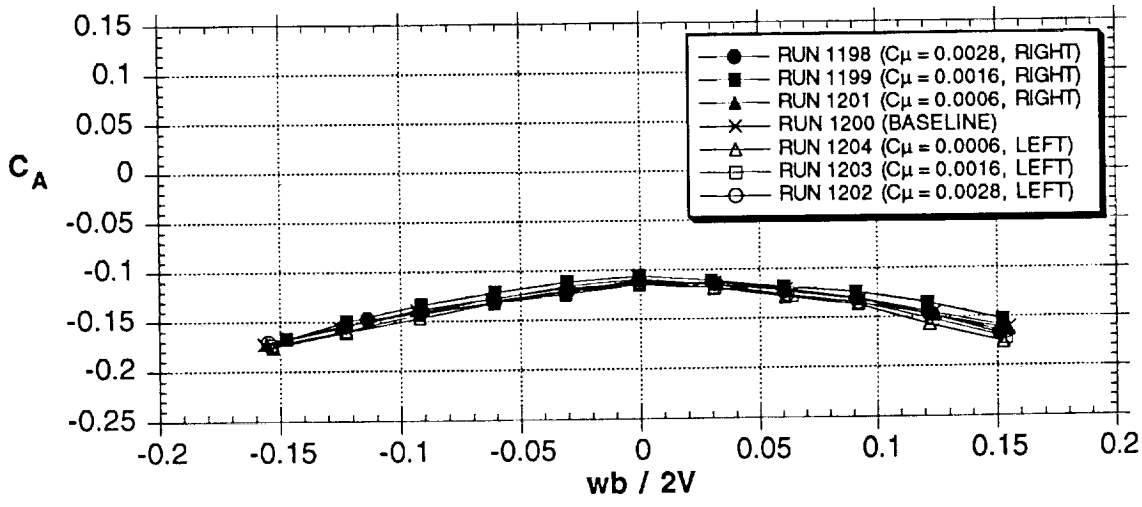

Figure 41 - Effects of SLOT AB blowing slot with sideslip angle of β = -10° at 51° AOA

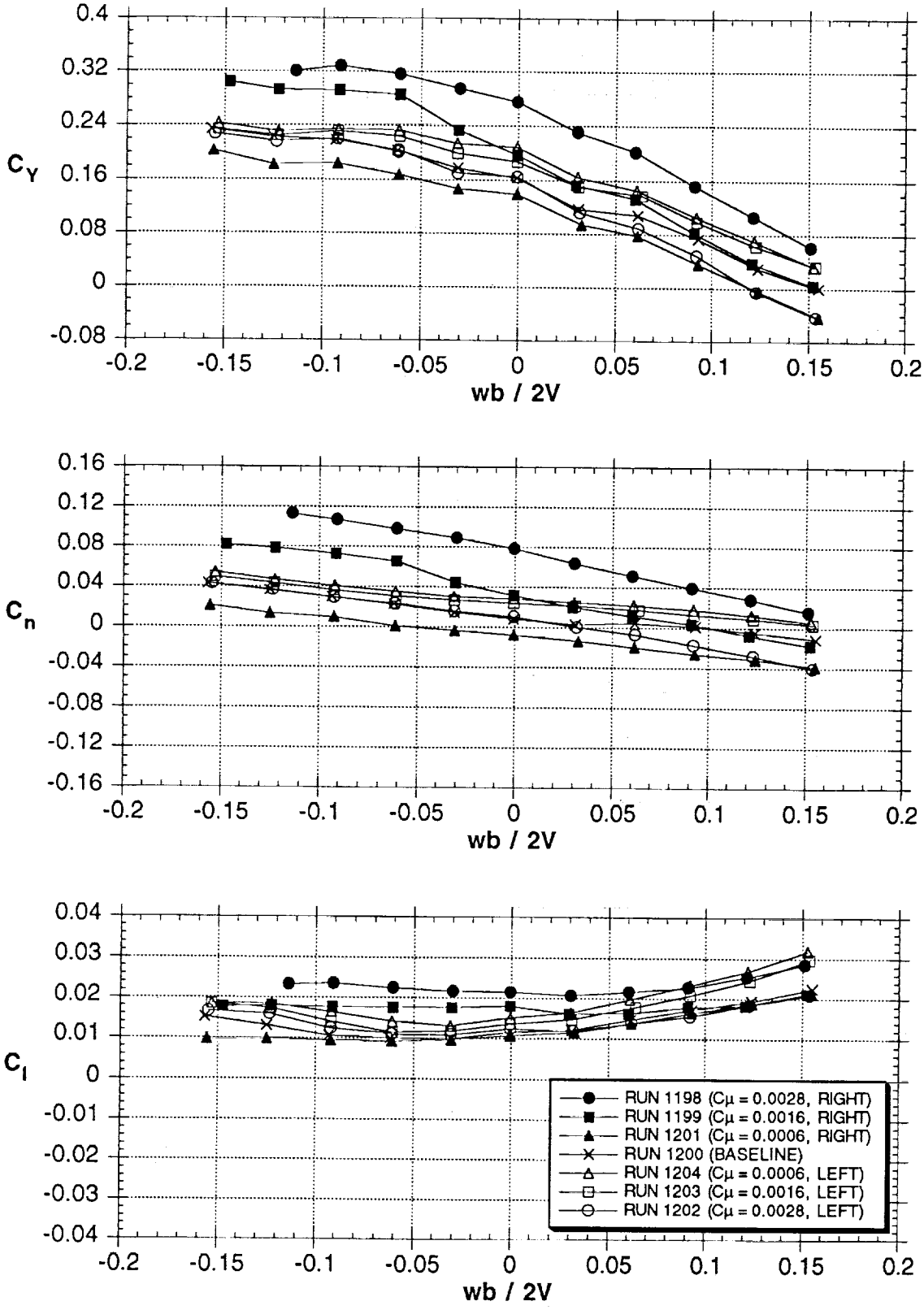

Figure 41 - Concluded

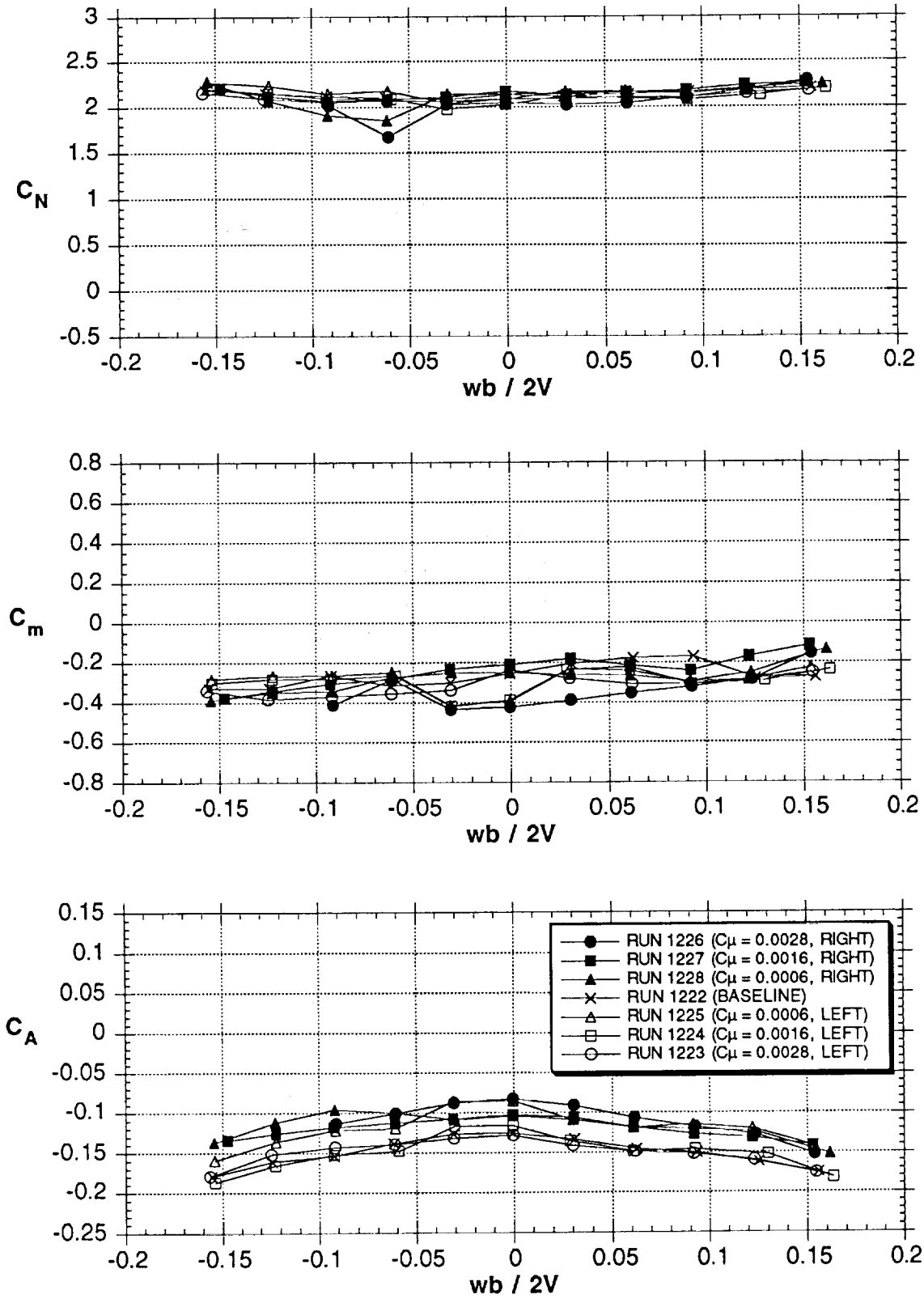

Figure 42 - Effects of SLOT AB blowing slot with sideslip angle of β = -10° at 60° AOA

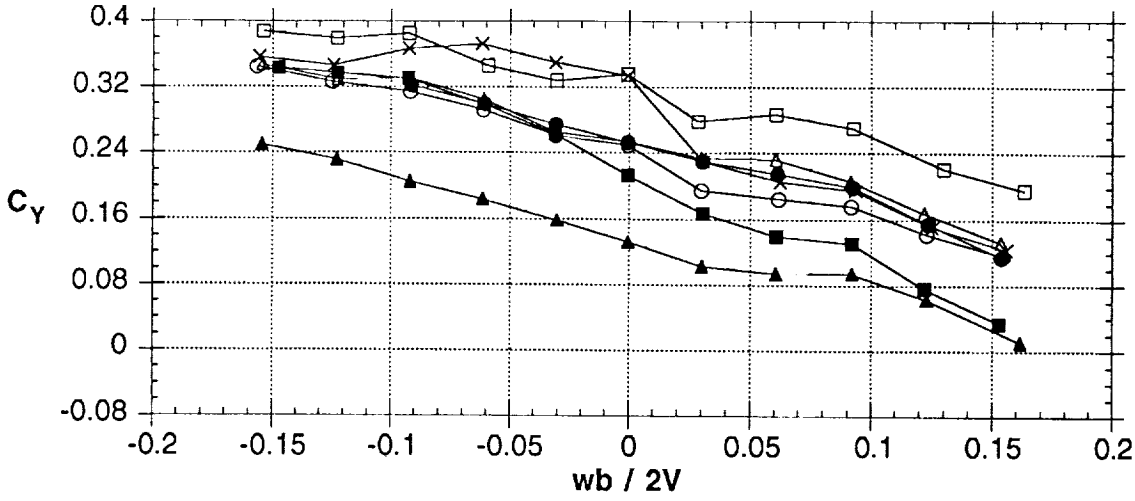

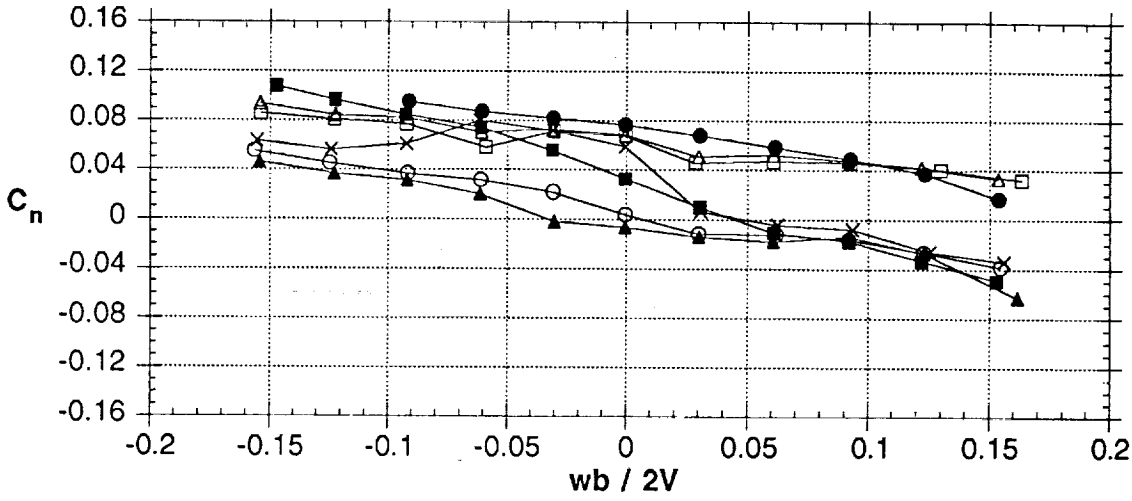

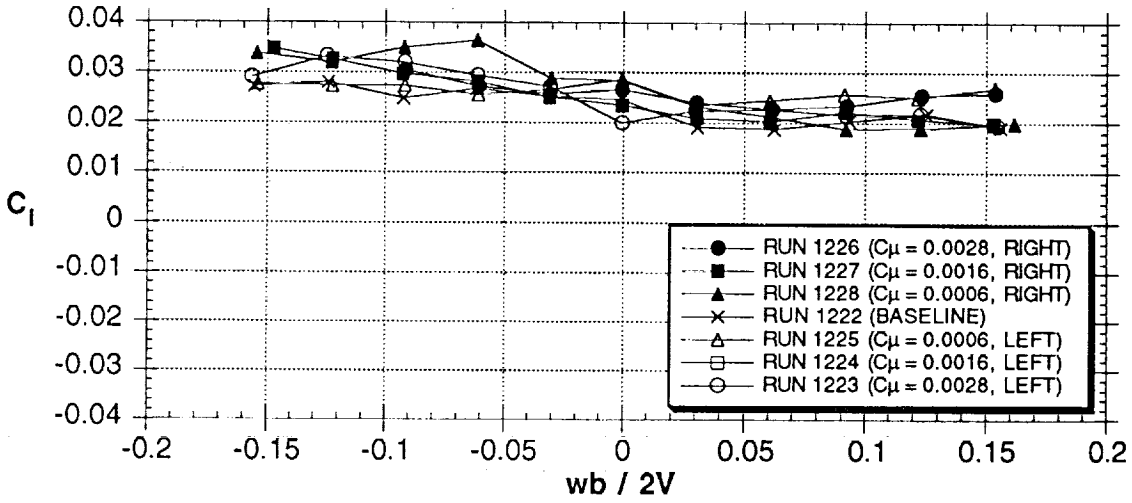

Figure 42 - Concluded

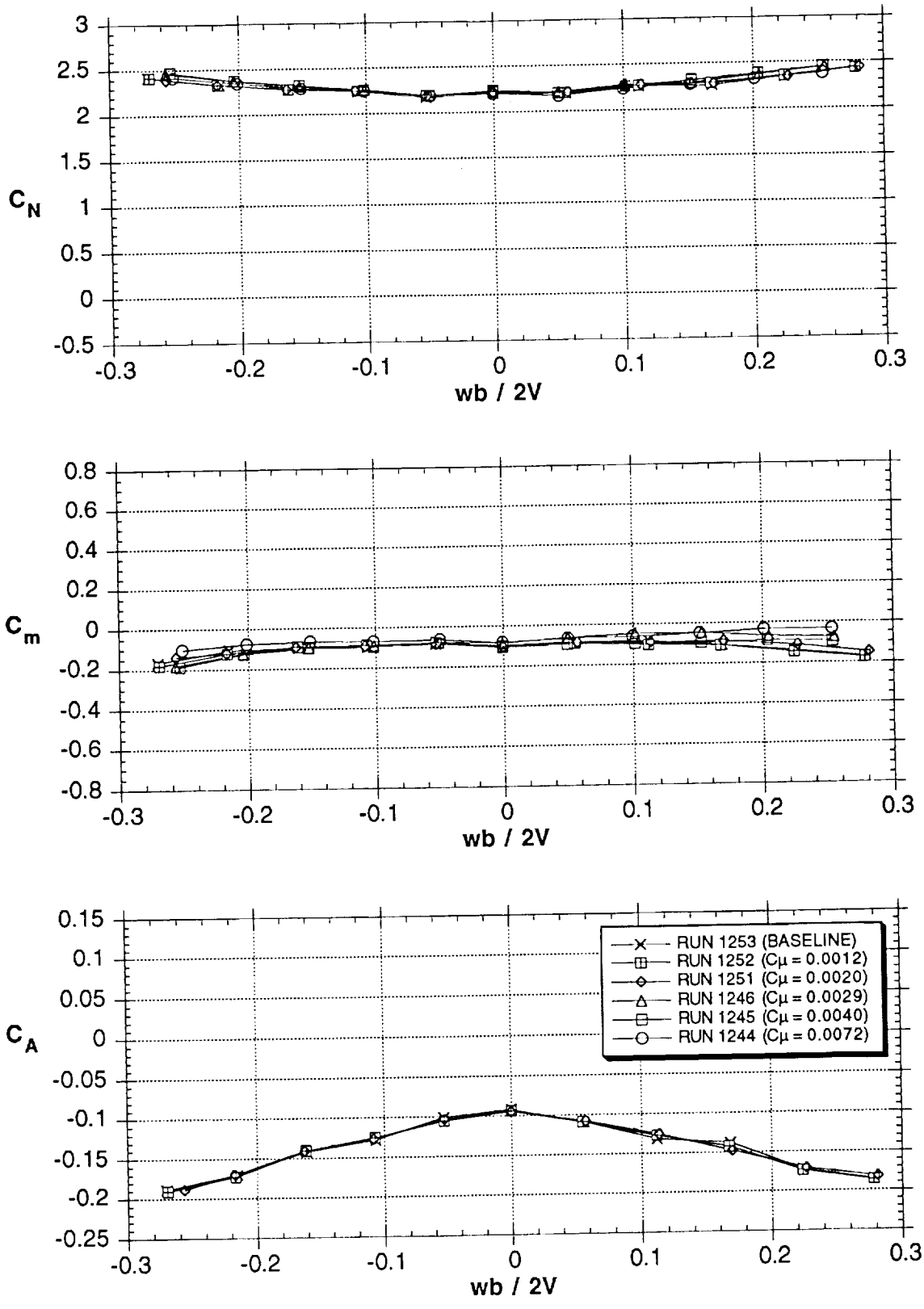

Figure 43 - Effects of SLOT AB blowing slot (left side only) at Q=10 psf (Rn=0.387x10^6), 45° AOA

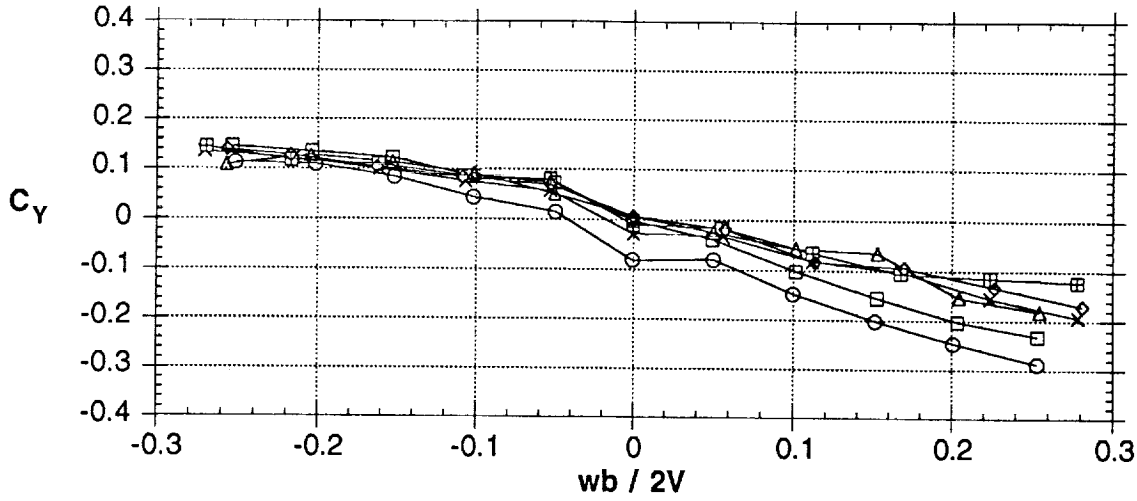

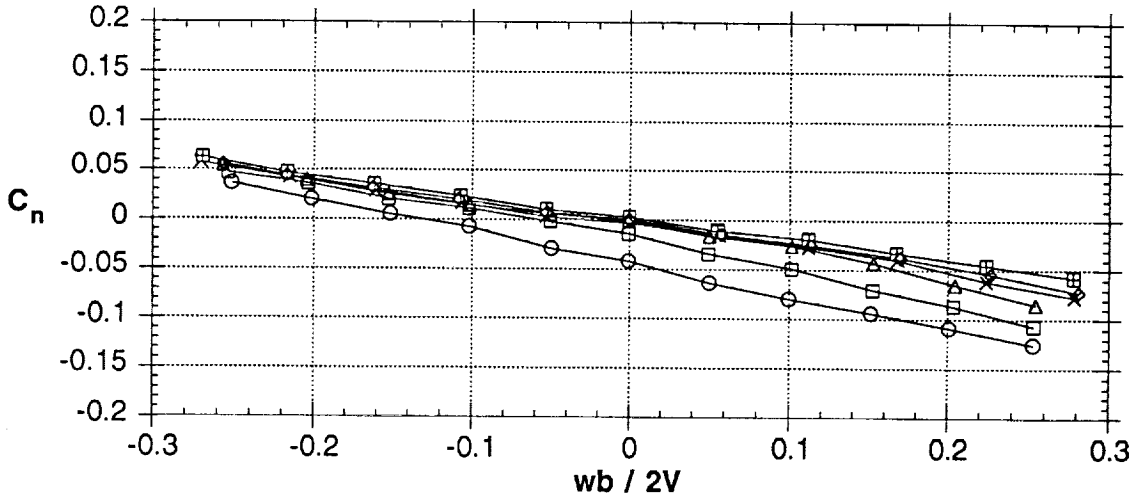

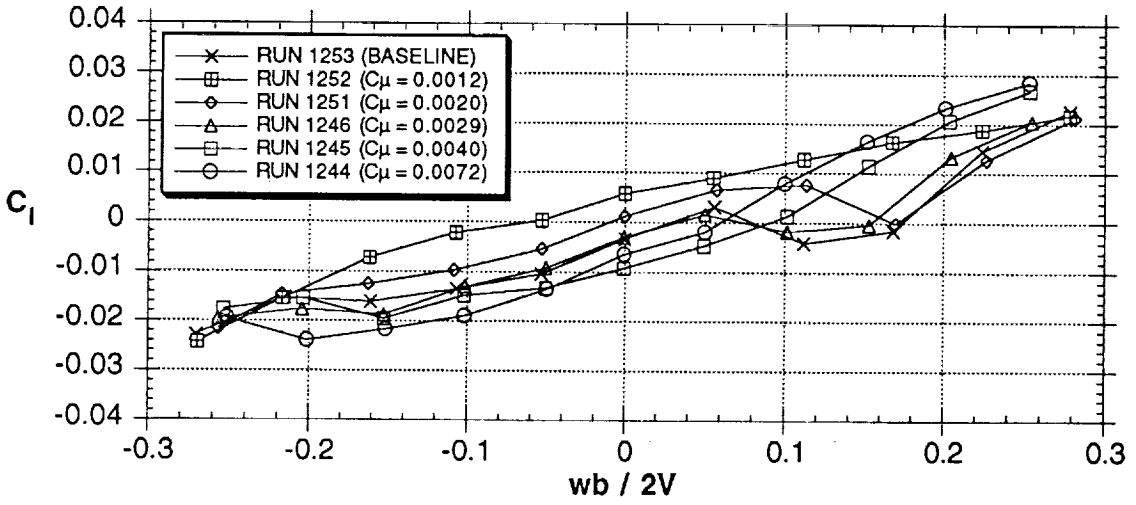

Figure 43 - Concluded

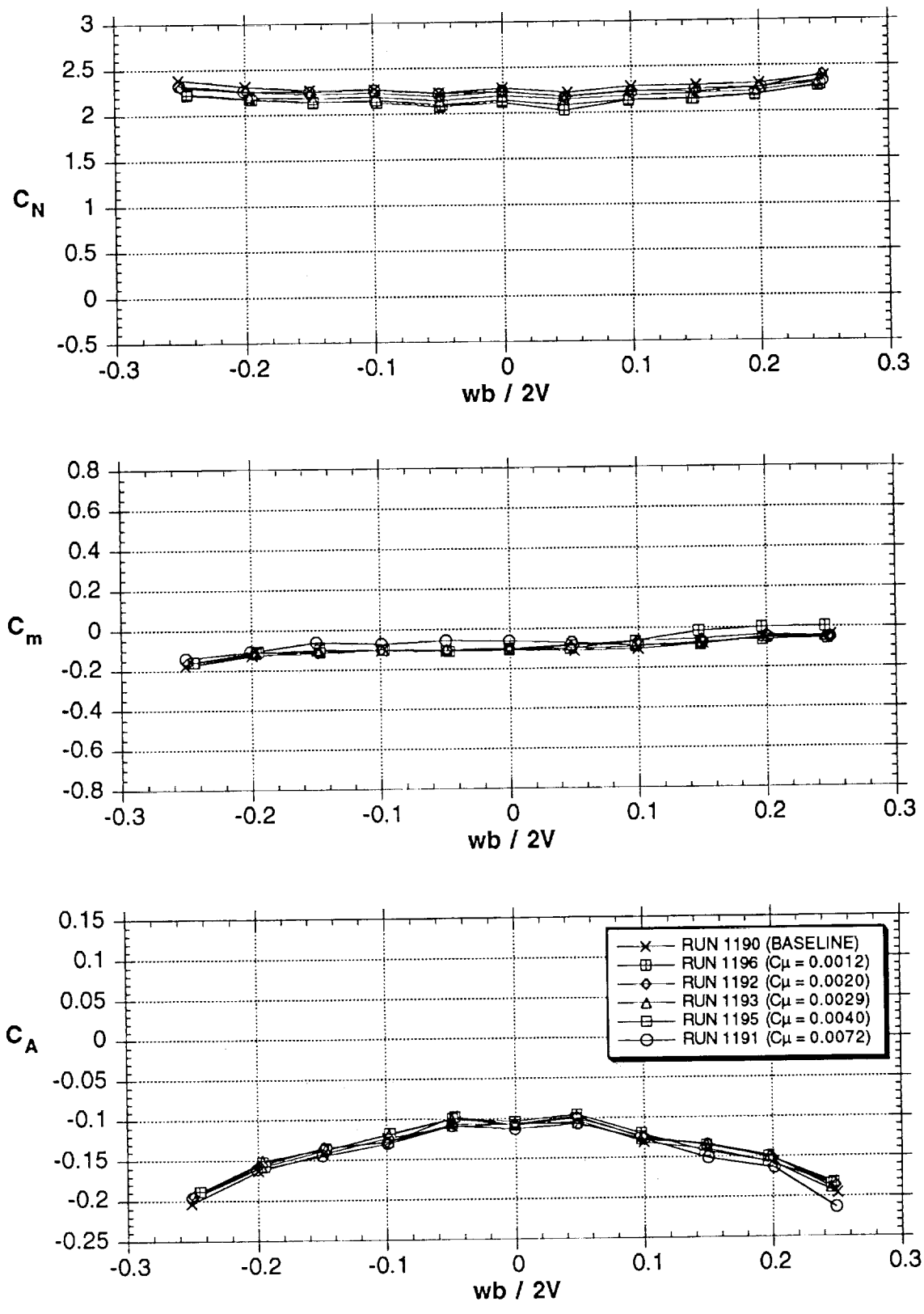

Figure 44 - Effects of SLOT AB blowing slot (left side only) at Q=10 psf (Rn=0.387x10^6), 51° AOA

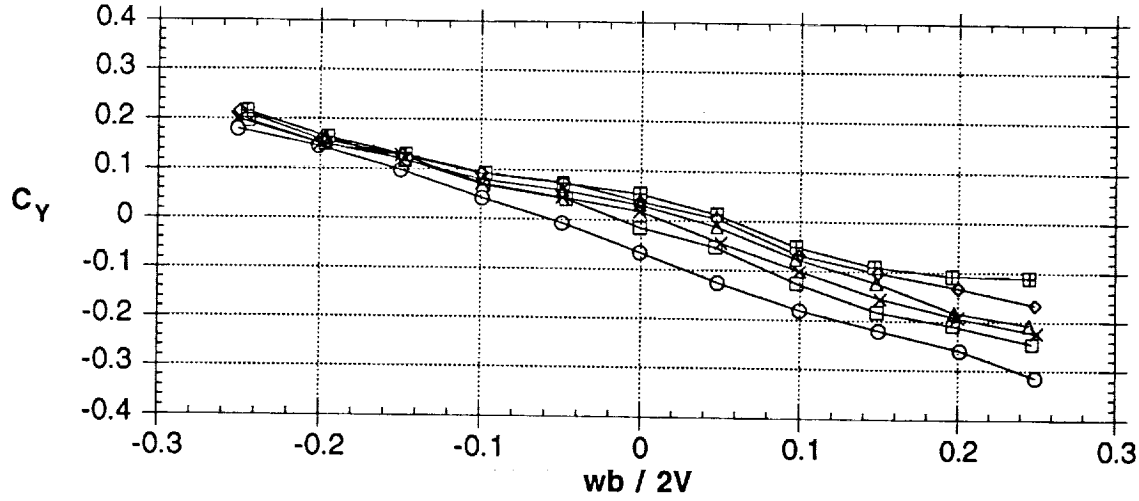

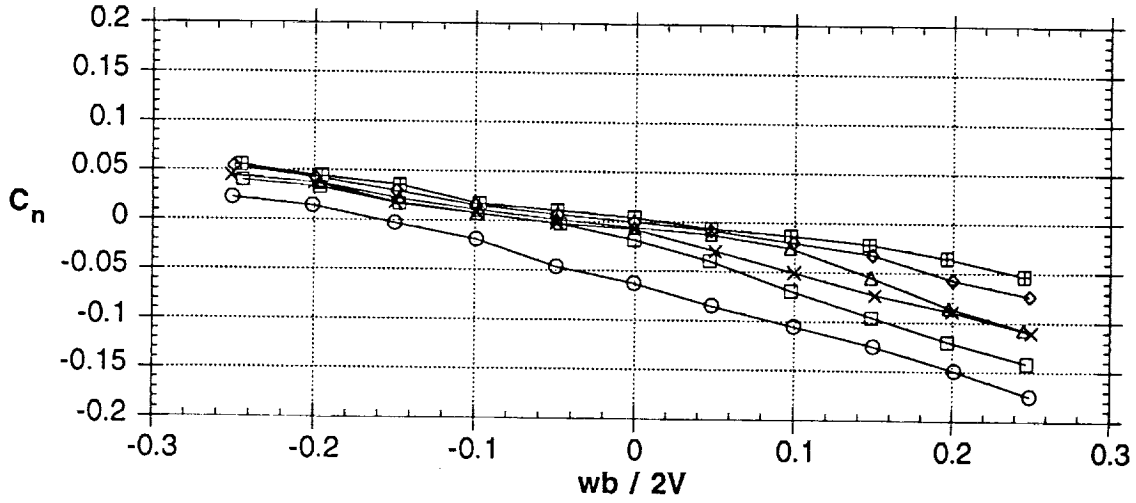

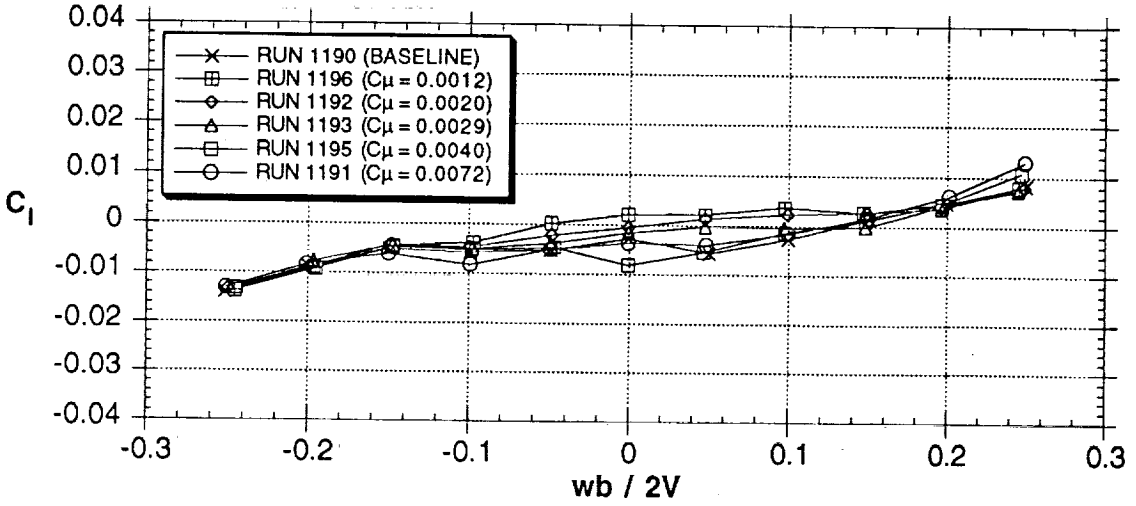

Figure 44 - Concluded

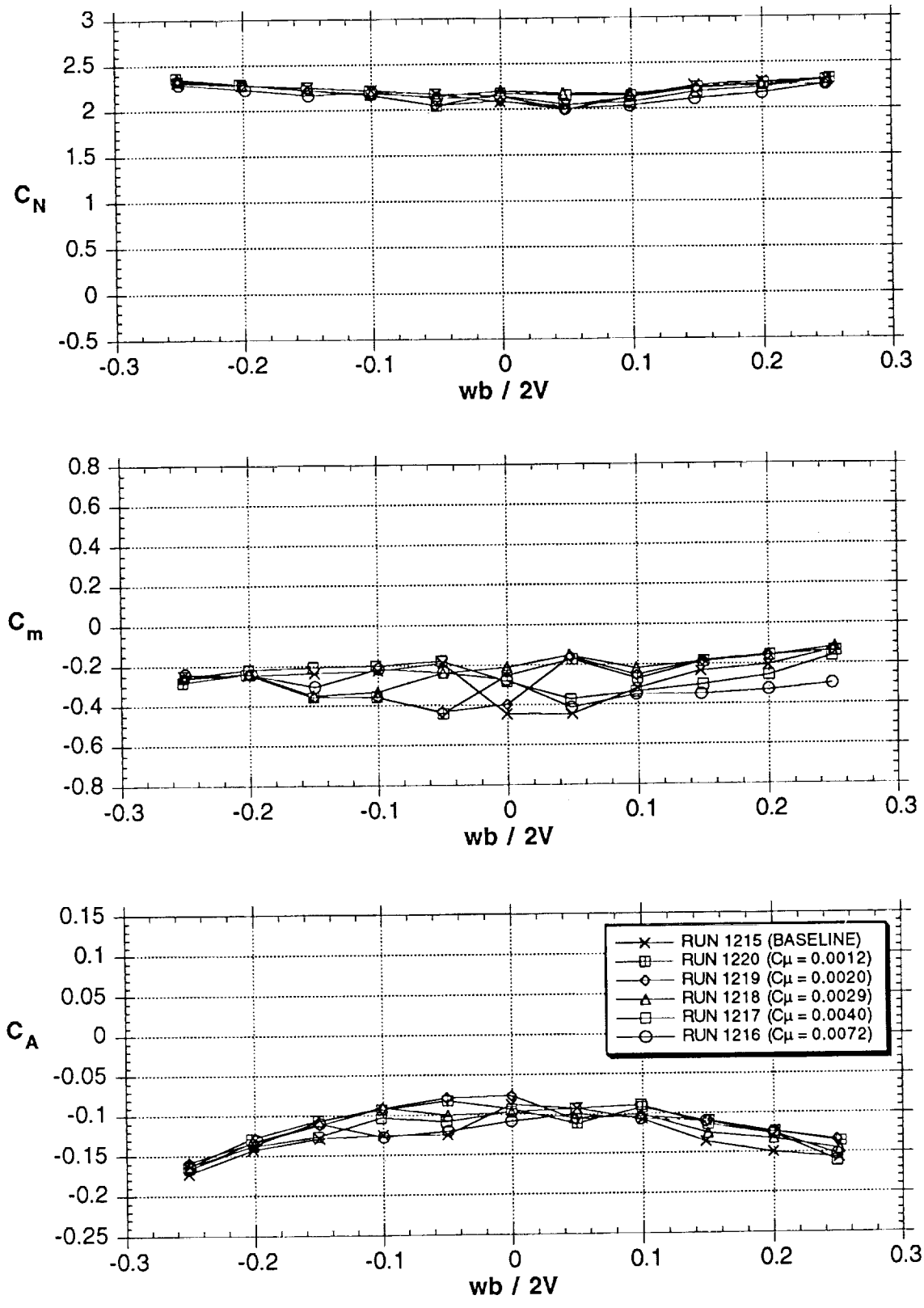

Figure 45 - Effects of SLOT AB blowing slot (left side only) at Q=10 psf ($Rn=0.387x10^6$), 60° AOA

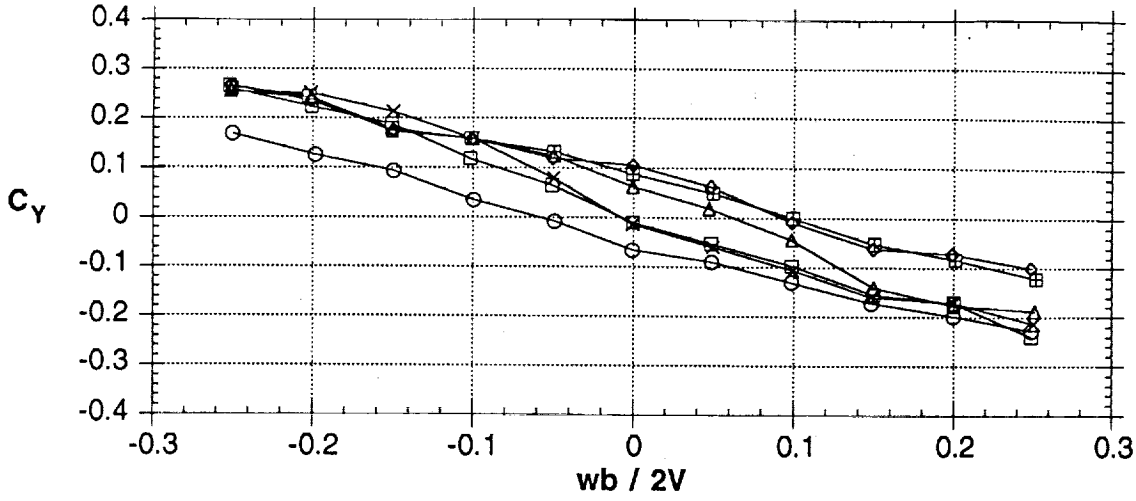

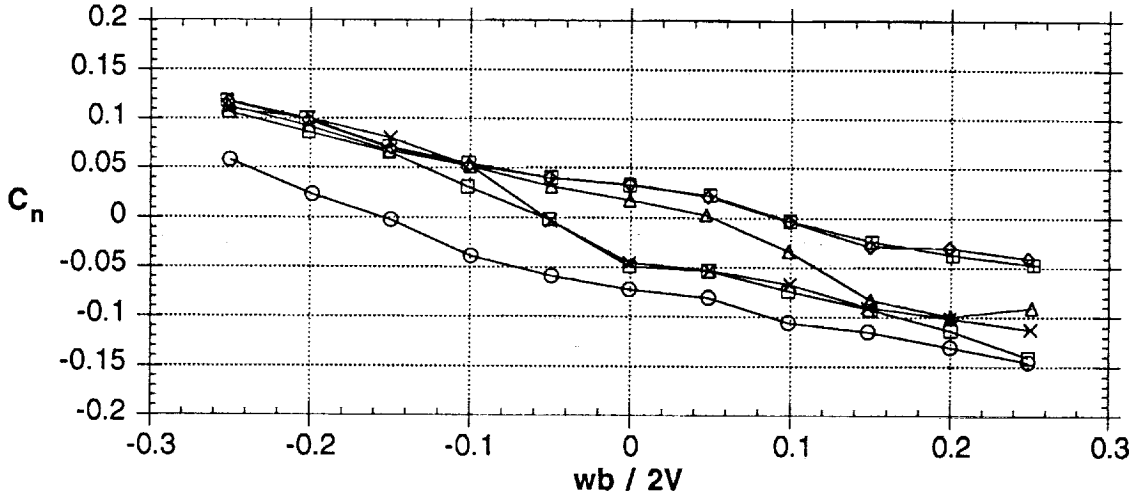

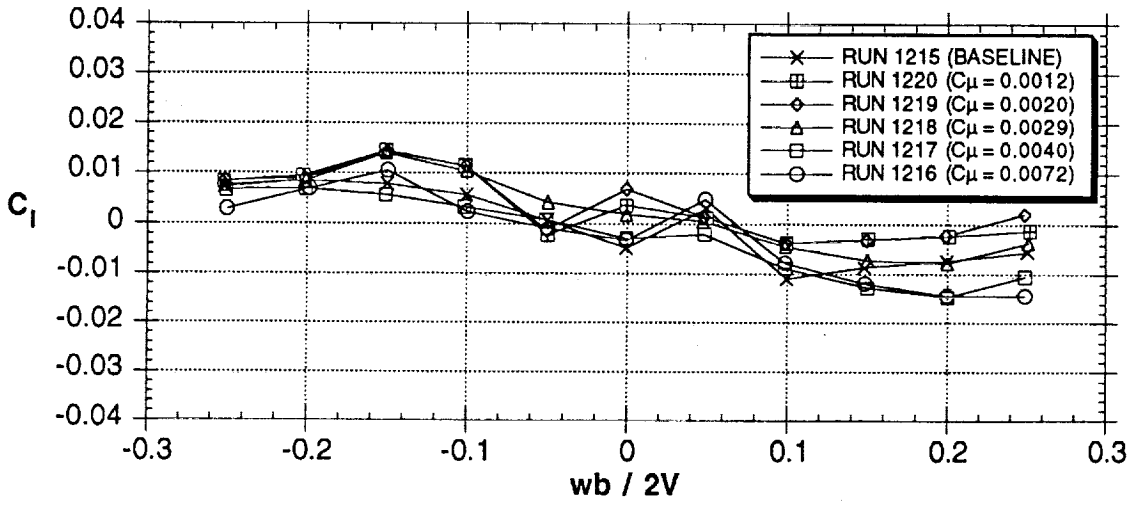

Figure 45 - Concluded

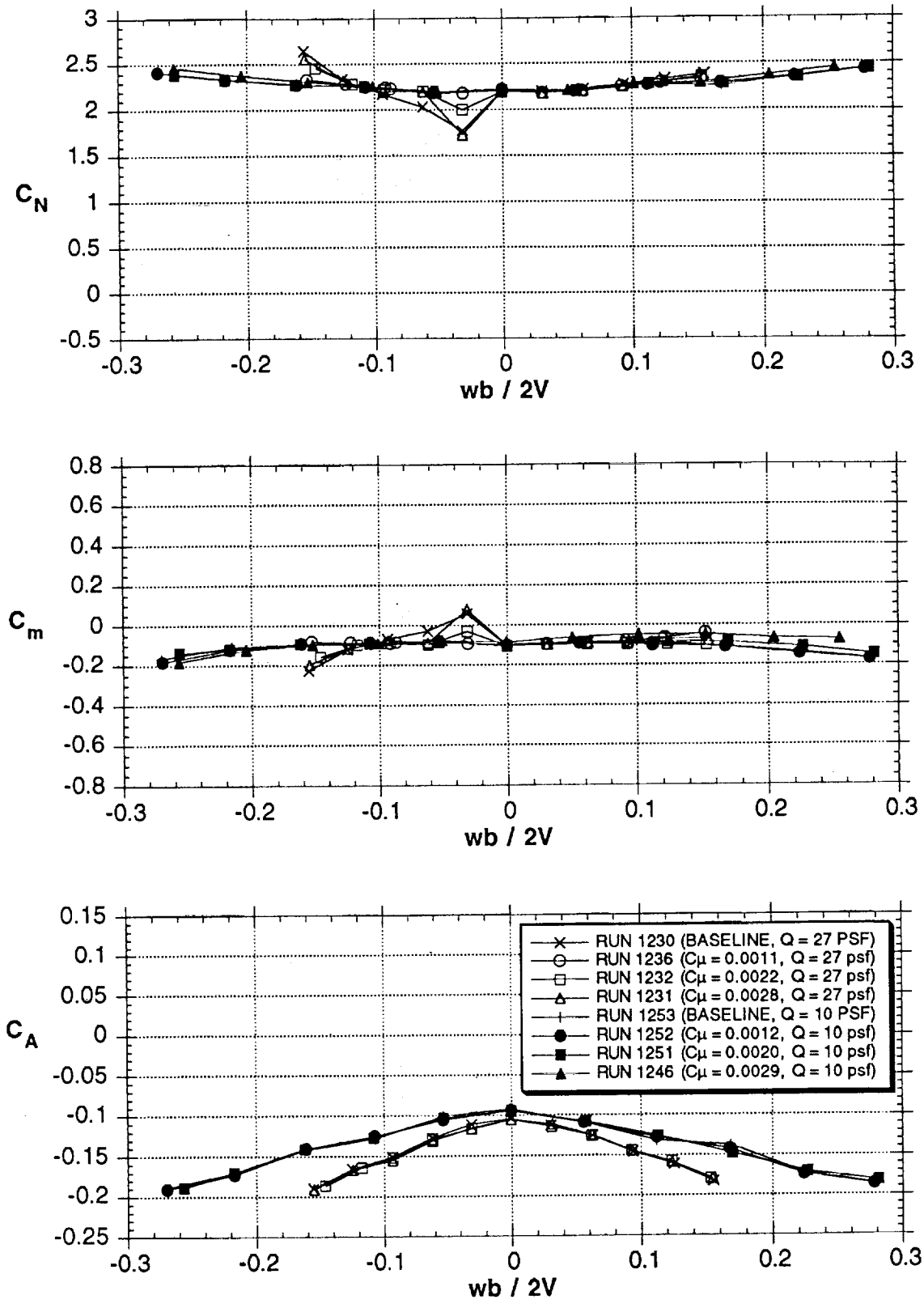

Figure 46 - Comparison of SLOT AB blowing slots (left side only) at Q=10 psf ($Rn=0.387 \times 10^6$) and Q=27 psf ($Rn=0.636 \times 10^6$), 45° AOA

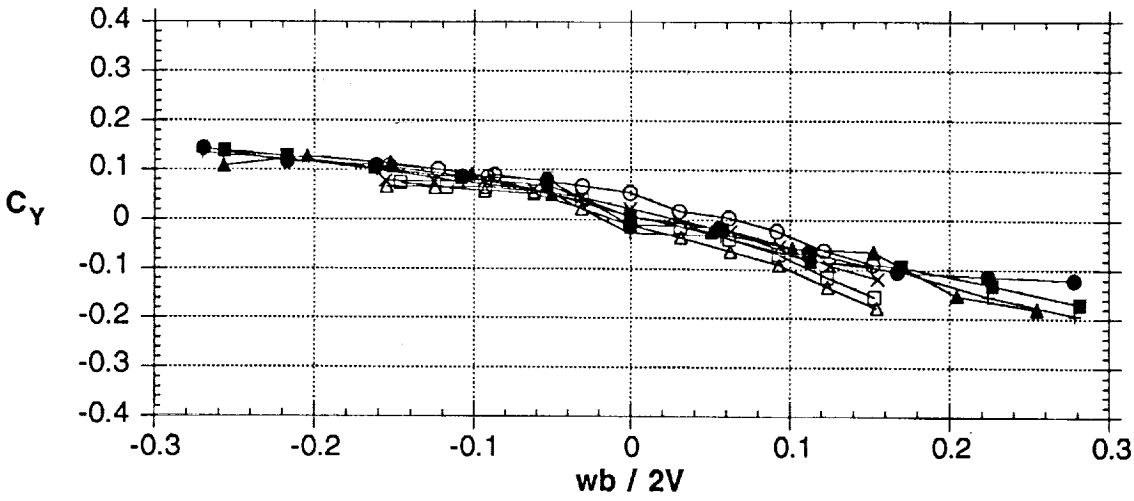

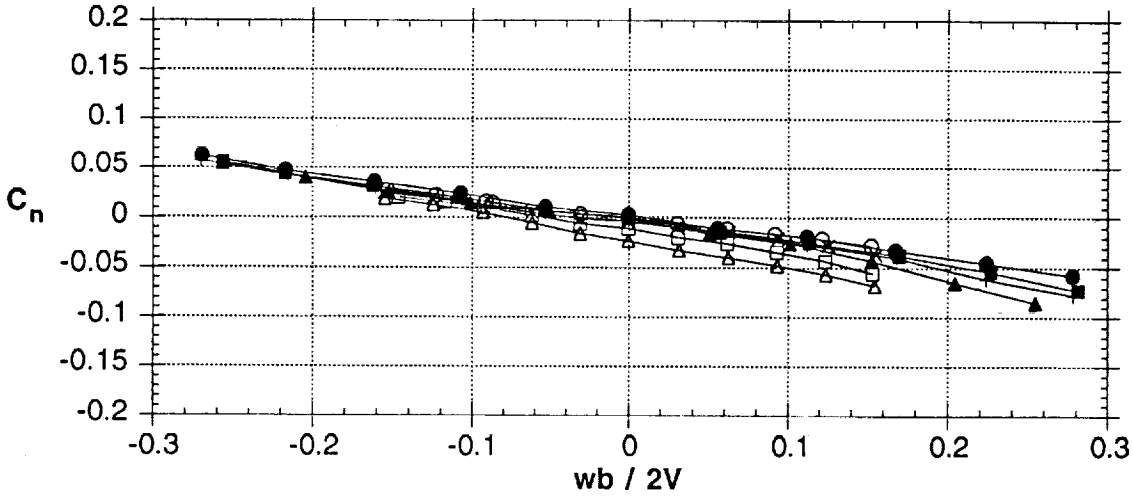

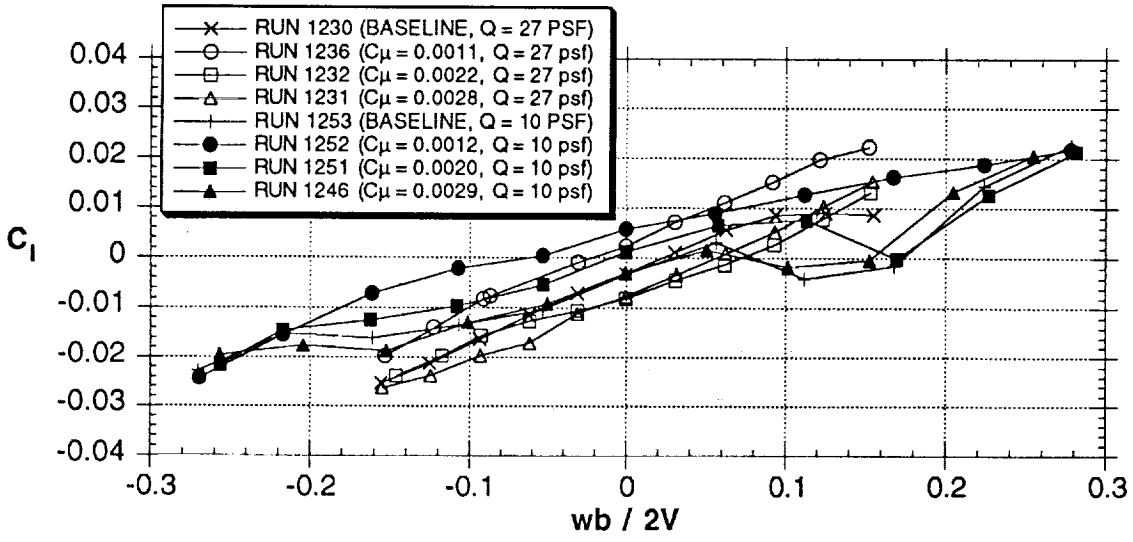

Figure 46 - Concluded

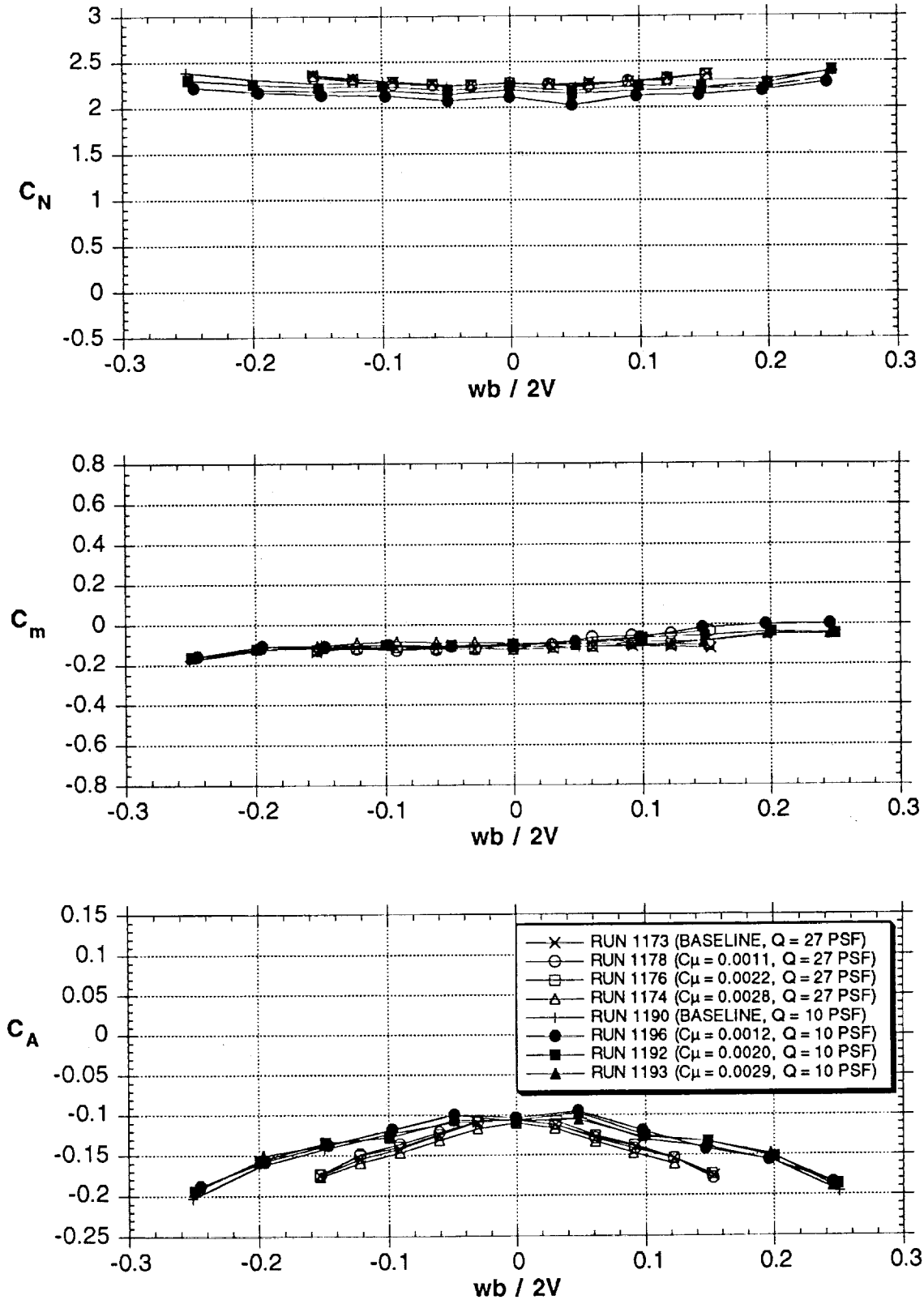

Figure 47 - Comparison of SLOT AB blowing slots (left side only) at Q=10 psf ($Rn=0.387 \times 10^6$) and Q=27 psf ($Rn=0.636 \times 10^6$), 51° AOA

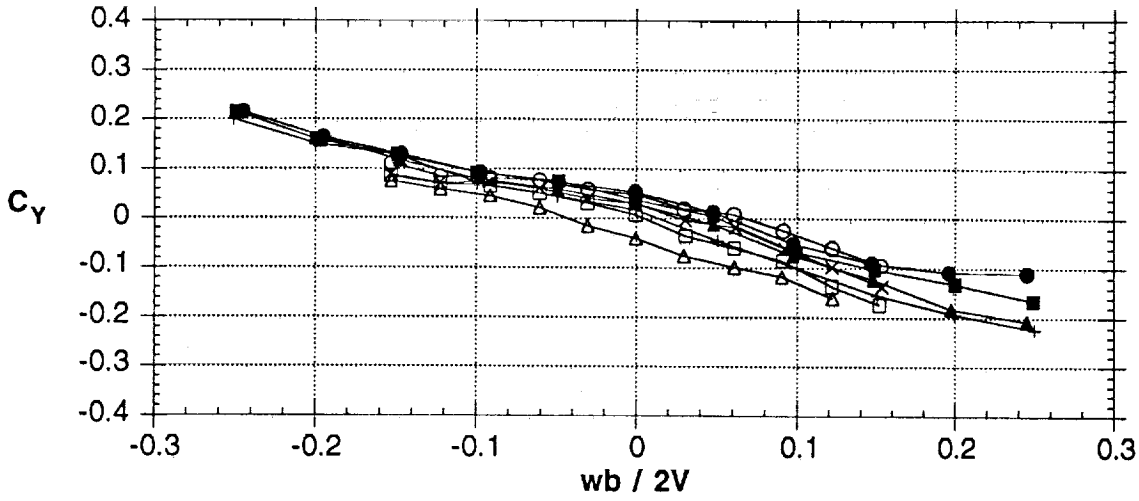

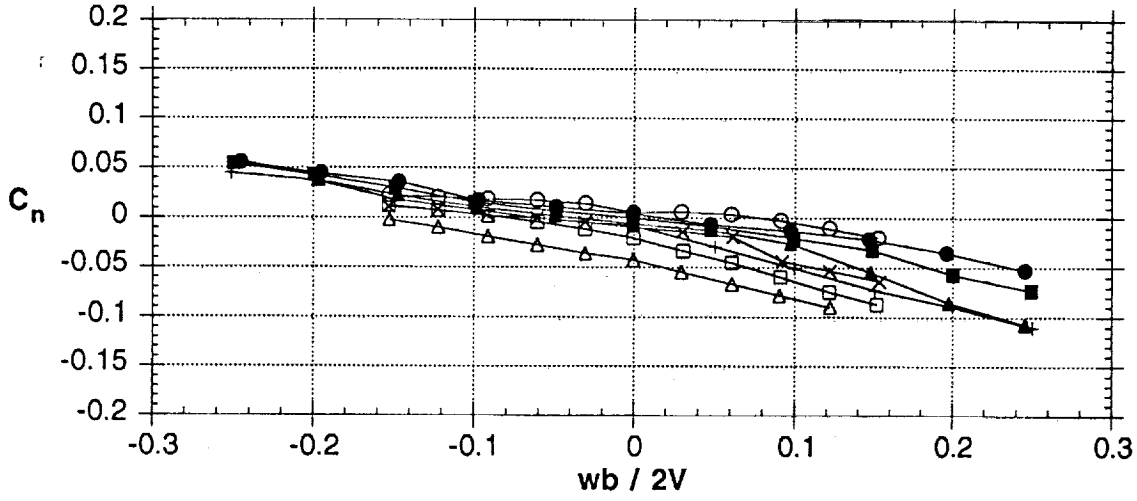

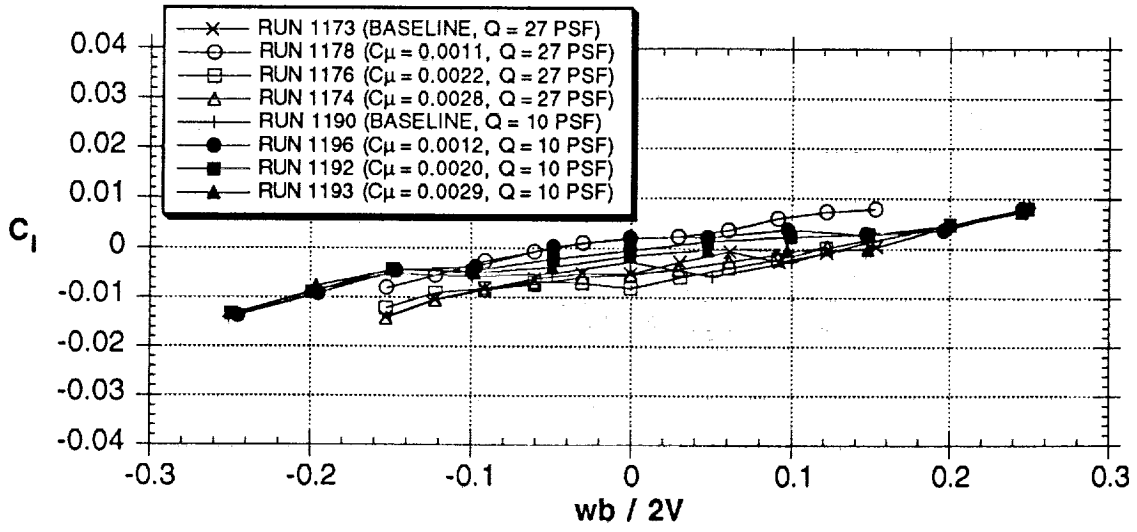

Figure 47 - Concluded

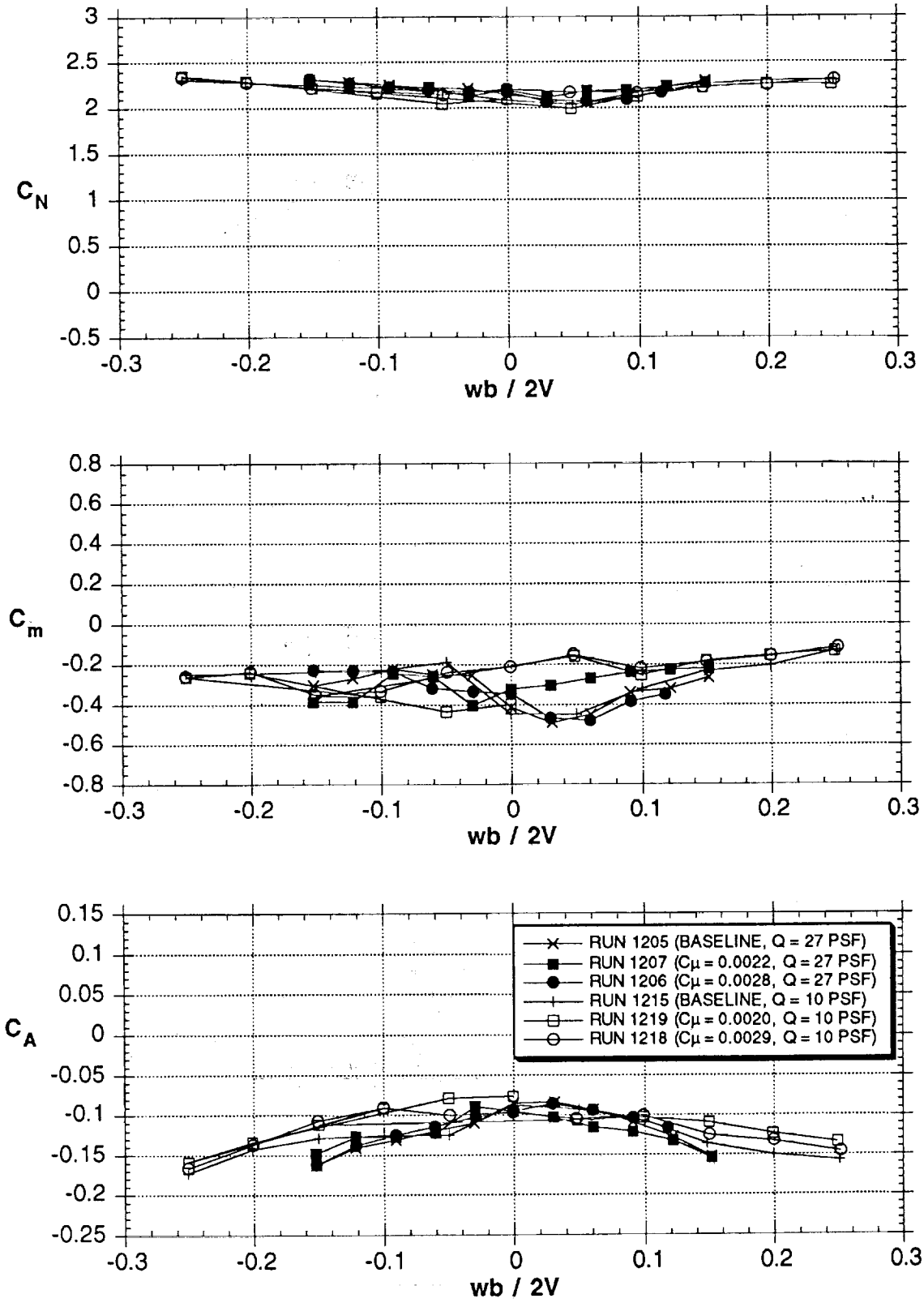

Figure 48 - Comparison of SLOT AB blowing slots (left side only) at Q=10 psf (Rn=0.387x10^6) and Q=27 psf (Rn=0.636x10^6), 60° AOA

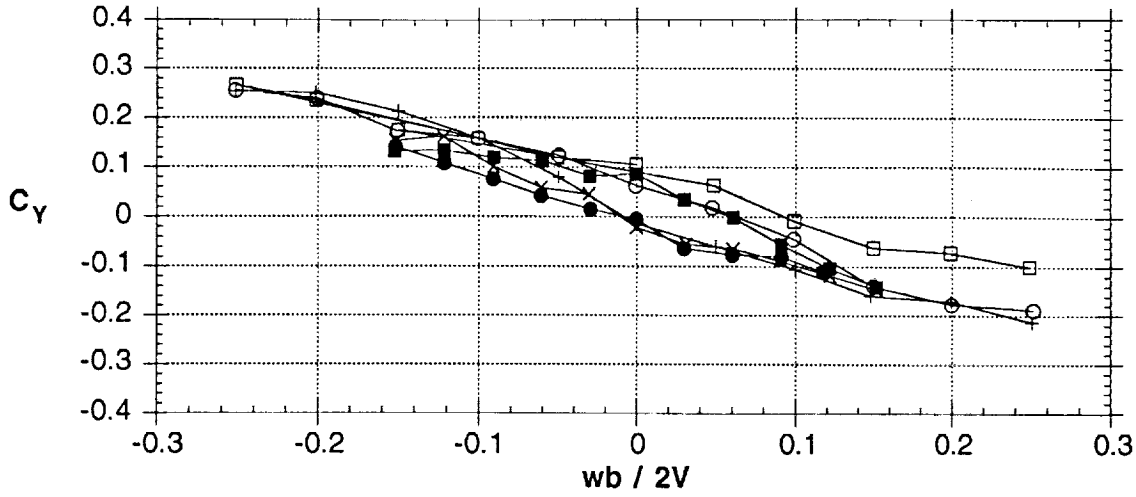

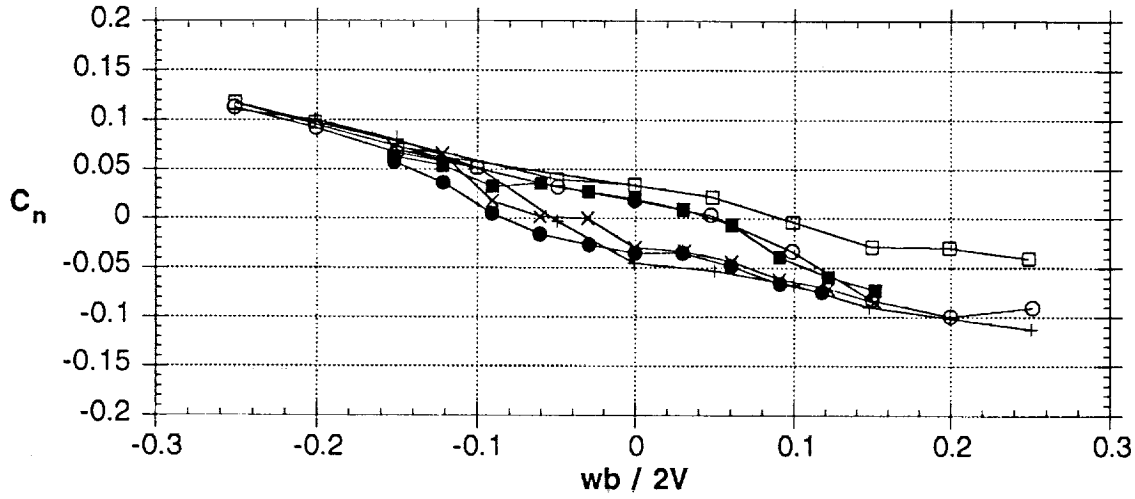

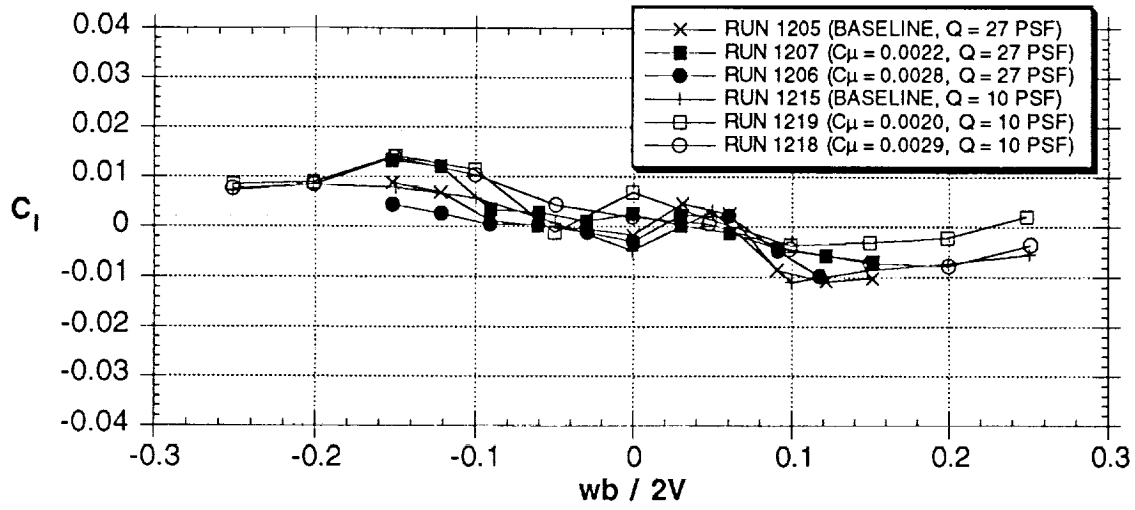

Figure 48 - Concluded

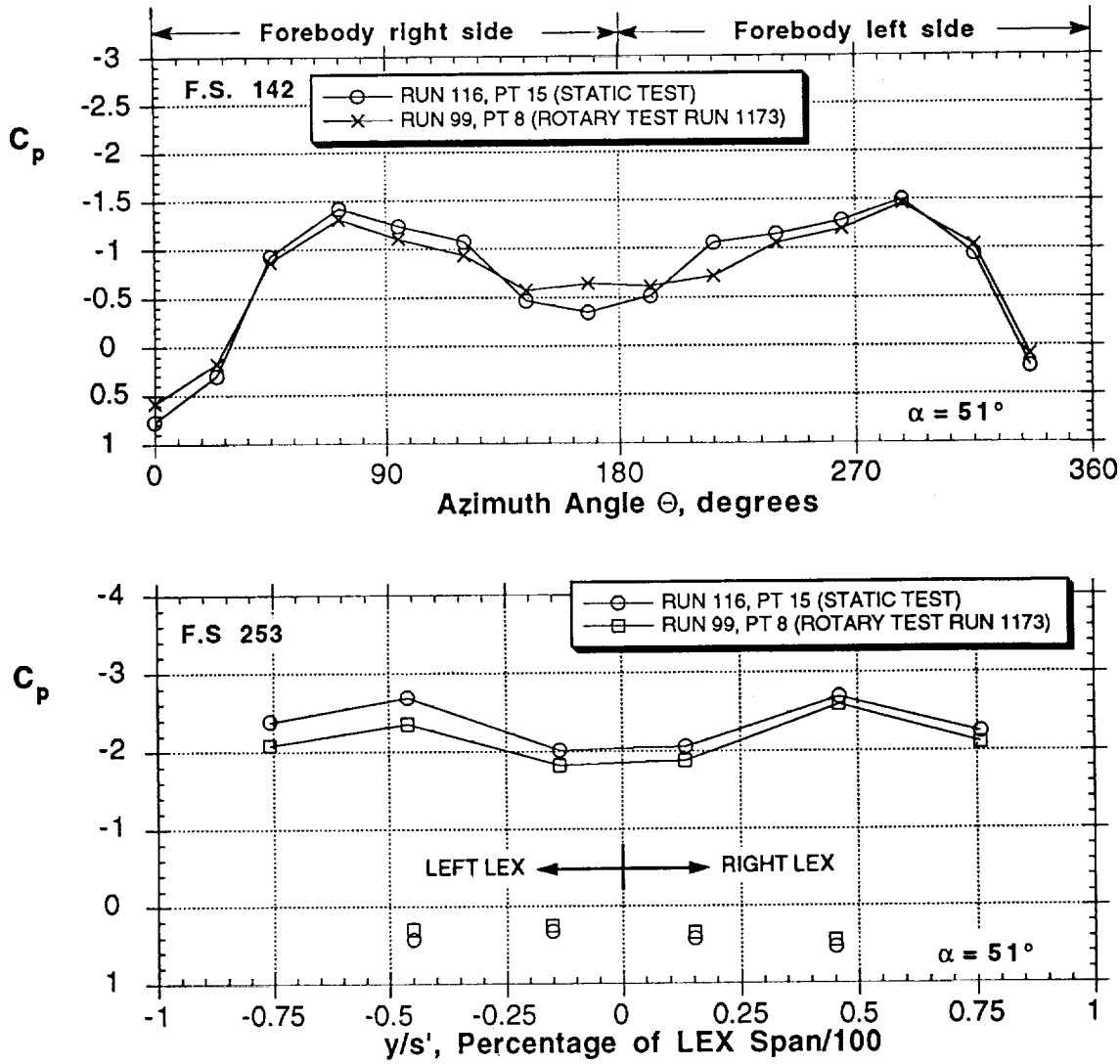

(a) Comparison to static test, Cμ = 0

Figure 49 - Slot AB pressure distribution, at 51° AOA

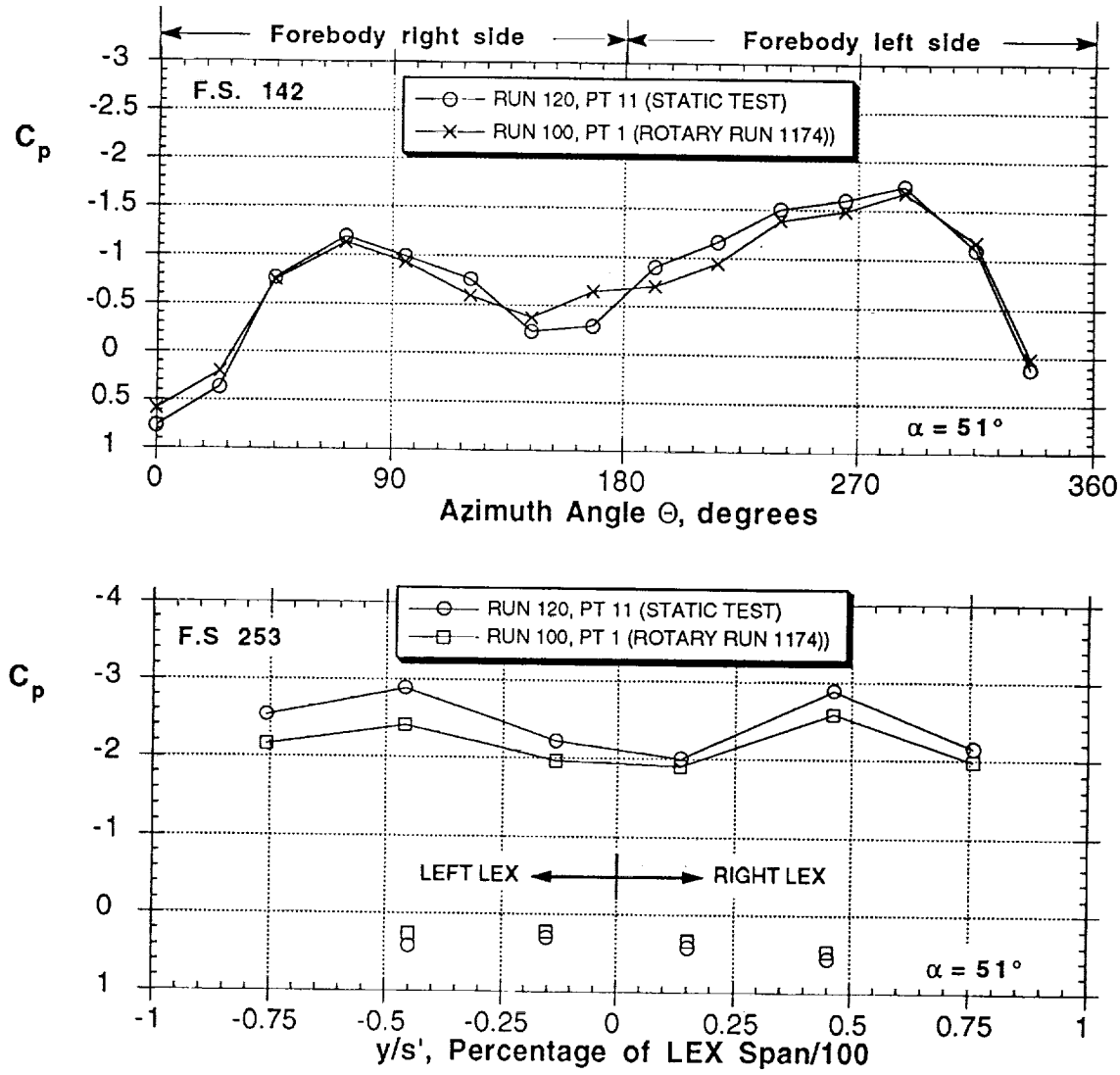

(b) Comparison to static test, Cμ = 0.0029, left

Figure 49 - Continued

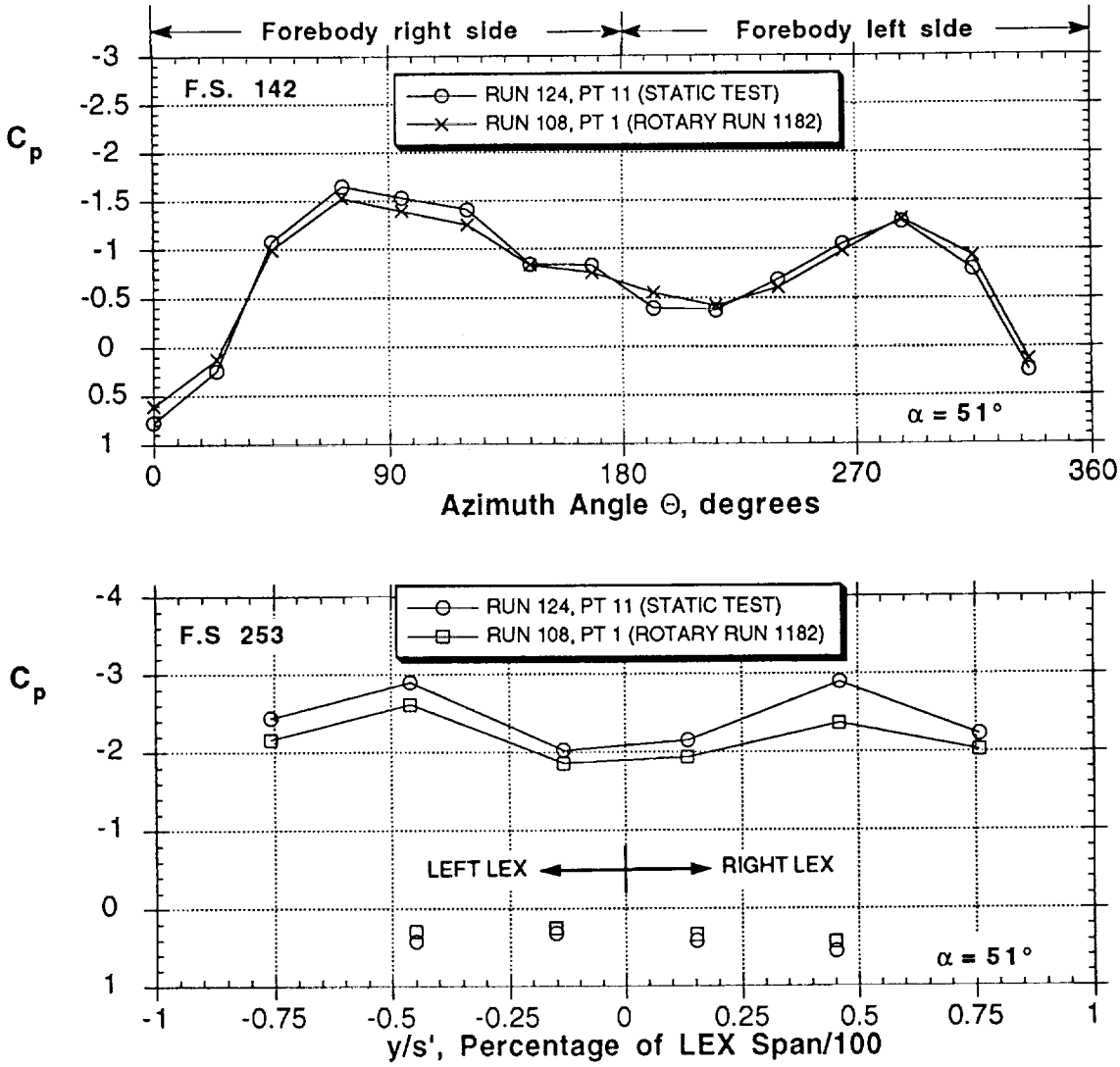

(c) Comparison to static test, $C\mu$ = 0.0029, right

Figure 49 - Continued

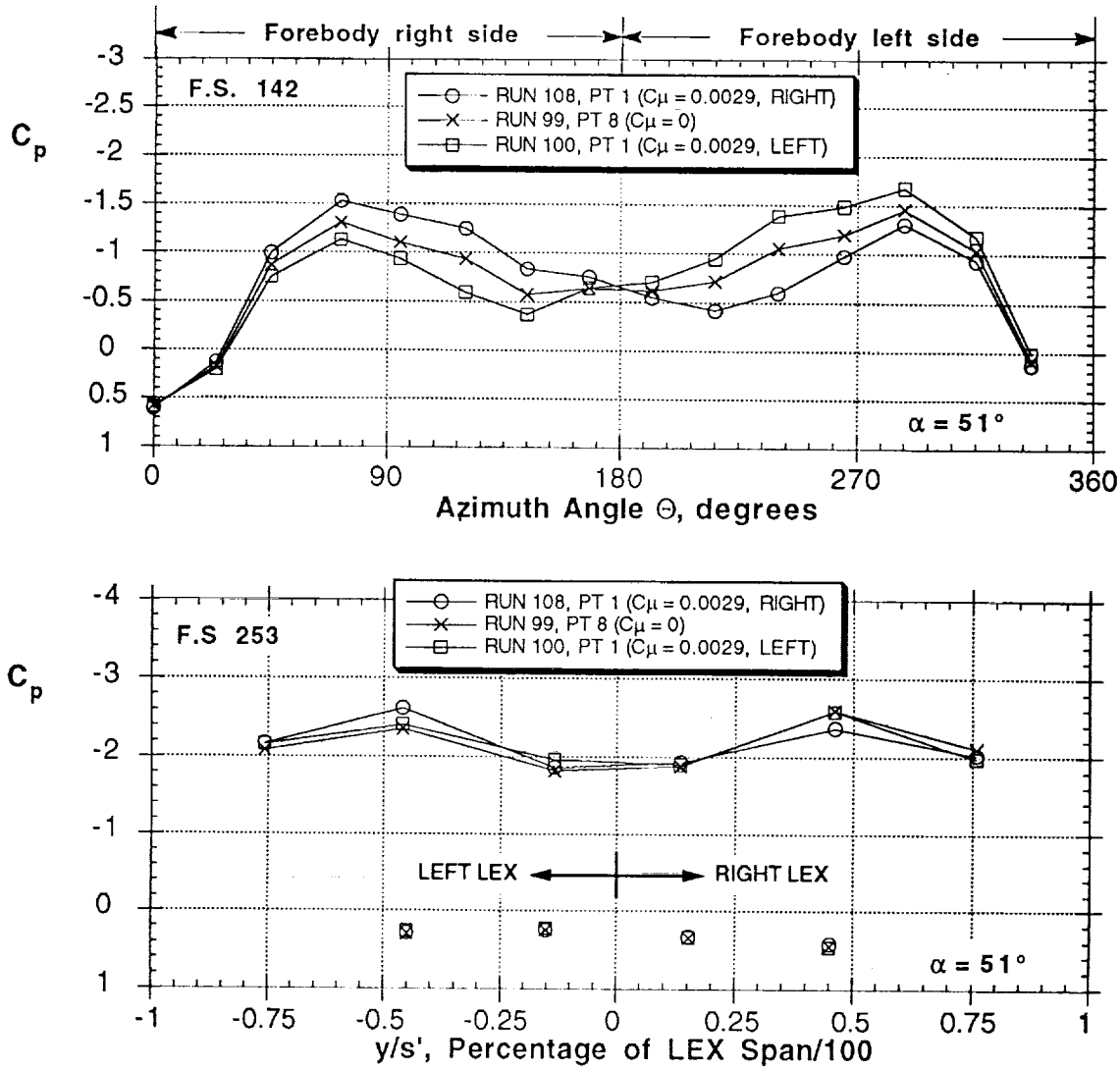

(d) Effect of Cμ, ωb/2V = 0

Figure 49 - Continued

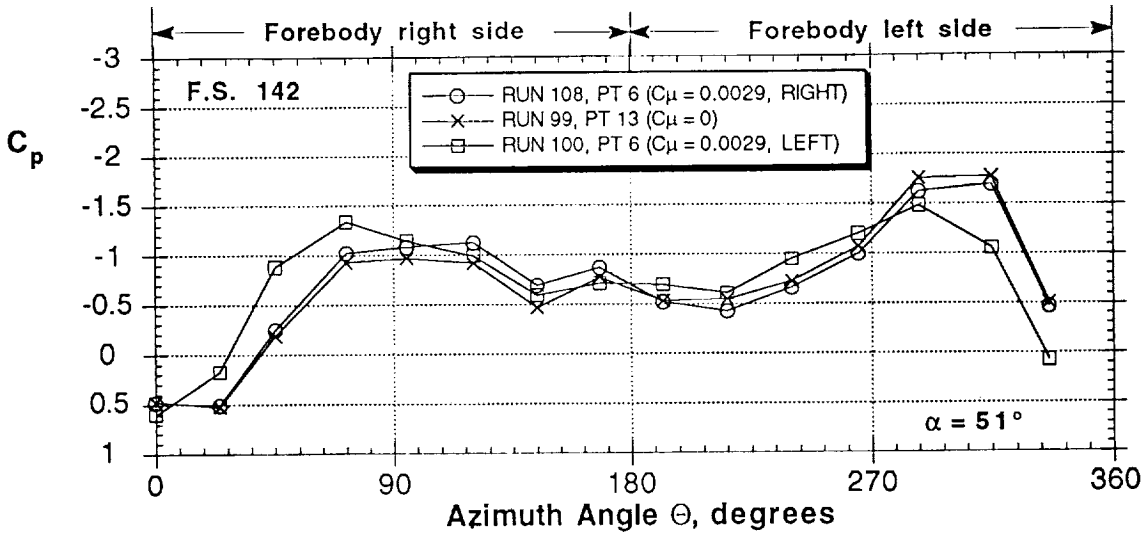

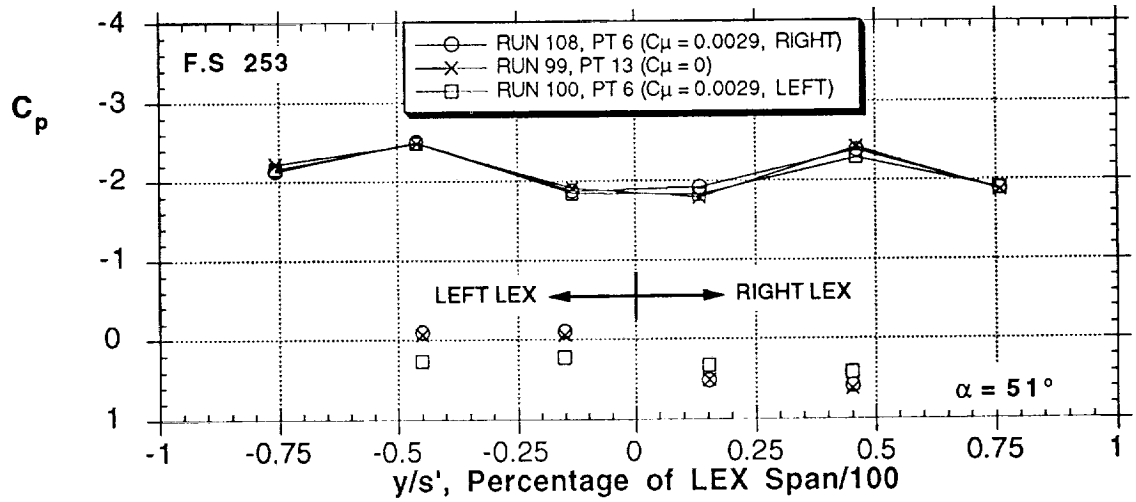

(e) Effect of Cμ, ωb/2V = 0.15

Figure 49 - Continued

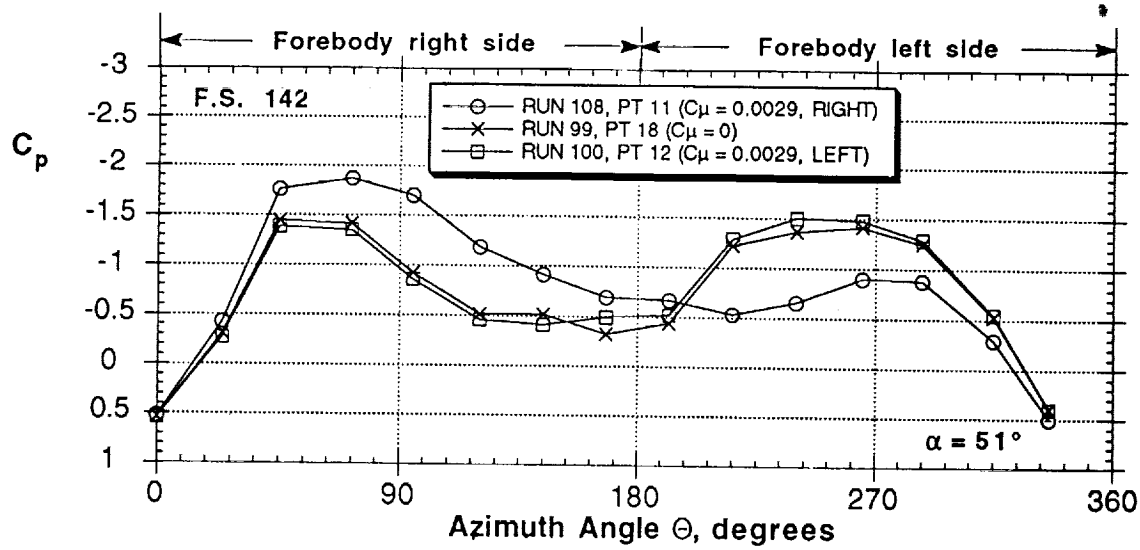

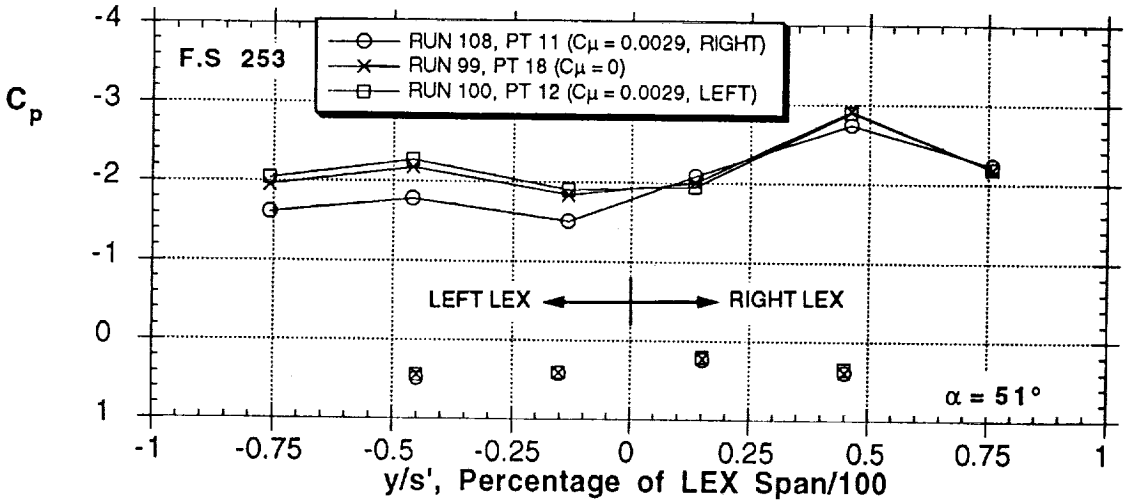

(f) Effect of Cμ, ωb/2V = -0.15

Figure 49 - Continued

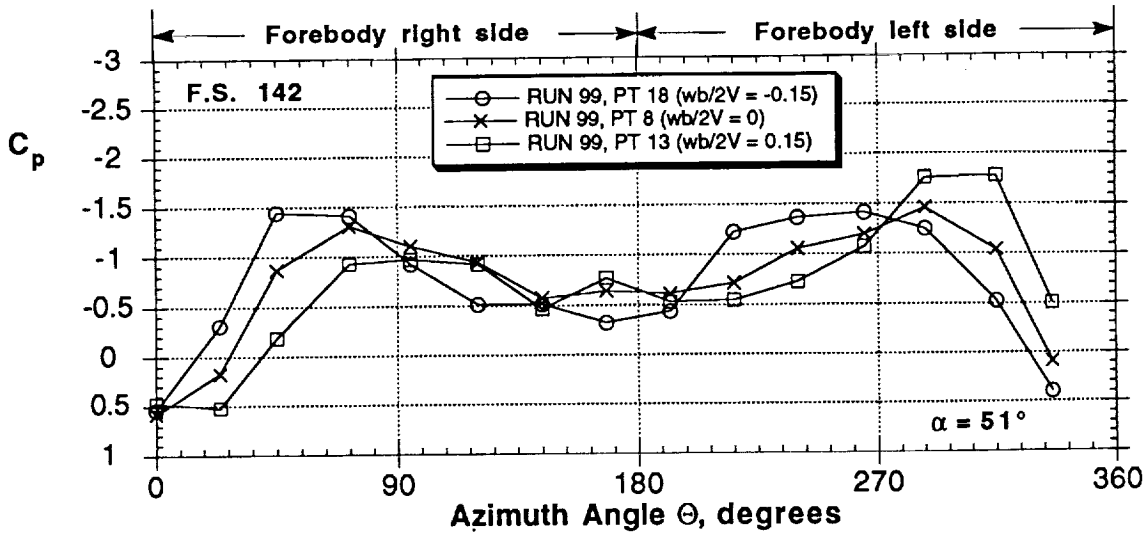

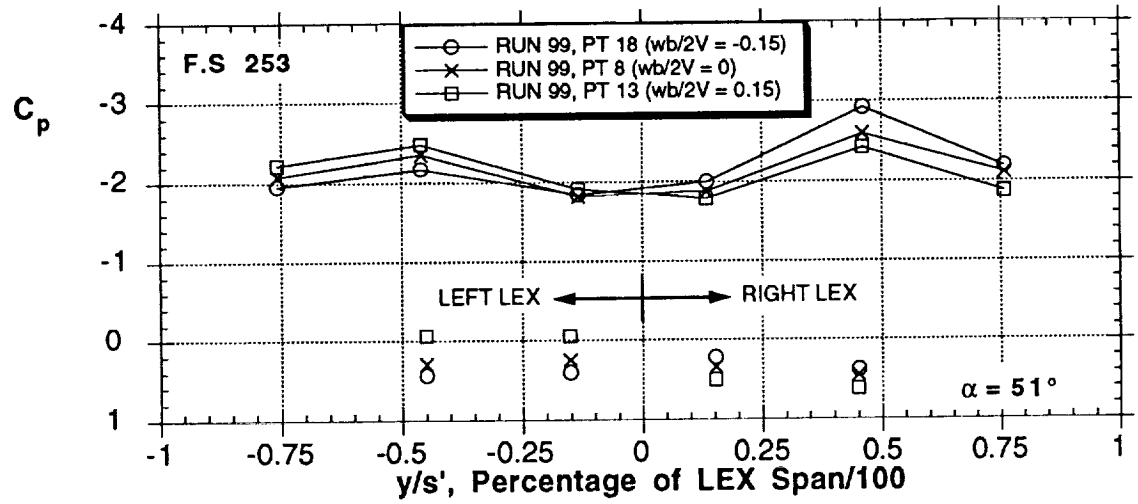

(g) Effect of ωb/2V, Cμ = 0

Figure 49 - Continued

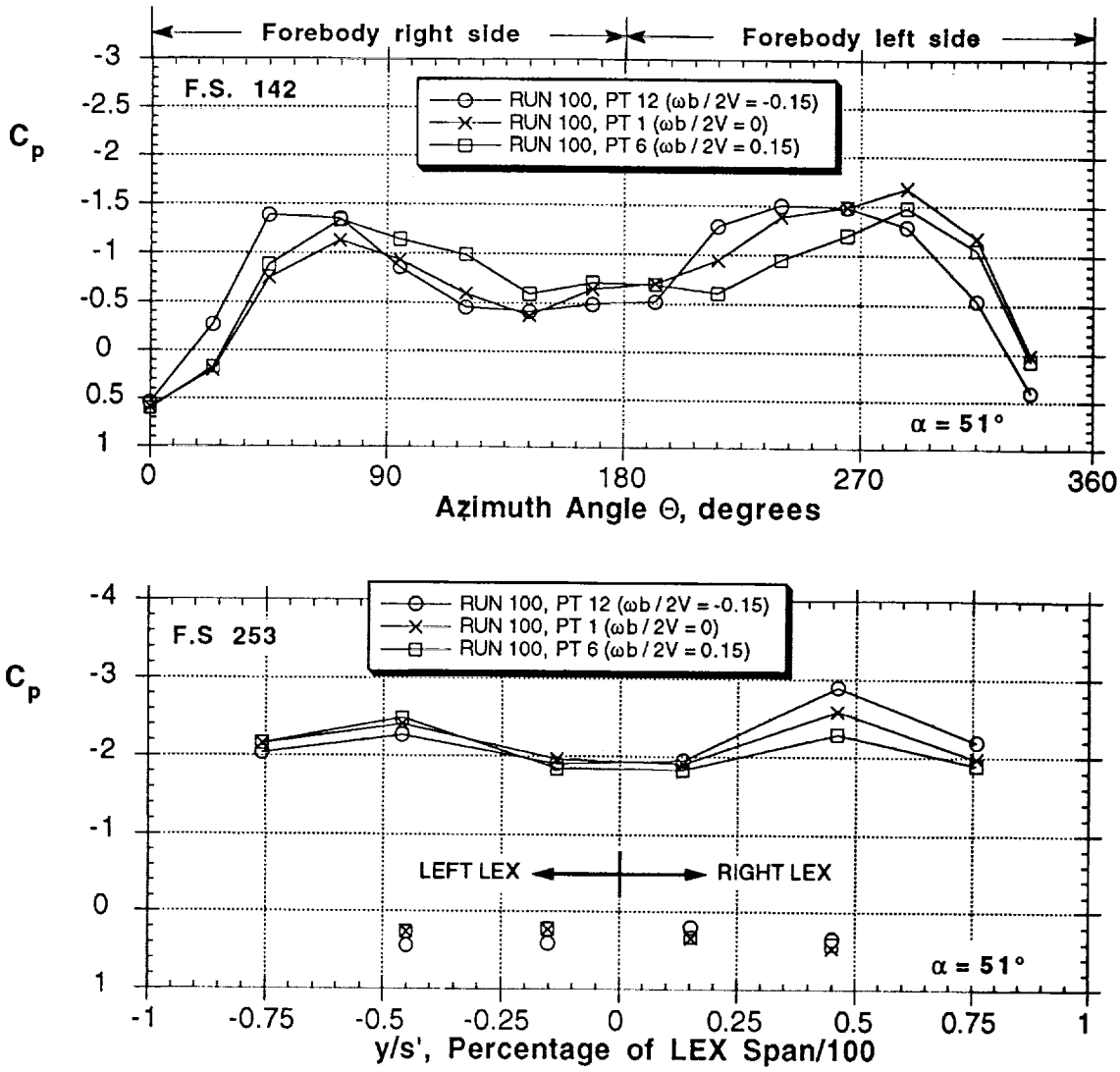

(h) Effect of ωb/2V, Cμ = 0.0029, left

Figure 49 - Continued

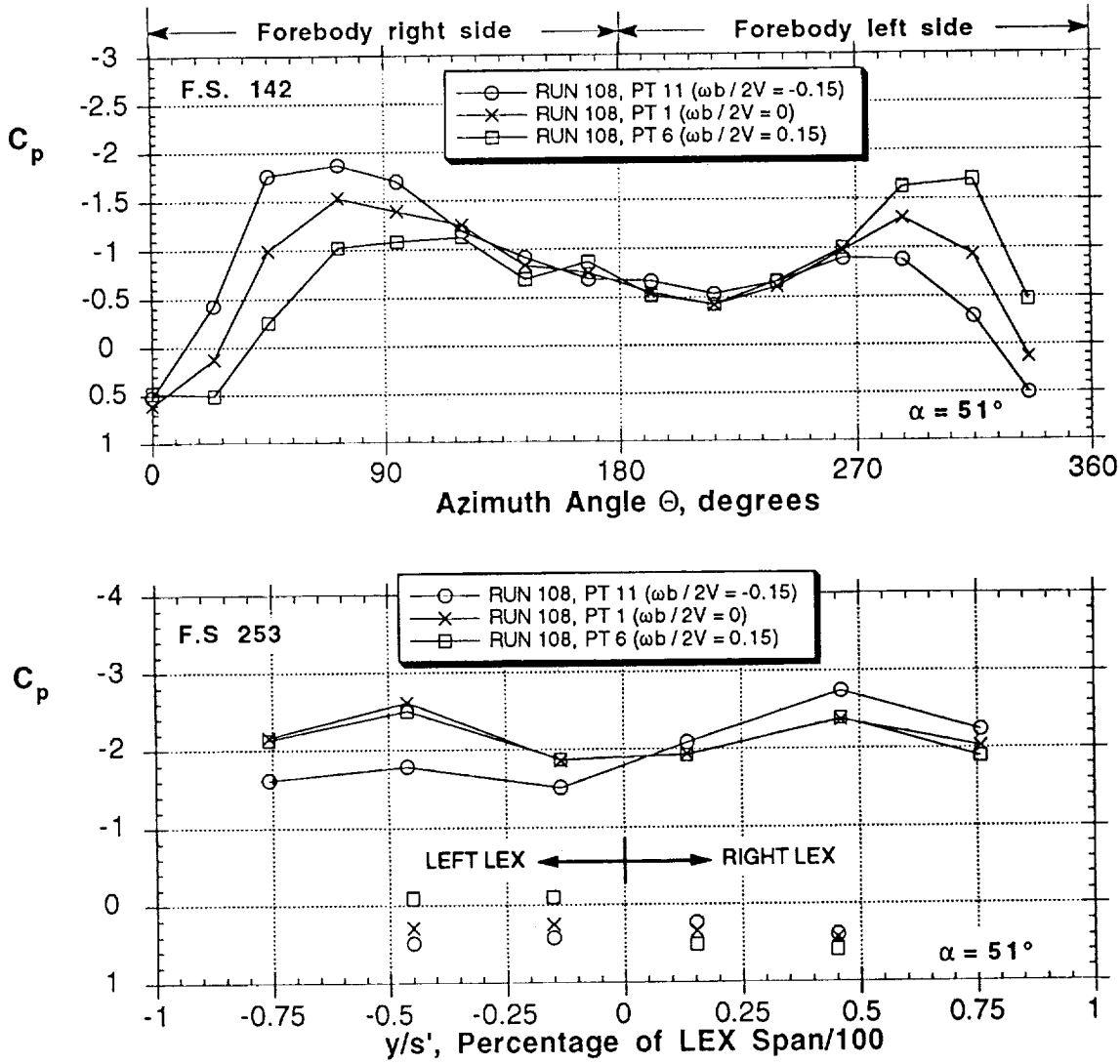

(i) Effect of ωb/2V, Cμ = 0.0029, right

Figure 49 - Concluded

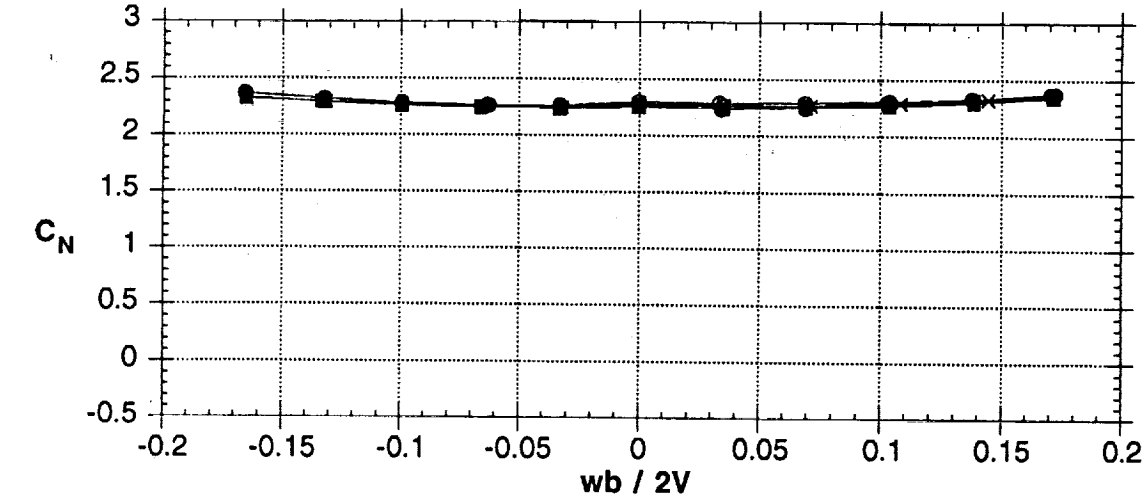

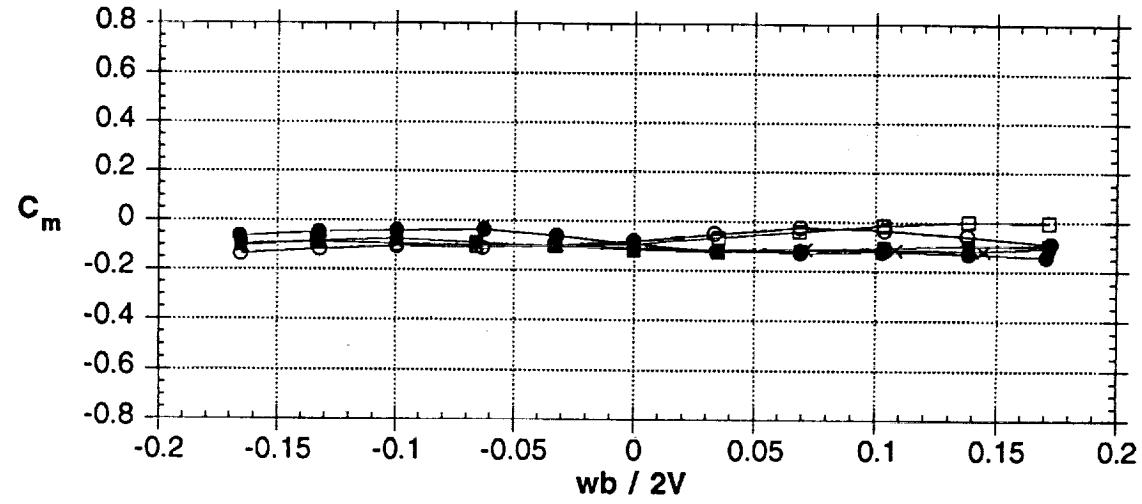

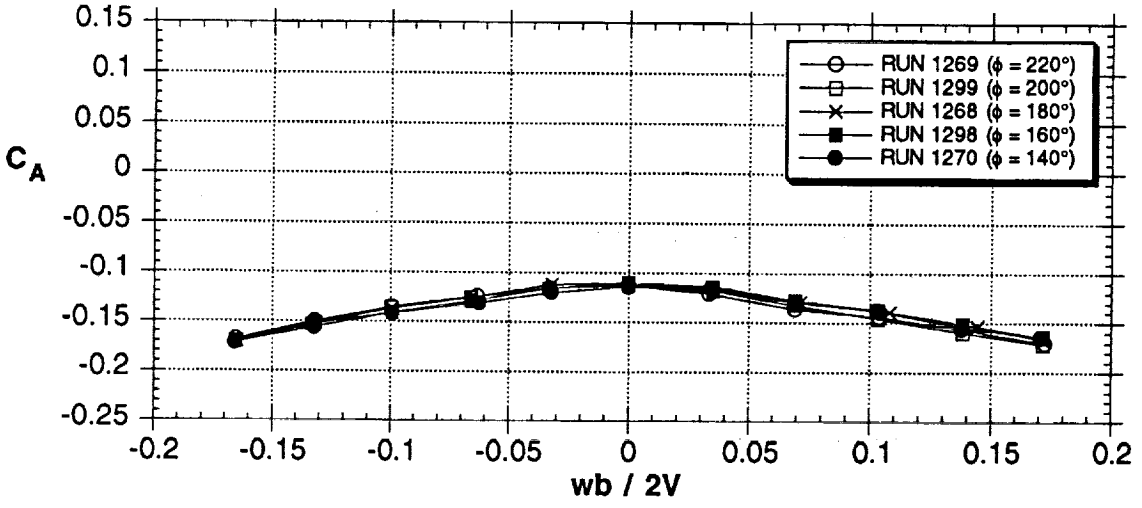

Figure 50 - Effects of single rotating nose-tip strake at 51° AOA

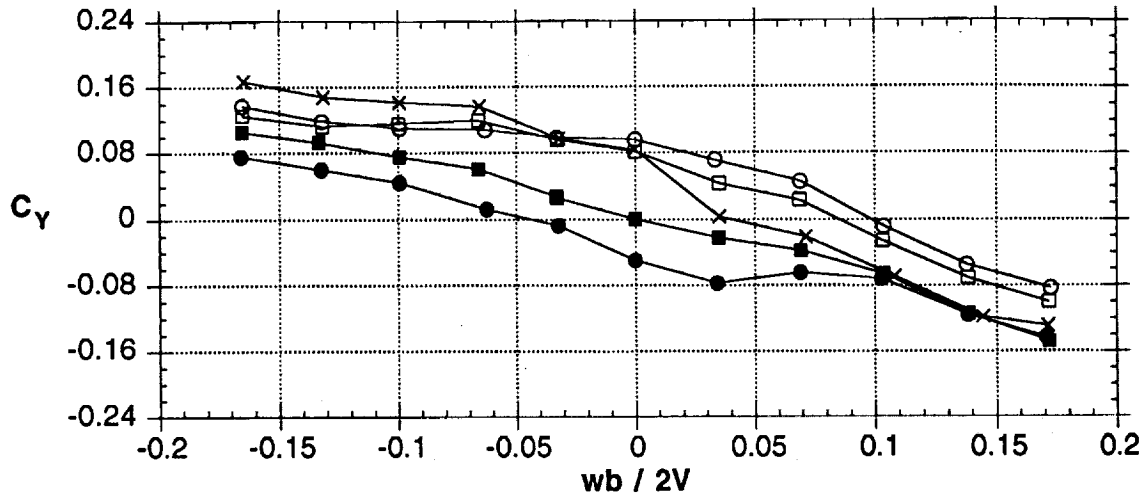

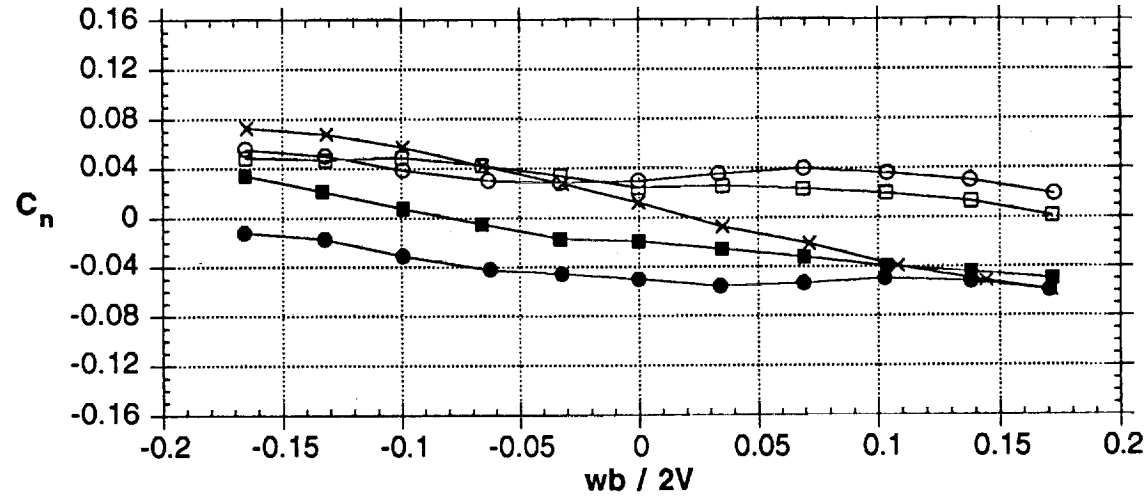

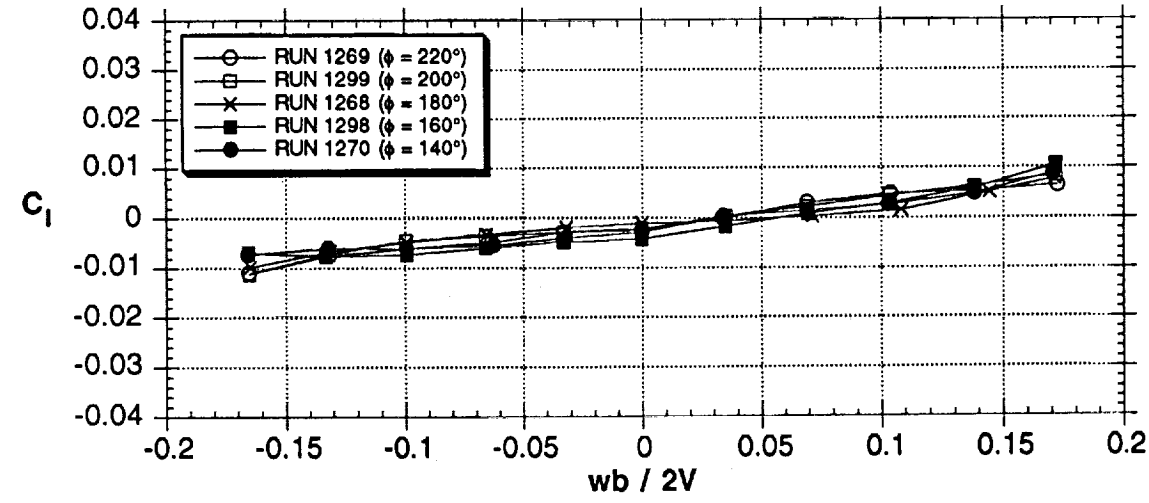

Figure 50 - Concluded

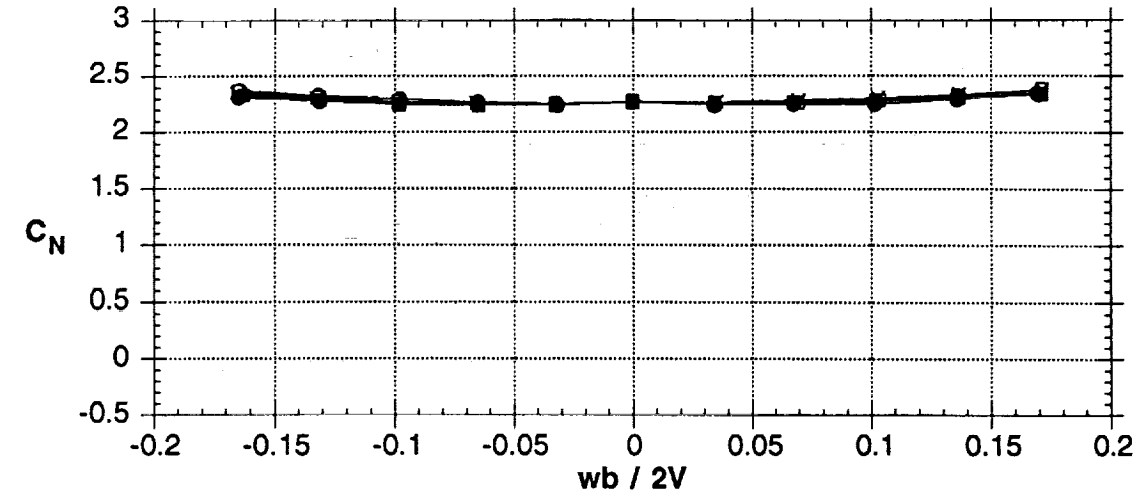

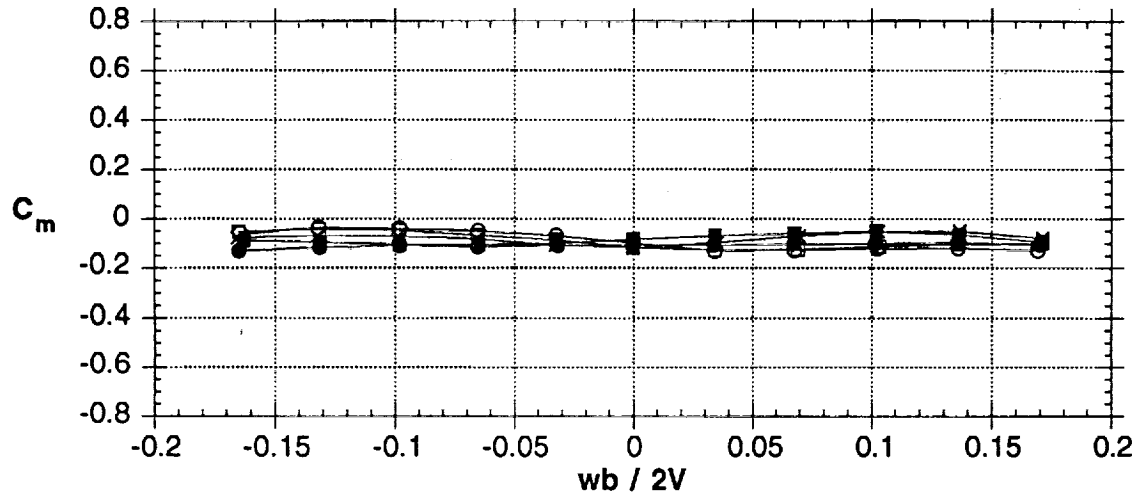

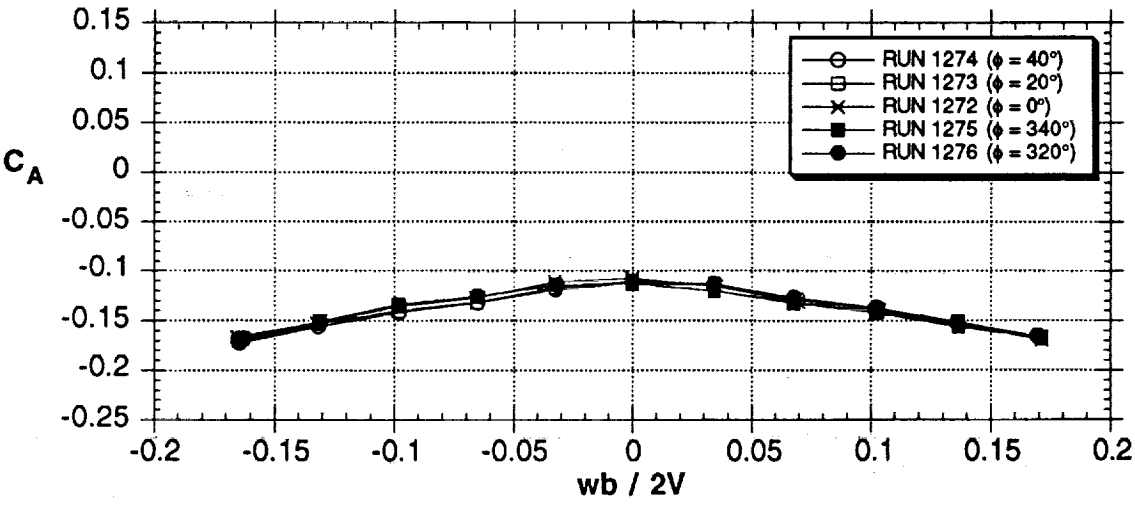

Figure 51 - Effects of dual rotating nose-tip strakes with 150° spacing, 51° AOA

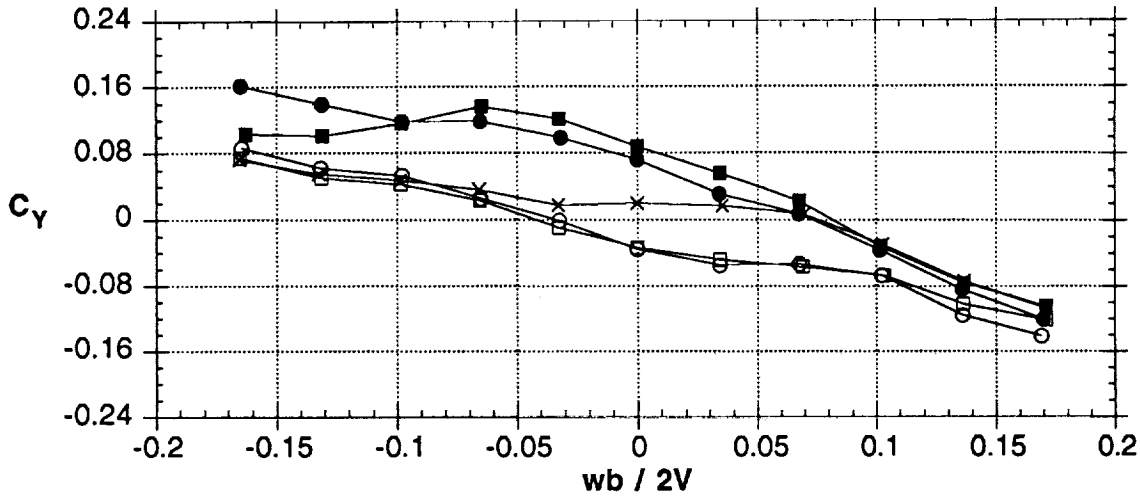

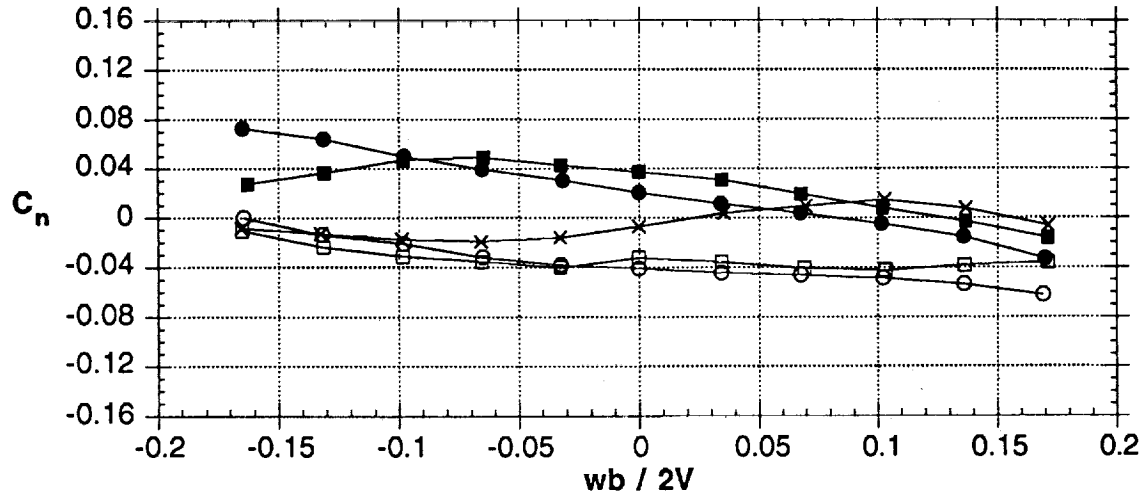

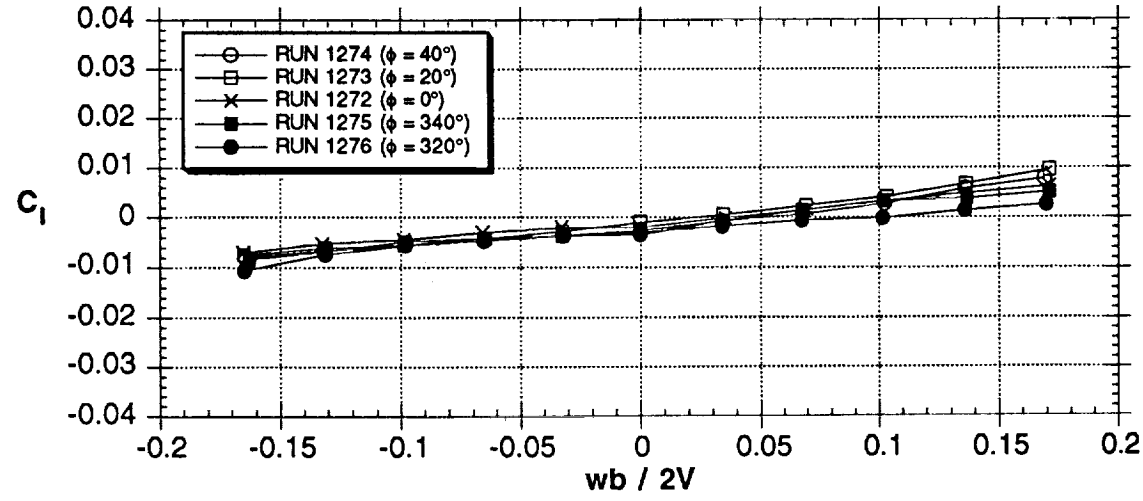

Figure 51 - Concluded

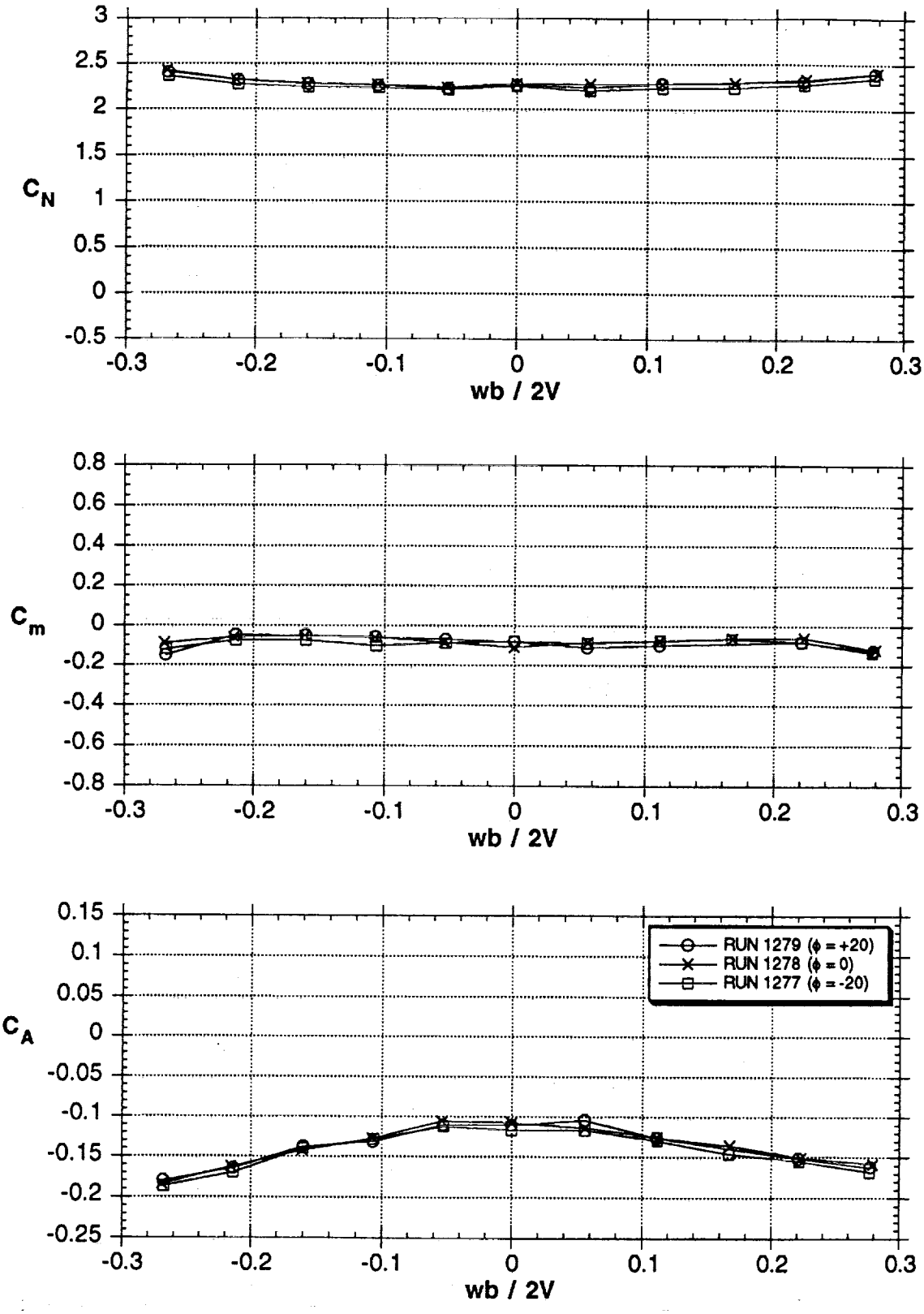

Figure 52 - Effects of dual rotating nose-tip strakes with 150° spacing at Q=10 psf (Rn=0.387x 10^6), 51° AOA

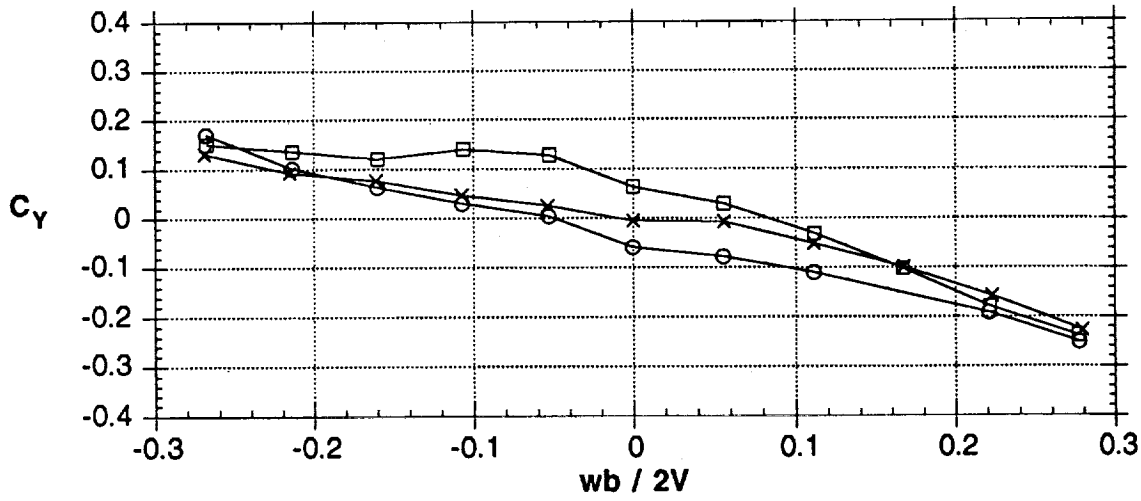

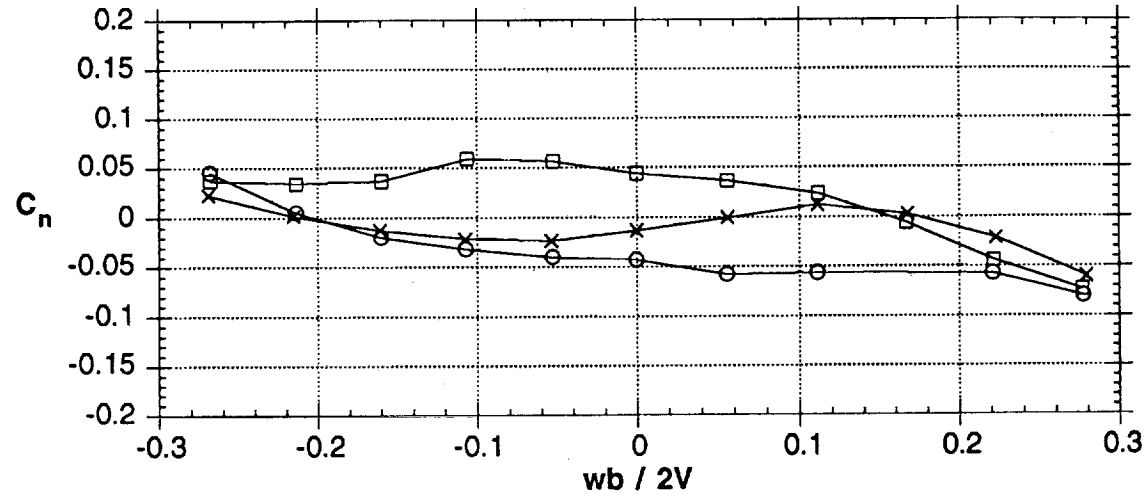

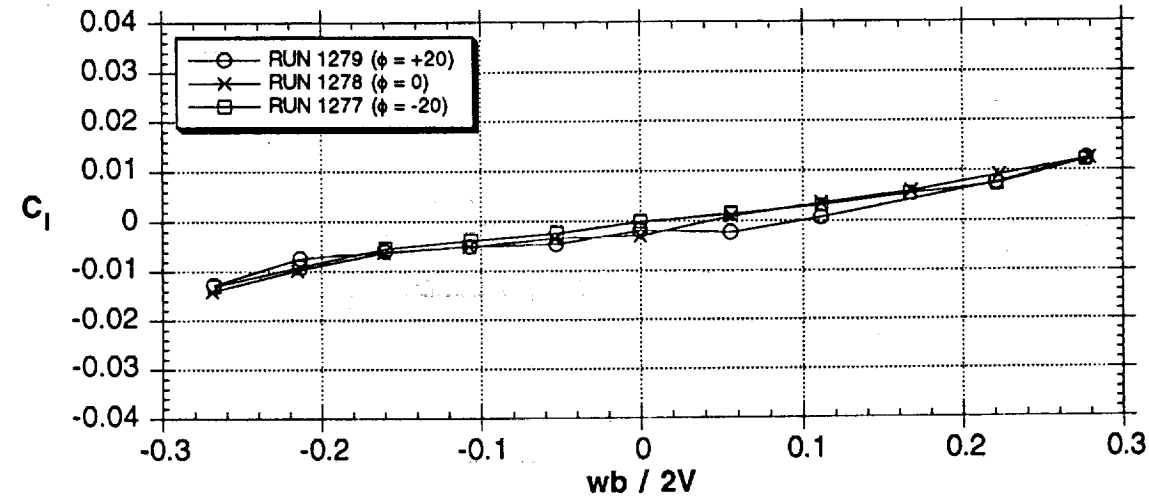

Figure 52 - Concluded

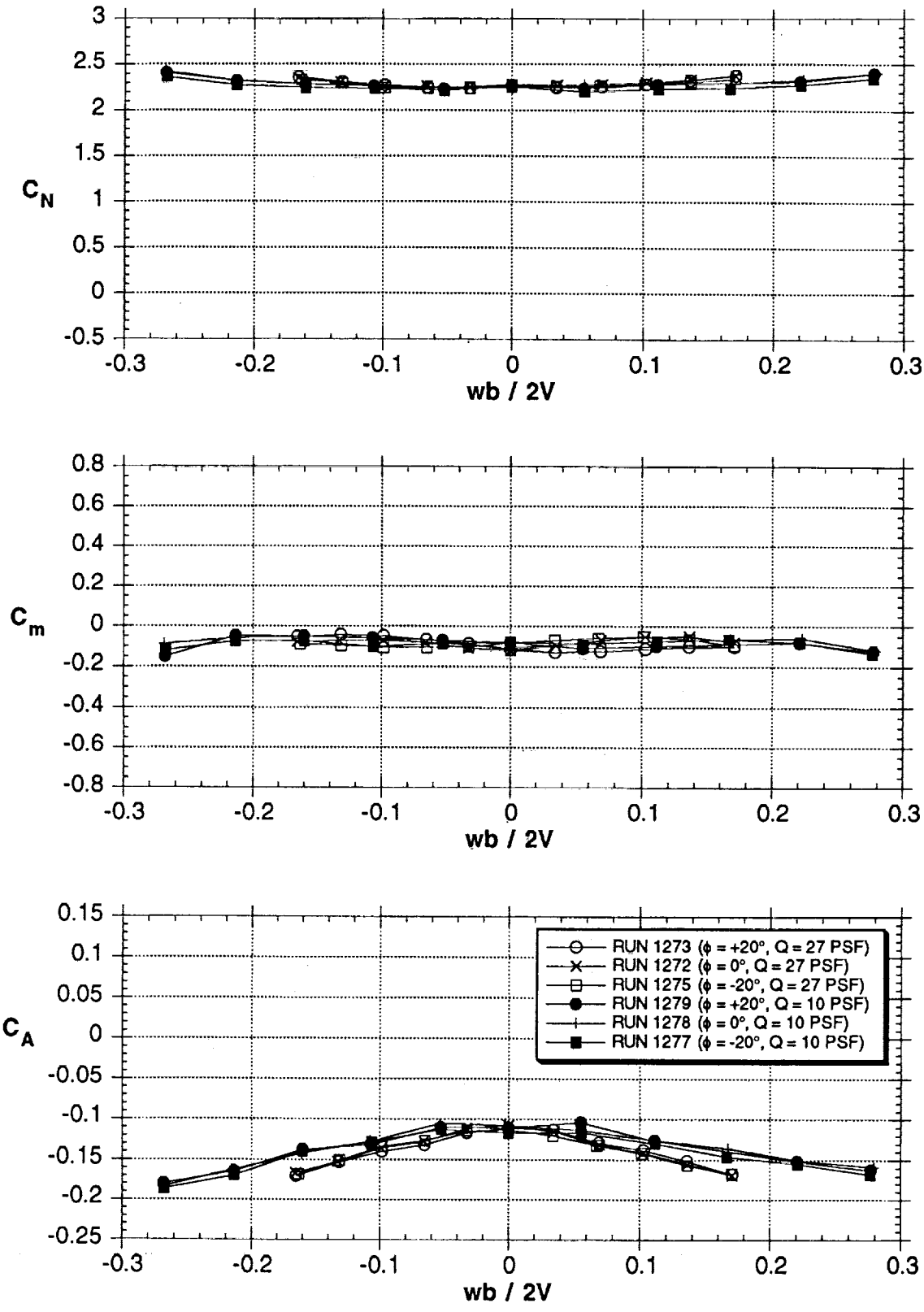

Figure 53 - Comparison of dual rotating nose-tip strakes with 150° spacing at Q=10 psf ($Rn=0.387 \times 10^6$) and Q=27 psf ($Rn=0.636 \times 10^6$), 51° AOA

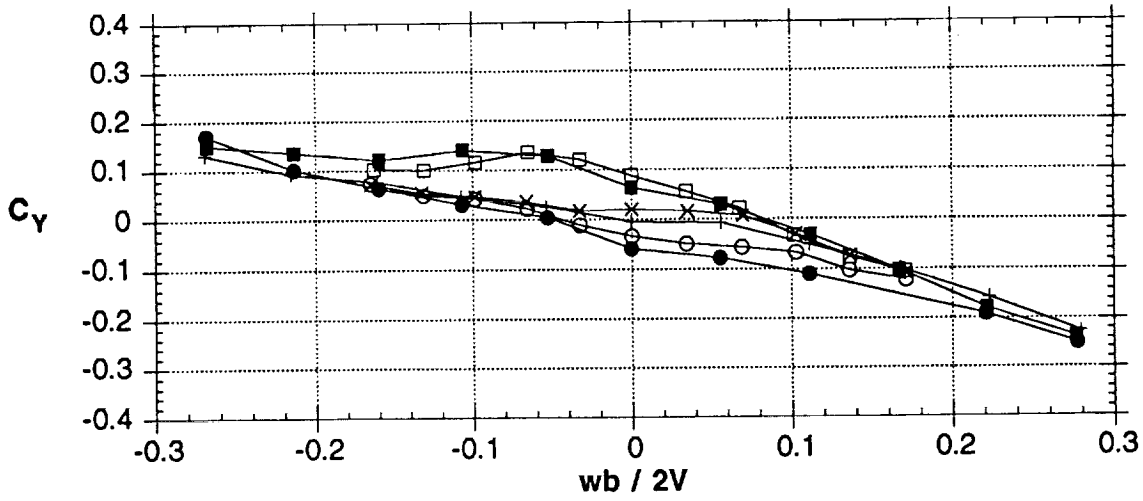

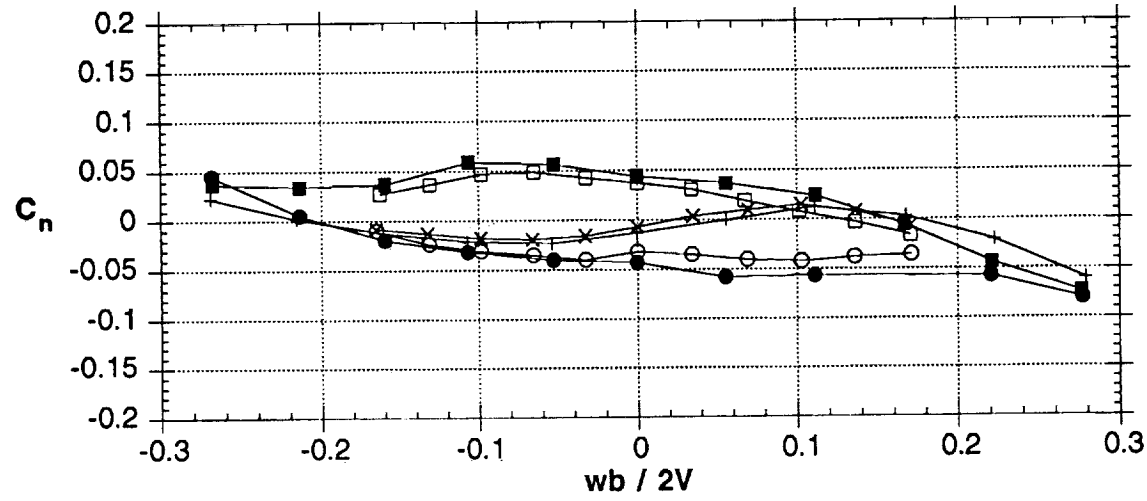

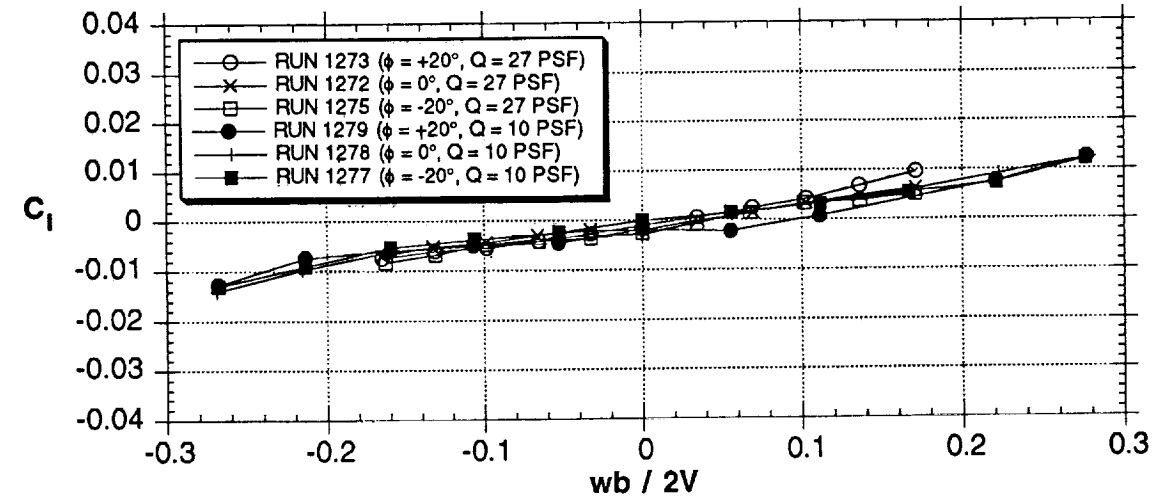

Figure 53 - Concluded

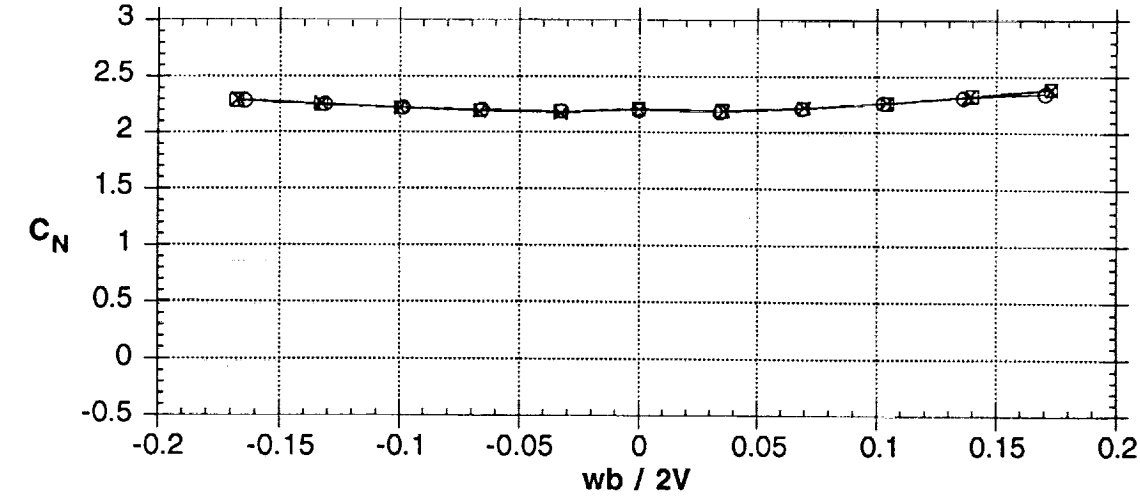

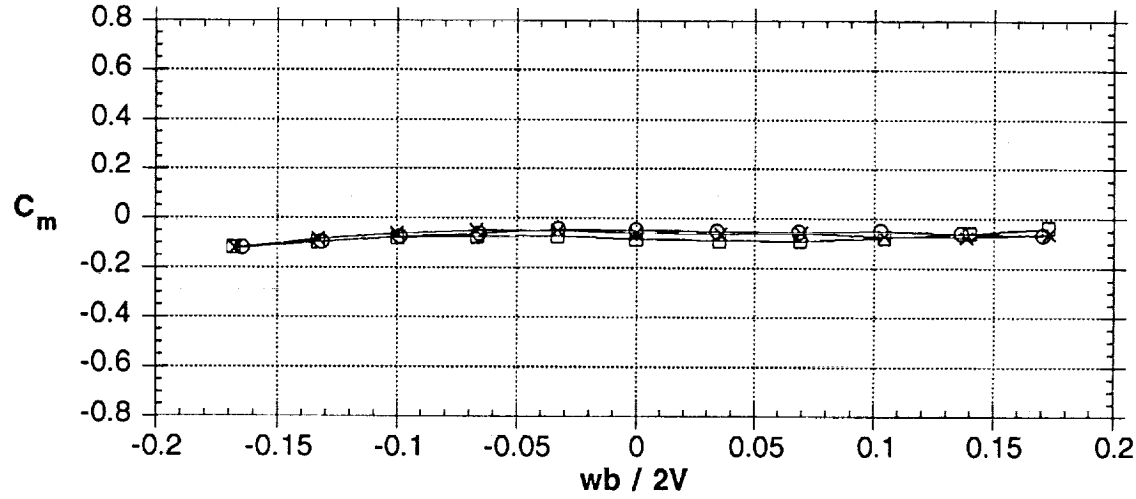

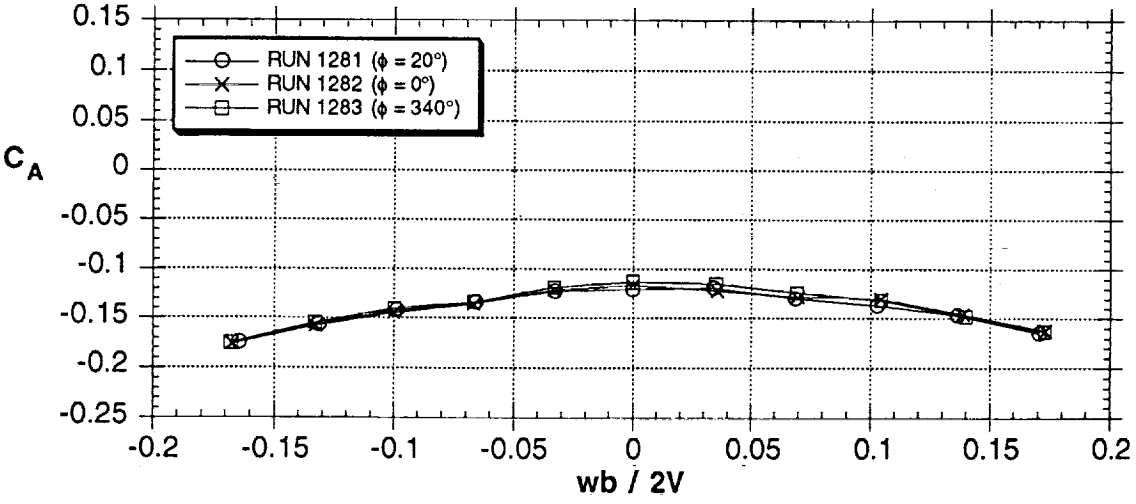

Figure 54 - Effects of dual rotating nose-tip strakes with 150° spacing at sideslip angle of β = -10°, 51° AOA

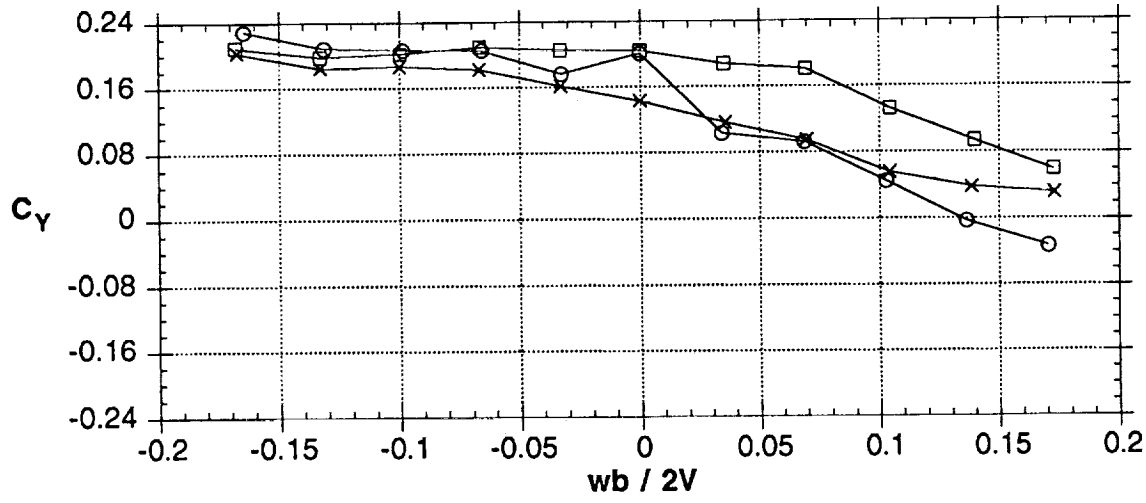

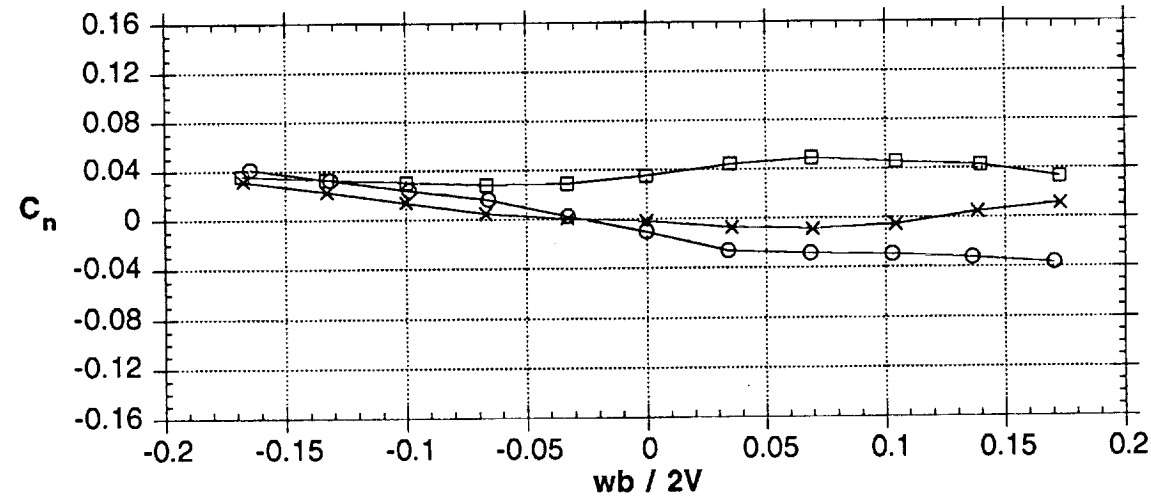

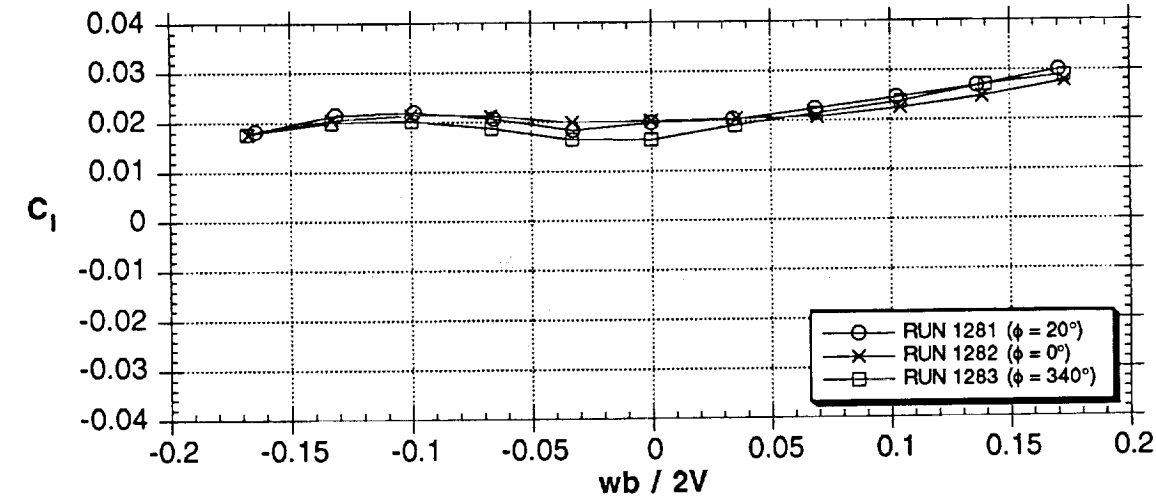

Figure 54 - Concluded

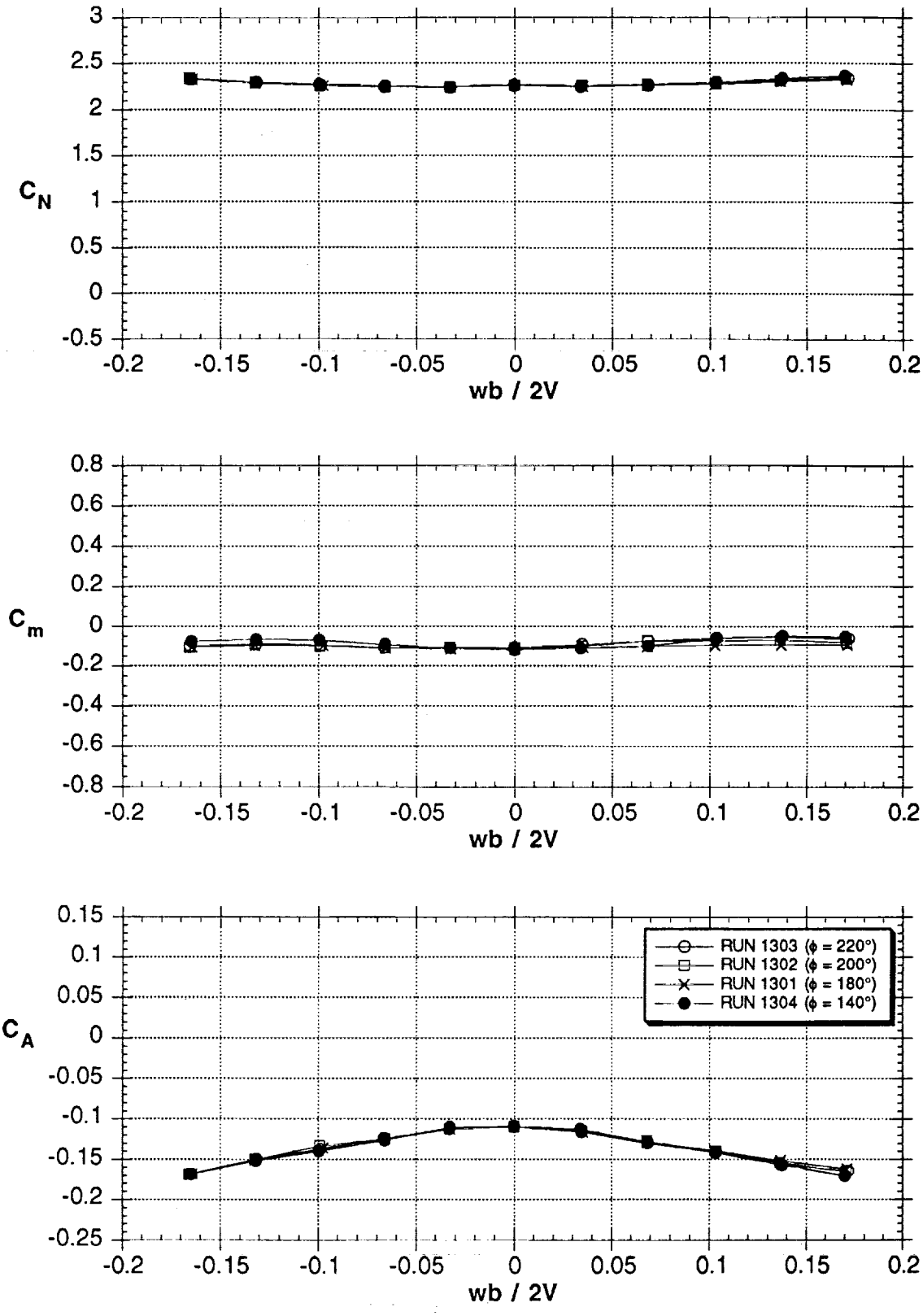

Figure 55 - Effects of dual rotating nose-tip strakes with 120° spacing, 51° AOA

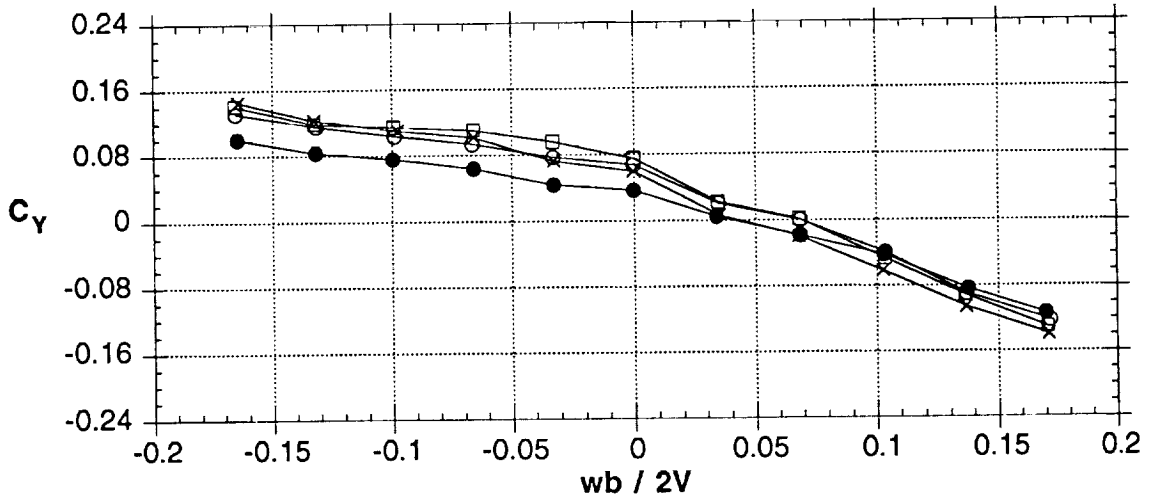

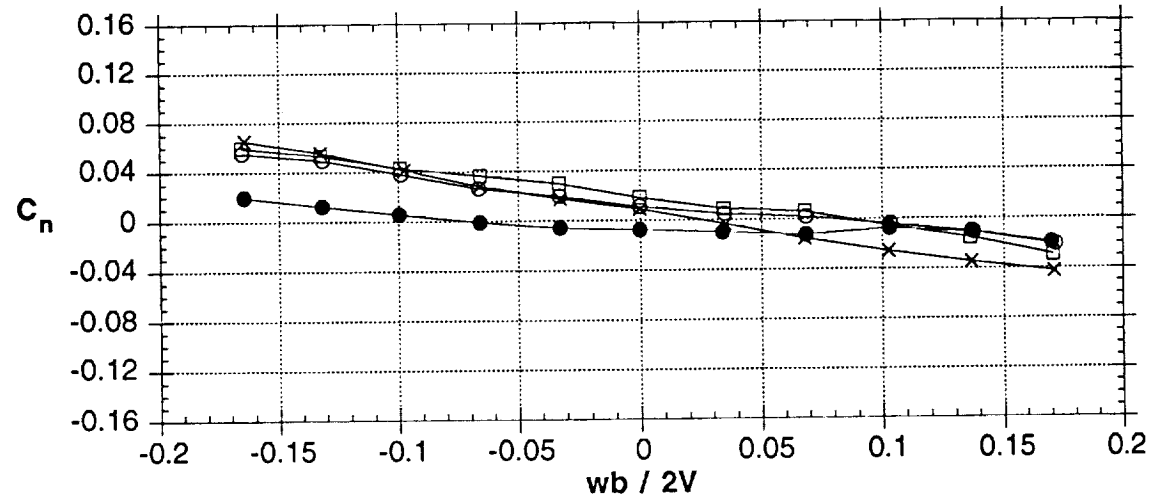

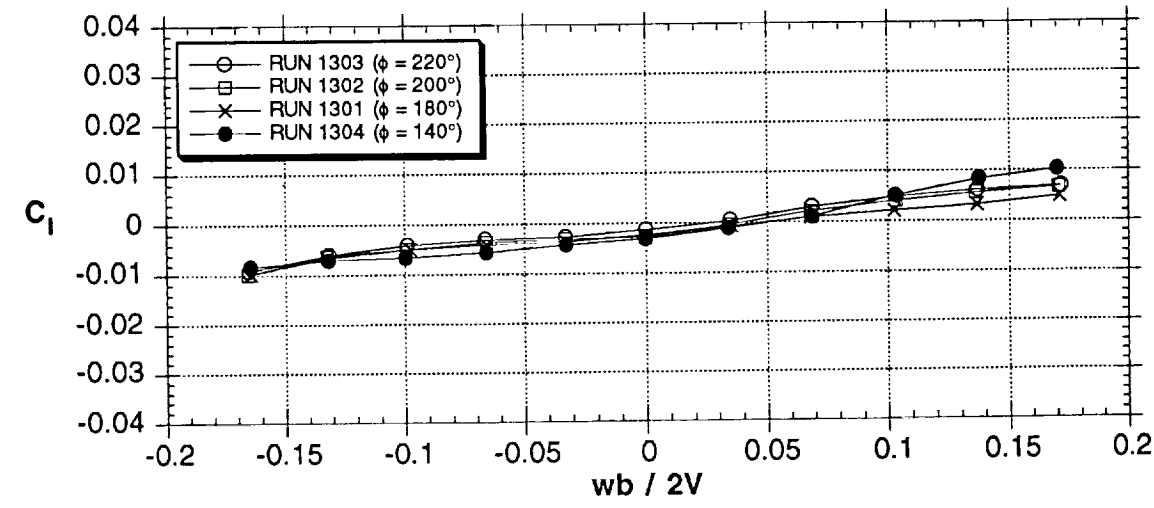

Figure 55 - Concluded

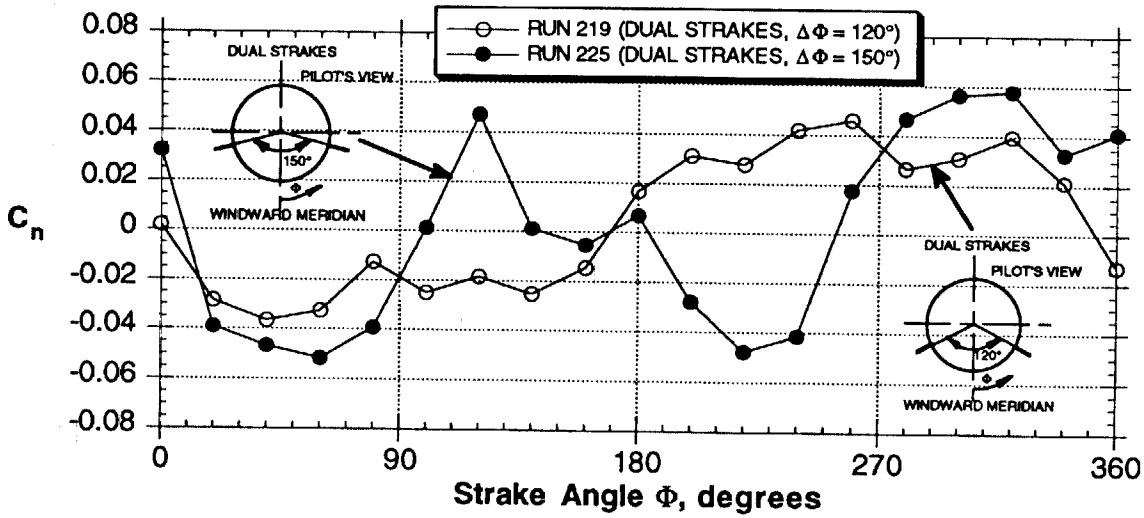

Figure 56 - Comparison of static results for rotating nose-tip strakes with 150° and 120° spacing, 51° AOA

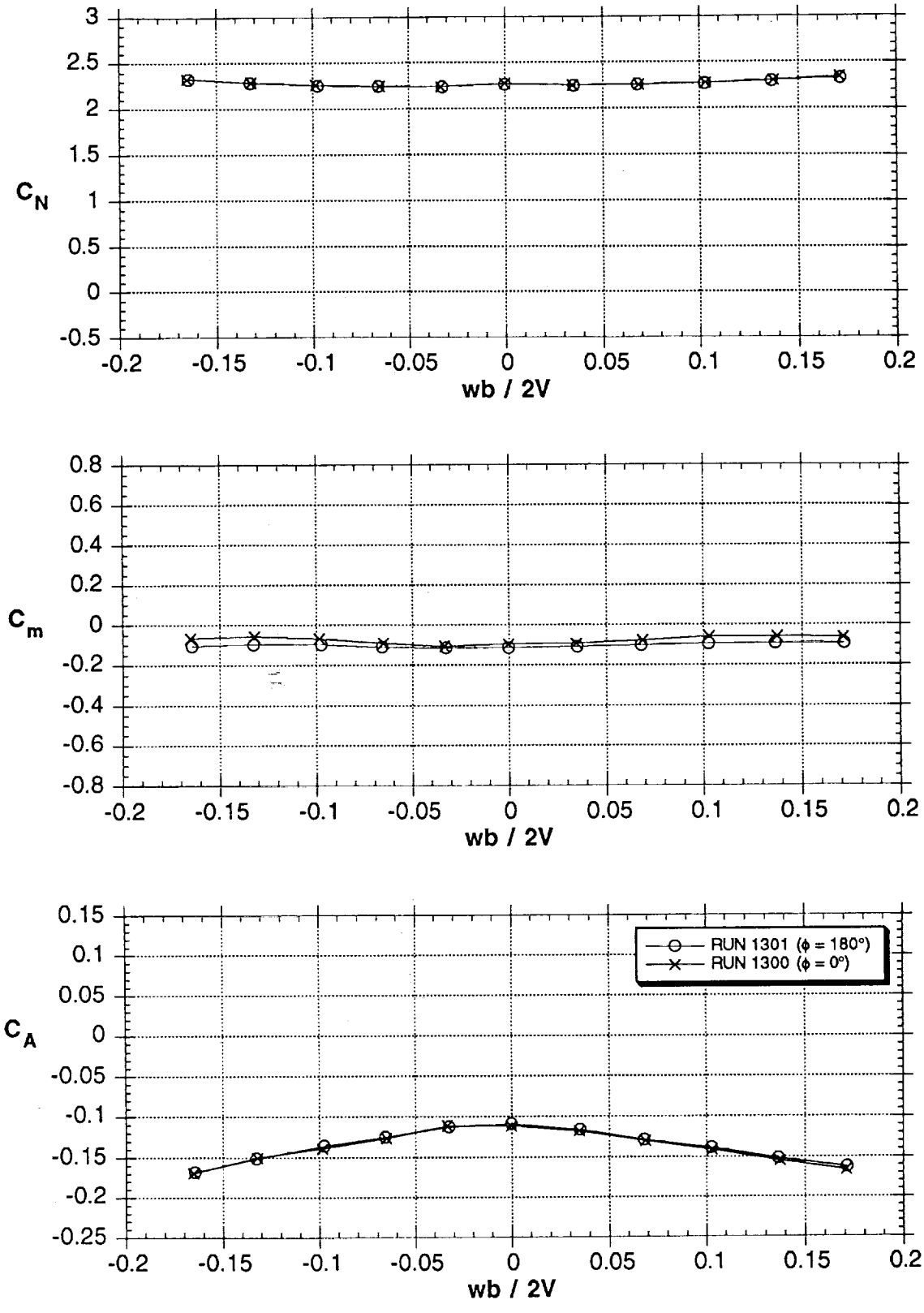

Figure 57 - Comparison of dual rotating nose-tip strakes with 120° spacing at references of Φ=0° and Φ=180°

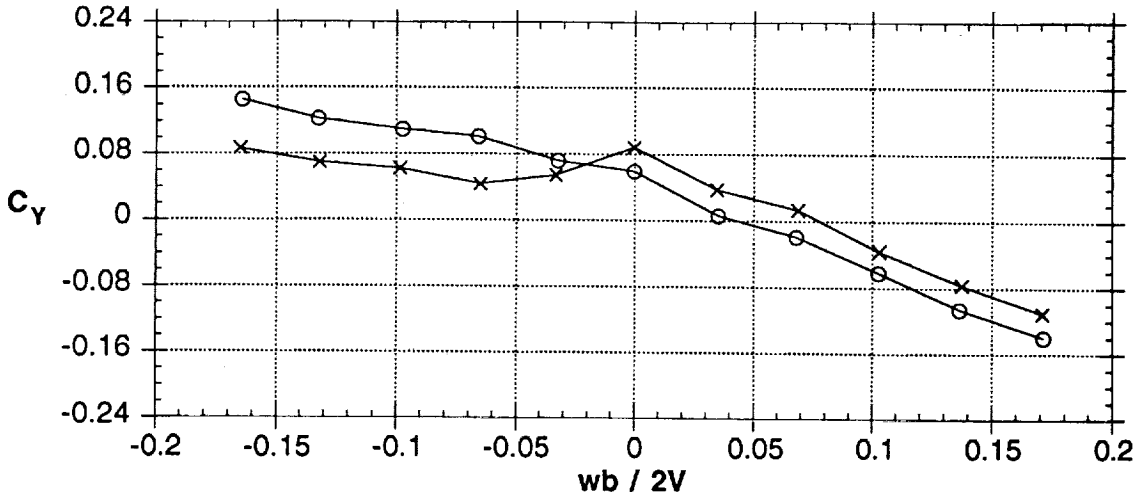

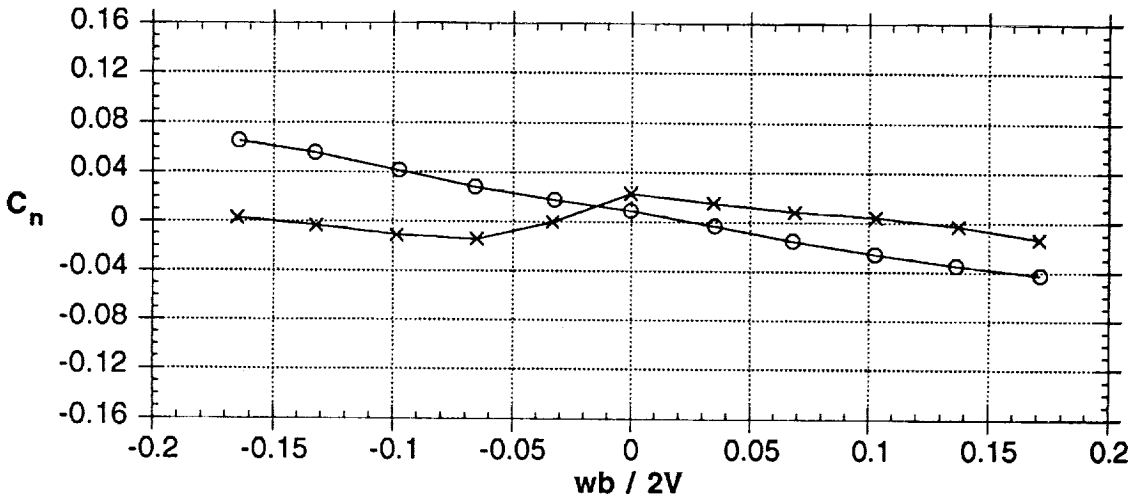

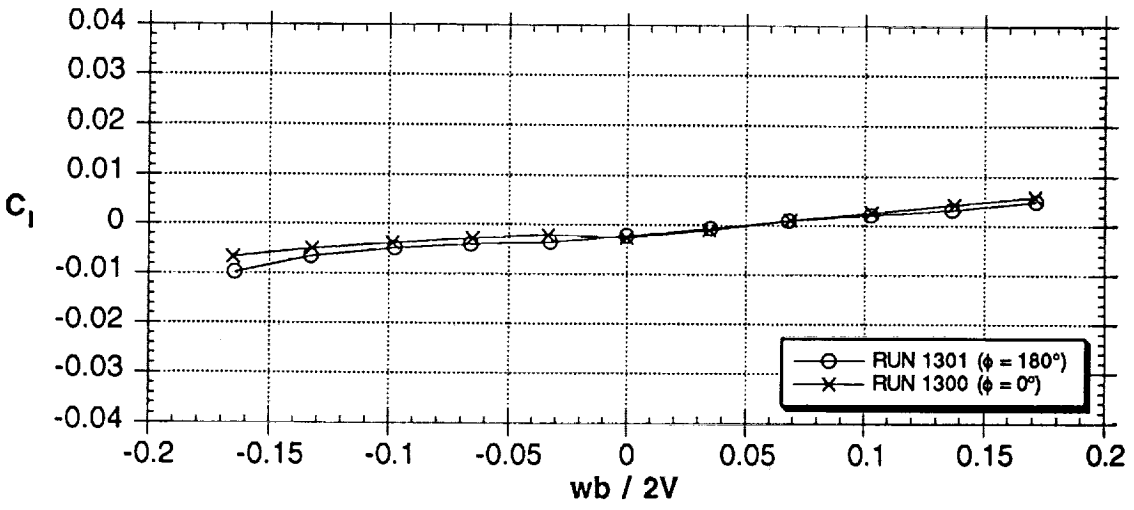

Figure 57 - Concluded

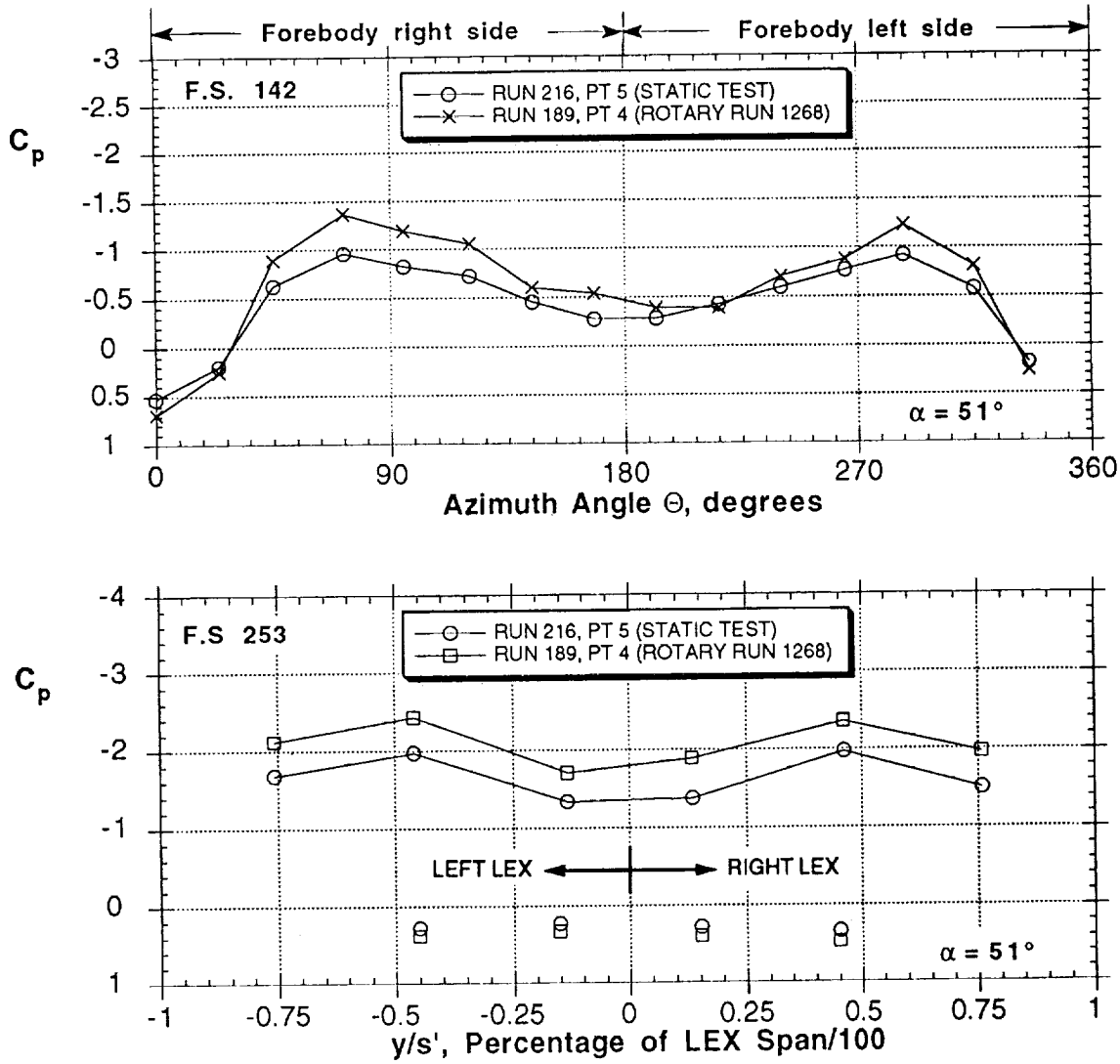

(a) Single Strake, comparison to static test, Φ = 180°

Figure 58 - Rotating strake pressure distribution at 51° AOA

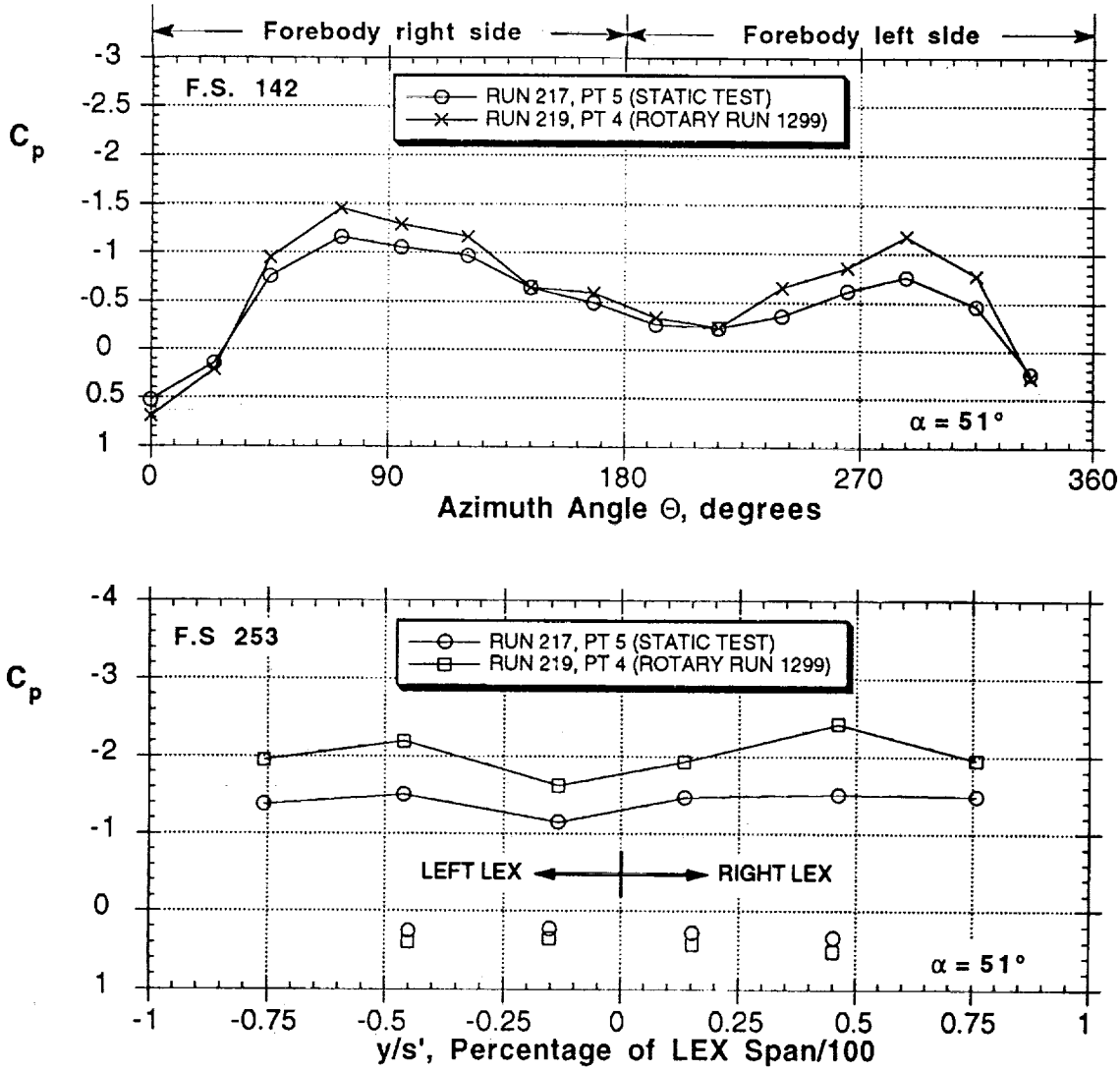

(b) Single Strake, comparison to static test, Φ = 200°

Figure 58 - Continued

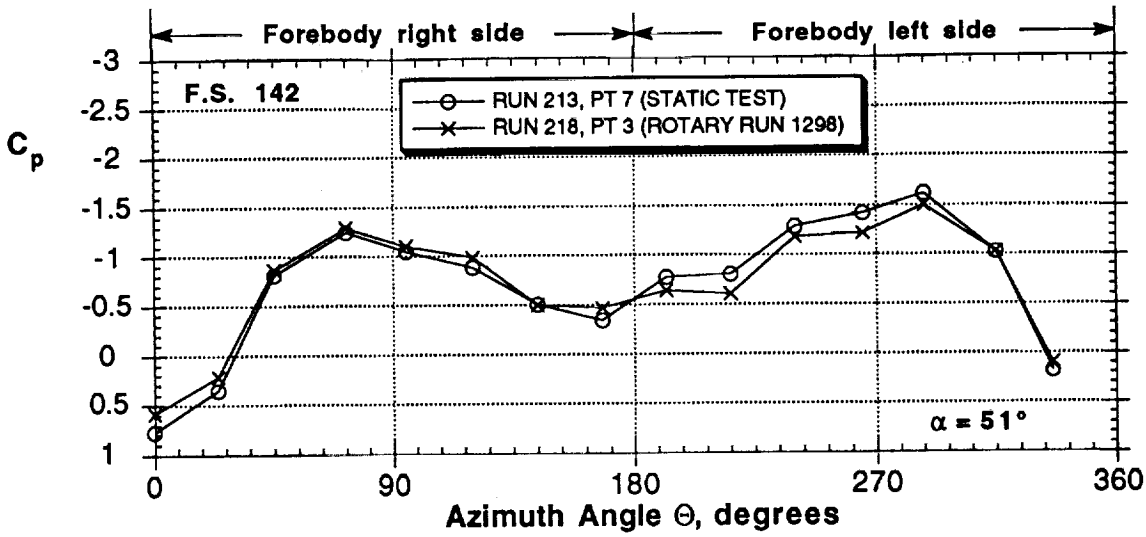

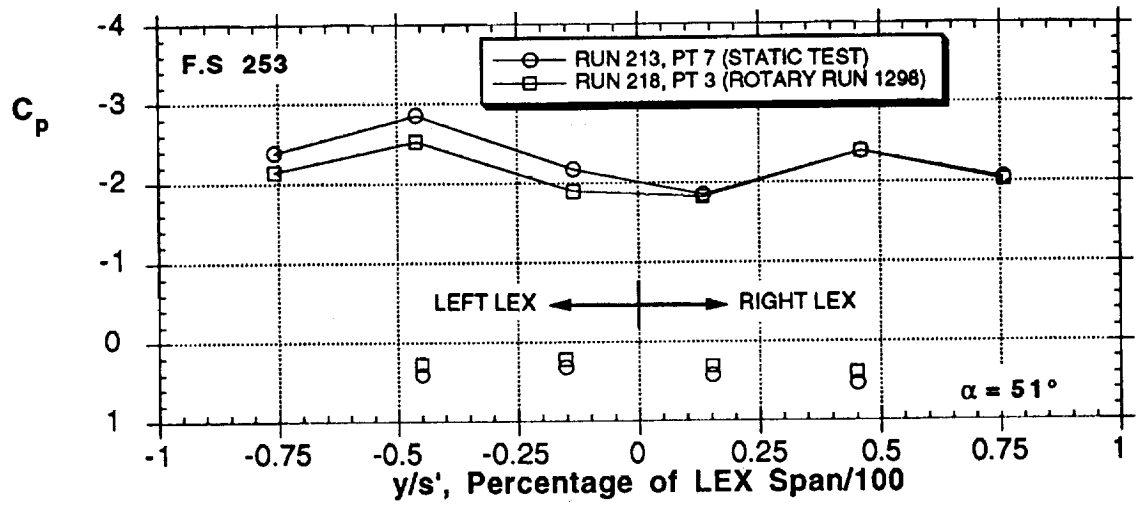

(c) Single Strake, comparison to static test, Φ = 160°

Figure 58 - Continued

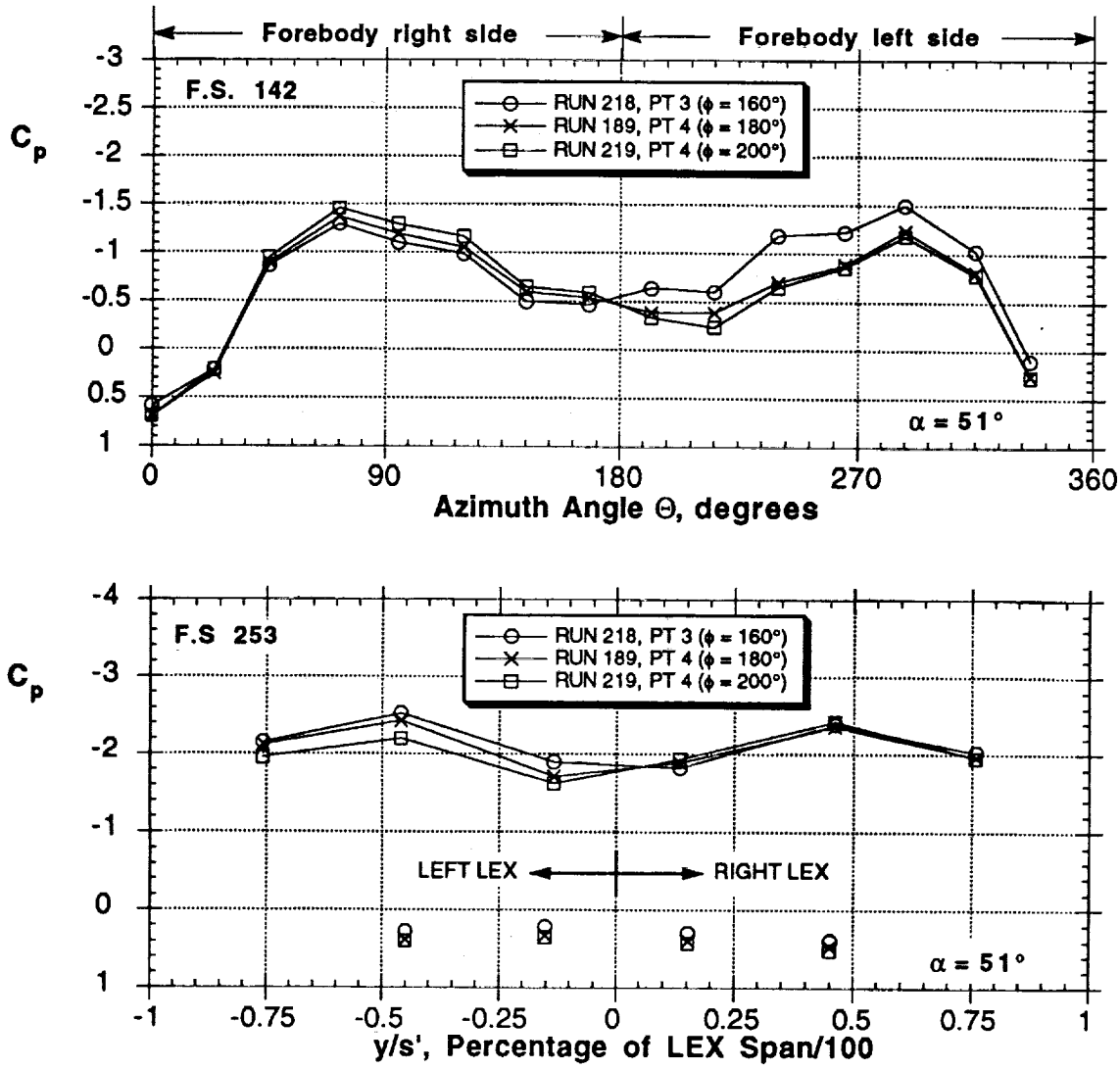

(d) Single Strake, effect of strake angle, $\omega b/2V = 0$

Figure 58 - Continued

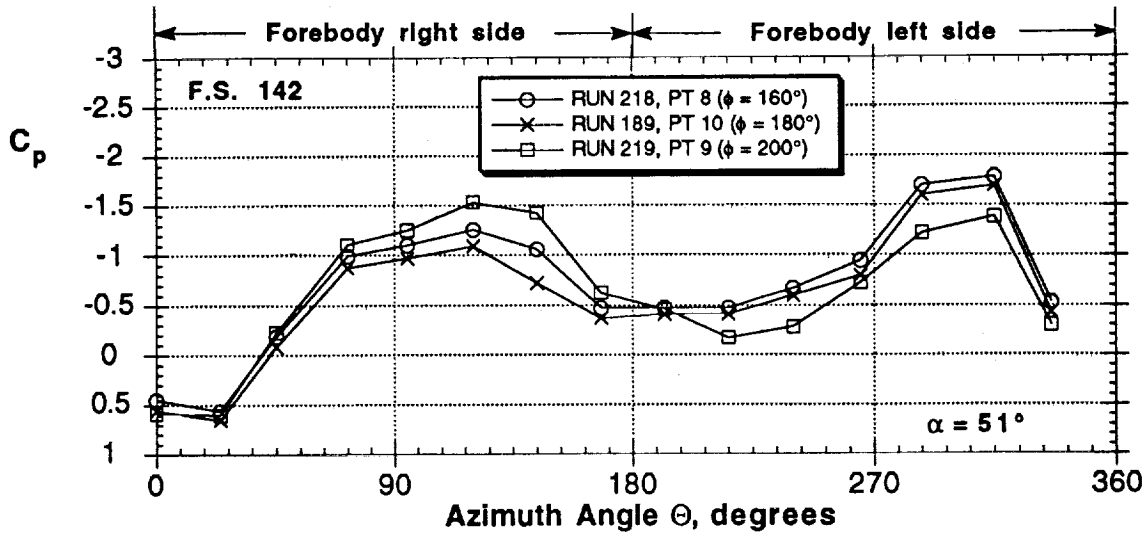

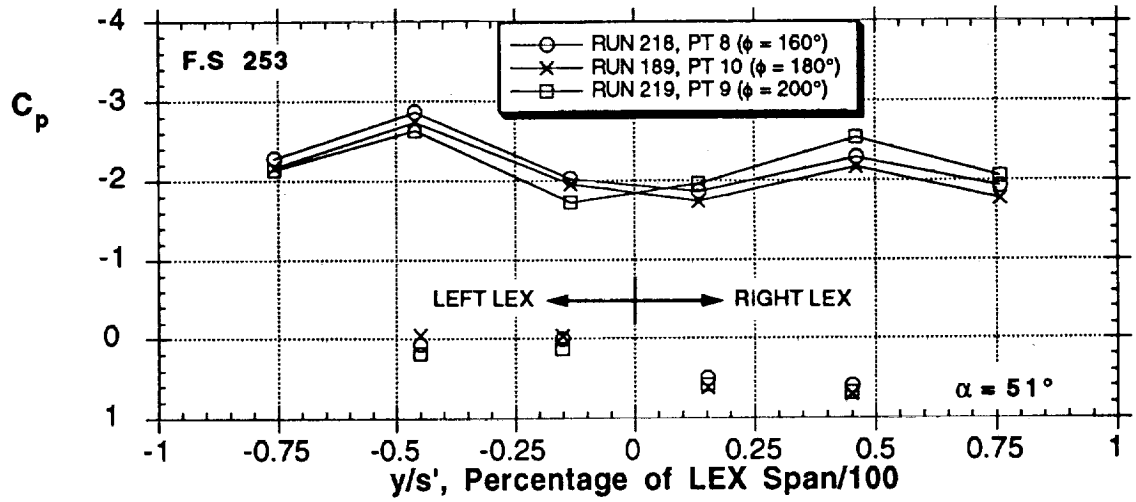

(e) Single Strake, effect of strake angle, ωb/2V = 0.15

Figure 58 - Continued

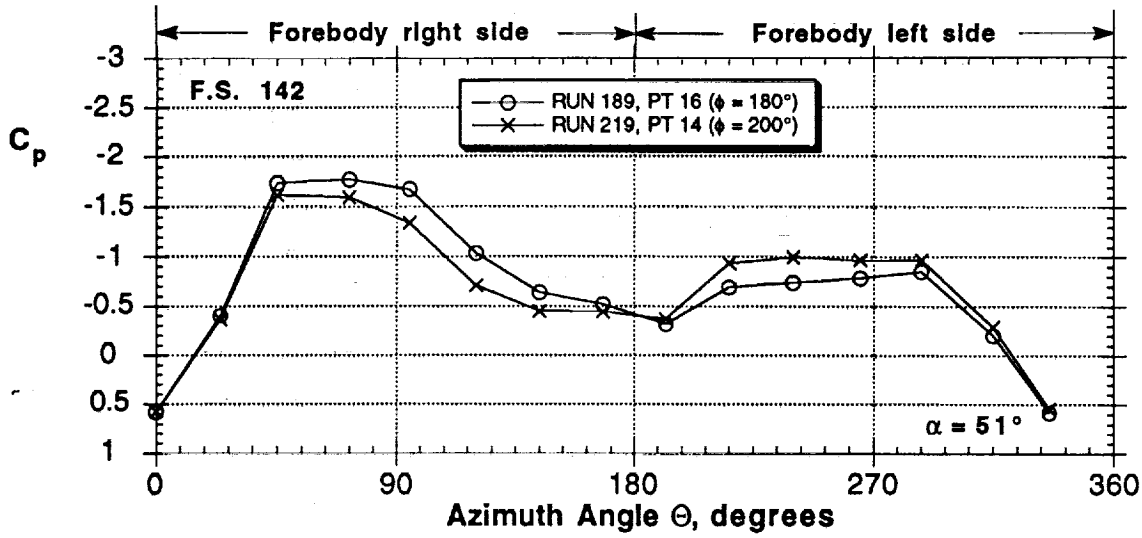

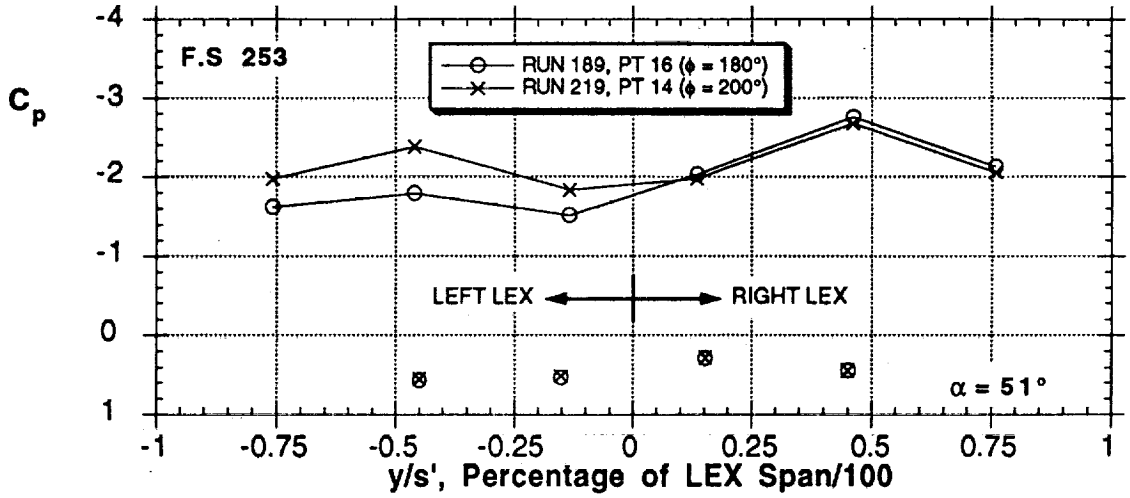

(f) Single Strake, effect of strake angle, $\omega b/2V = -0.15$

Figure 58 - Continued

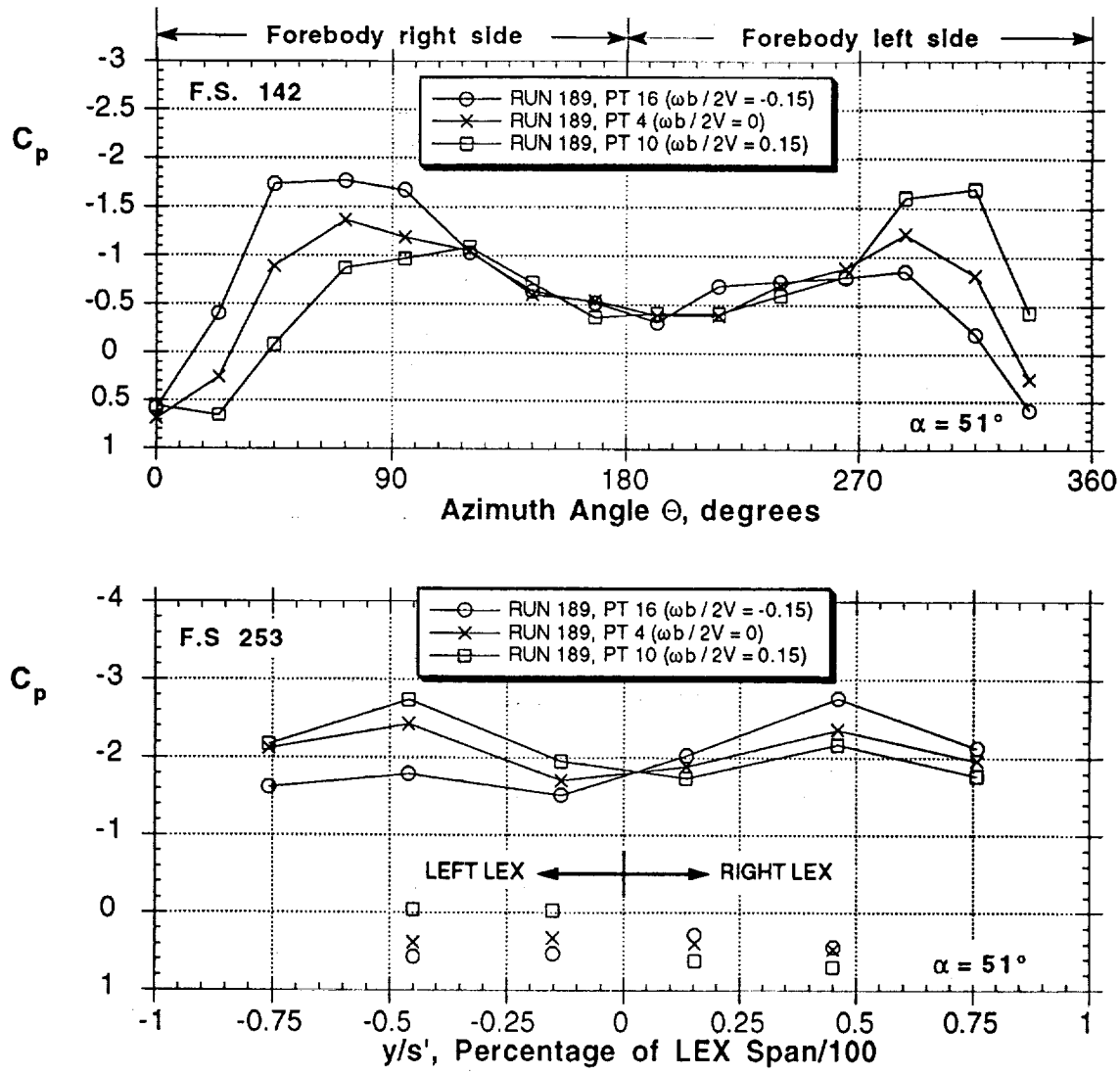

(g) Single Strake, effect of ωb/2V, Φ = 180°

Figure 58 - Continued

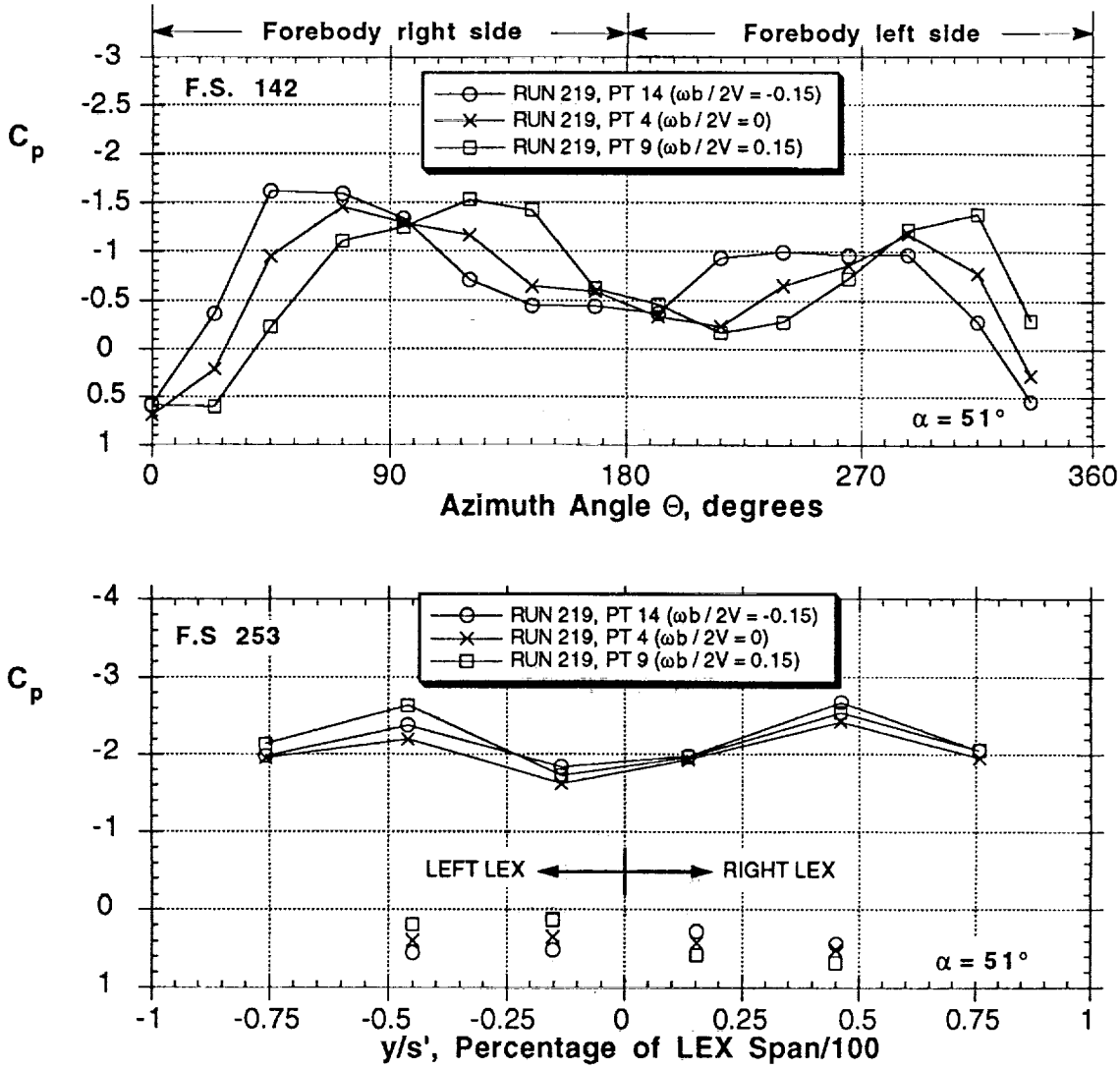

(h) Single Strake, effect of ωb/2V, Φ = 200°

Figure 58 - Continued

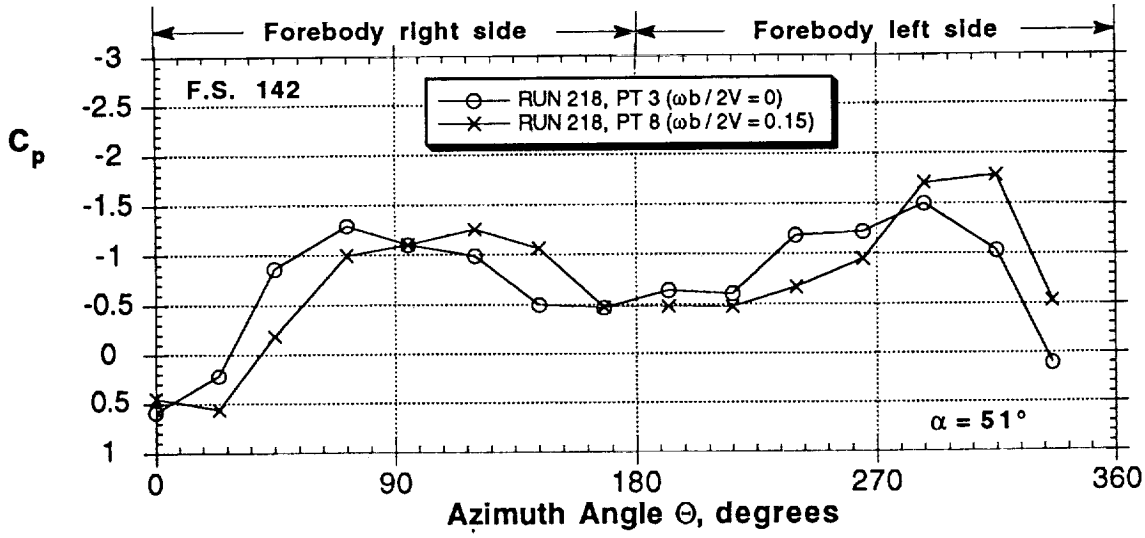

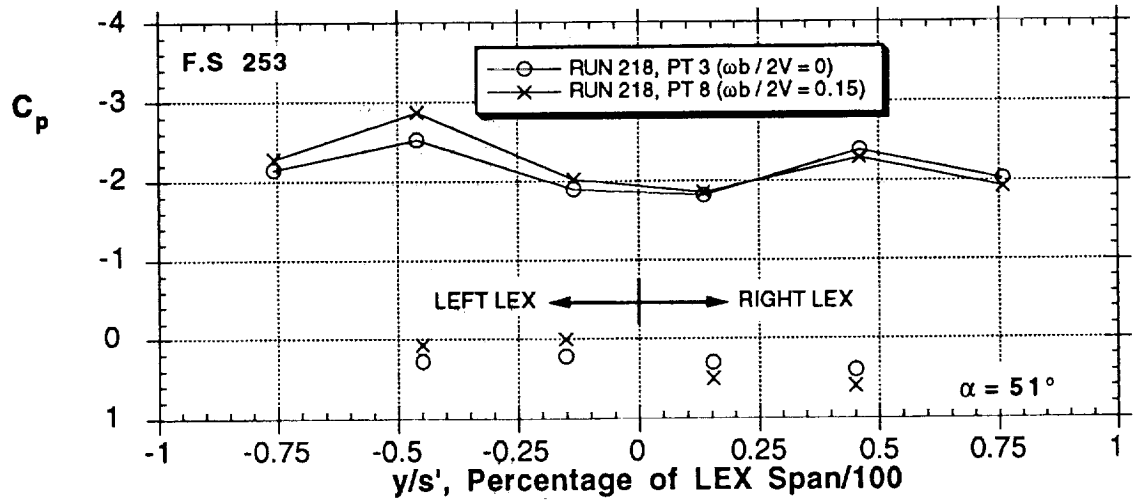

(i) Single Strake, effect of ωb/2V, Φ = 160°

Figure 58 - Continued

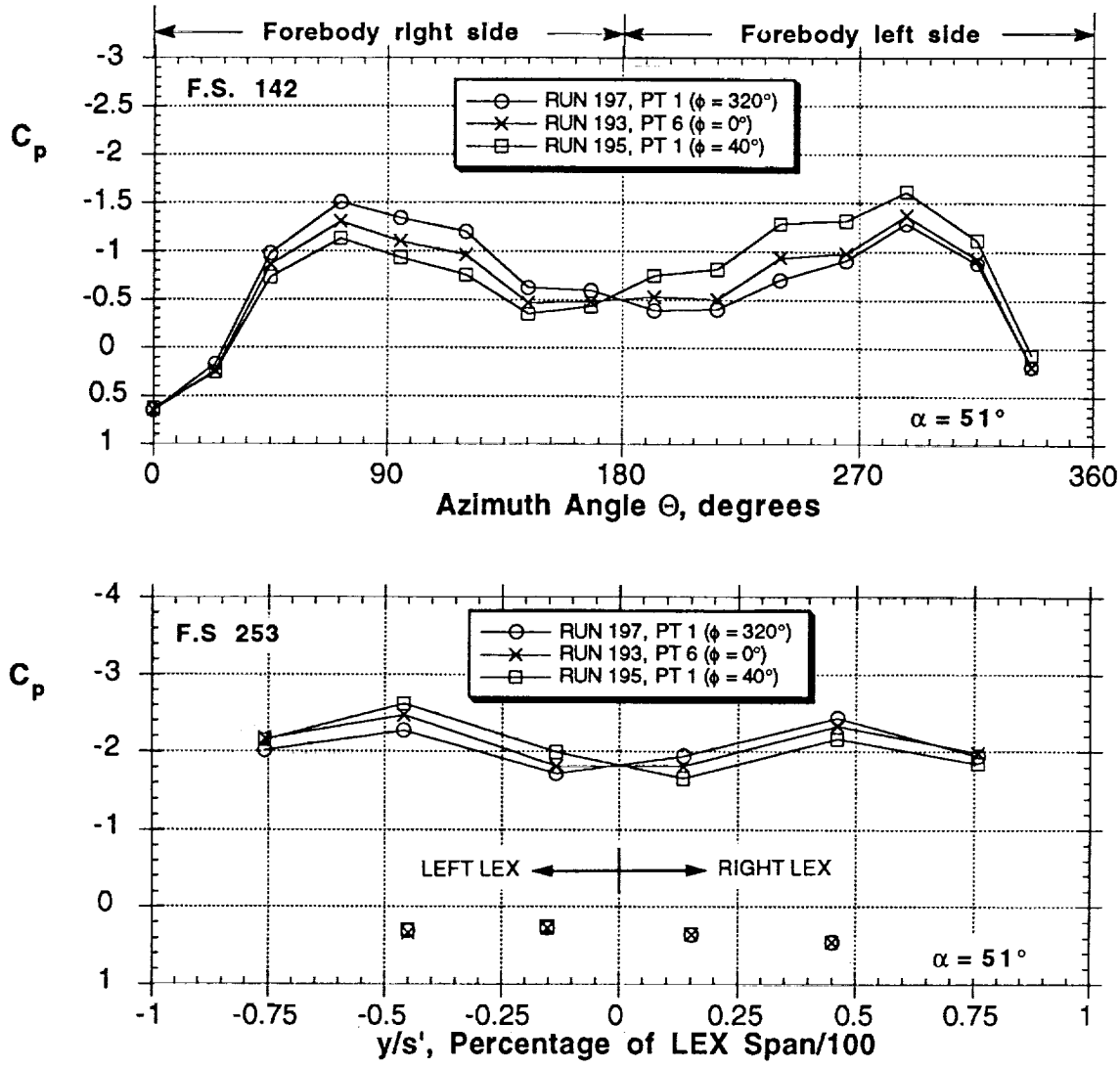

(j) 150° Dual Strakes, effect of strake angle, $\omega b/2V = 0$

Figure 58 - Continued

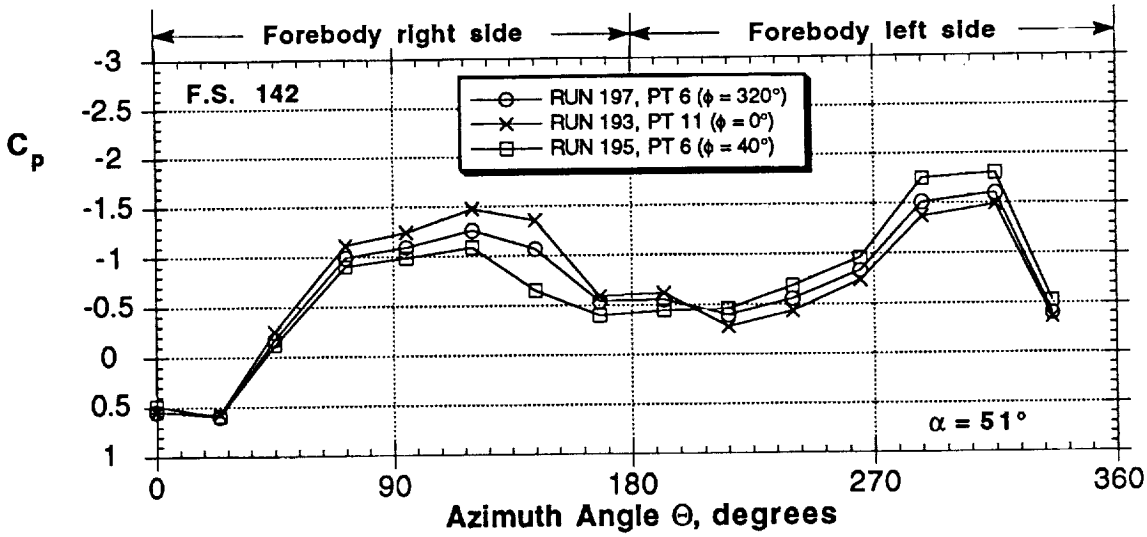

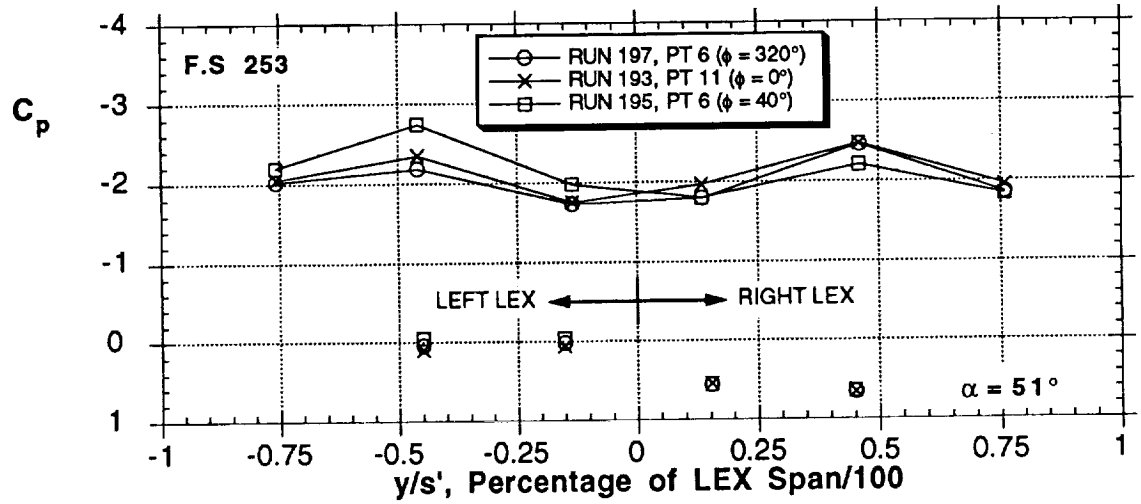

(k) 150° Dual Strakes, effect of strake angle, $\omega b/2V = 0.15$

Figure 58 - Continued

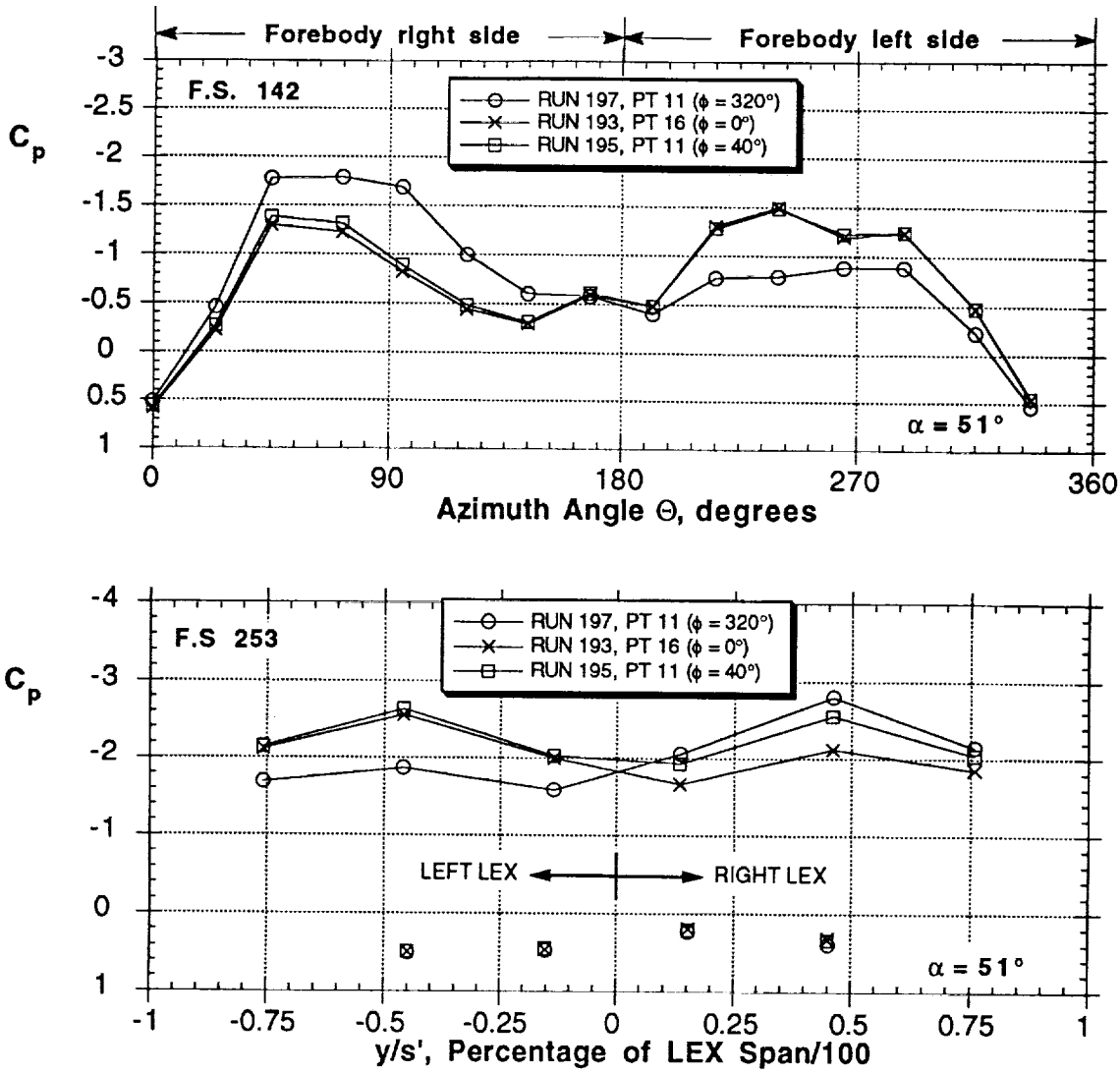

(l) 150° Dual Strakes, effect of strake angle, ωb/2V = -0.15

Figure 58 - Continued

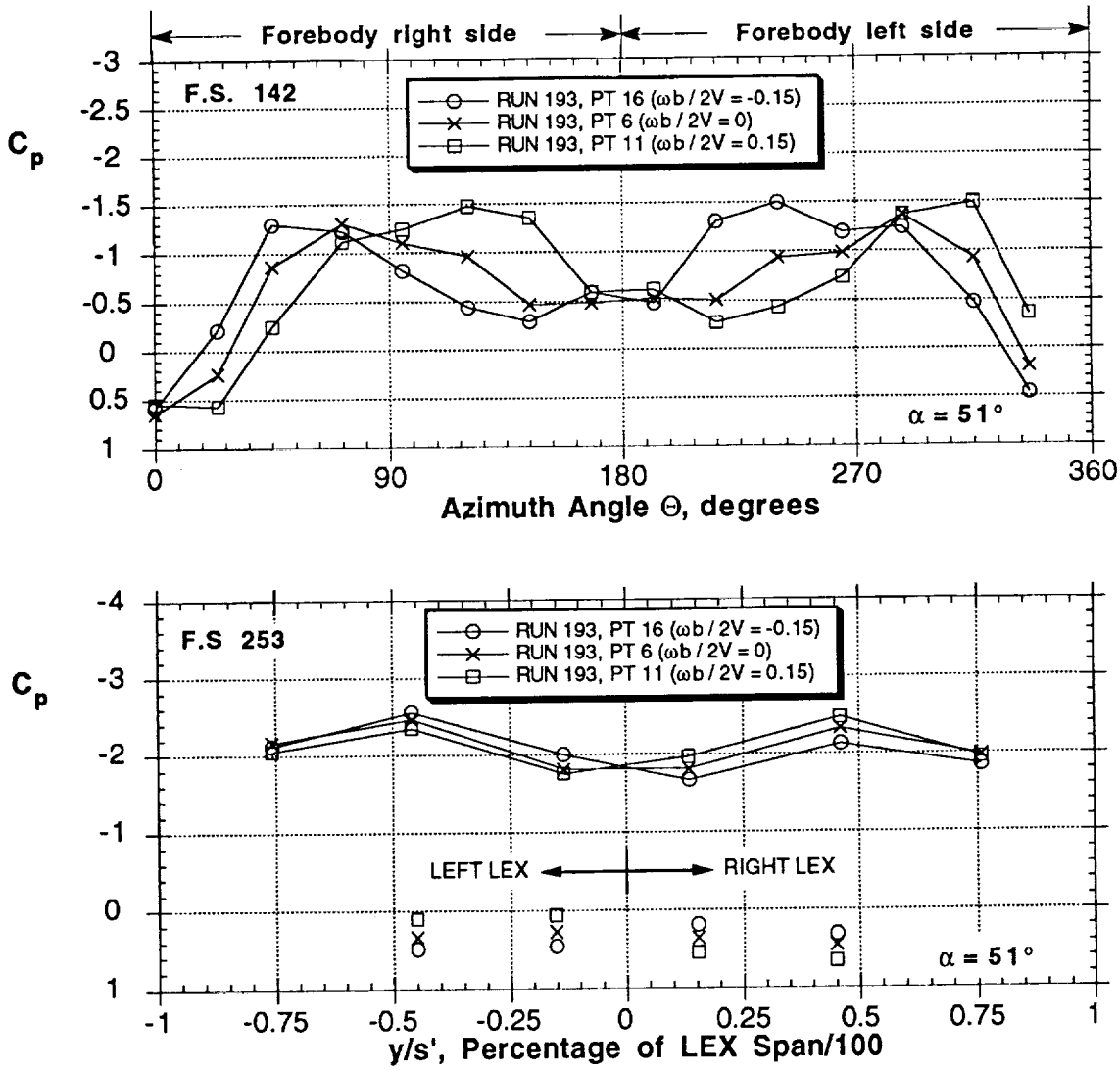

(m) 150° Dual Strakes, effect of ωb/2V, Φ = 180°

Figure 58 - Continued

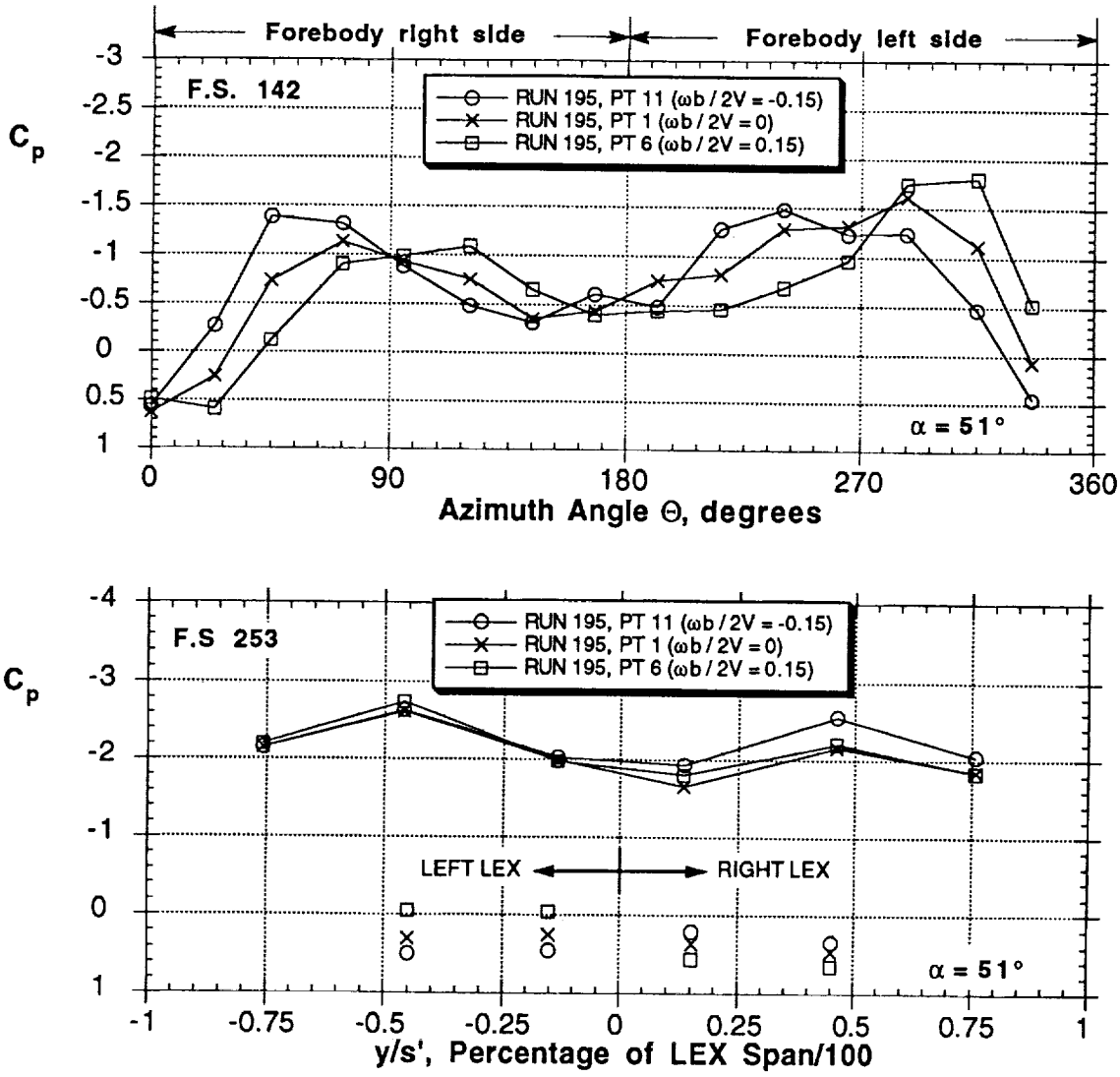

(n) 150° Dual Strakes, effect of ωb/2V, Φ = 40°

Figure 58 - Continued

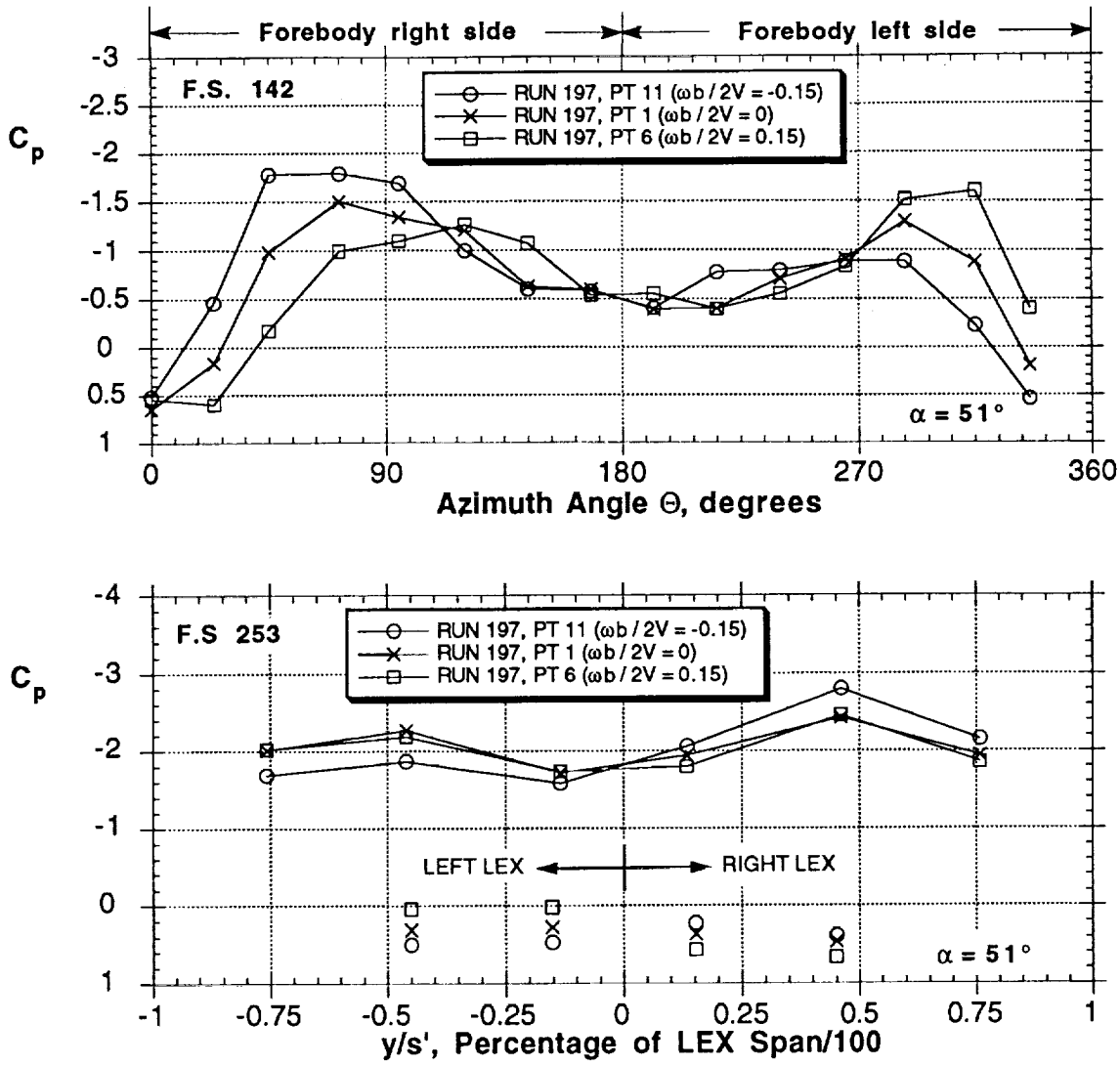

(o) 150° Dual Strakes, effect of ωb/2V, Φ = 320°

Figure 58 - Concluded

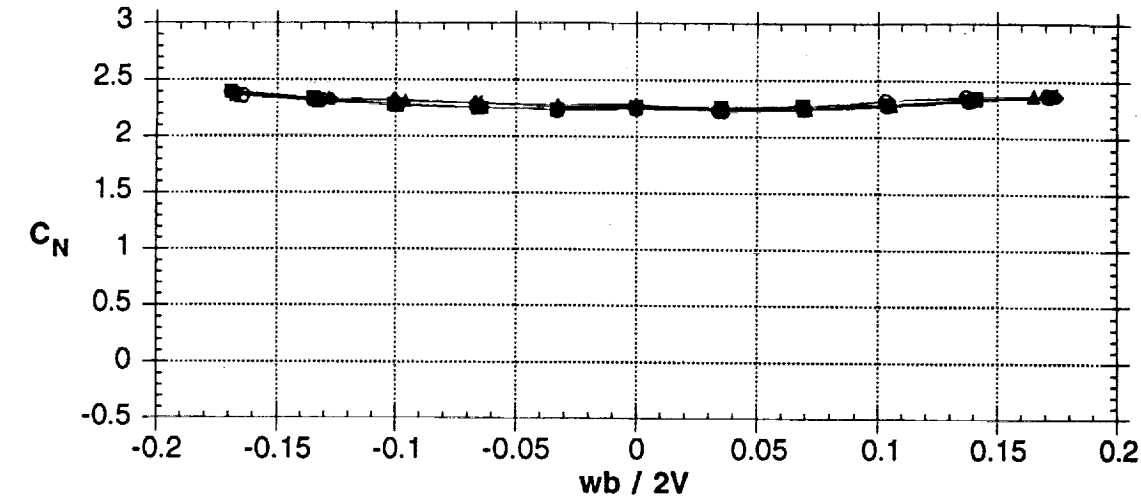

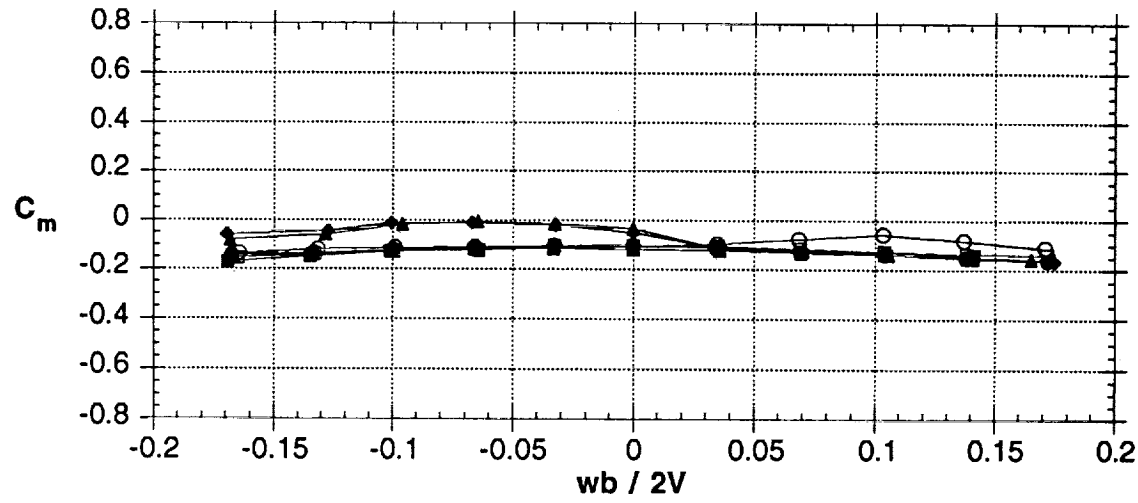

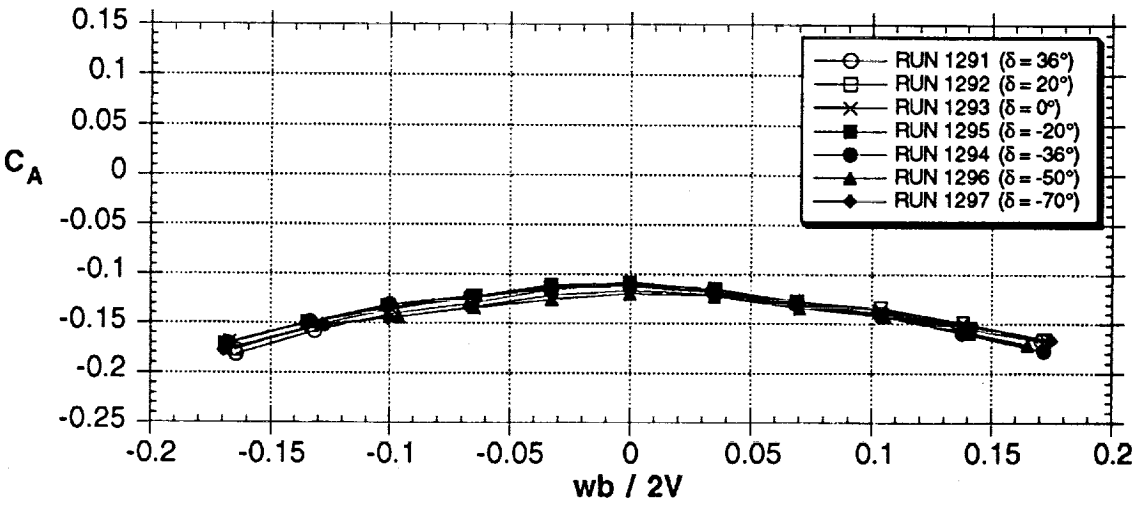

Figure 59 - Effects of vertical nose strake (Rhino-horn) at 51° AOA

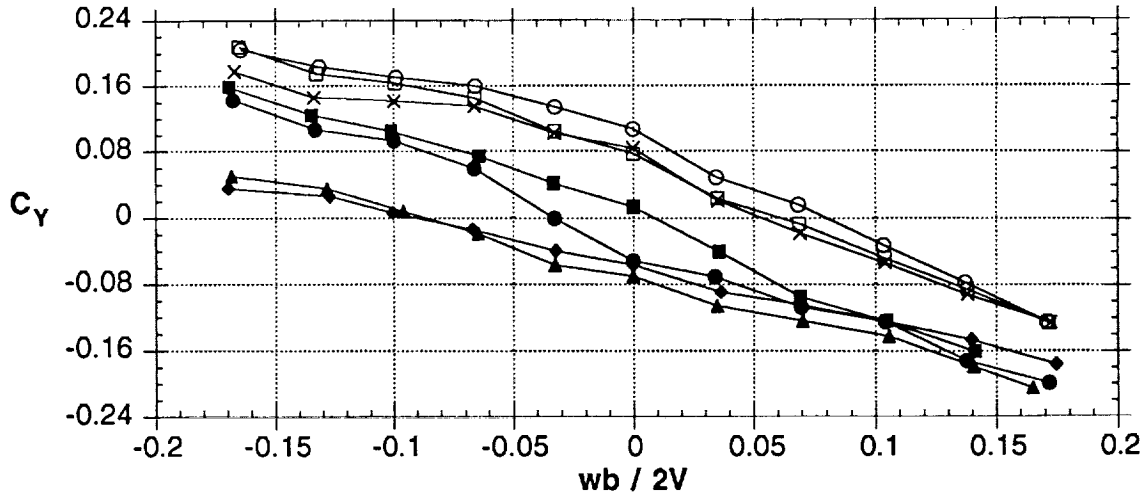

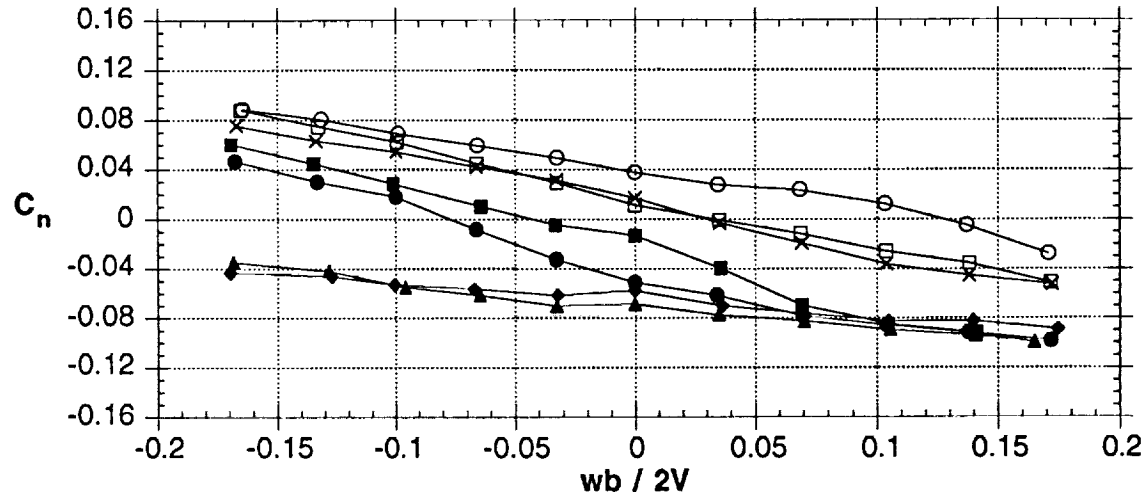

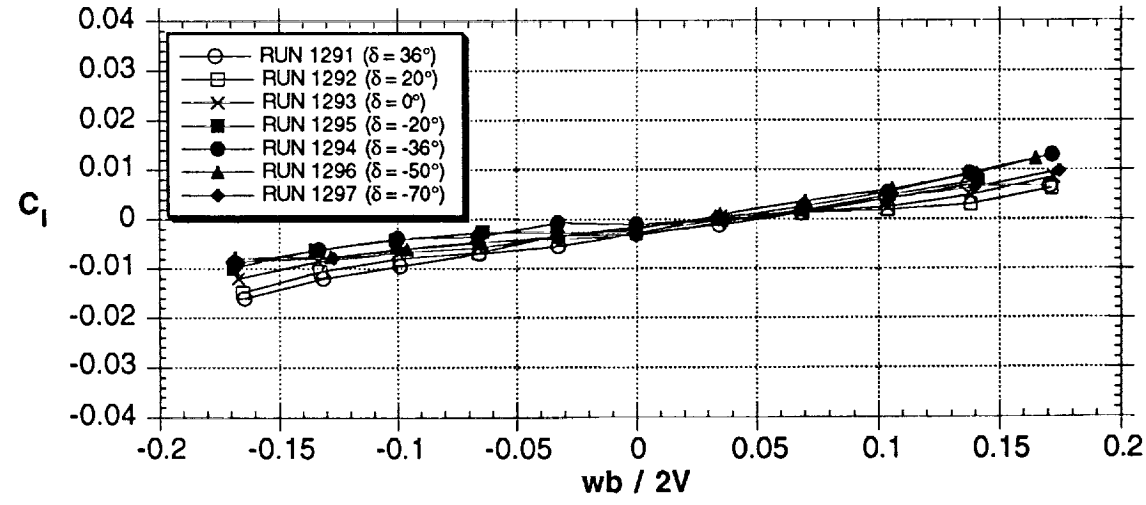

Figure 59 - Concluded

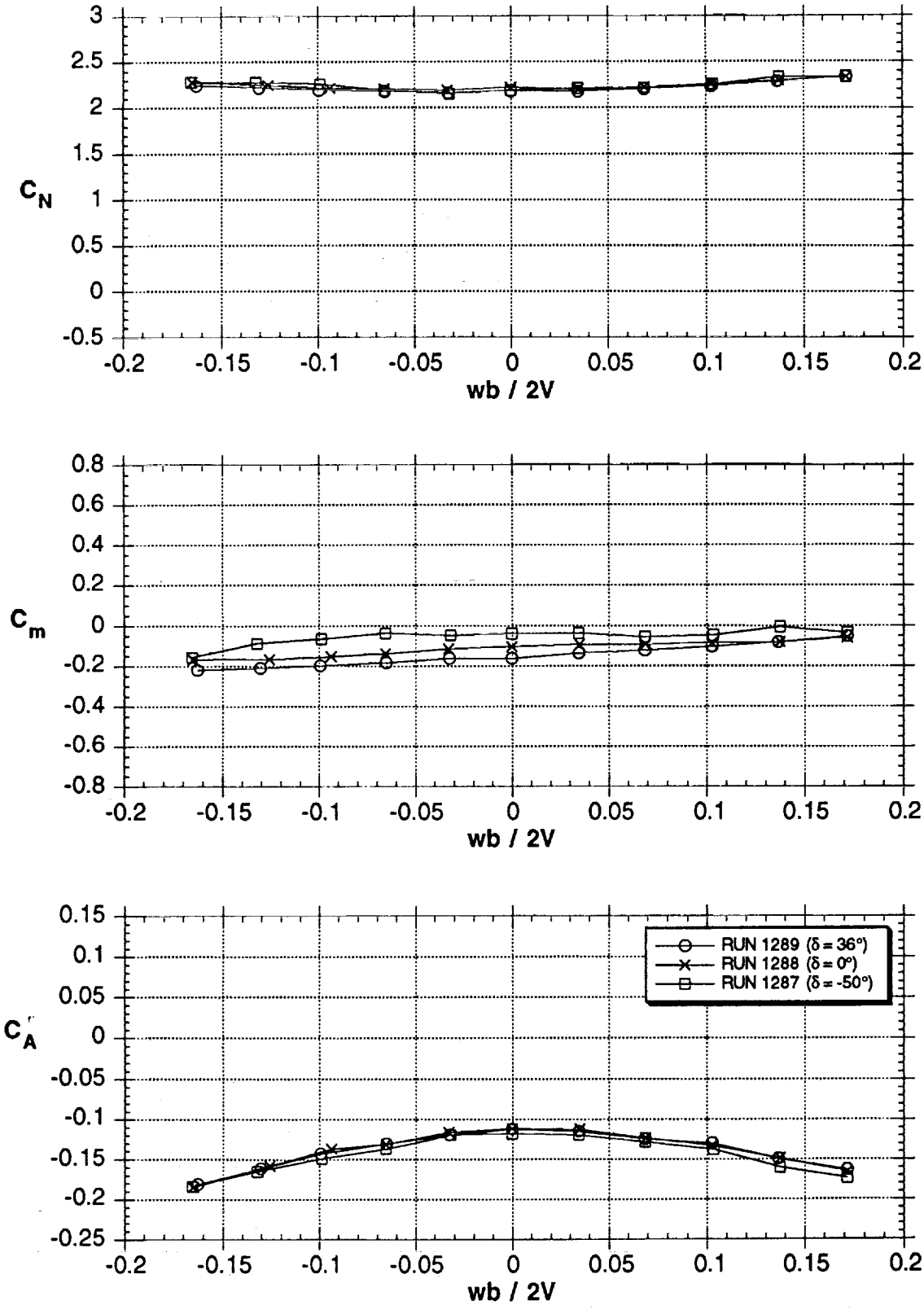

Figure 60 - Effects of vertical nose strake (Rhino-horn) at sideslip angle of β = -10°, 51° AOA

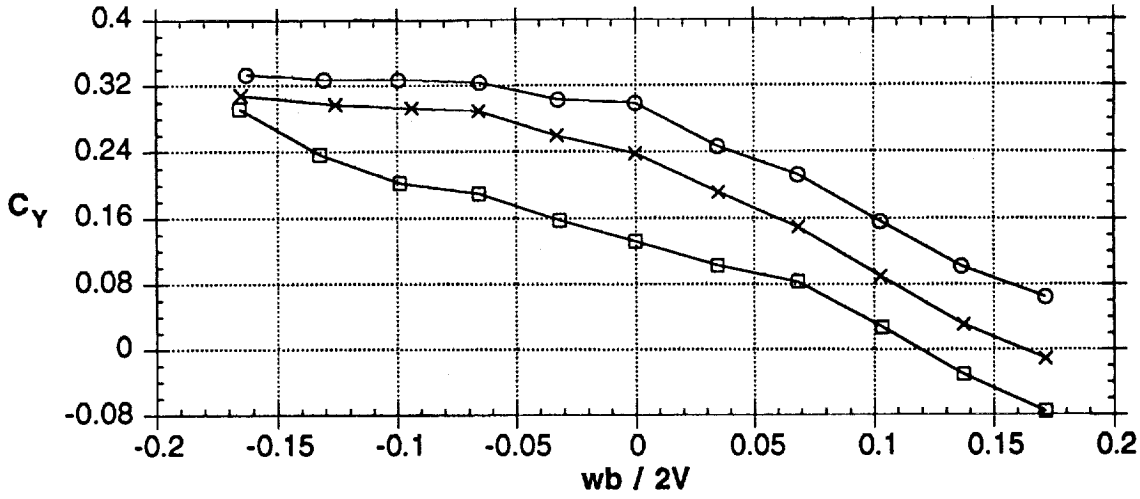

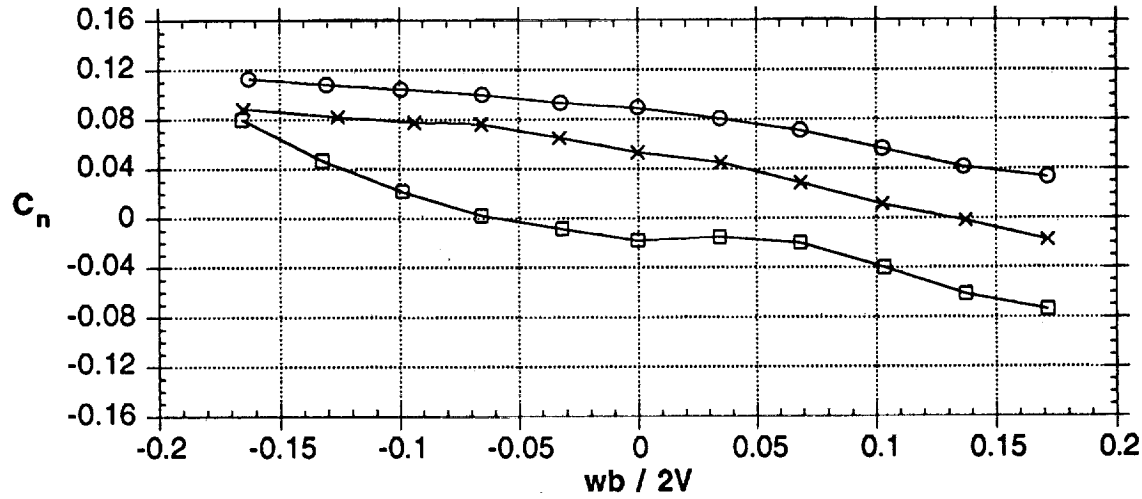

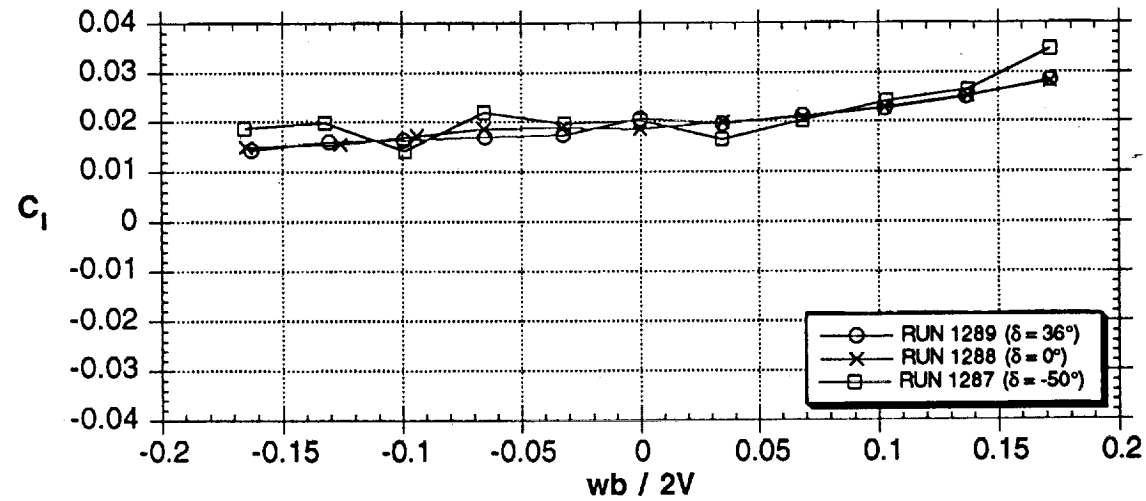

Figure 60 - Concluded

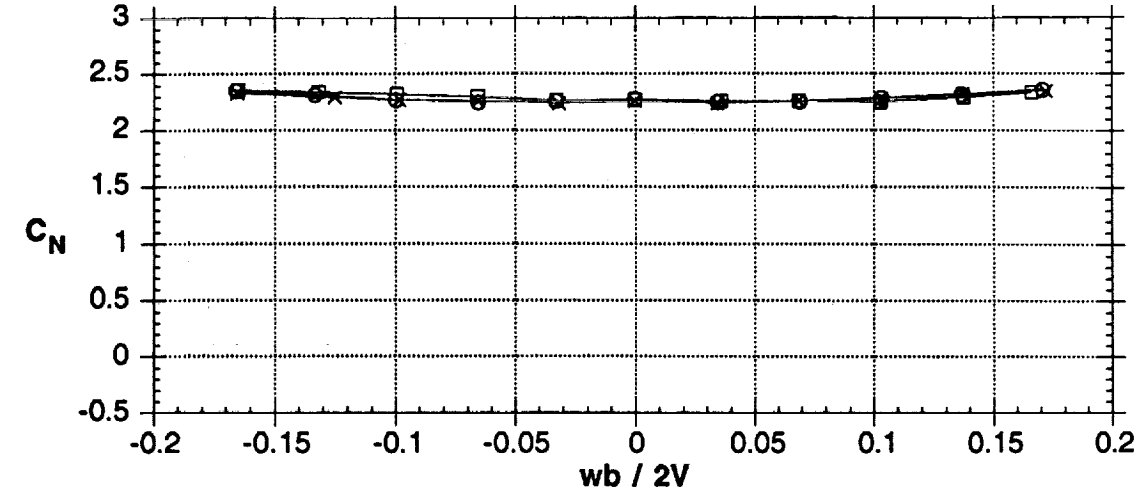

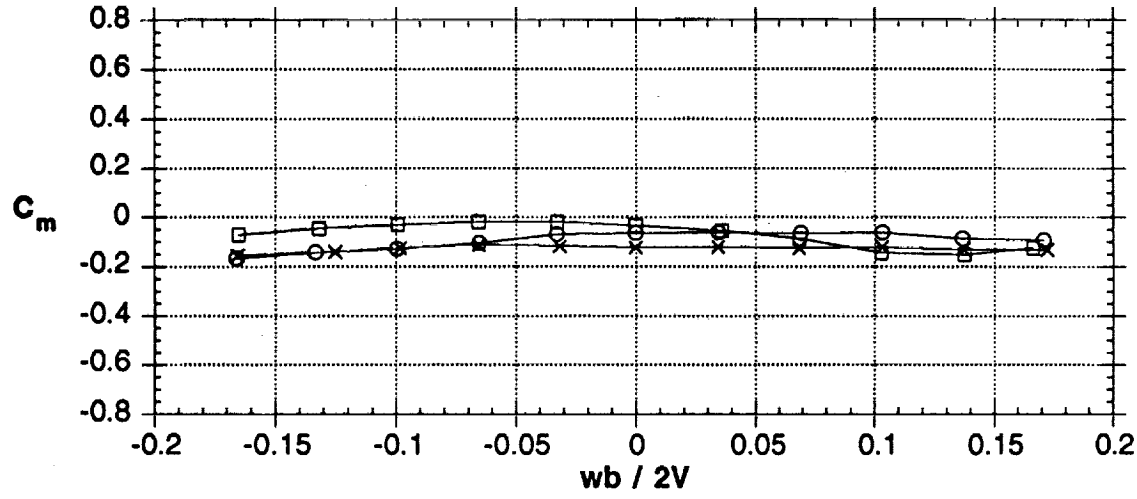

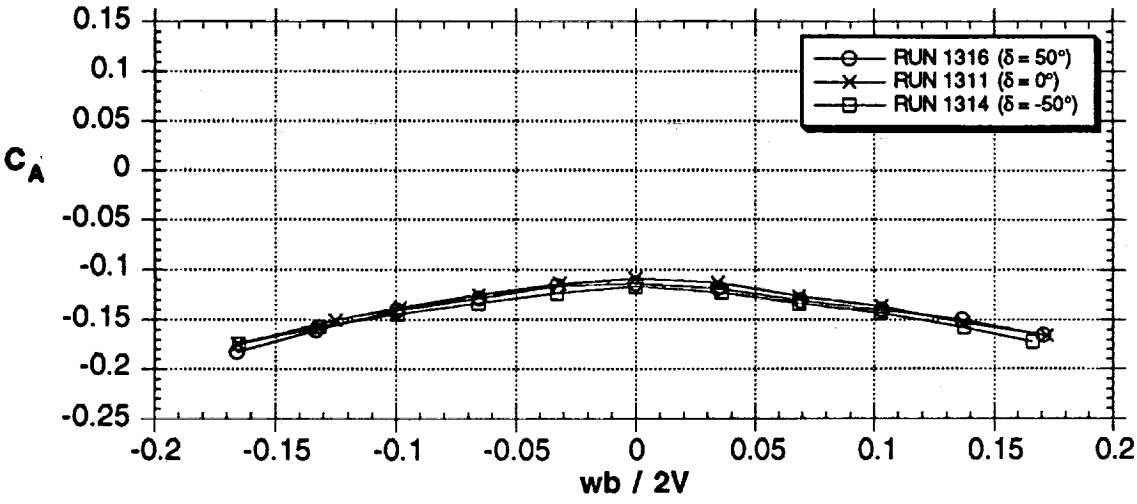

Figure 61 - Effects of modified (thin) vertical nose strake at 51° AOA

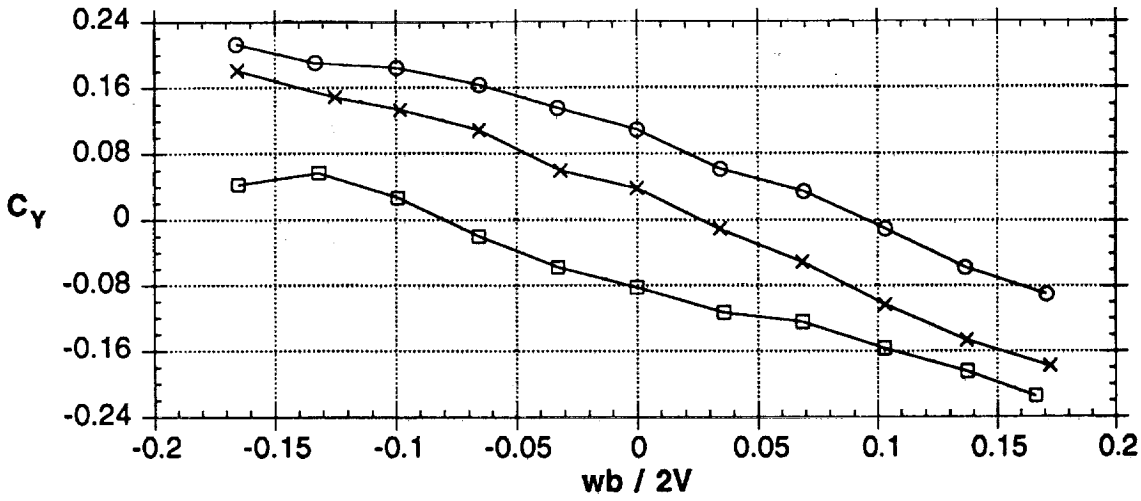

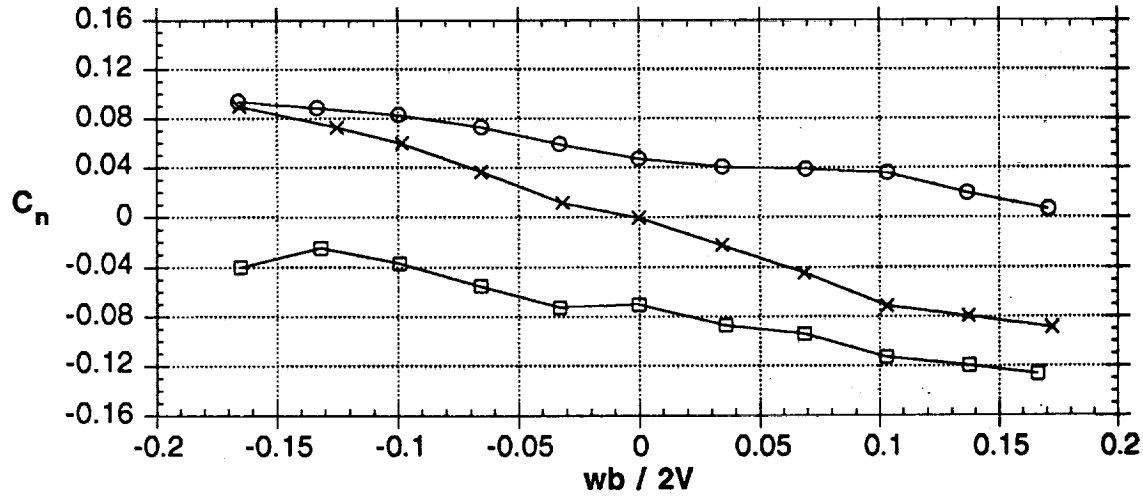

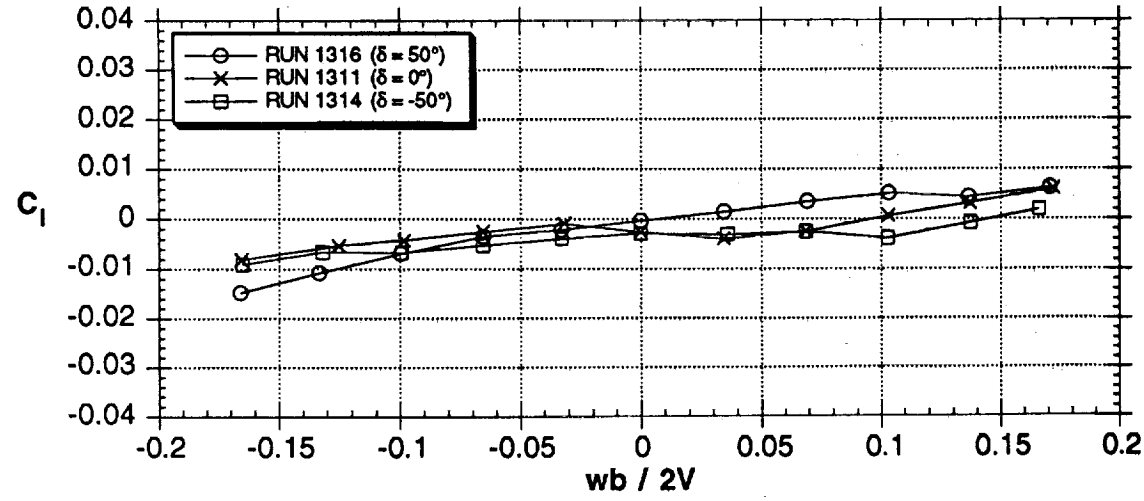

Figure 61 - Concluded

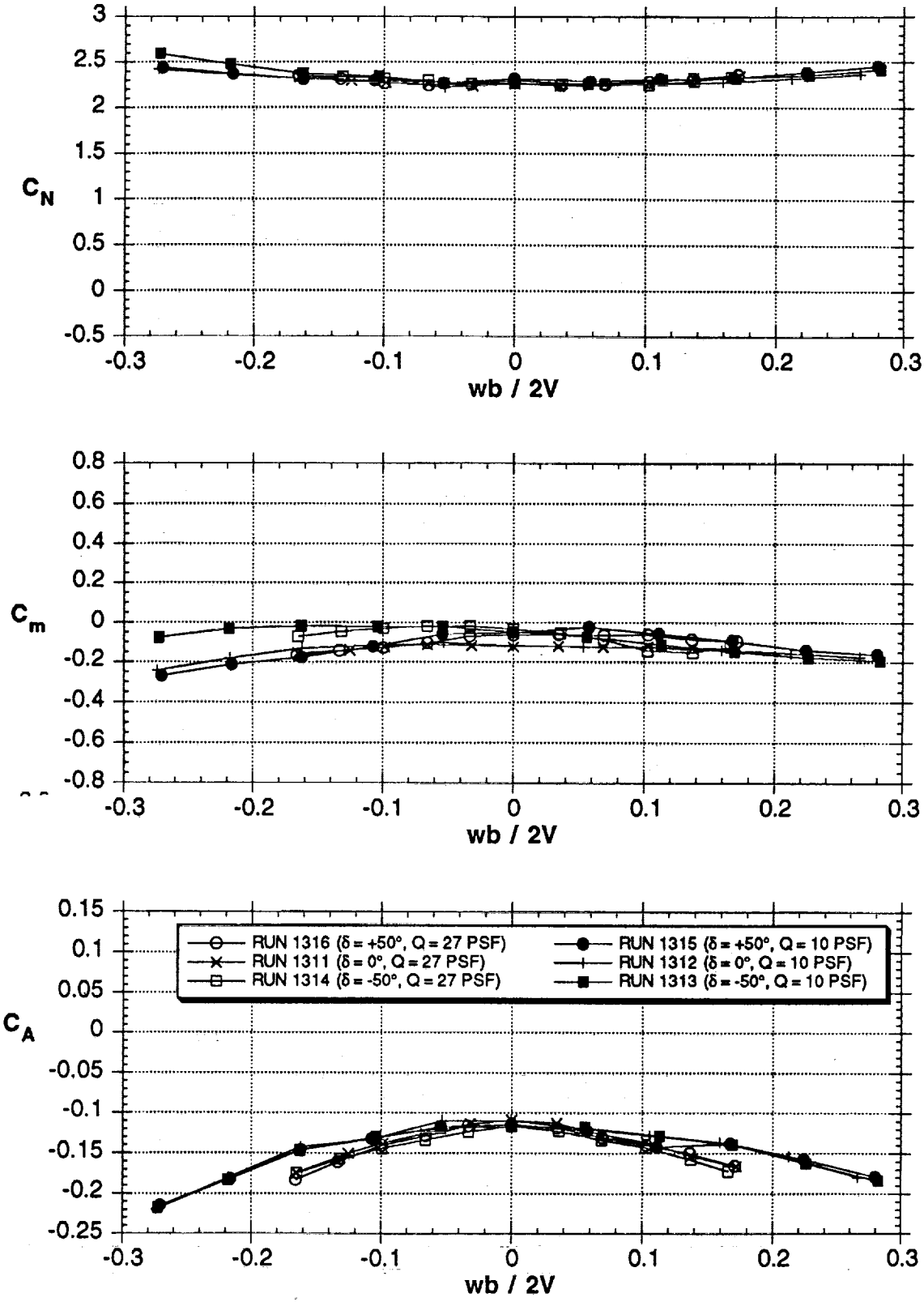

Figure 62 - Comparison of "thin" vertical nose strake at Q=10 psf (Rn=0.387x10^6) and Q=27 psf (Rn=0.636x10^6), 51° AOA

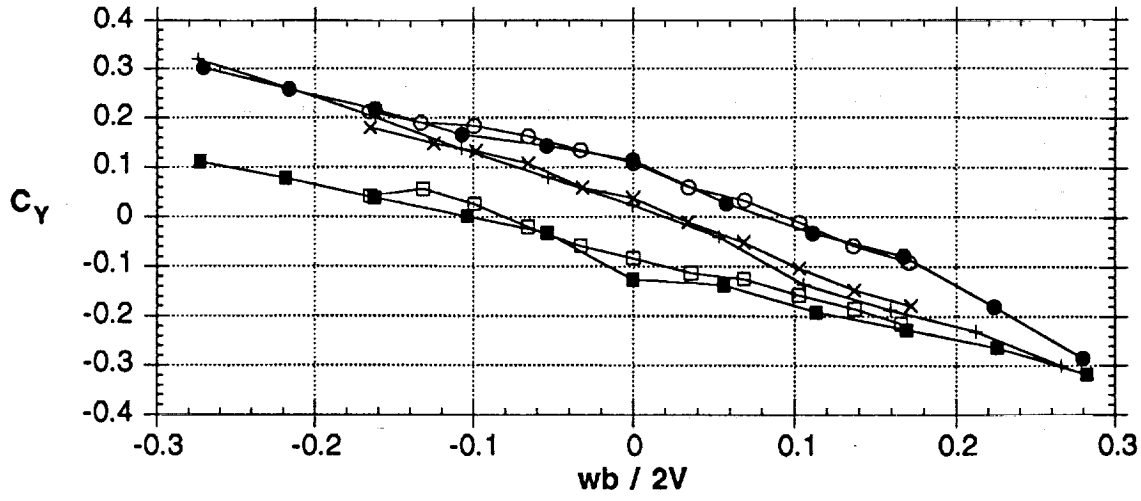

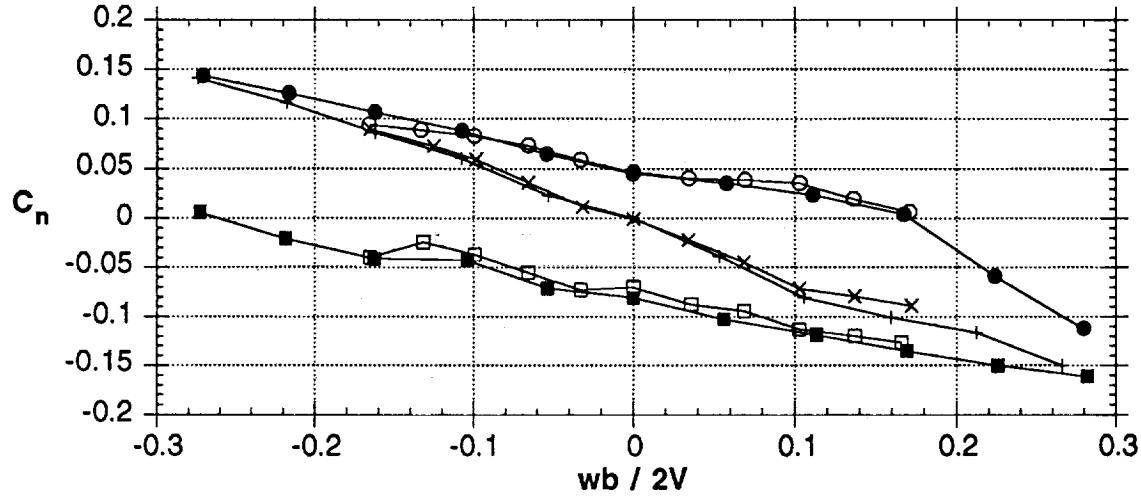

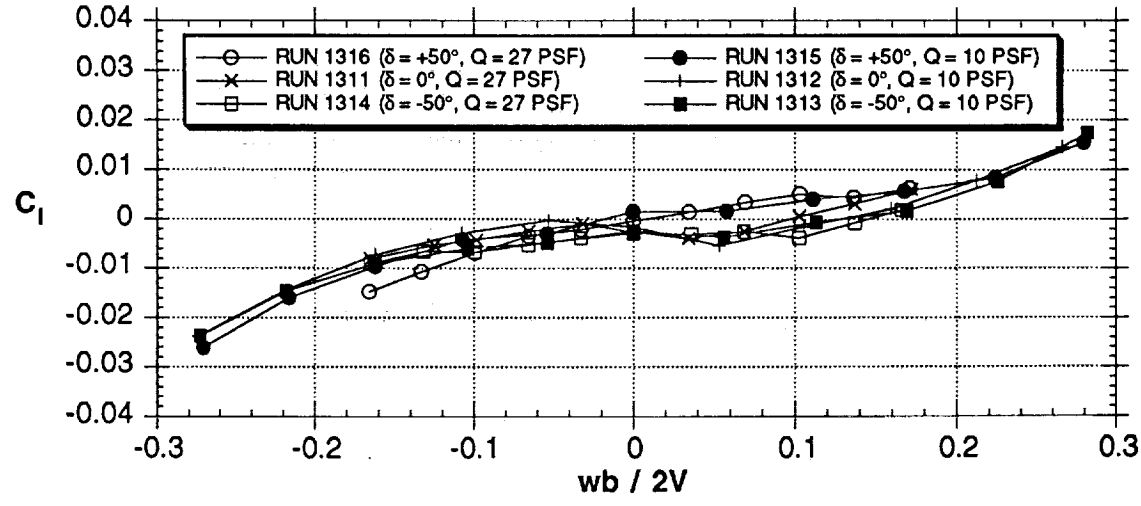

Figure 62 - Concluded

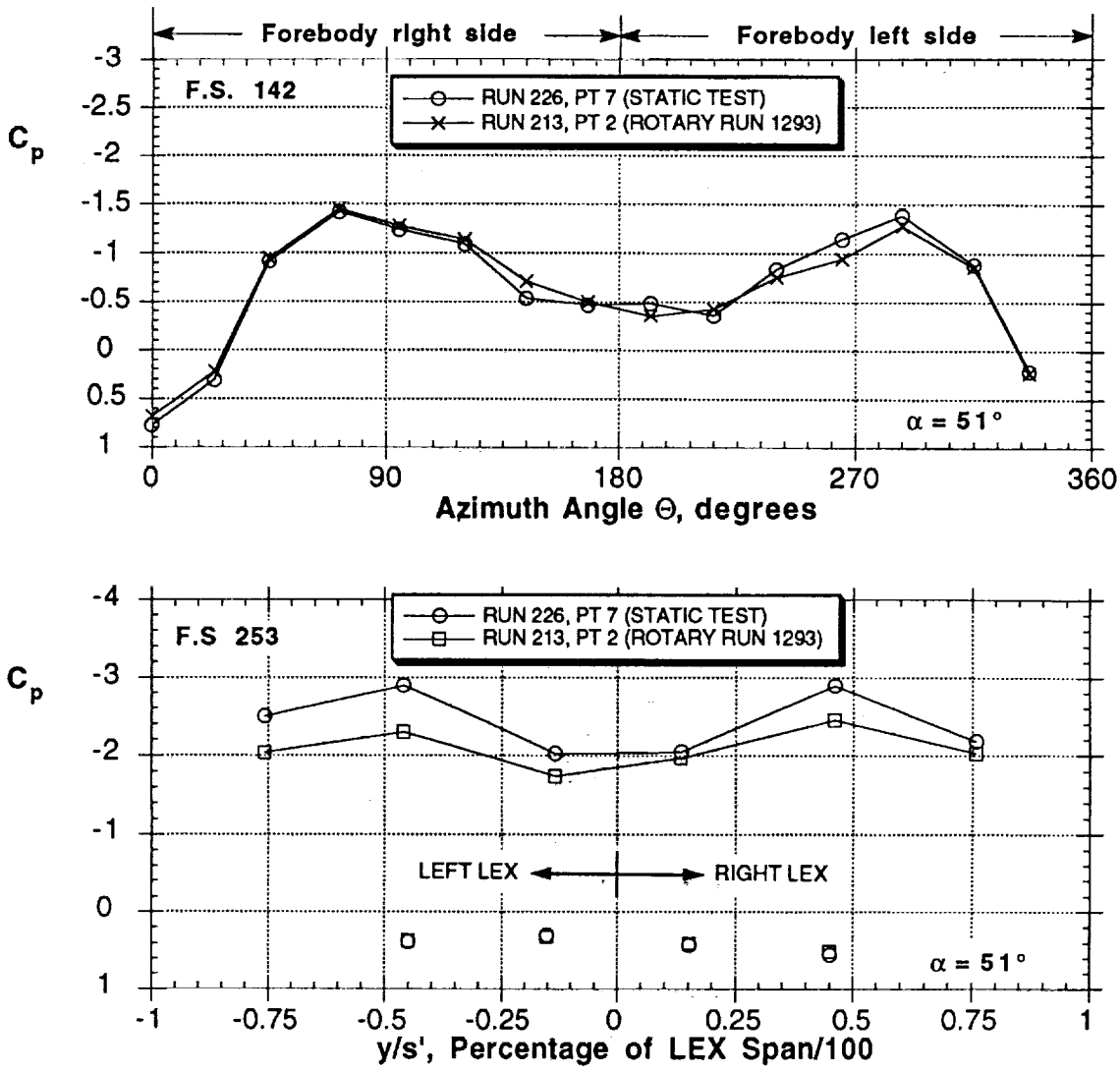

(a) Comparison to static test, $\delta = 0$

Figure 63 - Vertical nose strake pressure distribution at 51° AOA

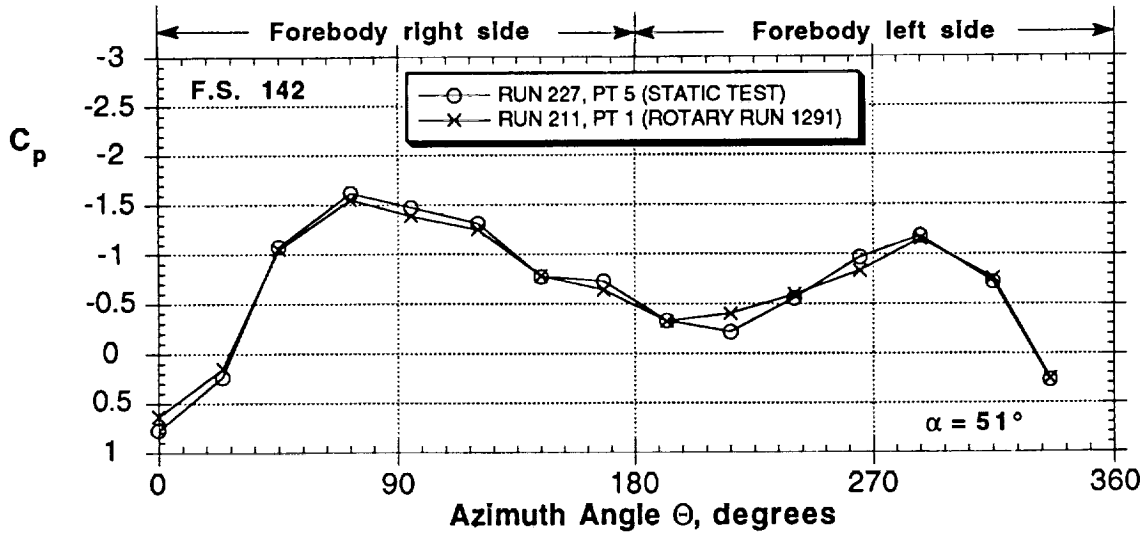

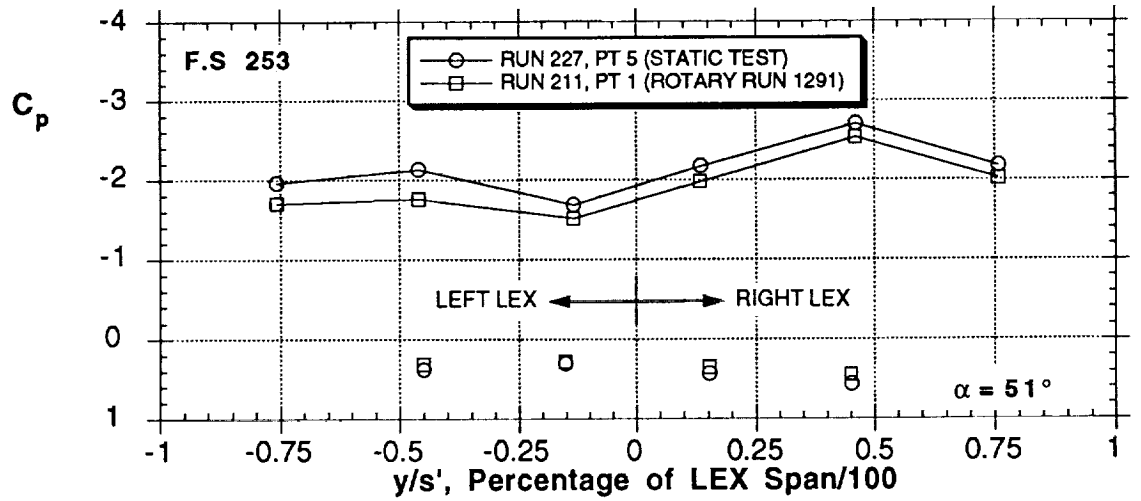

(b) Comparison to static test, δ = 36°

Figure 63 - Continued

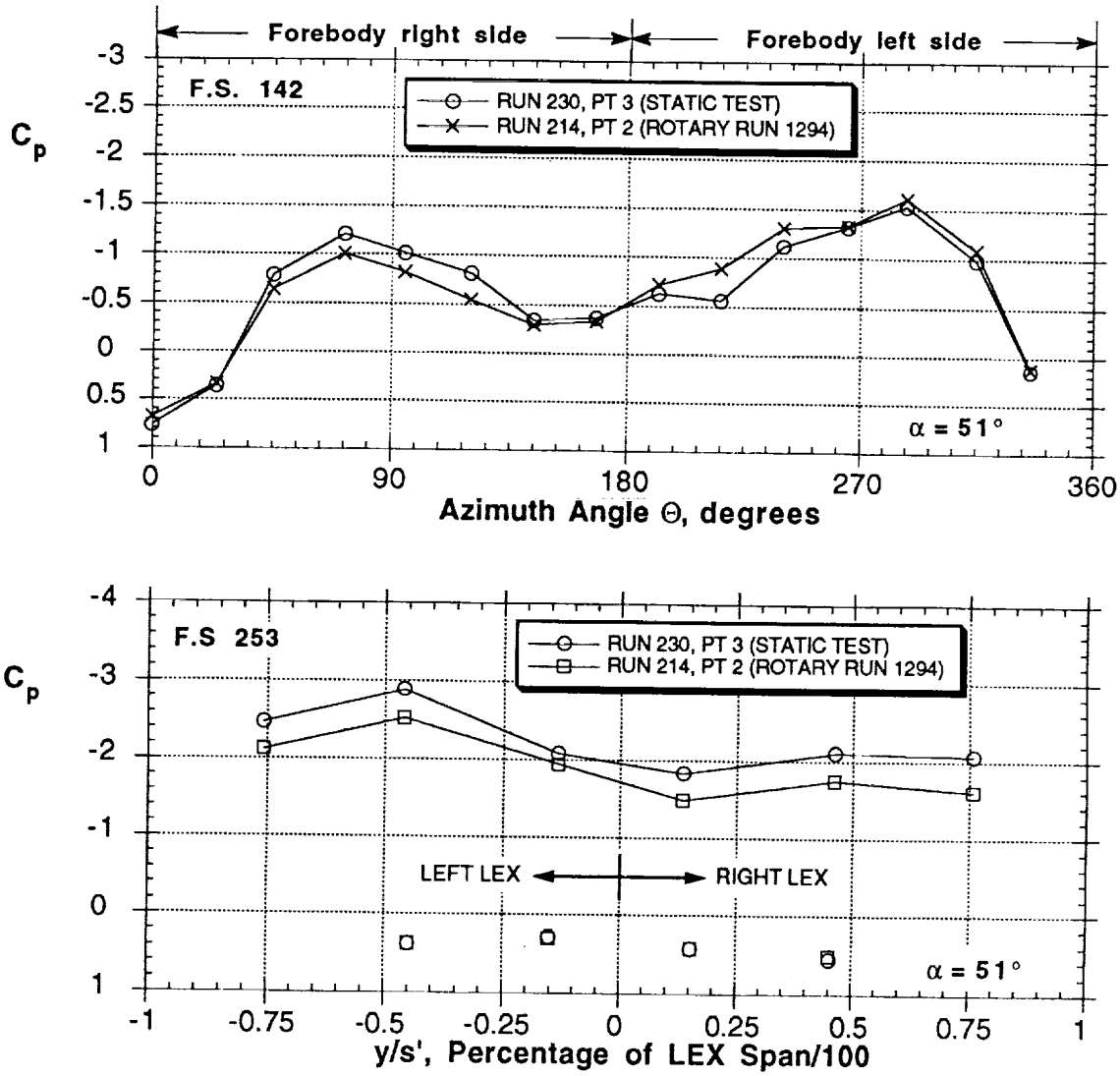

(c) Comparison to static test, δ = -36°

Figure 63 - Continued

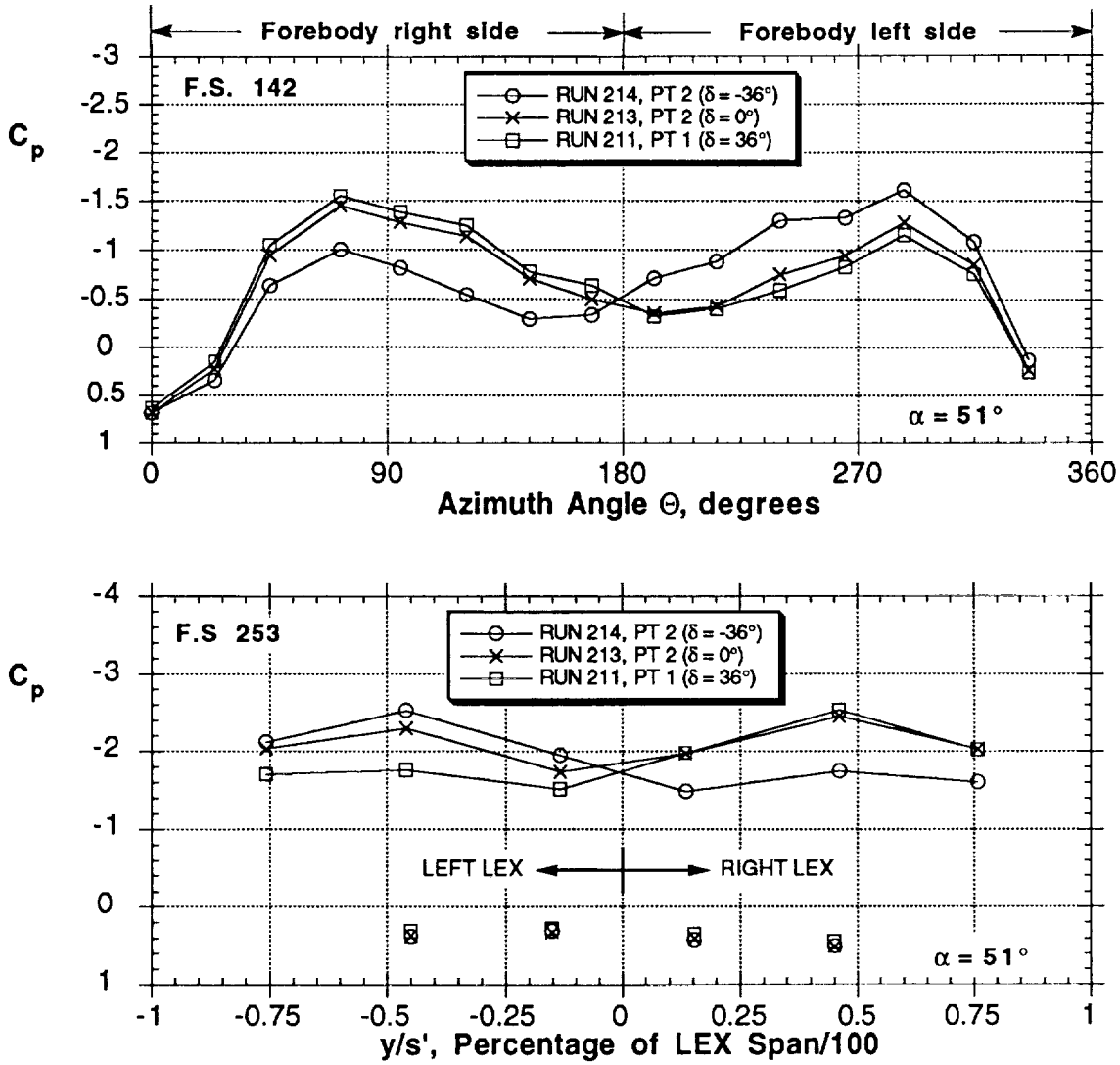

(d) Effect of strake deflection, $\omega b/2V = 0$

Figure 63 - Continued

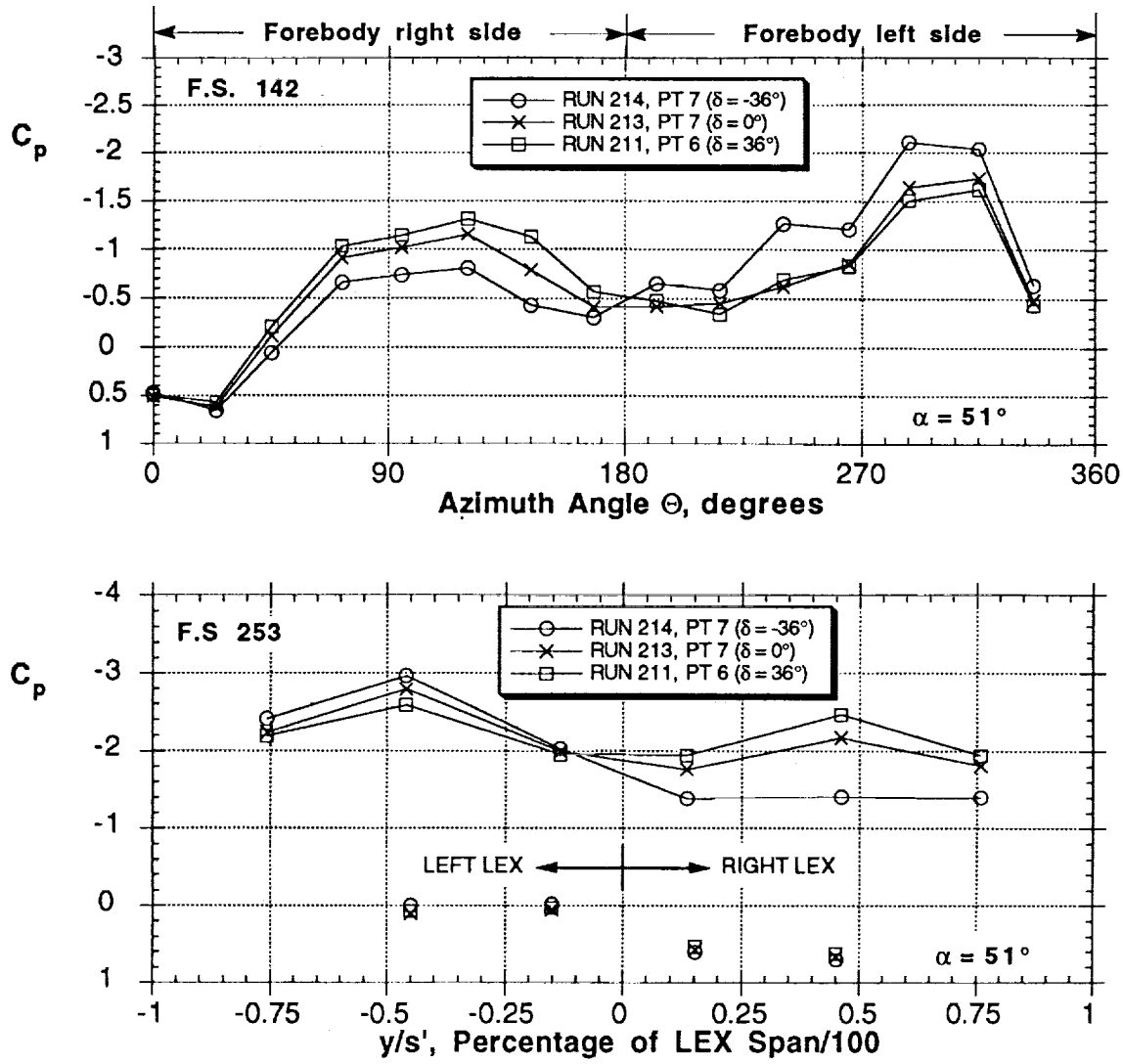

(e) Effect of strake deflection, ωb/2V = 0.15

Figure 63 - Continued

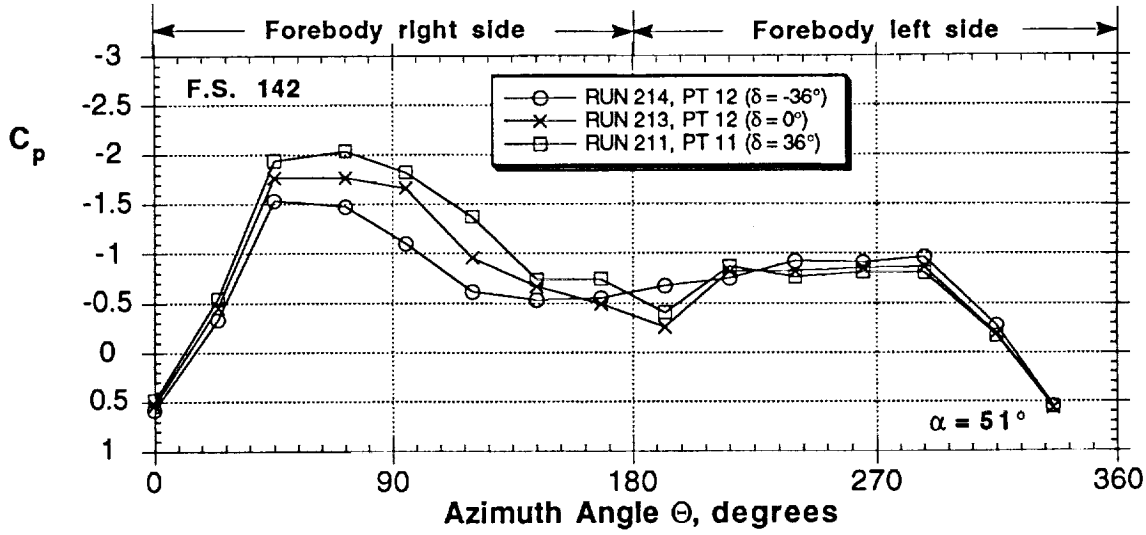

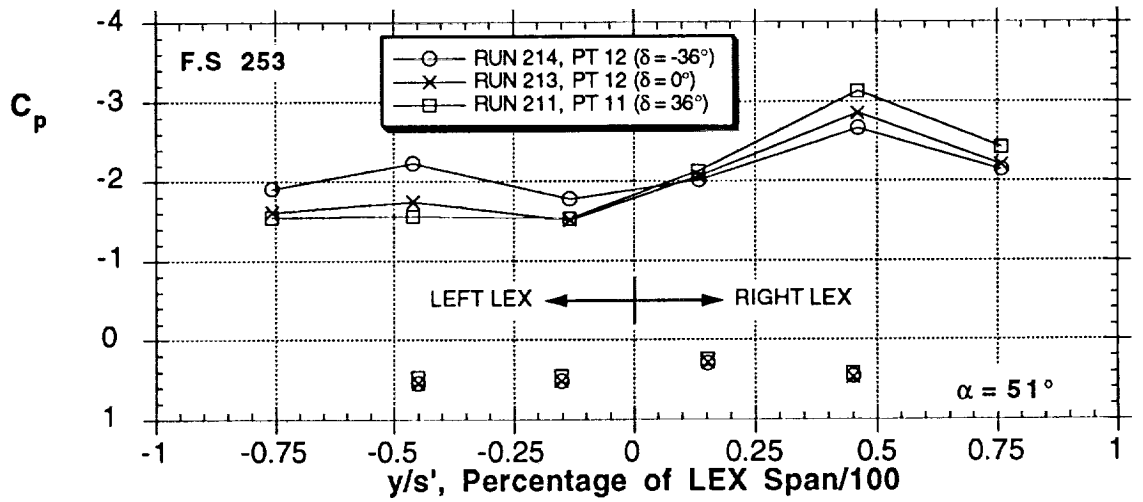

(f) Effect of strake deflection, $\omega b/2V = -0.15$

Figure 63 - Continued

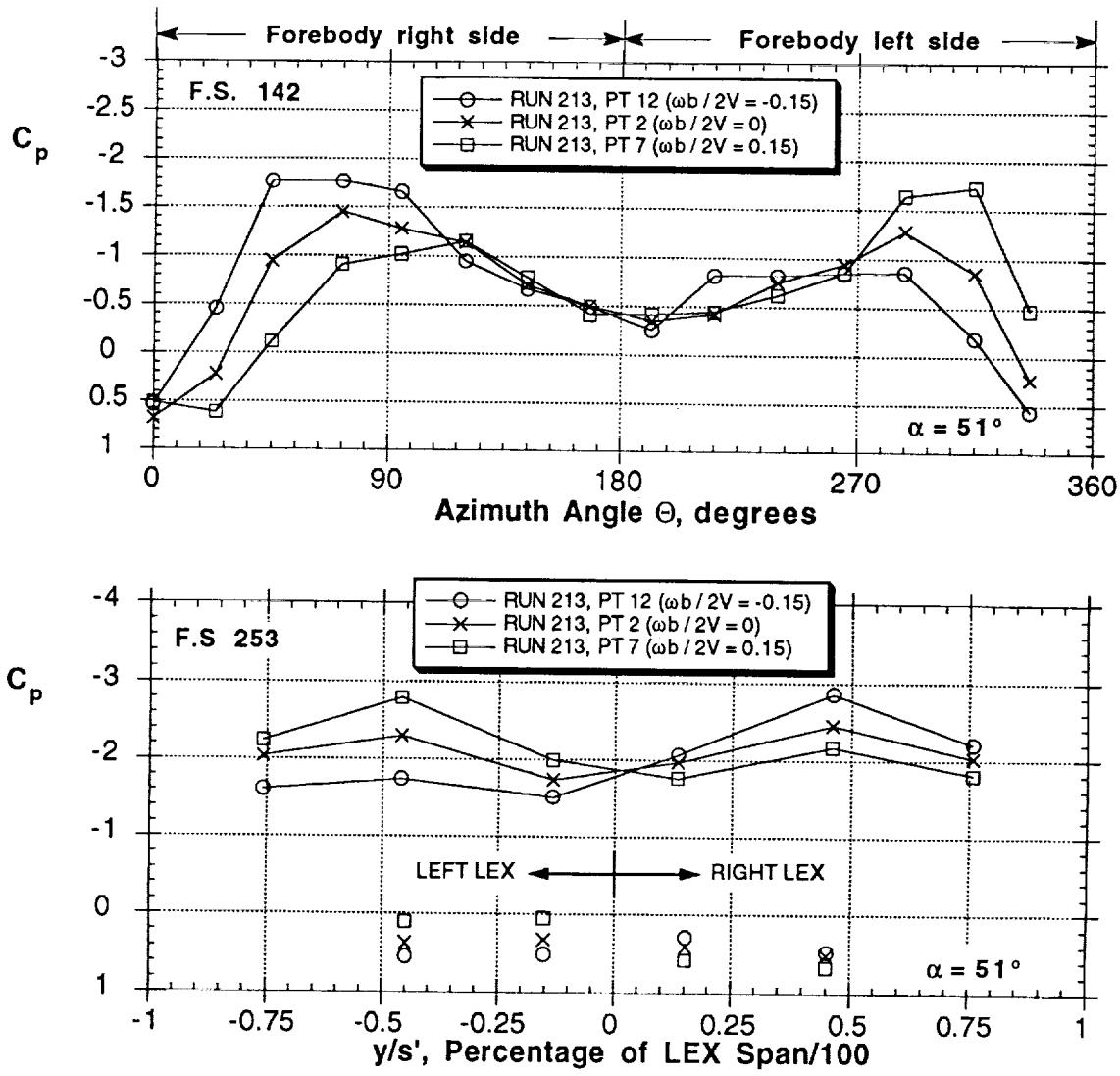

(g) Effect of $\omega b/2V$, $\delta = 0$

Figure 63 - Continued

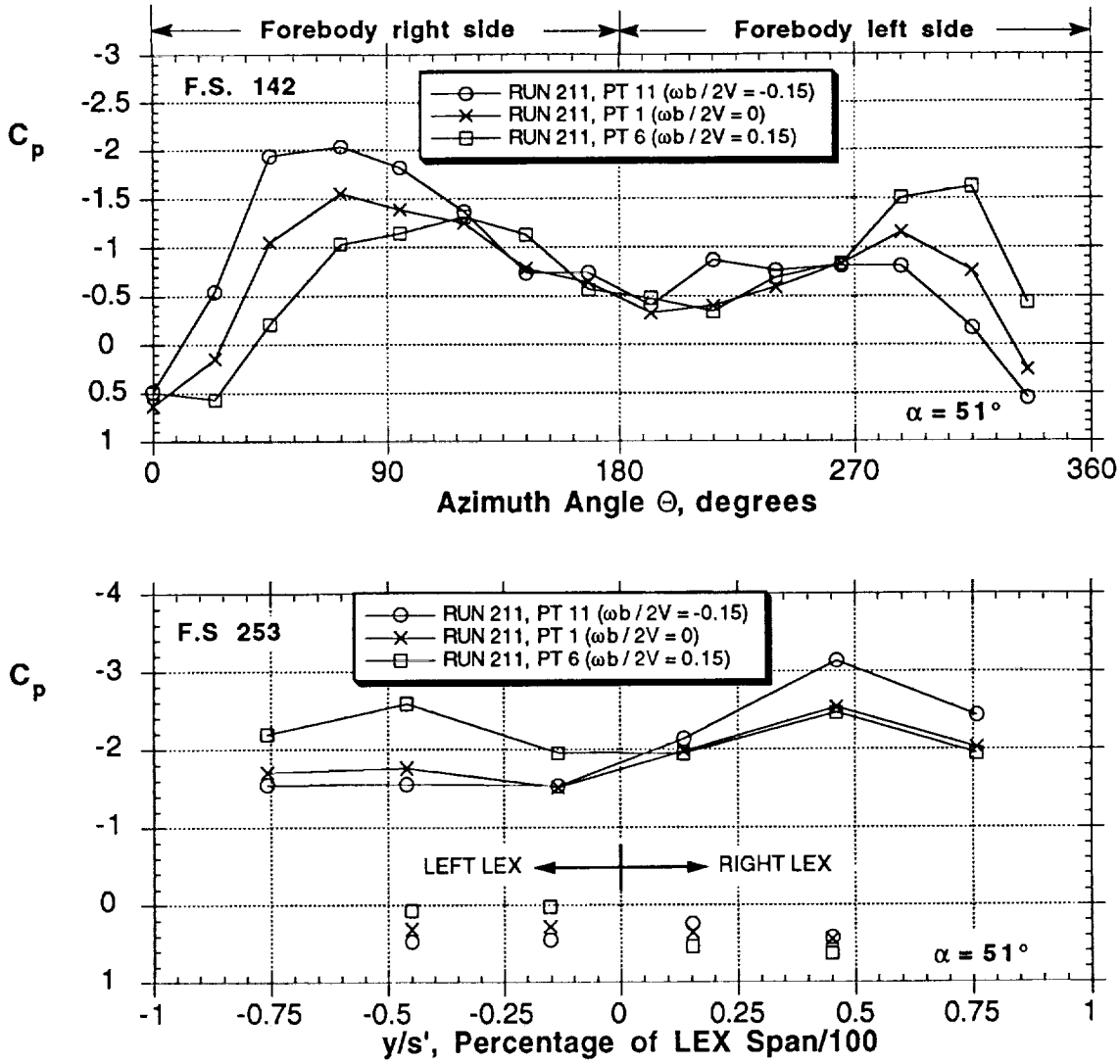

(h) Effect of ωb/2V, δ = 36°

Figure 63 - Continued

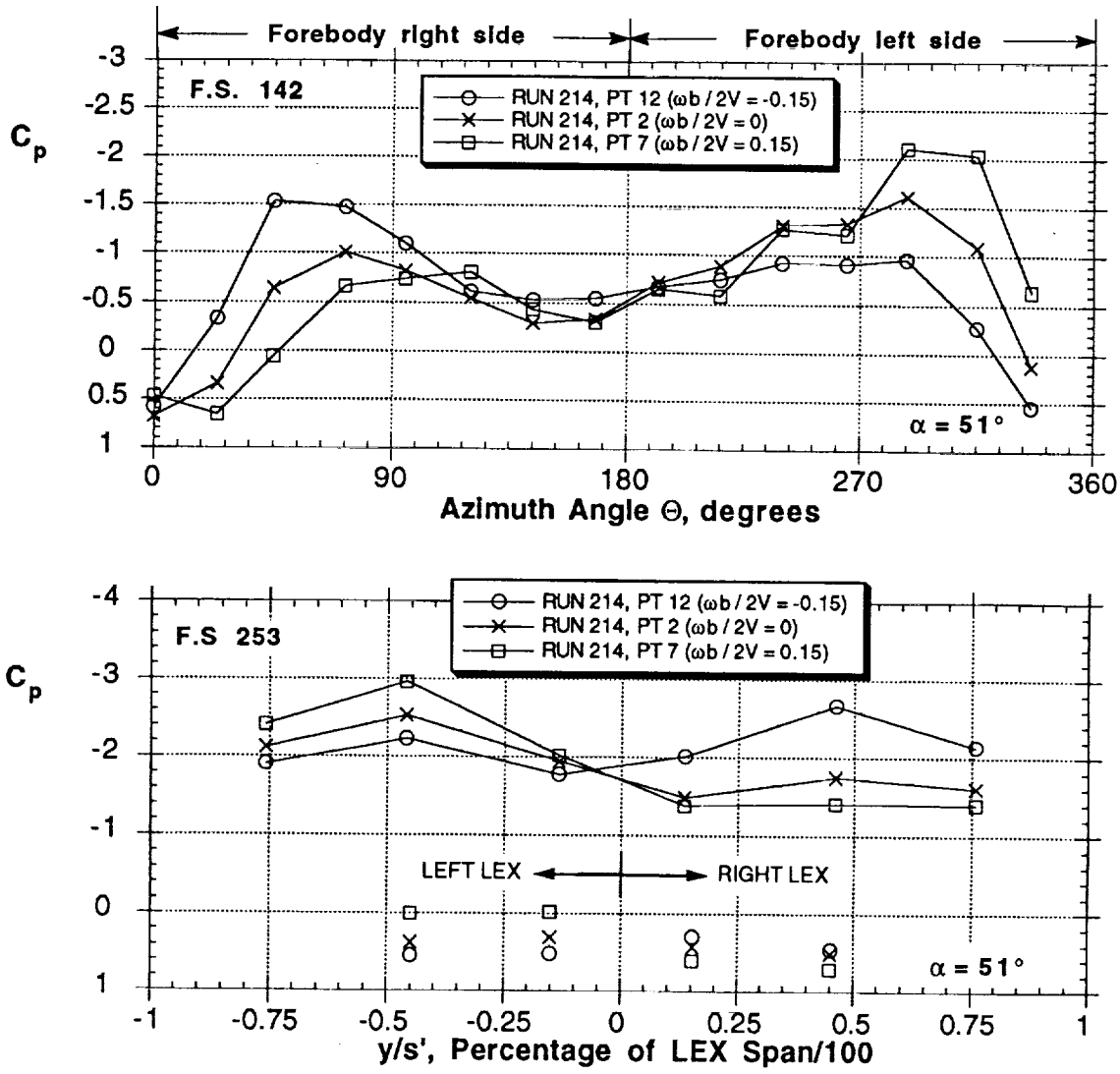

(i) Effect of ωb/2V, δ = -36°

Figure 63 - Concluded

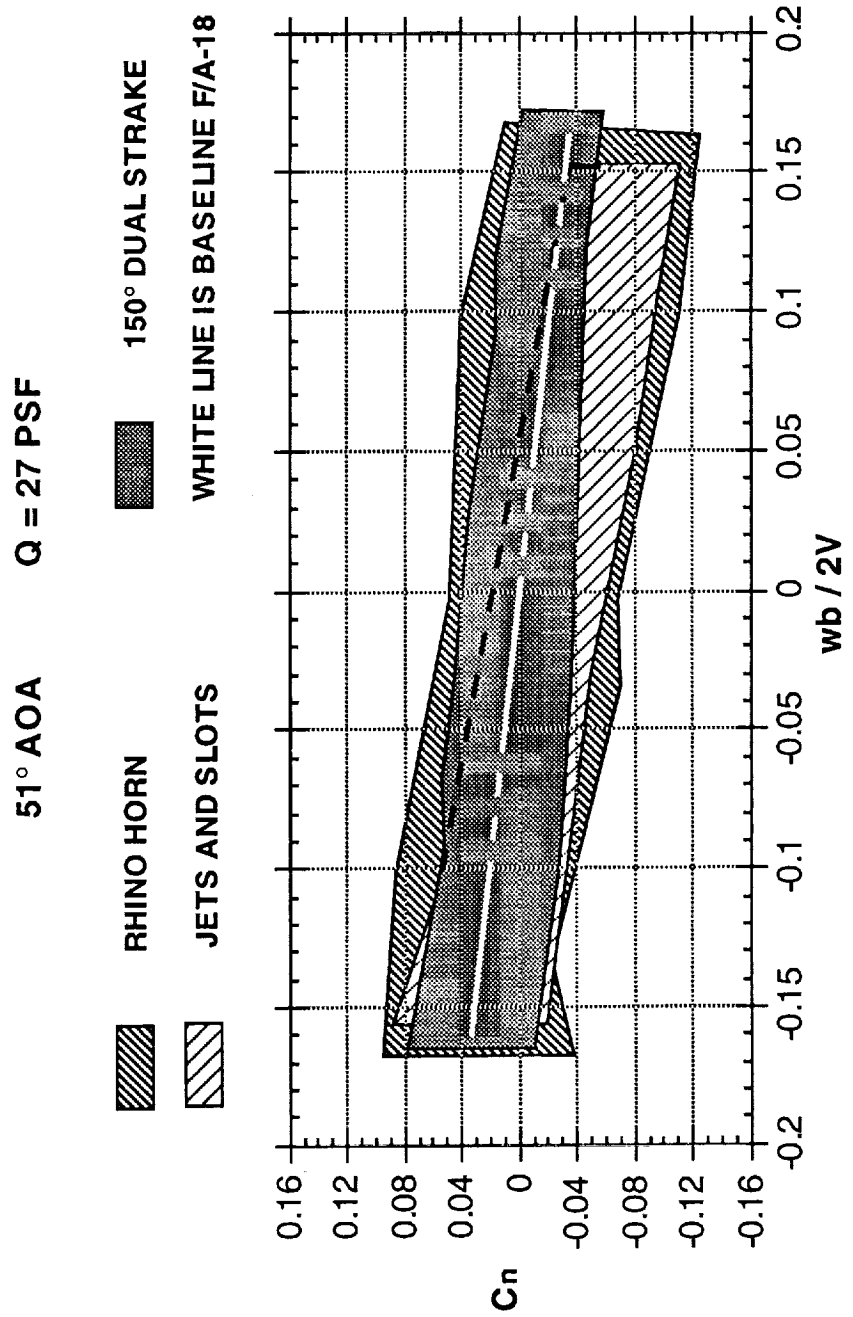

FIGURE 64: YAW CONTROL POWER ENVELOPE OF VARIOUS FVC DEVICES AT 51° AOA

REPORT DOCUMENTATION PAGE

Form Approved
OMB No. 0704-0188

1. AGENCY USE ONLY *(Leave blank)*	2. REPORT DATE	3. REPORT TYPE AND DATES COVERED
	March 1994	Contractor Report

4. TITLE AND SUBTITLE

F/A-18 Forebody Vortex Control
Volume 2—Rotary-Balance Tests

5. FUNDING NUMBERS

NAS2-13383

6. AUTHOR(S)

Brian R. Kramer, Carlos J. Suárez, Gerald N. Malcolm, and Bert F. Ayers

7. PERFORMING ORGANIZATION NAME(S) AND ADDRESS(ES)

Eidetics International, Inc.
3415 Lomita Blvd.
Torrance, CA 90505

8. PERFORMING ORGANIZATION REPORT NUMBER

A-94055

9. SPONSORING/MONITORING AGENCY NAME(S) AND ADDRESS(ES)

National Aeronautics and Space Administration
Washington, DC 20546-0001

10. SPONSORING/MONITORING AGENCY REPORT NUMBER

NASA CR-4582 – Vol-2

11. SUPPLEMENTARY NOTES

Point of Contact: Lewis Schiff, Ames Research Center, MS 258-1, Moffett Field, CA 94035-1000; (415) 604-4467

12a. DISTRIBUTION/AVAILABILITY STATEMENT

Unclassified — Unlimited
Subject Category 02

12b. DISTRIBUTION CODE

13. ABSTRACT ***(Maximum 200 words)***

A rotary-balance wind tunnel test was conducted on a six percent model of the F/A-18 at the NASA Ames 7 X 10-Foot Low Speed Wind Tunnel. The data reduction was specially written for the test in National Instruments' LabVIEW. The data acquisition, reduction and analysis was performed with a Macintosh computer. The primary objective of the test was to evaluate the effectiveness of several forebody vortex control configurations in a rotary flow field. The devices that were found to be the most effective during the static tests (Volume 1) were investigated and included both mechanical and pneumatic configurations. The mechanical systems evaluated were small, single and dual, rotating nose tip strakes and a vertical nose strake. The jet blowing configuration used nozzles canted inboard 60°. A two segment tangential slot was also evaluated. The different techniques were evaluated at angles of attack of 30°, 45°, 51°, and 60°. Sideslip and Reynolds number were varied for some of the configurations. All of the techniques proved to be effective in the rotating flow field. The vertical nose strake had the largest "envelope" of effectiveness. Forebody vortex control provides large, robust yawing moments at medium to high angles of attack, even during combat maneuvers such as loaded roll.

14. SUBJECT TERMS	15. NUMBER OF PAGES
F/A-18, Forebody vortex control (FVC), Rotary balance, Vortex, Wind tunnel test	217
	16. PRICE CODE: A10

17. SECURITY CLASSIFICATION OF REPORT	18. SECURITY CLASSIFICATION OF THIS PAGE	19. SECURITY CLASSIFICATION OF ABSTRACT	20. LIMITATION OF ABSTRACT
Unclassified	Unclassified		